

University of Southampton Research Repository ePrints Soton

Copyright © and Moral Rights for this thesis are retained by the author and/or other copyright owners. A copy can be downloaded for personal non-commercial research or study, without prior permission or charge. This thesis cannot be reproduced or quoted extensively from without first obtaining permission in writing from the copyright holder/s. The content must not be changed in any way or sold commercially in any format or medium without the formal permission of the copyright holders.

When referring to this work, full bibliographic details including the author, title, awarding institution and date of the thesis must be given e.g.

AUTHOR (year of submission) "Full thesis title", University of Southampton, name of the University School or Department, PhD Thesis, pagination

University of Southampton

Printable Thermoelectric Devices for Energy Harvesting

By

Zhuo Cao

A thesis submitted in partial fulfilment for the degree of Doctor of Philosophy

In the

Faculty of Physical Science and Engineering
Electronics and Computer Science

October, 2014

Abstract

This thesis describes the approaches of fabricating and testing thermoelectric generators (TEG) using screen printing. It includes the formation of the pastes, optimizing of the manufacture processes and the measurement of the thermoelectric properties.

A nickel/copper based high temperature TEG was made to demonstrating the screen printing can be applied to fabricate thermoelectric materials. A bismuth/antimony based low temperature TEG was fabricated to identify the proper polymer binder for low temperature TEG application. A flexible bismuth tellurium/antimony tellurium low temperature TEG with 4 thermocouples was presented with a generated voltage of 23 mV and an output power of 194 nW when ΔT =20°C. Moreover, a dispenser printed structured TEG was also demonstrated for its ability to achieve 3D structured thermocouples with a thickness of 500 μ m.

The objective of this work involves developing screen printable thermoelectric material pastes and suitable processes; a proper approach to transfer the printed TEGs from rigid substrate onto flexible substrate (Kapton). The flexibility allows the printed TEGs to be applied on heat sources with curved surface, such as, human body. An additional research on the interface material of textile is also presented.

Contents

Chapter	1.	Introduction	1
1.1	Ove	erview of research	1
1.2	Obj	ective and scope of the research	2
1.3	Do	cument structure	3
1.4	Nov	velty statement	4
Chapter	2.	Theoretical background	5
2.1	Intr	oduction	5
2.2	Prir	nciples of thermoelectric devices	5
2.2	.1	The Seebeck effect	5
2.2	.2	The Peltier effect	8
2.2	.3	The Kelvin relationship	9
2.3	Eva	aluation of thermoelectric properties	10
2.3	.1	Electrical resistivity and Hall coefficient measurement	11
2.3	.2	Thermal conductivity measurement	12
2.3	.3	Seebeck coefficient measurement	13
2.3	.4	Summary of the properties of some commonly used materials for TEGs	14
2.3	.5	Power output, conversion efficiency and figure of merit	15
2.4	Stru	acture of thermoelectric devices	18
2.5	Sur	nmary	20
Chapter	3.	Literatures of TEGs, printed TEGs and its application	22
3.1	Intr	oduction	22
3.2	Mic	cro-fabricated thermoelectric generators	22
3.2	.1	Micro-fabricated TEGs in literature	24
3.2	.2	Discussion	29
3.3	Thi	ck film technologies	30
3.3	.1	Screen printing technology	30
3.3	.2	Dispenser printing technology	34
3.4	Prir	nted thermoelectric generator devices	36
3.4	.1	Printed TEGs in literature	36
3.4	.2	Discussion	44
3.5	App	plications of thermoelectric generators on the human body	46
3.5	.1	Human body TEGs in literature	46
3.5	2	Discussion	49

3.6	Summary and discussion	50
Chapter	4. High temperature curing copper and nickel based thermocouples	52
4.1	Introduction	52
4.2	Experimental analysis of screen printed nickel thick films	52
4.2.	.1 Experiment procedure	52
4.2.	.2 Nickel thick film paste formation and adhesion improvements	53
4.2.	.3 Nickel thick film characterisation	60
4.3	Experimental analysis of copper paste	63
4.3.	.1 Copper thick-film pattern formation	63
4.3.	.2 Copper thick film characterisation	66
4.4	Screen printed Ni/Cu thermocouples	69
4.5	Summary and discussion	76
Chapter	5. Low temperature curing copper and nickel based thermocouples and	d
evaluati	ion of the interface material of the textile	78
5.1	Introduction	78
5.2	Low temperature curing copper paste	79
5.2.	.1 Polyurethane binder based copper paste	80
5.2.	.2 Silicone binder based copper paste	81
5.2.	.3 Epoxy binder based copper paste	83
5.3	Low temperature curing nickel paste	85
5.4	Low temperature curing nickel/copper based thermocouples	87
5.5	Failure analysis of low temperature Ni/Cu thermocouples	89
5.6	Approaches to textile surface treatment for depositing electronics	90
5.7	Quality of adhesion of silicone interface layer improvement	92
5.8	Summary and discussion	98
Chapter	6. Screen printing bismuth and antimony based thermocouples	99
6.1	Introduction	99
6.2	Experimental analysis of screen printed Bi thick films	99
6.3	Experimental analysis of screen printed Sb thick films	.104
6.4	Bismuth and Antimony based thermocouples	.107
6.5	Safety handling and processing in experiment	.111
6.6	Summary and discussion	.111
Chapter	7. Screen-printed flexible BiTe/SbTe based thermoelectric generator	. 114
7.1	Introduction	.114
7.2	Development of the screen printable BiTe and SbTe paste	.114

7.3	Bi	Γe/SbTe based thermocouples	119
7.4	De	vice characterization results	121
7.5	Su	mmary and discussion	124
Chapter structur		Dispenser printed BiTe/SbTe based TEGs with 3-Dimentional (3D 127))
8.1	Int	roduction	127
8.2	Ful	lly dispenser printed 3D-structured TEGs	128
8.2	2.1	Experiment set-up	128
8.2	2.2	Fabrication of TEGs	129
8.2	2.3	Measurement and results	133
8.3	To	p electrodes-binding dispenser printed TEGs	138
8.4	Dis	scussion and future work	140
Chapte	r 9.	Conclusion and future work	144

List of Figures

Figure 2.1 Schematic of the Seebeck effect in a thermocouple	5
Figure 2.2 An illustration of the voltage generated by carriers moving under a	
temperature gradient and the energy band	6
Figure 2.3 Schematic of Peltier effect	
Figure 2.4 Schematic of Thomson effect Error! Bookmark not defin	ned.
Figure 2.5 Principle of Hall effect measurement Error! Bookmark not defin	ned.
Figure 2.6 Principles of the Seebeck coefficient measurement	13
Figure 2.7 The schematic variation of Seebeck coefficient, electrical conductivity	r
and thermal conductivity depending on the increase of carrier concentration from	
insulator to metal [21]	14
Figure 2.8 Single thermocouple with load resistance	15
Figure 2.9 An equivalent circuit of thermoelectric generator with load resistor	16
Figure 2.10 s/ $(1+s)^2$ vs. s curve when s in the range from 0.5 to 1.5	16
Figure 2.11 Thermoelectric figure of merit for a number of thermoelectric materia	als
varying with temperature (a) n-type materials, (b) p-type materials [25]	18
Figure 2.12 Schematic of common thermoelectric generator devices [26]	19
Figure 2.13 Power output per area and conversion efficiency vs. the thermocouple	e
length at different temperature gradients [13]	20
Figure 3.1 Schematic of BiCMOS thermocouples realization [29]	25
Figure 3.2 Thermocouples fabrication process of the SEIKO wristwatch [34]	26
Figure 3.3 Schematics of the Cu-Ni thermocouples on Kapton, fabricated by	
photolithography and evaporation [36]	28
Figure 3.4 A flexible Bi-Te based μTEG. (a): SEM image of the vertically grew	
thermocouples. (b): up view of the completed TEGs and Au interconnections [38]	3].
	29
Figure 3.5 A co-sputtered thin film SbTe/BiTe μ TEG. (a): μ TEG on Kapton. (b):	
schematic of the thin film μTEG . [40]	
Figure 3.6 Diagram of screen printing process	
Figure 3.7 Illustration of pattern deposition by screen printing	
Figure 3.8 Schematic of a dispenser printer [51]	
Figure 3.9 Examples of needles and corresponding inner diameters used in disper	
printing	
Figure 3.10 Illustration of pattern realization by dispenser printing	
Figure 3.11 Thermocouples printed on polyester substrate [55]	
Figure 3.12 Process flow of a thermoelectric module fabricated using screen-prin	_
[27]	
Figure 3.13 Schematic of the coiled-up TEG [58]	39
Figure 3.14 Printed thermoelectric devices (a) on alumina substrate, and (b) on	
polymer substrate[59]	41

Figure 3.15 Images of (a) dispenser printed 50-couple planar thermoelectric device
on a flexible polyimide substrate and (b) coiled prototype with electrical connections
[60]42
Figure 3.16 Fabrication process for a planer dispenser-printed thermoelectric device
[60]42
Figure 3.17 Illustration and image of dispenser printed p-type Bi _{0.5} Sb _{1.5} Te ₃ planar
TEG [62]
Figure 3.18 Cross-section of cotton textile coated with PANI (left) and PEDOT:PSS
(right) [64]44
Figure 3.19 Body heat powered pulse oximeter [69]
Figure 3.20 (a): Electrocardiography system integrated in a shirt. (b): (1) TE modules
and (2) PV cells [72]
Figure 3.21 (a) Image of 20 dispenser printed single material thermocouples. (b)
Demonstration of bending ability. (c) Close view of the electrodes applied. (d) TEG
being worn on the human body [73].
Figure 3.22 Methods of integrating TEGs in cloths. Numbers denote: 1, Al plates. 2,
textile [74]
Figure 4.1 Process of the screen printing and machines used in fabrication
Figure 4.2 Illustration of poor adhesion of nickel thick-films to alumina substrate
when fired below from 370 – 950°C
Figure 4.3 Poor adhesion of nickel thick-films (Ni : binder = 80% : 20%) to alumina
substrate when fired at 1000°C
Figure 4.4 Nickel thick film with 30% glass binder fired at 950°C survived after tape
test
Figure 4.5 Ni electrode layer on evaporated Cr interface layer
Figure 4.6 Tape test of screen printed Ni layer on evaporated Al film
Figure 4.7 Screen printed Ni layer on evaporated Ti interface layer. (a) Sample
before firing, (b) Sample after firing
Figure 4.8 Tape test of screen printed Ni electrode patterns on dielectric composition
layer60
Figure 4.9 Screen printed square samples for Hall effect test
Figure 4.10 Sample holder for Hall effect test (left) and soldered sample (right) 62
Figure 4.11 SEM cross section view of nickel thick film on dielectric layer
Figure 4.12 Copper layer fired in 370 °C on alumina substrate, failed the tape test . 64
Figure 4.13 Copper layer fired in 750 °C on alumina substrate, intact after the tape
test
Figure 4.14 SEM image of high temperature firing Cu thick film surface
Figure 4.15 SEM cross-section micrograph of high temperature firing copper thick
film
Figure 4.16 SEM cross section micrograph of a copper thick film on a dielectric layer
Figure 4.17 Illustration of the high temperature Ni/Cu thermocouple screen printing
process
Figure 4 18 Screen printed Ni/Cu thermocouples with Silver electrodes 70

Figure 4.19 Schematic of Seebeck voltage measurement	71
Figure 4.20 Seebeck voltage measurement setup	72
Figure 4.21 Generated open-circuit voltage of printed 2 Ni/Cu thermocouples	73
Figure 4.22 Illustration of the power output measurement circuit setup	74
Figure 4.23 power output and voltage of the 8 Cu/Ni thermocouples as a function	of
load resistance at a 20K temperature difference	75
Figure 4.24 power output and voltage of the 8 Cu/Ni thermocouples as a function	of
load resistance at a 40K temperature difference	75
Figure 5.1 Adhesion demonstration of Cu- polyurethane thick film on a Kapton	
substrate	81
Figure 5.2 Adhesion demonstration of Cu-silicone thick film on Kapton substrate.	82
Figure 5.3 Molecular structure of the ingredient in resin 280 epoxy [101]	83
Figure 5.4 Cu-epoxy thick film pattern rolling on a pencil	84
Figure 5.5 SEM image of printed Cu paste with epoxy binder	
Figure 5.6 SEM image of printed Ni paste with epoxy binder	87
Figure 5.7 Fabrication process of low temperature Ni/Cu thermocouples	88
Figure 5.8 Screen printed low temperature Ni/Cu TEG	88
Figure 5.9 Generated thermoelectric voltage and current of 4 epoxy-Ni/Cu	
thermocouples on an alumina substrate	89
Figure 5.10 SEM image of polyester-cotton textile surface	
Figure 5.11 SEM of silver on silicone interface layer and fabric	93
Figure 5.12 Silicone interface layer with printed silver and cured in the oven	95
Figure 5.13 Example of hand printed stencil steel sample cured on hot plate	96
Figure 5.14 Example of IR dried hand stencil printed samples	96
Figure 5.15 Example of machine stencil steel printed sample, IR dried, 1 layer	
printed	97
Figure 5.16 Example of IR dried machine stencil printing sample with thickness	
building up	97
Figure 5.17 Silver electrode layer on non-fully cured silicone interface layer	98
Figure 6.1 Bi thick film samples (a) 200°C cured, polished, (b) 200°C cured,	
unpolished, (c) 250°C cured, polished, (d) 250°C cured, unpolished, (e) 270°C cur	red
sample after polish, (f) 300°C cured.	101
Figure 6.2 SEM image of unpolished Bi thick film surface	102
Figure 6.3 SEM image of polished Bi thick film surface	102
Figure 6.4 Surface SEM images of Sb thick films. (a): unpolished; (b): polished	104
Figure 6.5 Screen printed Sb samples cured in different temperature	106
Figure 6.6 Cracking of Bi thick films when (a) peeling off Kapton from alumina	
holder, (b) rolling on a ball pen with diameter of 13 mm	107
Figure 6.7 Fabrication process of screen printed Bi/Sb thermocouples	108
Figure 6.8 Screen printed 4 Bi-Sb thermocouples	108
Figure 6.9 Generated open circuit voltage and current of 4 printed Bi-Sb	
thermocouples	109
Figure 6.10 Power output and voltage over the load resistor of the 4 Bi-Sb	
thermocouples as a function of load resistance at a 20K temperature difference	109

Figure 6.11 Power output and voltage over the load resistor of the 4 Bi-Sb
thermocouples as a function of load resistance at a 40K temperature difference 110
Figure 6.12 Cross section image of Bi and Sb thick films
Figure 7.1 Free carrier concentration as well as figure of merit with respect to
material composition for Bi ₂ Te ₃ [115]
Figure 7.2 BiTe thick film samples cured at different temperatures. (a): Sample cured
at 250 °C. (b): Sample cured at 350 °C. (c): Most powders were scratched from the
alumina substrate for the sample cured at 270 °C. (d): Alumina substrate with a thin
melted BiTe layer exposed after scratching for sample cured at 270 °C
Figure 7.3 SEM images of printed thick films. (a): surface of the BiTe thick film. (b):
surface of the SbTe thick film. (c): Cross-section of BiTe thick film. (d): Cross-
section of SbTe thick film.
Figure 7.4 Resistivity of selected printed thick-films varying with time. (a):Bi _{1.8} Te _{3.2} ;
(b):Sb ₂ Te ₃
Figure 7.5 Printed BiTe/SbTe thermocouples. (a): SEM of the BiTe/SbTe junction
(b): sample size comparing with a 50 pence coin; (c): sample rolling on a 13 mm
diameter ball pen 120
Figure 7.6 Fabrication process of screen printed BiTe/SbTe thermocouple
Figure 7.7 Generated Seebeck voltage of 4 printed thermocouples, varying with time
121
Figure 7.8 Calculated Seebeck coefficient for single thermocouple varying with time
from Seebeck voltage measurement
Figure 7.9 The voltage across the load resistor and the power output vs. load
resistance of 4 BiTe/SbTe thermocouples with their fitted values
Figure 7.10 Power output of four printed BiTe/SbTe thermocouples varying with
load resistance over 50 days
Figure 7.11 Maximum power output and self-resistance of 4 printed BiTe/SbTe
thermocouples varying with time
Figure 7.12 Calculated Seebeck coefficient for a single thermocouple varying with
time from power output measurement
Figure 8.1 Comparison of TEGs fabricated by screen printing and dispenser printing
Figure 8.2 Dispenser printer systems
Figure 8.3 Illustration of a 3D-structured dispenser printed BiTe/SbTe thermocouple
Figure 8.4 Fabrication process of the fully dispenser printed TEGs
Figure 8.5 Images of a fully dispenser printed TEGs with 8 thermocouples in
different fabrication processes
Figure 8.6 Flexibility demonstration of 3 fully dispenser printed TEGs. Sample (a): 1
thermocouple with 1×2 cubes. Sample (b): 2 thermocouples with 2×2 cubes. Sample
(c): 8 thermocouples with 4×4 cubes
Figure 8.7 The Seebeck voltage and power output measurement setup
Figure 8.8 The temperature distribution over the Al blocks. (a) hot side. (b) cold side
134

Figure 8.9 Generated Seebeck voltages of dispenser printed TEGs increase with the
temperature gradient 135
Figure 8.10 The original and fitted voltage and power output on the load resistor,
ΔT=20 °C. (a): sample a. (b): sample b. (c) sample c
Figure 8.11 (a): The generated Seebeck voltage of sample b in 7 days. (b): calculated
Seebeck coefficient of single thermocouple in 7 days
Figure 8.12 (a): The power output of sample b with the changing of load resistance in
7 days. (b): calculated Seebeck coefficients and resistance of single thermocouple in
7 days
Figure 8.13 Fabrication process of the dispenser printed TEGs
Figure 8.14 Images of a fully dispenser printed TEGs with 8 thermocouples in
different fabrication processes
Figure 8.15 The generated Seebeck voltage of top electrodes-binding dispenser
printed TEGs
Figure 8.16 The power output of top electrodes-binding dispenser printed TEGs,
$\Delta T = 20$ °C
Figure 8.17 Time to print the thermoelectric materials cubes for different samples 141
Figure 8.18 An illustration of inkjet printing head with 5 nozzles [121]141
Figure 8.19 Printed BiTe/SbTe thermocouples on silver electrodes

List of Tables

Table 2.1 Transport properties of commonly used thermoelectric materials [16, 19,	,
23]	15
Table 3.1 Characteristics and performance of μTEGs in literatures	23
Table 3.2 Comparison of technology features between screen printing and dispense	er
printing	36
Table 3.3 Printed thermocouples and their features from literature	37
Table 3.4 Comparison of literatures between different methods of integrating TEGs	S
in textile	48
Table 4.1 Formulation of high temperature nickel ink	54
Table 4.2 Formulations and firing conditions of high temperature curing nickel ink	S
	54
Table 4.3 Sheet resistivity of Ni thick films with different binder ratio on alumina	
substrate	57
Table 4.4 Hall effect and resistivity in nickel screen printed thick-film and their	
comparison with values reported in literature	
Table 4.5 Formulation of high temperature copper ink	
Table 4.6 Thickness (in μm) measurement of copper thick film by different method	ds
	66
Table 4.7 Hall effect and resistivity of copper screen-printed thick-film and a	
comparison with values reported in literature	
Table 4.8 Summarize of calculated values from Seebeck voltage and power output	
measurements with different temperature difference	76
Table 4.9 The resistivity increase of printed thick films compared with their bulk	
counterpart	77
Table 5.1 Fabrication conditions and properties of low temperature Cu thick film	
deposited by screen printing	
Table 5.2 The ratio of the constituents in the polyurethane binder system	
Table 5.3 Optimized ingredients and ratio of Silastic silicone binder system	
Table 5.4 Resistance change of Cu thick film before and after peel-off from alumin	ıa
substrate	
Table 5.5 Transportation properties of Cu paste with epoxy binder	
Table 5.6 Ni paste with 3M Scotchast Resin 280 binder	
Table 5.7 Transport properties of Ni paste with epoxy binder	
Table 5.8 Resistance changes of printed nickel sample before and after peel-off	87
Table 5.9 Resistance change of the thermocouples before and after Seebeck voltage	e
test	89
Table 5.10 Ratio of high temperature cured samples' transport properties to low	
temperature cured ones (samples cured at 850°C/samples cured at 250°C)	
Table 5.11 Properties comparison of common polyurethane and Silicone [100-102]]
	91

Table 5.12 Silicone paste for interface layer used in the experiment with ratio ar	ıd
viscosity	92
Table 5.13 Results of the adhesion test for samples fabricated using different	
processes and curing methods	94
Table 6.1 Screen printing conditions of Bi paste with epoxy binder	100
Table 6.2 Resistivity of Bi thick film samples cured at different temperatures	
compared with bulk value	100
Table 6.3 Elements ratio on Bi thick film surface before and after polish	102
Table 6.4 Transport properties of Bi thick films	103
Table 6.5 Experiment Seebeck coefficients of Bi thick film sample	103
Table 6.6 Screen printing conditions of Sb paste with epoxy binder	105
Table 6.7 Transport properties of Sb screen printed samples	105
Table 6.8 Summarize of calculated values from Seebeck voltage and power outp	out
measurements with different temperature difference of 4 Bi/Sb thermocouples	110
Table 6.9 The changing ratios in percentage between experiment values and bul	k
values of Bi and Sb	112
Table 7.1 Conclusion of fabricating conditions of BiTe and SbTe pastes	115
Table 7.2 Transport properties summary of screen printed BiTe and SbTe thick	film
with the comparison of their bulk counterpart [23]	118
Table 7.3 Seebeck coefficient of screen printed Bi ₂ Te ₃ and Sb ₂ Te ₃ thick-films	119
Table 7.4 The BiTe thick film sheer resistance increasing due to the re-curing et	ffect
	119
Table 7.5 Deviations between experiment values and bulk values of BiTe and S	bTe
(thick film value/bulk value)	125
Table 8.1 The Seebeck coefficient α and resistance R for single BiTe/SbTe	
thermocouple	137
Table 8.2 Resistance of different functional parts in the above 8 planar	
thermocouples	142
Table 9.1 The Seebeck Coefficients, resistivity and carrier concentration of the	
developed pastes	145

List of Symbols

Symbol	Name	Units
V	Electric Voltage	V
α	The Seebeck	$\mu V/K$
ΔT	Temperature gradient	K or °C
$\dot{\mathrm{Q_P}}$	Transferred heat	J
Ï	Electric current	A
π	Peltier coefficient	V
β	Thomson coefficient	$\mu V/K$
Z	Figure of merit	K ⁻¹
ZT	Dimensionless figure	N/A
R_{H}	Hall coefficient	cm^3/C
μ	Carrier mobility	$cm^2/V \cdot s$
ρ	Electric resistivity	Ω ·cm
σ	Electric conductivity	S/cm
λ	Thermal conductivity	W/m°C
n	Carrier concentration	cm ⁻³
R	Load resistance	Ω
P	Power output	W (Watt)
k	Boltzmann's constant	$1.38 \times 10^{-23} \text{ J/K}$
e	Electron charge	1.6×10 ⁻¹⁹ C
m	Weight	g
	Volume	ml
	Viscosity	cP=mPa·s
	Pounds per Square	psi

Glossary

TEGs	thermoelectric generators
μTEGs micro thermoelectric genera	
MEMS	MicroElectroMechanical Systems
ICT	information and communications
IC I	technology
e-textiles	electronic textiles
WBSs	wearable biomedical systems
MFP	mean free path
3D	three dimension
IC	integrated circuits
RIE	reactive ion etching
CMOS	Complementary Metal-on-Oxide
CIVIOS	Semiconductor
ASD	aerosol deposition
HIP	hot isotactic pressing
ECD	electrochemical deposition
TETs	thin-film transistors
RTP	rapid thermal processing
MA	mechanically alloyed
PEN	polyethylene naphthalate
	Poly(3,4-
PEDOT:PSS	ethylenedioxythiophene):poly(4-
	styrenesulfonate)
PANI	polyaniline
ECG	electrocardiography
PV	photovoltaic
PET	Polyethylene terephthalate
CVD	chemical vapour deposition
PVD	physical vapour deposition
PECVD	Plasma-enhanced chemical vapour
	deposition
SEM	Scanning Electron Microscope
EDX	Energy-dispersive X-ray
	spectroscopy
IPL	Intense Pulsed Light
IR	infrared
UV	ultraviolet
CIP	cold isostatic pressing

Acknowledgement

With this opportunity, I shall firstly give my respectful thanks to my supervisors, Professor Steve Beeby and Dr John Tudor. They not only helped me on research, but also taught me a lot on exploring the life and culture in UK.

Professor Steve Beeby, who always makes you pleased to work with. He helped me to go through tough experiments with scientific thought and very effective communication. Outside the office, there are also lots of places for me to learn from him, gym, football ground and pubs. Thanks to Steve for introducing me lots of tasty larges and ales. Dr John Tudor, who is more like a friend rather than a supervisor for me. We shared various comments on different things during Friday's lunch and other events: the mortgage rules in UK, my broken jeans and the strange dancer in ECS Christmas party.

I would also like to give my thanks to Dr Russel Torah, Dr Elena Koukharenko, Dr Kai Yang, Dr Yang Wei, Dr Yi Li and every person in energy harvesting and smart textile research group. I have been enjoying the friendly working environment for the past four years.

My parents, who gave me both spiritual and financial supports during my PhD career. Without them I do not even have a chance to meet the nice people mentioned above and enjoy this pleasant four years.

Thanks, the University of Southampton.

Chapter 1.Introduction

1.1 Overview of research

A thermoelectric module generates electrical power when a temperature difference is maintained across its thermocouples. Typically, each thermocouple is comprised of two different thermoelectric materials as two elements. A thermoelectric module which is capable of delivering power to an external load is called a thermoelectric generator (TEG). The working principles of TEGs will be introduced in chapter 2.

A thermocouple is the basic unit in TEG devices. It is comprised of two bars or strips of different thermoelectric materials which are electrically connected at one end. In the typical thermoelectric module structure, several thermocouples are connected electrically in series and thermally in parallel. The detailed discussion about the structure of TEGs are presented in section 2.2.5. TEGs are able to harvest energy from waste heat and as such could be used to power autonomous systems as an alternative to batteries. They provide a reliable method for energy conversion and exhibit no noise or vibration because there are no mechanical moving parts. However, the energy conversion efficiency, defined as the ratio of output electrical power to transferred thermal energy, is relatively low for current TEGs. Most examples in the literature have an energy conversion efficiency under 5% [1, 2]. For now, they have been used in specialised medical, military and space applications, such as radioisotope power for deep space probes [3], and for supplying remote powered applications, such as oil pipelines and sea buoys, where cost is not a main consideration [4]. In recent years, because of pressure from energy crises and concerns about global warming, TEGs have attracted increasing attention as a renewable and flexible source of electricity able to meet a wide range of power requirements [1].

The human body constantly generates heat as a by-product of metabolism. Heat from the human body can be considered as a potential power source for on-body electronic devices. The available thermal energy on the skin surface is about 3–5 mW/cm² when the ambient temperature is around 20–25°C [5]. The surface area of an adult human body is around 2 m², which equates to a total dissipated heat power of 60 – 100 W. This value is corroborated by Sarpeshkar who calculated an average available thermal power of 81 W from an adult human [6]. Obviously it is not practical to cover the

entire body with TEGs but for the amount of available energy suggests that useful amounts of power can be harvested from the human body. As such, body heat could be used as a power source for some low-power autonomous sensors and MicroElectroMechanical Systems (MEMS).

Electronic textiles (e-textiles) are a combination of information and communications technology (ICT) and textiles. This technology incorporates sensing, actuating, communication and computing functionalities on textiles as required for different applications. For example, e-textile wearable biomedical systems (WBSs) involve the integration of sensors into wearable devices to allow physiological signals to be continuously monitored during normal daily activities [7]. This provides more data than infrequent clinical visits which only provides a brief window into the physiological status of the patient. These systems can be used for medical applications but also to monitor the vital signs of people in dangerous jobs, such as soldiers or firemen.

Textiles can also be used for energy harvesting by integrating suitable transduction elements into textiles. From previous discussions it can be seen that the potential electric energy from the human heat is considerable. Thermocouples integrated directly on to textile substrate is a suitable method to provide power for e-textile applications because of the large area that could potentially be covered by such a device.

In order to integrate TEGs on textiles a suitable fabrication method should be selected. Printing technologies such as screen, inkjet and dispenser printing are appropriate fabrication processes because they are well suited to mass-production and low-cost fabrication, and are compatible with textiles. They are also suited to the manufacture of thermocouples with large area, which can increase the output electrical voltage and power of such a generator.

1.2 Objective and scope of the research

The objective of this project is the development of materials and processes that enable the fabrication of thermocouples on flexible substrate using printing technology. Screen printing and dispenser printing were both investigated for thermoelectric devices fabrication.

In this thesis, the first step involves screen printing thermocouples on alumina substrates, which have good temperature stability and enable the use of high temperature curing printable pastes. The second phase in this project is screen printing low temperature curing thermocouples onto flexible polymer substrates, such as Kapton. The third phase involves the attempt of migrating this technology on to textiles. Each step involved the formulation of materials into a paste, which can be deposited using standard screen printing technology. The thermoelectric properties of the fabricated thermocouple-devices were measured and optimised at every phase.

The flexibility enable the TEGs devices have the potential to integrate with textile. However, the rough surfaces of woven textiles makes them unsuitable for printing intricate structures. In this work, polyurethane or silicone rubber interface layers are printed to create a smooth surface on woven textiles. Silicone rubber is more flexible and stretchable than polyurethane, but its low surface energy makes it difficult for subsequent printed layers to adhere to it. A short study on improving the surface energy of silicone interface layers is also included in this thesis.

1.3 Document structure

Chapter 1 provides a brief introduction to the research presented in this thesis. The objectives of the research, structure of this thesis and the specific novelty claims arising from this research are also presented.

Chapter 2 introduces the theory behind thermoelectric generator devices. The performance evaluation methods for thermoelectric generator device are also presented.

Chapter 3 presents a literature review of micro-fabricated and printed TEGs devices. In particular, the application of TEGs on body heat energy harvesting is described in this chapter.

Chapter 4 describes high temperature curing Cu-Ni thermocouples on alumina substrates.

Chapter 5 discusses the development of low temperature Cu-Ni thermocouples and the silicone rubber interface layer.

Chapters 6 and 7 describe the fabrication and performance of low temperature Bi-Sb and BiTe/SbTe thermocouples respectively.

Chapter 8 presents dispenser printed TEG devises and chapter 9 describes the conclusions from this thesis.

1.4 Novelty statement

The specific novelty points of this thesis are:

- Novel inks for printing technology including high temperature curing copper
 (Cu) and nickel (Ni) inks and lower temperature cured bismuth (Bi) and antimony (Sb) inks.
- The demonstration of Ni/Cu thermocouples with improved adhesion of nickel thick films to an alumina substrate.
- A screen printed low temperature Bi/Sb TEG on alumina substrate.
- Planar SbTe/BiTe TEGs on flexible substrates fabricated by screen printing technology.
- Dispenser printed 3D structured BiTe/SbTe TEGs on flexible substrate.

Chapter 2. Theoretical background

2.1 Introduction

An understanding of solid state thermoelectric theory is essential to this project. This study will allow the performance of the developed TEG devices to be understood and improved. The basic working principles, the evaluation methods and the typical structure of TEGs will be described.

2.2 Principles of thermoelectric devices

The thermoelectric theories describe the energy transfer and conversion between heat and electricity in solid state devices, including three thermoelectric effects: Seebeck effect, Peltier effect and Thomson effect. Different applications are based on different effects. For example, TEGs are based on Seebeck effect while thermoelectric heaters and coolers are based on the Peltier effect. The basic concepts such as the Seebeck effect and figure of merit will be introduced in this chapter.

2.2.1 The Seebeck effect

The Seebeck effect describes the generation of electrical power when a temperature difference exists between two ends of a thermocouple [8]. The Seebeck voltage is defined as the open circuit voltage occurred when a temperature difference exists on the junctions formed by two different conductors or semiconductor materials a and b. These two materials must be in contact or electrically connected with one another because charge carriers must be able to flow between the materials. This is shown in figure 2.1.

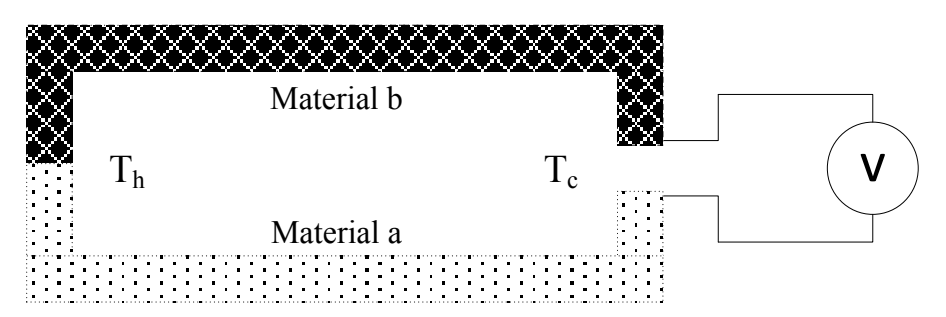


Figure 2.1 Schematic of the Seebeck effect in a thermocouple

2.2.1.1 Seebeck coefficient for semiconductors

Three factors may affect the Seebeck voltage in semiconductors: carriers diffusion due to the carrier concentration difference, velocity difference of the carriers and phonon drag [9].

When a temperature gradient exists across a semiconductor bar, the carrier concentration and carrier velocity at the hot end will be higher than that at the cold end, which leads to a net diffusion of carriers from hot to cold end. Figure 2.2 illustrates the movement of charge carriers, in this case electrons, when a temperature gradient exists across a semiconductor bar. Firstly, the carrier density in hot end will increase and be higher than the cold end because more electrons are excited from the valence band (E_v) to the conduction band (E_c). The Fermi level (E_F) is closer to intrinsic band (E_i) when the temperature is higher. Hence, Electrons diffuse from the hot end to the cold end. Secondly, the kinetic energy of electrons at the hot end will be higher than the cold end, as a result they will have greater velocities than those at the cold end. Hence, there is a net diffusion of electrons from the hot end towards the cold end which leaves behind holes in the hot region and accumulated electrons in the cold region. Thirdly, the interaction between lattice vibrations and charge carriers, which is so called phonon drag, will increase the accumulation of carriers in the cold end [10, 11]. The quantity of phonons is higher at the hot end and they also diffuse from the hot end towards the cold end. The phonons-carriers collision will transfer the momentum from phonons to carriers, increasing the velocity of the carriers and enhance the diffusion of the carriers.

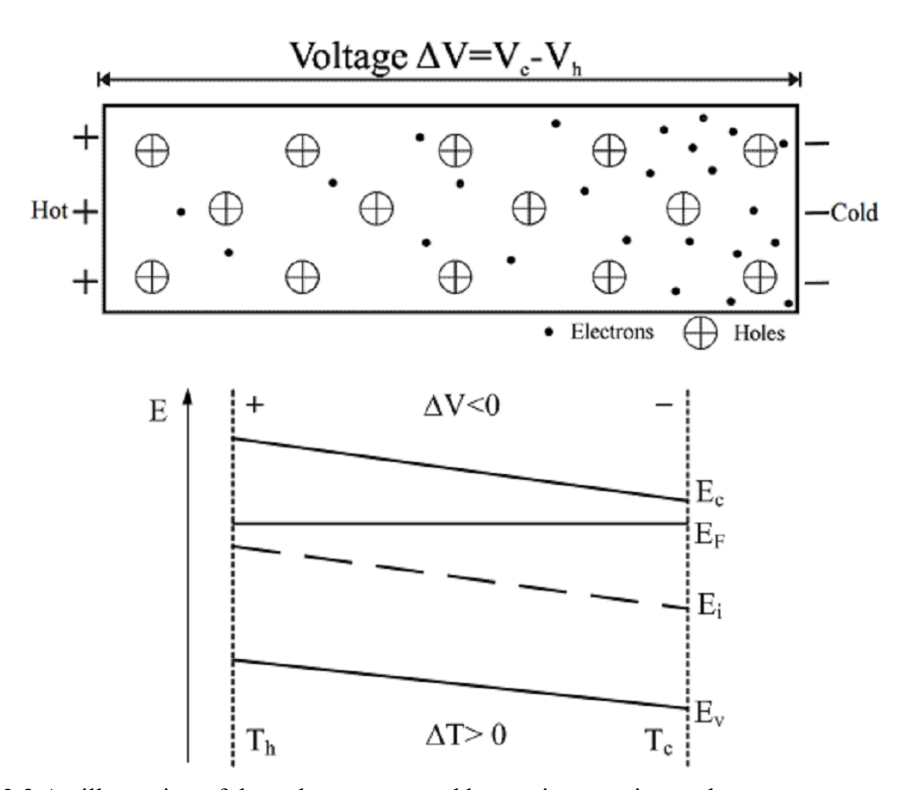


Figure 2.2 An illustration of the voltage generated by carriers moving under a temperature gradient and the energy band

The accumulation of charge carriers at both ends will then build up an electrical field. A DC voltage is therefore developed with the hot end at positive potential.

Equation 2.1 describes the Seebeck coefficient of the semiconductor bar shown in figure 2.2 when a temperature difference ΔT is applied across it. The Seebeck coefficient α is defined as the potential developed, in Volts (V), per unit temperature difference, in Kelvins (K):

$$\alpha = \frac{dV}{dT} \cong \frac{V_c - V_h}{T_h - T_c} \tag{2.1}$$

In this equation, V_h is the voltage at the hot end while V_c is that of the cold end. The polarity of V_c with respect to the V_h determines the polarity of α . For n-type semiconductors, where the majority charge carriers are electrons, the accumulated electrons in the cold end will give a negative potential, while the holes left in the hot end will generate a positive potential. This gives a negative Seebeck coefficient.

For p-type semiconductors, holes will diffuse from the hot end to the cold, giving the cold end a positive potential and therefore a positive Seebeck coefficient [9].

2.2.1.2 Seebeck coefficient for metals

The Seebeck Effect mechanism in metals is different from semiconductors, which is affected by two aspects: diffusion of velocity difference and scattering. Firstly, the carriers at the hot end have higher velocity and mean free path (MFP), which is the main reason makes the diffusion of carriers. The carrier concentration could be considered as constant in metals, thus, no diffusion caused by the carrier concentration difference. Secondly, the conduction electrons are scattered by the interactions with the metal ions and the lattice vibrations. For normal metals, such as nickel (Ni), the scattering is weak and the MFP increases with temperature. Thus, the sign of Seebeck coefficient is negative. For other metals, such as copper (Cu), the scattering is dominating and the MFP decreases with temperature increasing. The sign of Seebeck coefficient will then be positive [12].

2.2.1.3 Seebeck coefficient for thermocouples

In order to gain a higher Seebeck voltage, a thermocouple normally consists two types of materials. In figure 2.1, material a is n-type semiconductor which has a negative Seebeck coefficient while material b is p-type semiconductor which has a positive

Seebeck coefficient. If the thermocouples are connected electrically in series and thermally in parallel, the stable open circuit potential difference, which is the Seebeck voltage of the circuit, is given by:

$$V = n \cdot \alpha_{ab} \cdot \Delta T = n \cdot \alpha_{ab} \cdot (T_b - T_c) \tag{2.2}$$

Here, α_{ab} is the Seebeck coefficient of the junction between the materials a and b, ΔT is the temperature difference and n is the number of the thermocouples. The value of α_{ab} is calculated as [13],

$$\alpha_{ab} \cong \frac{V}{n \cdot \Delta T} (at \Delta T \to 0)$$
 (2.3)

It means that, for small temperature variations, the thermoelectric voltage V and Seebeck coefficient α_{ab} are approximately directly proportional. The Seebeck coefficient is a physical property which can only be measured from the junction between different materials. Consequently it is sometimes referred to as the relative Seebeck coefficient. The unit of the Seebeck coefficient is V/K or more often in μ V/K, and the value can be either positive or negative. If the current flow is from b to a in hot junction, the value of α_{ab} is positive.

2.2.2 The Peltier effect

Another application of thermoelectric devices, refrigeration, is based on the Peltier effect. Instead of applying a temperature difference across a thermocouple, a voltage is applied across the thermocouple junctions. Depending on the direction of the current flow through the junction, it can absorb or dissipate heat. The transferred heat \dot{Q}_P is given by [13]:

$$\dot{Q_P} = \pi_{ab} \cdot I \tag{2.4}$$

Where I is the applied current and π_{ab} is the Peltier coefficient of the thermocouple, which is also a parameter determined by the physical properties of material a and b in the thermocouple. The unit of the Peltier coefficient is Watts (W)/Amp (A)=V. In figure 2.3, the value of Peltier coefficient π_{ab} is positive when the current flow is clockwise, which causes the left junction to absorb heat from its surroundings. When ΔT is approaching 0, the definition of the Peltier coefficient is given by:

$$\pi_{ab} = \frac{\dot{Q}_P}{I} (at \Delta T \to 0)$$
 (2.5)

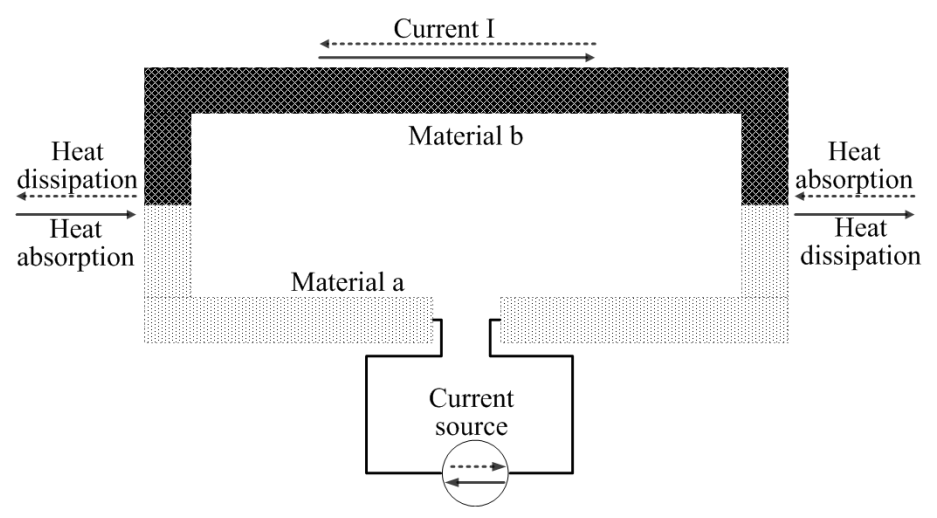


Figure 2.3 Schematic of Peltier effect

The transferred heat $\dot{Q_P}$ must be measured in thermally isolated conditions, the temperature at both sides of the junction should be the same. Unlike the Joule heat equation, $Q=R\cdot I^2$, which provides an invariably positive Q value, the transferred heat $\dot{Q_P}$ can be either positive or negative depends on the sign of electric current I. When the transferred heat $\dot{Q_P}$ of a junction is positive, it is releasing heat and is the hot side of a Peltier Device. When $\dot{Q_P}$ is negative, this junction is absorbing heat and is the cold side of a Peltier Device. This is the mode used in a thermoelectric refrigerator.

Another thermoelectric effect is called Thomson Effect. According to Beeby [13], when a current I and a temperature gradient ΔT exist in a single material simultaneously, it will cause heat absorption or dissipation. Thomson Effect usually has a minimal impact on thermoelectric devices [14]. When the Thomson coefficients of the two conductors/semiconductors in a thermocouple are well matched, there is no net heat exchange [14].

2.2.3 The Kelvin relationship

These two thermoelectric effects are related by the Kelvin Relationship, which is given in the following equation [15]:

$$\alpha_{ab} = \frac{\pi_{ab}}{T} \tag{2.6}$$

Equation 2.6 shows the relationship between the Seebeck effect and the Peltier effect. The Seebeck coefficient is proportional to the Peltier coefficient, which indicates that a material which has appropriate thermoelectric properties for use in a power generator

will also be a good material for thermoelectric refrigeration and vice versa, because these effects are reversible.

The Seebeck and Peltier effects occur at the junction between two materials in ohm contact, while the Thomson coefficient occurs in a single conductor or semiconductor. Hence, there are the Seebeck coefficient (α_{ab}) and the Peltier coefficient (π_{ab}) for the junction between material a and b.

The Seebeck coefficient of the junction between materials a and b is equal to the difference between their individual Seebeck coefficients. If the Seebeck, Peltier and Thomson coefficients of materials a and b are represented by α_a/α_b and π_a/π_b , this gives equation 2.7.

$$\alpha_{ab} = -\alpha_{ba} = \alpha_a - \alpha_b$$
 and $\pi_{ab} = -\pi_{ba} = \pi_a - \pi_b$ (2.7)

So, if the Seebeck coefficient of material a in thermocouple a/b is already known, such as $1.51 \,\mu\text{V/K}$ of silver [16], the α value for another material b can be derived from the measured Seebeck coefficient for the a/b junction based on equation 2.7. This is equally true for the Peltier coefficient.

In addition, the Kelvin relationship shows that all three thermoelectric effects exist simultaneously when a device is operated in either a thermoelectric generating or refrigerating mode.

2.3 Evaluation of thermoelectric properties

In order to evaluate the thermoelectric properties of different materials, the figure of merit Z can be used. Typically, a higher value of Z indicates a better thermoelectric performance. The definition of figure of merit for a single thermocouple Z_{tc} is given by [13]:

$$Z_{tc} = \frac{\alpha_{ab}^2}{\rho_{tc} \cdot \lambda_{tc}}$$
 (2.8)

Here, α_{ab} is the Seebeck coefficient of the thermoelectric junction between n-type thermoelectric material a and p-type thermoelectric material b, which is also defined in section 2.2.1.3; ρ_{tc} is the equivalent electric resistance of the thermoelectric junction; λ_{tc} is the thermal conductivity of this junction. Calculating this requires independent

measurements of the Seebeck coefficient, thermal conductivity and electrical resistivity of the material.

In order to gain a high figure of merit, the thermoelectric junction should have a high Seebeck coefficient, low electric resistance and low thermal conductivity. In practice, any material is a compromise between these three parameters. This will be discussed further later in the thesis.

In this section, the methods and parameters used to evaluate the performance of a TEG will be explained. The parameters discussed below are electrical resistivity, thermal conductivity, the Seebeck coefficient, the figure of merit, the power output and the conversion efficiency.

2.3.1 Electrical resistivity and Hall coefficient measurement

The measurement of electrical resistivity for individual material, ρ , can be obtained simultaneously with a Hall effect measurement from a Hall effect test setup. The setup of a Hall effect measurement is illustrated in figure 2.5.

In such a measurement the resistivity of the tested material can be obtained by measuring the voltage across two points, a and b, based on the following equation:

$$\rho = R \frac{A}{l} = \frac{V_{ab}}{l} \cdot \frac{w \cdot d}{l}$$
 (2.9)

Here, d is the thickness, w is the width, and l is the length. A is the cross section area through which the current I passes. R is the resistance from end to end of the whole bar of conductive material. V_{ab} is the voltage between a and b.

When there is a current I flowing through a solid in a magnet field B, the charge carriers will flow to one or other end of the material depending on their charge type. When an electric current passes through a conductor or semiconductor in which there is a perpendicular magnet field, the Lorentz Force will lead the positive charge carriers to accumulate at the front and the negative carriers to accumulate to the back based on the right-hand rule. This is shown in figure 2.4. The accumulated charges will cause a voltage across the sample which slows down the movement of charge carriers. When this potential is sufficiently high the generated electric field will produce a force on the charge carriers equal and opposite to the Lorentz force, giving a balanced Hall voltage V_H.

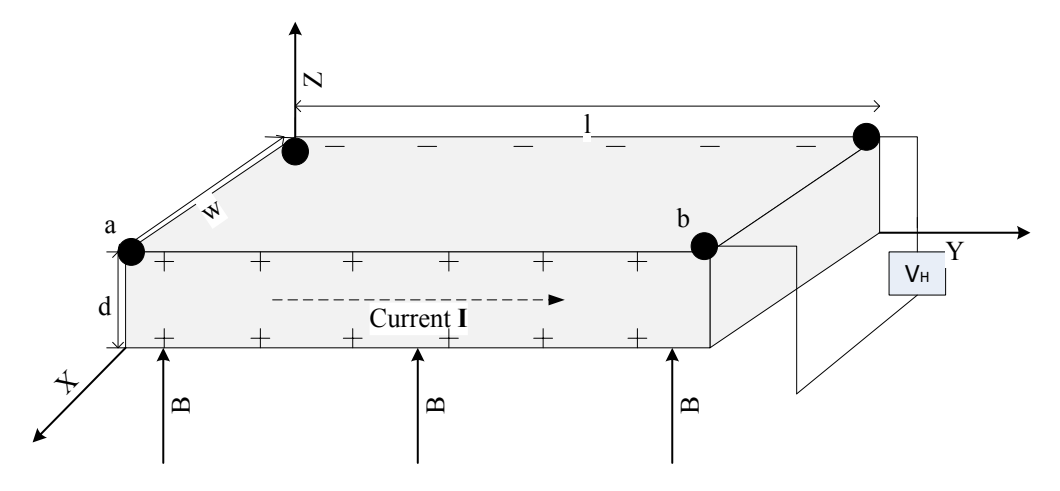


Figure 2.4 Principle of Hall effect measurement

According to Chien [17], the Hall coefficient R_H is defined as

$$R_{\rm H} = \frac{E_{\rm X}}{i_{\rm V}B} = \frac{d \cdot V_{\rm H}}{I \cdot B} = \frac{1}{ne}$$
 (2.10)

Where E_X is the electric field formed by the accumulated charges, j_Y is the current density along Y direction, n is the carrier concentration and e is the charge of a single electron. From the Hall Effect measurement, we can learn the carrier type (n or p-type) and carrier concentration.

- a. Sample type: The sign of the Hall coefficient determines the type of the sample (n-or p-type with mobile electrons or holes respectively). If V_H is positive the charge carrier is positive (p-type) for the tested sample. If it is negative, the charge carrier is negative (n-type).
- b. Carrier concentration n: The carrier concentration can be calculated as $n = 1/(|R_H| \cdot e)$ as described in equation 2.10.
- c. Carrier mobility: The relationship between carrier mobility and conductivity is given in equation 2.11:

$$\mu = \frac{1}{\text{ne}} \cdot \frac{1}{\rho} = |R_{\text{H}}| \cdot \frac{1}{\rho} \tag{2.11}$$

Here, μ is the carrier mobility. When resistivity has been measured, the mobility can then be calculated.

2.3.2 Thermal conductivity measurement

The thermal conductivity of a material is defined by the following equation [15]:

$$\lambda = \frac{Q/A}{\Delta T/\Delta I} \tag{2.12}$$

Where Q is the heat transferred through the cross section A when there is a temperature gradient ΔT across a distance of Δl . So, thermal conductivity λ can be calculated if Q and ΔT have been measured. The two main types of methods used to measure thermal conductivity are steady methods and non-steady methods [18].

When the ambient temperature is low, for example room temperature, λ can be measured directly by the longitudinal steady method because the heat loss by radiation is relatively low. When doing a measurement with a high temperature difference between the specimen and environment, the heat loss due to radiation cannot be ignored. In this case, non-steady methods, such as the laser flash method which indirectly obtains thermal conductivity by measuring the thermal diffusivity [19].

For most conductors and semiconductors, the thermal conductivity is determined by two parameters: λ_e from charge carriers and λ_l from lattices. In insulators, the main contribution is from lattices, while in metals the higher concentration of charge carriers will contribute more to the heat transfer in solid. This can be seen in figure 2.6.

2.3.3 Seebeck coefficient measurement

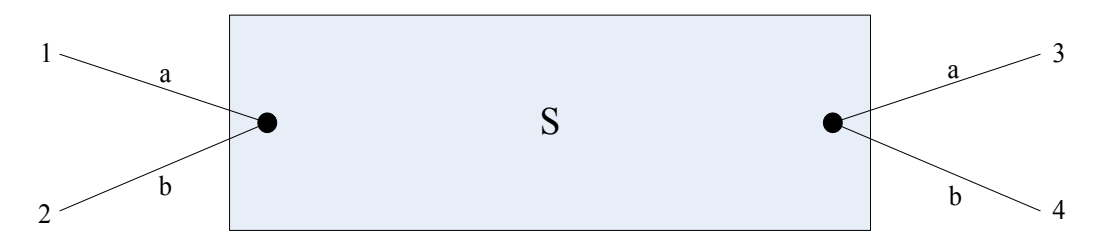


Figure 2.5 Principles of the Seebeck coefficient measurement

The measurement of the Seebeck coefficient for a particular material is based on equation 2.3. In figure 2.5, thermocouple a and b are connected to joint ends which are then attached with the thermoelectric material S. A voltage V is applied between 1 and 3 and ΔT is the temperature difference maintained between these two thermocouple junctions. The Seebeck coefficient of thermocouple a and b are already known to a high degree of accuracy.

The main difficulty with this measurement is that the Seebeck coefficient varies with temperature, giving a nonlinear variation of potential ΔV with ΔT . Hence, a dense sequence of measurements of ΔV and ΔT as the temperature is slowly increased is required to get an accurate value for the Seebeck coefficient. Shubha and co-workers

developed an operational amplifier based system which achieves an accuracy greater than 99% in measuring the Seebeck coefficient. The specific equation used in this work to calculate the Seebeck coefficient of the junction between materials S and a is given in equation 2.13 [20]:

$$\alpha_{Sa} = \lim_{V_{13} \to V_{24}} \left(\frac{V_{13}}{V_{13} - V_{24}} \right) \tag{2.13}$$

Where V_{13} is the voltage measured across the sample connections 1 and 3 and V_{24} is the voltage across connections 2 and 4 (in figure 2.6).

By coupling an unknown material with a Seebeck coefficient value close to 0, α_s can be considered approximately equal to α_{Sa} .

2.3.4 Summary of the properties of some commonly used materials for TEGs

Generally, metals have high electrical conductivity and low Seebeck coefficient, while semiconductors have higher Seebeck coefficient and lower electrical conductivity. An increase in electrical conductivity through material selection will be accompanied by a decrease in the Seebeck coefficient and an increase in thermal conductivity.

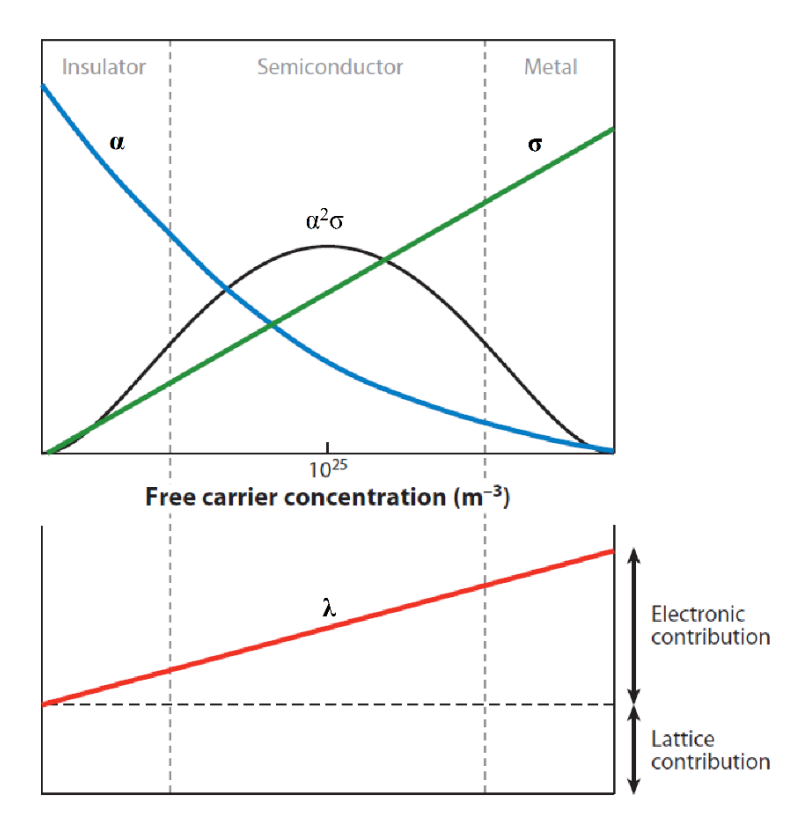


Figure 2.6 The schematic variation of Seebeck coefficient, electrical conductivity and thermal conductivity depending on the increase of carrier concentration from insulator to metal, after Shakouri [21]

Figure 2.7 shows the variation in the Seebeck coefficient, thermal conductivity and electrical conductivity for insulators, semiconductors and metals, which are differentiated by their carrier concentration. The position of the broad maximum in the $\alpha^2\sigma$ curve is found in the carrier concentration range on the orders from $10^{18} - 10^{20}$ cm⁻³ ($10^{24} - 10^{26}$ m⁻³) based on the literature [8, 22].

Materials	ρ (Ω·cm)	$\lambda \left(W/(m \cdot K) \right)$	α (μV/Κ)
copper	1.712×10 ⁻⁶	401	1.83
nickel	7.12×10 ⁻⁶	90.7	-19.5
Bismuth	1.07×10 ⁻⁴	7.87	-70
Antimony	3.9×10 ⁻⁵	18.4	40
p-Bi ₂ Te ₃	1.4-3.8×10 ⁻³	1.5-2.5	224
n-Bi ₂ Te ₃	(intrinsic value)	(intrinsic value)	-227
Sb ₂ Te ₃	2.5-6×10 ⁻⁴	2.8-7.3	110

Table 2.1 Transport properties of commonly used thermoelectric materials [16, 19, 23]

Typically, the optimal values for the Seebeck coefficient, electrical resistivity, and thermal conductivity are in the ranges of $150-230~\mu\text{V/K}$, $1-3\times10^{-3}~\Omega\cdot\text{cm}$, and $1.5-3~\text{W/(m\cdot K)}$ respectively [13].

In table 2.1, the typical transport properties around room temperature (298 K–300 K) of several thermoelectric materials (also used in the experiments in this thesis) are listed. Copper and nickel are metals; Bismuth and antimony are semi-metals; the alloys are semiconductors.

2.3.5 Power output, conversion efficiency and figure of merit

When the thermocouple is connected with a load resistance R_L as shown in figure 2.8, the generated current will deliver electric power to the load resistor.

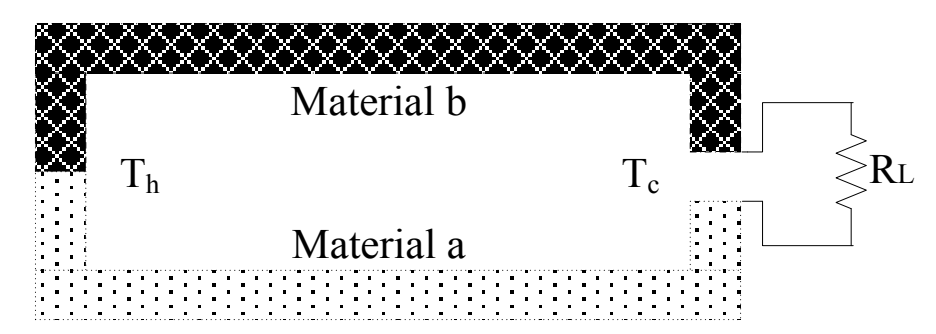


Figure 2.7 Single thermocouple with load resistance

The thermocouple can be thought of as a battery with equivalent resistance R, as shown in figure 2.8. In practice, for a TEG, one of the two materials in the thermocouple is an n-type material and the other is a p-type material. The Seebeck coefficient for this thermocouple is denoted α_{ab} . Hence, from equation 2.3, the Seebeck voltage of such a

thermocouple is $V_{tc} = \alpha_{ab} \cdot \Delta T$. The equivalent electric resistance R represents the total series resistance of both thermoelectric materials and the junctions.

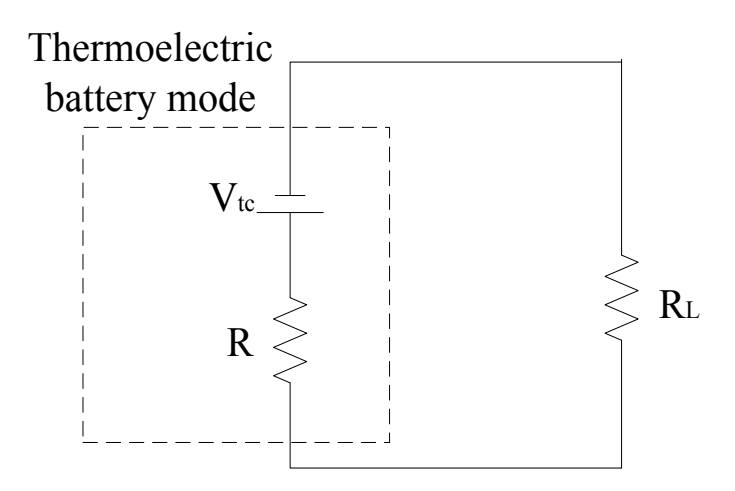


Figure 2.8 An equivalent circuit of thermoelectric generator with load resistor. The electric power dissipated in the load resistor is given by:

$$P = V \cdot I = \frac{\frac{R_L}{R}}{\left(1 + \frac{R_L}{R}\right)^2} \frac{V_{tc}^2}{R} = \frac{s}{(1+s)^2} \frac{(\alpha_{ab} \cdot \Delta T)^2}{R}$$
(2.14)

Where $s=R_L/R$ is the ratio of the load resistance to thermal resistance. V and I are the voltage and current applied to the load resistor respectively. V_{tc} is the Seebeck voltage generated by the thermocouple.

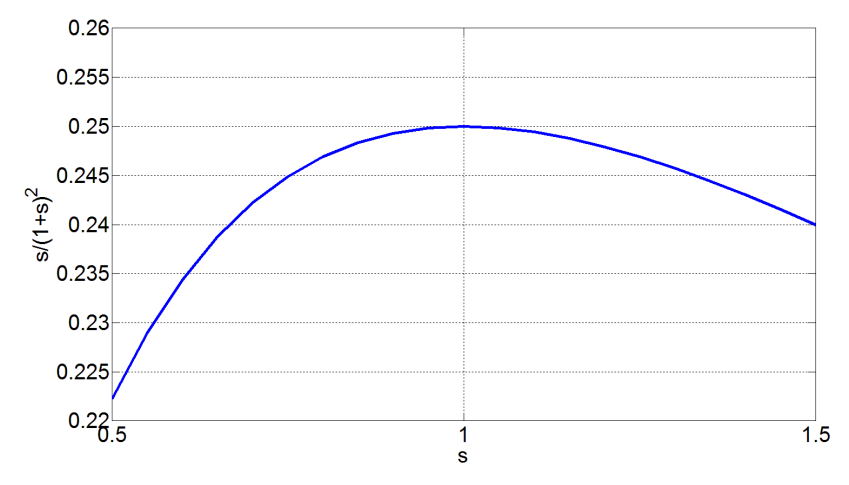


Figure 2.9 $s/(1+s)^2$ vs. s curve when s in the range from 0.5 to 1.5

According to Goldsmid [24], around the temperature range from 0 °C to 100 °C, the value of Seebeck coefficient is stable. Thus, under a fixed temperature gradient, the term $(\alpha_{ab}\cdot\Delta T)^2/R$ can be considered as a fixed value. Hence the power output P only

varies when s varies. Figure 2.9 shows a typical P-s curve. It shows that when R_L=R and s=1, the power reaches its maximum value:

$$P_{\text{max}} = \frac{(\alpha_{\text{ab}}\Delta T)^2}{4R}$$
 (2.15)

The conversion efficiency ϕ of such system is:

$$\phi = \frac{\text{power comsumed by the load (P)}}{\text{heat energy absorbed in the thermocouple(Q)}}$$
(2.16)

The heat absorbed in system, \dot{Q} , is comprised of Peltier heat $Q_p = \alpha_{ab} T_H I$, conducted heat $Q_c = \lambda' (T_H - T_C)$ and Joule heat $Q_J = -\frac{1}{2} I^2 R'$, where λ' is the parallel thermal conductance of n-type and p-type thermal materials and R' is their series electric resistance, equals to R+R_L. The conversion efficiency can then be written as [15]:

$$\phi = \frac{I^2 R_L}{\alpha_{ab} T_H I + \lambda' (T_H - T_C) - \frac{1}{2} I^2 R'}$$
 (2.17)

This equation can be simplified to:

$$\phi = \left(\frac{T_{H} - T_{C}}{T_{H}}\right) \left[\frac{R_{L}/R'}{\frac{3}{2} - T_{C}/2T_{H} + 1/ZT_{H}}\right]$$
(2.18)

Here, $Z=(\alpha_{ab})^2/\lambda'R'$ is the figure of merit of a thermocouple, which is the most important characteristic to evaluate the thermoelectric material. Furthermore, we have $R_L/R' < 1$ and $T_H > T_C$ results $T_C/2T_H < 1/2$. The term in the square brackets has a maximum value less than 1 because the numerator is less than 1 while the denominator is greater than 1. Hence, the conversion efficiency of a TEG is the Carnot efficiency $(T_H-T_C)/T_H$, reduced by a factor which is dependent on the value of Z.

According to Rowe [15], with an acceptable degree of approximation, the figure of merit Z of the thermocouple can be expressed as follows:

$$Z_{tc} = \frac{(\alpha_b - \alpha_a)^2}{[(\rho_a \cdot \lambda_b)^{1/2} + (\rho_a \cdot \lambda_b)^{1/2}]^2}$$
(2.19)

Based on equations 2.8 and 2.19, figure of merit of single thermoelectric material can be obtained from equation 2.20:

$$Z = \frac{\alpha^2}{\rho \cdot \lambda} \tag{2.20}$$

Given the physical properties of semiconductors, when the carrier concentration n is increasing both the Seebeck coefficient α and the reciprocal of thermal conductivity $1/\lambda$ will decrease. This relationship was shown previously in figure 2.6.

Generally, semiconductor materials have the highest values of Z. The unit of figure of merit Z is K⁻¹.

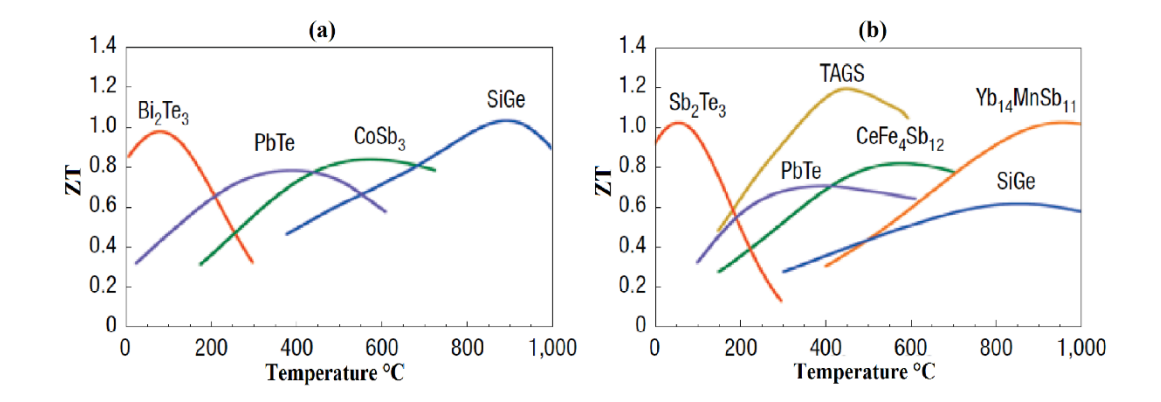


Figure 2.10 Thermoelectric figure of merit for a number of thermoelectric materials varying with temperature (a) n-type materials, (b) p-type materials, after Snyder [25]

In order to get a dimensionless figure of merit, ZT is used instead of Z. The highest ZT value in the literature for Bi-Sb-Te based solid thermoelectric generators is around 1 [8].

In figure 2.10, it can be seen that the figure of merit varies with temperature. At room temperature, Bi₂Te₃ and Sb₂Te₃ alloys provide the highest ZT values, which demonstrates that they are suitable for room temperature thermoelectric energy harvesting applications.

2.4 Structure of thermoelectric devices

As shown in figure 2.11, a typical thermoelectric device consists of several n and p-type thermocouples connected electrically in series and thermally in parallel. The two different thermal materials are fabricated into bar or leg structures depending on the fabrication technology used. The adjacent elements either need to be electrically connected by a metal with a high electric conductivity, or the two thermocouples need to be in physical contact at the ends of the legs to form an Ohmic contact junction.

Depending on the fabrication technology used, the structures of TEGs may have slight variations. However, they all need to connect the thermoelectric elements in series to

gain a high output voltage and power. For example, planar thermoelectric elements can be coiled up to form a cylindrical structure. This will be discussed further in chapter 3 of this thesis.

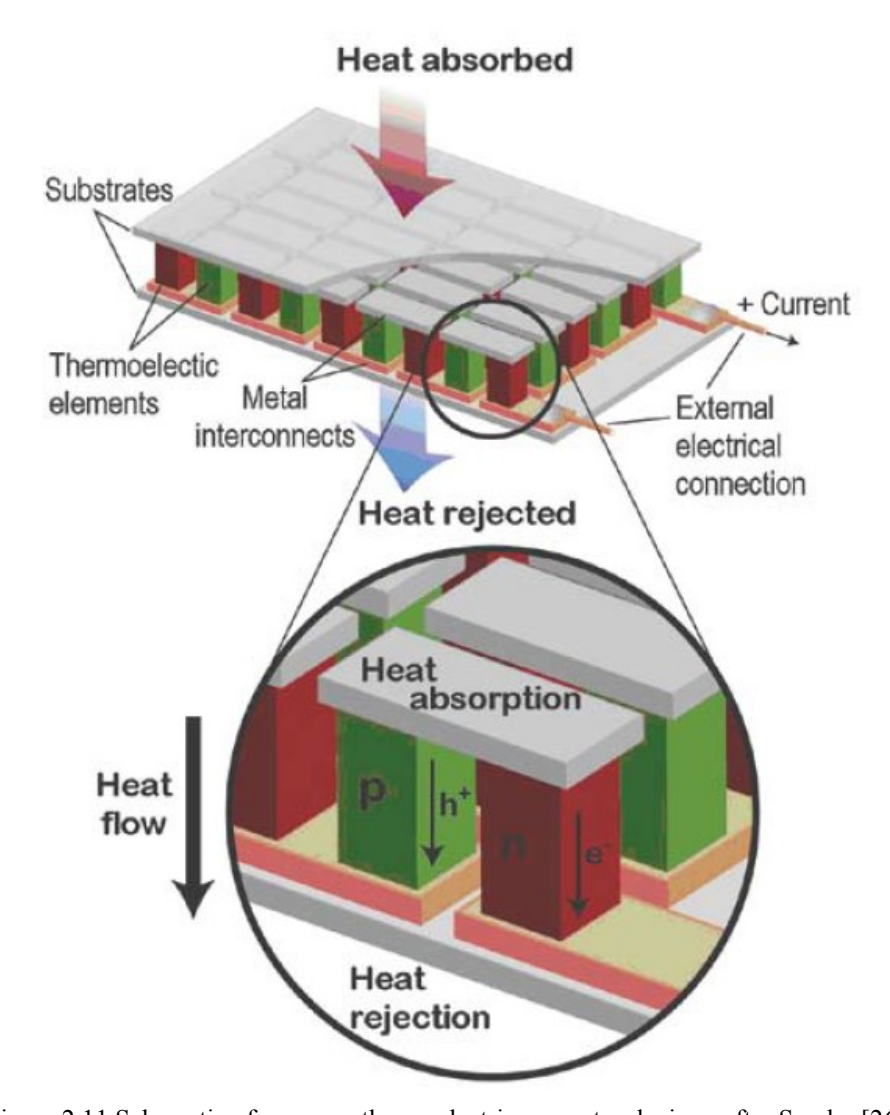


Figure 2.11 Schematic of common thermoelectric generator devices, after Snyder [26] geometry of an individual thermocouple is based on of the specific require

The geometry of an individual thermocouple is based on of the specific requirements of different applications. For example, when the device dimensions are too small to neglect the thermal and electrical contact effects there is a trade-off between the power output and the conversion efficiency [13]. According to Gao's research (shown in figure 2.12), a thermocouple with length in the range from 0.5 to 1 mm is required to obtain a larger power output than those with length below 500 µm.

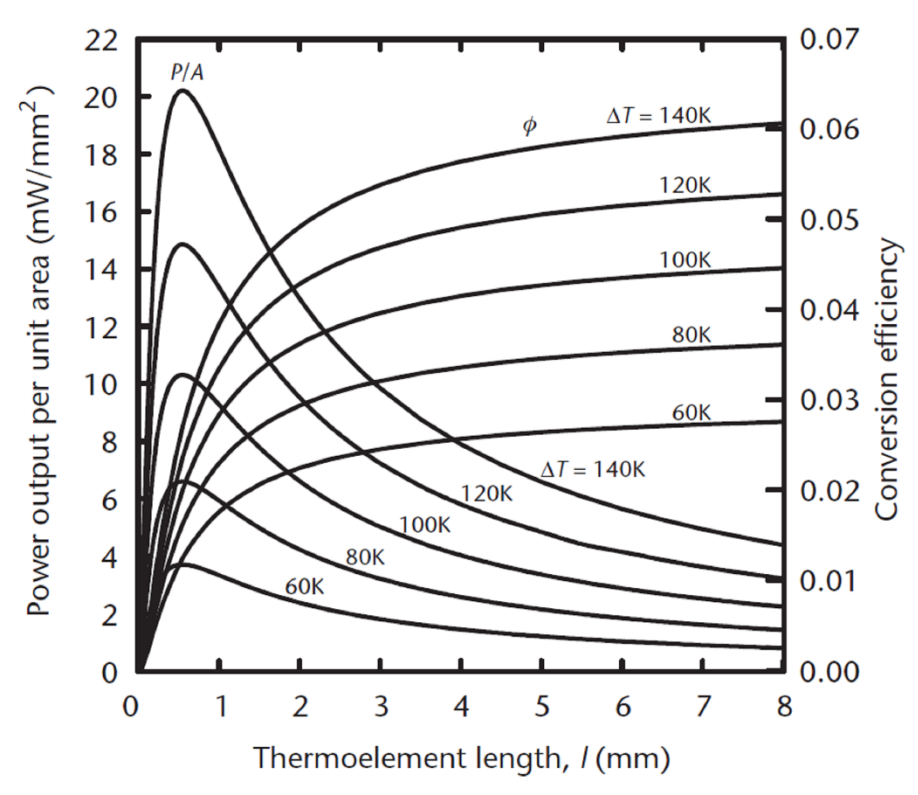


Figure 2.12 Power output per area and conversion efficiency vs. the thermocouple length at different temperature gradients, after Gao [13]

2.5 Summary

Thermoelectric converter designed for electrical power generation is based on Seebeck effect. Although the Peltier effect and Thomson effect exist simultaneously when thermoelectric generator devices operating, according to Lossec et al. [27], they can be ignored because their effects are negligible in comparison to the Seebeck effect when focusing on human body heat energy harvesting application.

The conversion efficiency from thermal energy into electrical energy is limited by Carnot efficiency. For human heat energy harvesting applications, the body temperature is around 37 °C (310 K) while the ambient temperature is around 22 °C (295 K). Then the Carnot efficiency is (310 K–295 K)/310 K = 4.8%. The thermoelectric power comes from human body skin based on this calculation is then in the range of 2.88–4.8 W. The efficiency level is further reduced based on the figure of merit, Z. In conclusion, the conversion efficiency of a TEG used for body temperature energy harvesting is lower than 5% and will be affected by Z. A higher Z value will give higher conversion efficiency.

So, figure of merit is used to evaluate the performance of thermoelectric materials. The expression of figure of merit is shown in equation 2.20. To calculate ZT value, 3

material properties must be measured. These are Seebeck coefficient, electric resistivity and thermal conductivity of the individual material. The power output of the TEGs and the open circuit voltage are used to evaluate their performance of the thermocouples at a device level.

In the room temperature range, defined here as 290K to 300K, the alloys of Bi, Sb and Te have the highest ZT value. This was shown in figure 2.10. Consequently they have attracted the most attention among the various thermoelectric materials that have been examined for room temperature thermoelectric energy harvesting devices.

Chapter 3. Literatures of TEGs, printed TEGs and its application

3.1 Introduction

This research is concerned with producing a printable thermoelectric material ink suitable for use on a flexible substrate. This review will focus on the types of materials, thermoelectric structure design and the printing technologies used in the fabrication of thermoelectric devices.

Various materials have been applied in the published literature to implement thermocouples in TEGs using micro-machining technologies in research. The different thermoelectric properties of the materials are described along with the methods to evaluate the performance of the thermocouples.

Screen and dispenser printing technologies are introduced. These processes are low-cost and suitable for use with flexible substrates such as Kapton and textiles.

Finally, the state of the art in printed TEGs and the application of TEGs in wearable electronics is reviewed.

3.2 Micro-fabricated thermoelectric generators

Conventional TEGs fabrication processes are based on bulk solid materials, e.g., cutting and dicing a solid thermoelectric material bar formed by hot isotactic pressing [19]. The conventional TEGs have limitations in size, flexibility and cost. The fabrication technologies used in Micro Electromechanical Systems (MEMS) have the potential to manufacture TEGs with smaller size and lighter weight. Hence, 12 research papers (see Table 3.1) on micro thermoelectric generators in the field of power MEMS published during last decade have been reviewed.

Thermocoup	le material		e Fabrication methods	Deposition thickness (μm)	Highest processing temperature (°C)	Seebeck coefficient (µV·K·1)	Resistivity (Ω·cm)	TE- efficiency factor (μW·K ⁻ ² cm ⁻²)	ZT	Reference
p-leg	n-leg	Substrate								
p-Si	n-Si	Si on sapphire	Ion implanting, RIE	0.4	925	530	> 100	0.0011	N/A	[28]
p poly-Si	n poly-Si	Si	CVD, ion implanting	0.4	670	160	1.514	0.0426	0.0043	[29, 30]
Poly-Si with SiGe quantum well	Poly-Si	Si	Ultra-high vacuum CVD (UHV-CVD), doping	0.3 (0.05 for SiGe)	N/A	160	p: 0.22×10 ⁻³ n: 0.08×10 ⁻³	0.251	0.566	[31]
Cr	Ni	Si	PECVD	0.15	N/A	35.6	p: 1.29×10 ⁻⁵ n: 0.72×10 ⁻⁵	0.0312	N/A	[32]
(Bi, Sb) ₂ Te ₃	Bi ₂ Te ₃	Si	Co-sputtering, dry etching	20	300	340	N/A	2.4	0.9	[33]
Bi-Te-Sb	Bi-Te	Si	Hot pressing, electroplating, dicing	600	250	200	N/A	5	0.75	[34]
$Bi_{0.3}Sb_{1.7}Te_3$	Bi_2Te_3	Glass	Aerosol deposition	350	400	260	1.3-1.7×10 ⁻³	9.3	N/A	[35]
Cu	Ni	Kapton	Evaporating	0.2/0.1	N/A	16	N/A	7.4×10 ⁻⁵	0.003	[36]
(Bi _{0.25} Sb _{0.75}) ₂ Te ₃	Bi ₂ (Se _{0.1} Te _{0.9}) ₃	Kapton	Sputtering	1	300	370	p: 2.2×10 ⁻³ n: 1.7×10 ⁻³	0.089	N/A	[37]
Bi _{1.61} Te _{3.39}	Bi _{2.68} Te _{2.32}	SU-8 mould	Electrochemical deposition	350	200	340	1.5×10 ⁻³	12.5	0.02	[38, 39]
Sb ₂ Te ₃	Bi ₂ Te ₃	Kapton	RF magnetron co- sputtering	0.5	225	108	p: 1.9×10 ⁻³ n: 1.0×10 ⁻²	9.52×10 ⁻⁷	N/A	[40]

Table 3.1 Characteristics and performance of $\mu TEGs$ in literatures

3.2.1 Micro-fabricated TEGs in literature

The TEGs fabricated by micro-machining technologies are normally called micro-TEGs (μ TEGs). The review of μ TEGs in this part is summarized in table 3.1. All the reported values were obtained around room temperature, which is consistent with the objectives of this work. Some typical μ TEGs are explained in detail in this section.

3.2.1.1 Si, SiGe compounds and metals based TEGs

Silicon (Si) and poly-Si based μ TEGs can be fabricated using existing Integrated Circuits (IC) manufacturing processes (e.g., photo-lithography, etching, vapour deposition, etc.). Also, Si is a low cost material compared to Bi, Sb and Te. A typical example is a silicon based μ TEG with high-voltage and low-power output on a sapphire substrate developed by Rowe and co-workers [28]. In each thermocouple, the n-type thermoelectric material was doped with phosphorous (P) while boron was used as a p-type dopant. The unimplanted silicon between the active parts was removed by reactive ion etching (RIE) to achieve electrical isolation. The interconnections were realized with a thin aluminium layer. The thermocouples were designed in two different dimensions of strips, 4.5 mm by 100 μ m with a separation of 100 μ m. The doping depths (thickness of the thermoleg) was 0.4 μ m. The implanted carrier concentration for both the p- and n-type were 5×10^{19} cm⁻³, which yielded a Seebeck coefficient of 530 μ V/K. At a temperature difference of 10K, the open circuit voltage for one thermocouple with doping depth of 0.4 μ m was 5 mV; and the output power per area is 0.11 μ W/cm².

M. Strasser *et al* [29] also developed micro TEGs using CMOS (Complementary Metal-on-Oxide Semiconductor) based process. The structure of a single generator cell is shown in figure 3.1, with an area of 49 μ m × 10.9 μ m. Poly-Si and poly-SiGe based thermocouples were both fabricated to test the thermoelectric performance. The figure of merit for poly-Si thermocouples with a carrier concentration of 2.5×10^{20} cm³ was 0.0043, which is lower compared to 0.0064 for the poly-SiGe version. The Seebeck coefficient and electrical conductivity of Poly-Si thermocouples are higher than that of poly-SiGe, but it has a larger value of thermal conductivity which is not a desirable characteristic for thermoelectric generator material.

The fabrication process enable 15872 thermocouples in an area of 3.2 mm \times 2.2 mm to be realised. A poly-Si μ TEG with a temperature gradient of 10 °C generates an open circuit voltage per area of 27 V/cm² and an output power per area of 6 μ W/cm² [30].

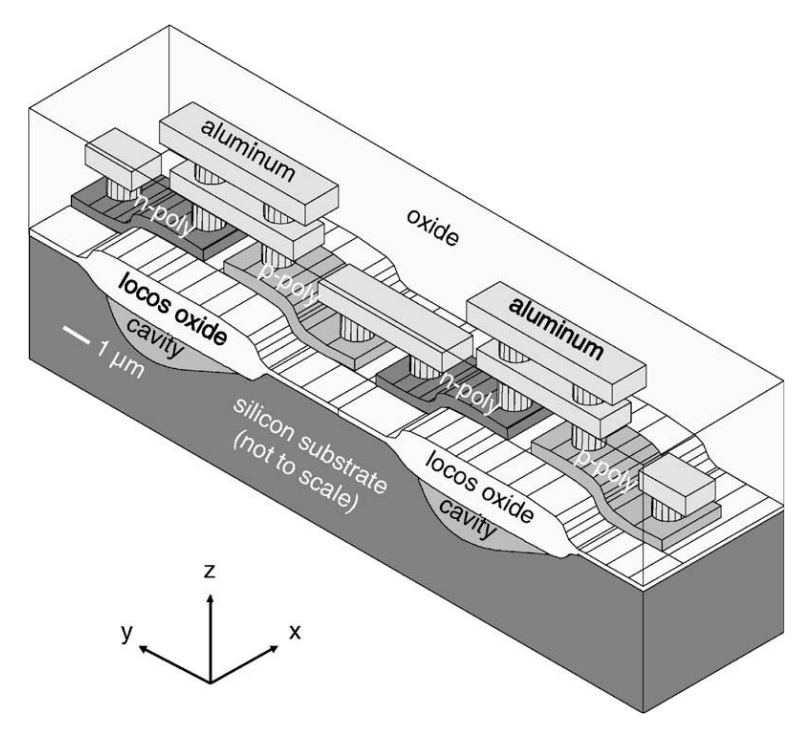


Figure 3.1 Schematic of BiCMOS thermocouples realization, after Strasser [29]

With the state-of-the-art CMOS fabrication process, Yang and co-workers [31] presented a poly-Si based μ TEG with SiGe quantum well under P-type poly-Si film to increase the asymmetry between the hot/cold electrons transport, which could reach a ZT value of 0.566 at room temperature.

The use of metals as thermoelectric materials also attracted some attentions because of their low cost. Topal and co-workers [32] developed 48 Cr-Ni (Chromium-Nickel) thermocouples which generated a voltage of 17.1 mV and a peak power of 10.32 nW within a temperature difference of 10 °C using MEMS technology. However, 6 masks had been used to pattern the thermocouples and electrodes in that fabrication process which increased the fabrication cost. Because each mask involved a photolithography, an etching and a deposition process.

Although micro-fabricated silicon and some metals based μ TEGs have advantages such as compatibility with IC technologies, and the benefit of scaling the size down to μ m range, the cost of the fabrication process is still high. Moreover, for Si-Ge based μ TEGs, the figure of merit is relatively low in the room temperature range (seen from figure 2.11). It increases with the temperature and reaches its maximum value around

900 °C. Micro fabricated Si-Ge and metal based TEG devices are unlikely to be applied on room temperature energy harvesting applications.

3.2.1.2 Bi-Sb-Te based TEGs

Similar thin-film fabrication technologies have also been applied in the fabrication of Bi-Sb-Te based μ TEGs. Böttner and co-workers [33] obtained 20 μ m thick p-(Bi,Sb)₂Te₃/n-Bi₂Te₃ thermocouples using co-sputtering and dry etching followed by a wafer bonding process. The key process for device fabrication is the precise thickness deposition of the p- and n- material between the upper and lower substrate. Like other Bi-Te based thermoelectric devices, it has a high Seebeck coefficient, giving a power factor of 15.7 μ Wcm⁻¹K⁻² for n-material and 25.3 μ Wcm⁻¹K⁻² for p-material. Hence, the combined power factor is nearly 40 μ Wcm⁻¹K⁻². Here, power factor (α ²/ ρ) is applied to describe the power generating ability of the thermoelectric material.

In contrast to laterally fabricated devices with lateral heat flow [37], vertically fabricated devices have a higher thermoelectric efficiency factor because of their higher thermal active material density with the same size of area [33, 39]. Technologies such as sputtering and vapour deposition are unlikely to achieve thermocouples with thickness higher than 50 μ m. The growth rates of sputtered BiTe is in the range of 5 μ m/h [33]. Based on this limitation, researcher developed other micro-machining processes in order to obtain better performance thermocouples.

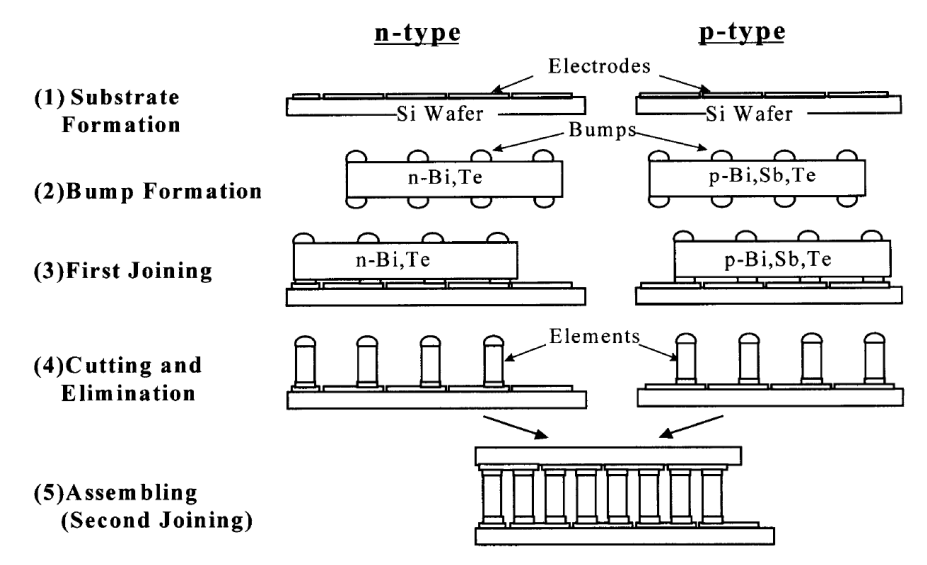


Figure 3.2 Thermocouples fabrication process of the SEIKO wristwatch, after Kishi [34] A research group in SEIKO Corporation [34] developed a Bi-Te based μTEG device to act as the energy source for a wristwatch. The process was also based on micro-

machining technology (in figure 3.2). The figure of merit of this thermocouple is 0.75, and a 2 mm \times 2 mm \times 1.3 mm sized module with 104 thermocouples (80 μ m \times 80 μ m \times 600 μ m for each element) will generate a voltage of 5 V at a temperature gradient of 60K. Inside the wristwatch, 10 of these modules were connected together by gold (Au), contributing a constant conversion voltage of 300 mV and a power of 22.5 μ W when it is worn on the wrist (the ambient temperature is 295 K). The calculated conversion efficiency is 0.047% at 300K when the temperature difference is 1K.

Kouma *et al* [35] presented a vertical fabricated high-aspect-ratio TEG using aerosol deposition (ASD) method to deposit high density nano-sized thermoelectric material particles into photosensitive glass mold followed by a Hot Isotactic Pressing (HIP). With the glass mold, the thermocouple achieved a very high aspect ratio of 7 and a pitch size of 150 μm. The author claimed that the high aspect ratio and high integration density of thermocouples could help to increase the open-circuit voltage efficiency and output power efficiency, which are quite important for harvesting energy from low temperature gradient heat source such as the human body. The thermoelectric performance is conclude in table 3.1.

3.2.1.3 Micro-machined Flexible TEGs

In the last few years, there has been a trend to the design of TEGs on flexible substrates in order to meet the bending requirements on portable devices. Itoigawa *et al* [36] reported a thermoelectric generator on polyimide substrate. As shown in figure 3.4-a, the main part of this TEG is the corrugated sheet located between a heat absorber sheet and heat sink sheet. The corrugated sheet consisted Cu and Ni acting as p-type and n-type thermoelectric material respectively. Polyimide can be used as the flexible substrate because of its high elastic coefficient and electrical insulation property. Cu/Ni thermocouples and interconnections are formed by photolithography, evaporation and lift-off. The finished corrugated structure is glued on to the heat sink and absorber sheets. Several changes were implemented to increase the flexibility of the device:

- 1. Forming a thicker Cu pattern (200 nm) and thinner Ni pattern (100 nm) to strength the Cu-Ni junction.
- 2. Design a corrugated and narrow Ni junction pattern, which can increase the contact length between Cu and Ni junction
- 3. Slits on thermocouples substrate, the heat sink and absorber sheets.

With these adjustments, the author claimed the μ TEG has a bending radius of curvature of 9 mm. For single thermocouple, the Seebeck coefficient is 20.6 μ V/K.

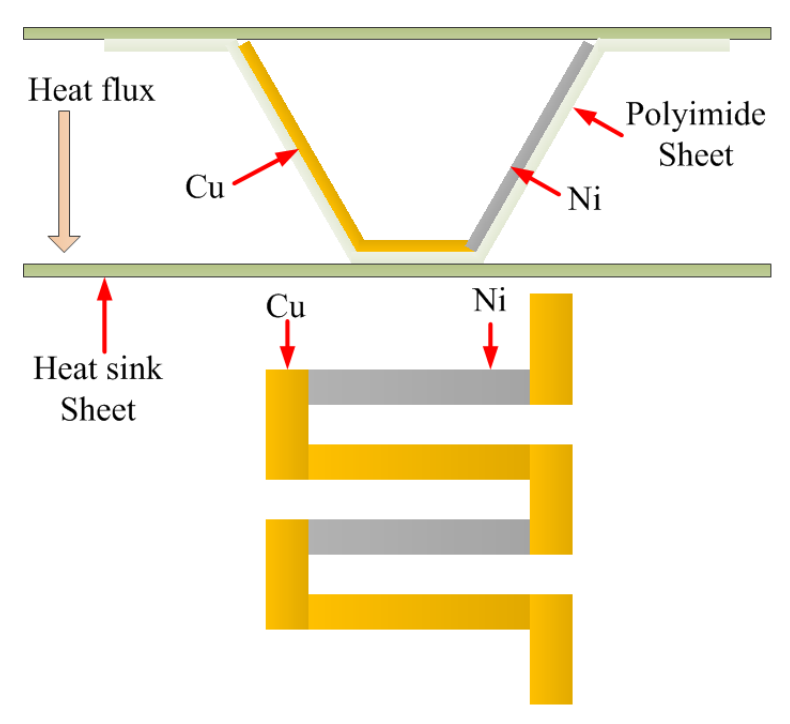


Figure 3.3 Schematics of the Cu-Ni thermocouples on Kapton, fabricated by photolithography and evaporation [36]

Bi-Sb-Te based thermoelectric materials could also be fabricated on polyimide substrate by thin film technologies. Stark et al. presented flexible planer p- $(Bi_{0.25}Sb_{0.75})_2Te_3/n-Bi_2(Se_{0.1}Te_{0.9})_3$ thermocouples on polyimide substrate using dc-magnetron sputtering [37]. The finished TEG is a stack of thin foils electrically connected in series.

Glatz and co-workers used structured SU-8 to form a Bi-Te based flexible thermocouples by electrochemical deposition (ECD) [38]. The deposited thermocouple legs are shown in figure 4-a, where the p-leg is Bi_{2.68}Te_{2.32} with 46% Te content and the n-leg is Bi_{1.61}Te_{3.93} with 69.4% Te content. Au is used as both the seed layer electrodes and interconnects. The image of this device is shown in figure 4-b. The power per unit area of the Bi-Te thermocouples is nearly 100 μ W/cm² at a temperature gradient of 20 °C, which is 20 times higher than the Cu-Ni device fabricated with the same structure size and technology by the same research group [39]. The higher Seebeck coefficient and lower thermal conductivity values of Bi-Te thermocouples resulted a higher figure of merit value than that of Cu-Ni counterpart.

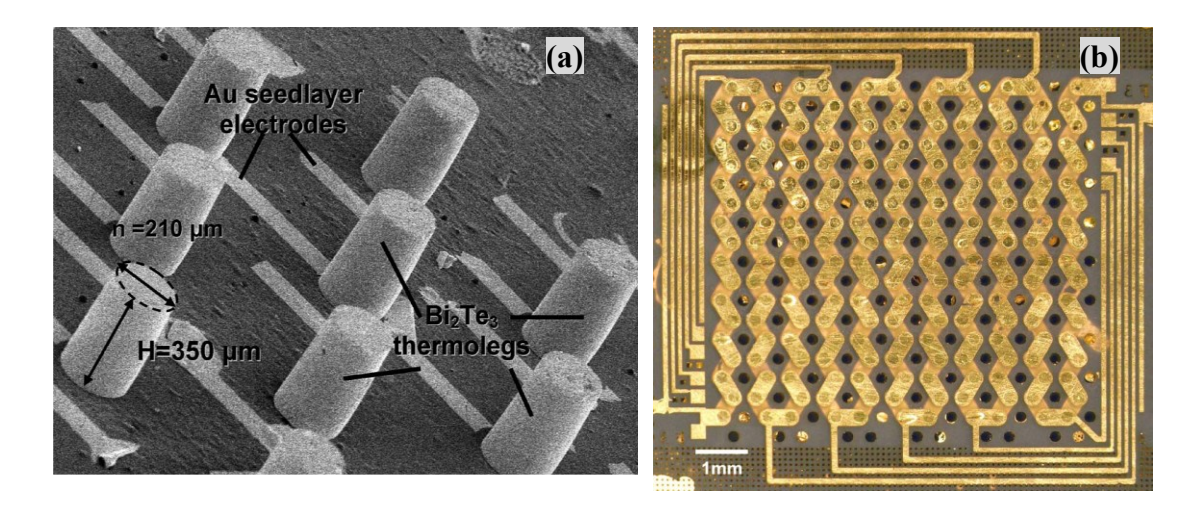


Figure 3.4 A flexible Bi-Te based μ TEG. (a): SEM image of the vertically grew thermocouples. (b): up view of the completed TEGs and Au interconnections, after Glatz [38]

Francioso *et. al.* [40] reported a co-sputtered Sb₂Te₃/Bi₂Te₃ thin film μTEG on Kapton substrate. As seen in figure 3.5-b, the area of BiTe pattern was bigger than that of SbTe pattern. The area ratio of BiTe pattern to SbTe pattern was optimized to achieve the highest conversion efficiency. Au was deposited as the electrodes and the comb-like cold junction radiators.

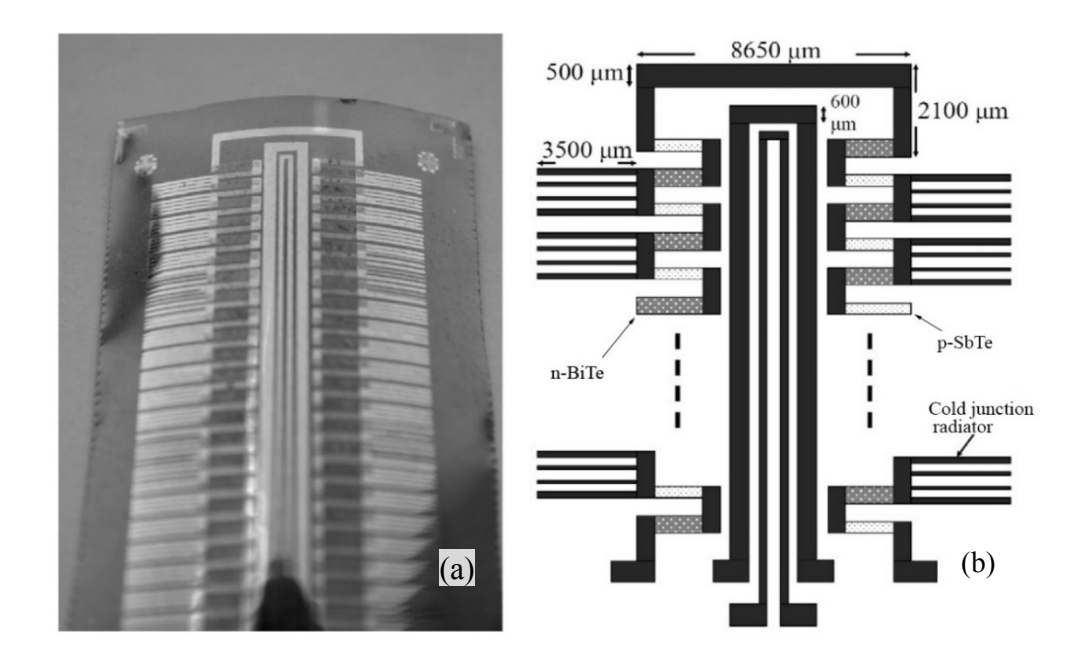


Figure 3.5 A co-sputtered thin film SbTe/BiTe μ TEG. (a): μ TEG on Kapton. (b): schematic of the thin film μ TEG, after Francioso [40]

3.2.2 Discussion

From table 3.1, in room temperature, the Si based thermocouples had the highest values of Seebeck coefficient, but they had a low power output. This is possibly due to the extremely high electric resistivity of the thermoelectric materials which limits

the electric current generated in thermocouples ($\rho > 100~\Omega \cdot cm$). However, their benefits include an easily industrialized fabrication process, and the high figure of merit of Si & SiGe compound at a temperature around 900°C. Hence, they are more suited to high temperature energy harvesting devices.

On the contrary, power output of metals (Cr/Ni, Cu/Ni) based thermocouples were also low despite their high electrical conductivity. The low Seebeck coefficient limited their thermoelectric performance.

In between, Bismuth-Antimony-Tellurium based alloys have balanced α and ρ . They have the potential to be applied in room temperature thermoelectric energy harvesting.

For the fabrication technologies, the conventional micro-fabrication processes were always difficult to form thermocouples with high thickness. For example, the highest growth rate of the conventional micro-machining deposition processes listed in section 3.2 is only around 50 μ m/h [39]. From table 3.1, improved thermoelectric performance is feasible at higher thicknesses. In this case, thick film technologies might give a potential solution for the μ TEGs fabrication because of its quick thickness building up and high production rate.

3.3 Thick film technologies

In this thesis, screen printing and dispenser printing were both investigated for thermoelectric devices fabrication in order to get a high yield. Hence, a brief introduction to screen printing and dispenser printing is given in this section.

In the electronics industry, the thick film technologies were firstly introduced to deposit resistors on a circuit board. The typical thick film process is screen printing, which was used originally in traditional graphic art reproduction [41]. Screen printing is based on the formation of pattern through the use of meshed screen masks and viscous pastes/inks [41]. Direct write thick film technologies such as dispenser printing do not need a specific mask. The software can transfer the input digital patterns into the movements of the stage and the nozzle.

3.3.1 Screen printing technology

Originally, screen printing was developed to print resistors, inductors and capacitors on circuit board in electronics industry. With different loading powders and paste formation, various functional thick films were developed. White et al. [42] reviewed

screen printed sensors such as piezoresistive sensors, thermistors and magnetic sensors, which demonstrated screen printing technology had its potential for fabricating various electronic devices.

The basic difference between electronics screen printing and conventional printing is that the former has a higher requirement on the degree of printing sophistication and the nature of screen material [42]. The typical thick film screen is made from stainless steel or polyester woven mesh with a patterned emulsion layer formed by photographical technology, which offers a higher resolution of printed patterns.

Generally, screen printing contains 4 processes: paste formation, pattern deposition, drying and curing (firing). These processes for screen printing thermal curable paste are shown in figure 3.6. In this thesis, the pastes with ceramic binder always require a curing temperature around or higher than 800°C. These pastes are classified into high temperature cured ones. In order to deposit the thick films on flexible substrate, pastes need to be developed with polymer binder to decrease the curing temperature lower than 300 °C, which are low temperature pastes.

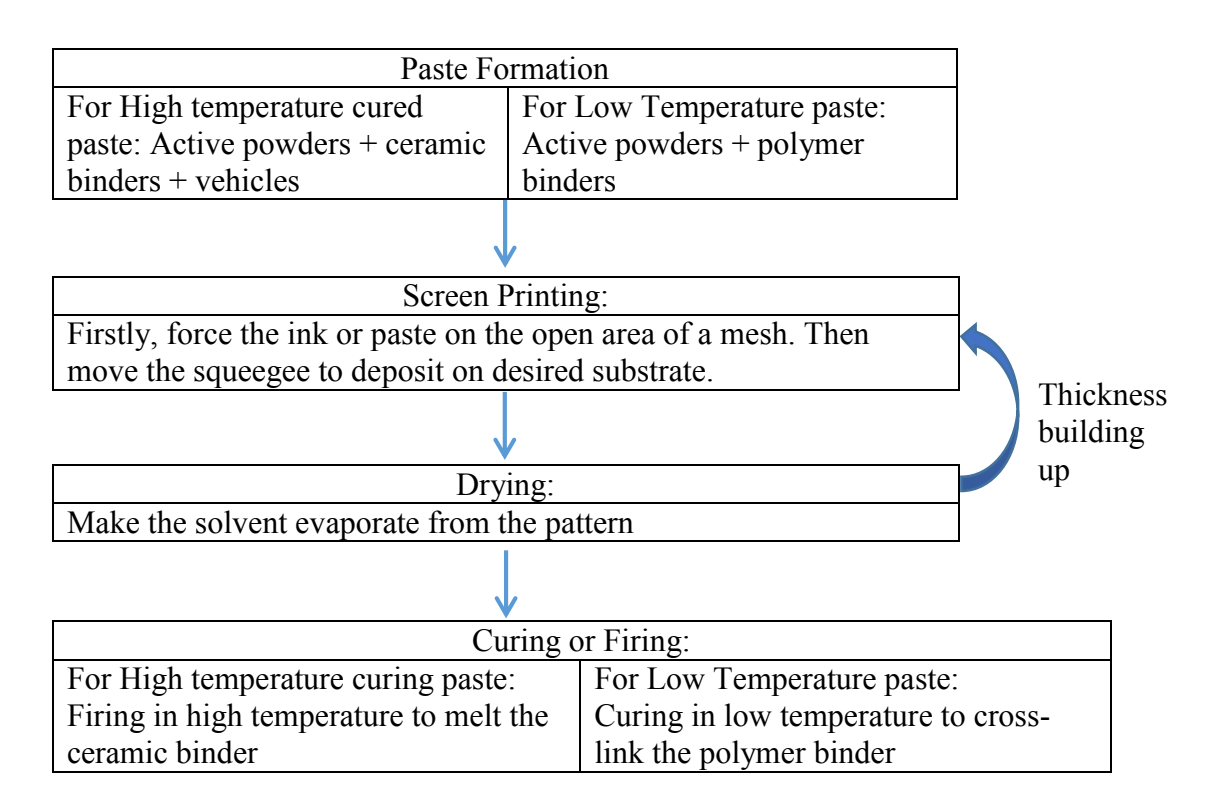


Figure 3.6 Diagram of screen printing process

Firstly, a suitable screen with suitable mesh size and emulsion thickness should be specified depending upon the ink being used and to meet the geometric and resolution requirements of the design. The rheological properties of the paste, such as the liquidity, thixotropy and viscosity, will affect the paste quality [43]. Typical screen printable inks have viscosities in the range of 3000 to 25000 cP [44].

The printing process can be simply divided into 3 steps. Firstly, the pastes are added to the screen and smeared across the surface by the blade. Then, the pressured squeegee will force the pastes through the openings onto the substrate. Finally, the screen lifts off from the substrate leaving the designed patterns on substrate. These simple steps are shown in figure 3.8. The off contact printing mode, having an air gap between the substrate and the screen [45], is usually applied in this work to print electronic materials.

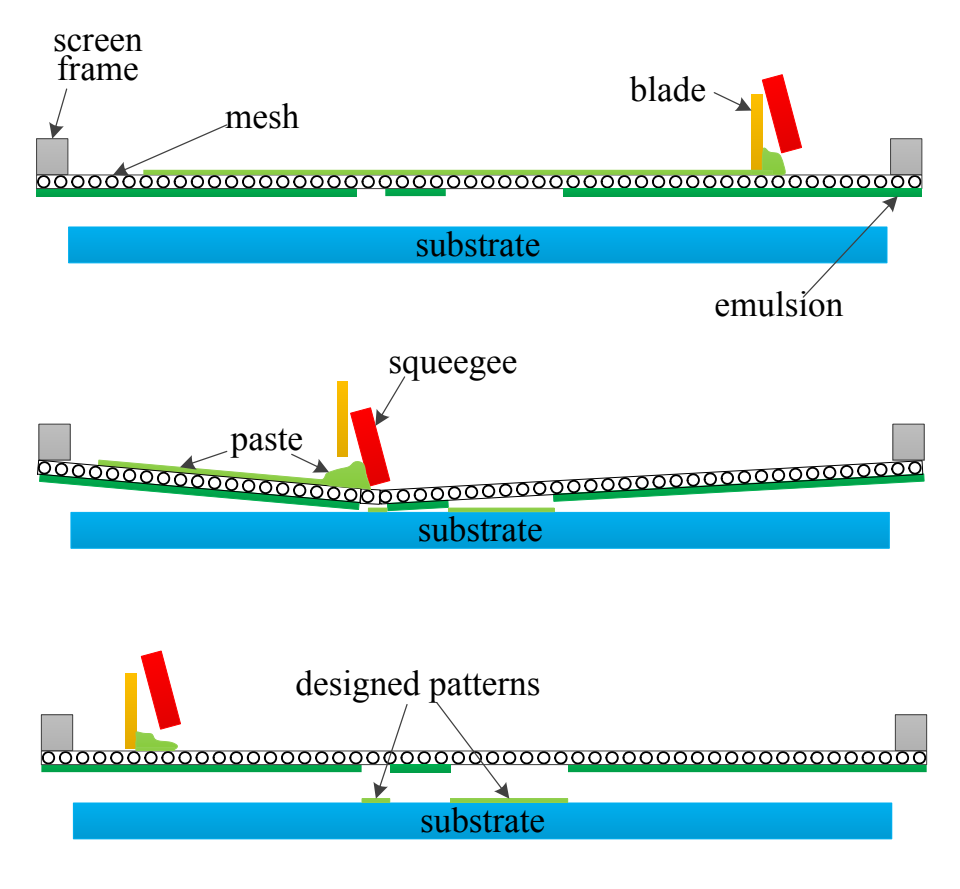


Figure 3.7 Illustration of pattern deposition by screen printing

Film thickness can be built up by printing several layers of the same pattern, drying each patterned layer in turn. After the printing of the first layer, a drying process was necessary to evaporate the liquid component of the ink before printing the second layer. This is preventing the ink from dispensing around due to pressure from subsequent prints. The drying condition is determined by the physical and chemical properties of the organic solvents used in the paste. For one layer of thick-film, usually, two

depositions are applied. The typical thickness for a single layer can be $10 \mu m - 100 \mu m$ depending on the printing setting and the size of filler in the paste.

Finally, a curing or firing process is performed to make the printed pattern adhere properly to the substrate and achieve the desired mechanical functional properties of the film. The curing conditions depend on the properties of the active materials and binders used in the paste. For example, the firing of ceramic binder based pastes is performed in a belt furnace at a peak temperature of around 850 °C [42]. Pastes that use some specific polymer binders only require a curing temperature of 80°C [44]. Moreover, the paste with UV sensitive polymer binder only needs to be cured under UV light in room temperature.

The attributes of printing technology compared with other micro machining technologies summarized by Gilleo *et al.* [46] are low cost of entry, fast time to market, environmentally benign, materials are easily adjusted and modified and simple manufacturing with few variables. For instance, Yang and co-workers [44] screen printed a 5-layers capacitive motion sensor on standard polyester cotton fabric with a sacrificial layer. Garnier *et al* [47] reported a fabrication process for organic thin-film transistors (TFTs) that included two screen printing steps with smallest feature of 200 μ m. A graphite-based polymer gate, drain and source electrodes were screen printed on each side of a 1.5 μ m-thick polyester film which acted as both the dielectric layer and insulating film simultaneously. The field-effect mobility μ_{FET} is 6×10^{-2} cm²V⁻¹s⁻¹, which is close to that of conventional amorphous hydrogenated silicon TETs (between 10^{-1} and $1 \text{ cm}^2\text{V}^{-1}\text{s}^{-1}$) [48]. The authors both pointed out that the products fabricated by printing technology are easy to be industrialized.

Although screen printing is widely used in industry, it has limitations. It cannot achieve the high resolutions typically achieved in micro-fabrication and MEMS processes. The resolution of screen printing is limited by the mesh opening and filament diameter. The minimum line with that screen printing can reach is around 25 μ m [41], while the typical dimensions are around 1 μ m in the plane of wafer in IC industry [49].

In addition, it cannot print nicely on uneven surface. Other printing technologies such as ink jet and dispenser printing can overcome this disadvantage by adjust the distance between the printing heads and the substrate [50].

3.3.2 Dispenser printing technology

For screen printing, a suitable screen with suitable mesh size and emulsion thickness should be specified depending upon the ink being used and to meet the geometric and resolution requirements of the design. The rheological properties of the paste, such as the liquidity, thixotropy and viscosity, will affect the paste quality [43]. Typical screen printable inks have viscosities in the range of 3000 to 25000 cP [44]. Film thickness can be built up by printing several layers of the same pattern, drying each patterned layer in turn. The typical thickness for a single layer can be $10 \, \mu m - 100 \, \mu m$ depending on the printing setting and the size of filler in the paste. After printing, a curing or firing process is performed to make the printed pattern adhere properly to the substrate and achieve the desired mechanical functional properties of the film.

Dispenser printing is a direct-write technology developed to additively deposit materials in paste/ink form. Figure 3.8 shows a basic structure of a dispenser printer. The inks are extruded out from the syringe by the air pressure onto the substrate attached on a 3-axes moving stage. After deposition, the patterns are also dried and cured similar to screen printing. It is also called pneumatic dispenser printer.

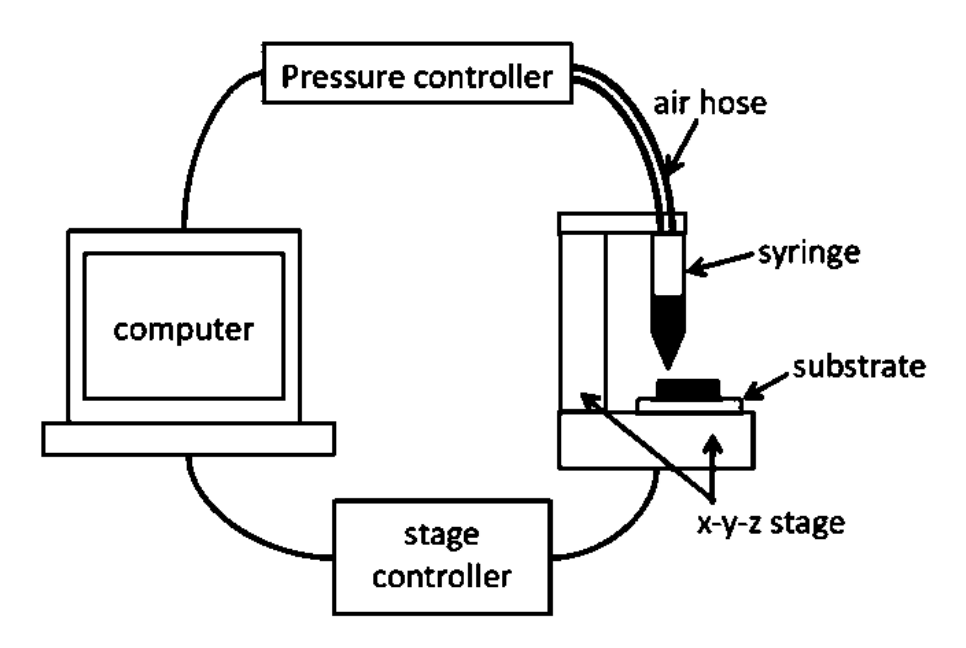


Figure 3.8 Schematic of a dispenser printer, after Wright [51]

The dispenser printer allows inks with a typical viscosity range of 100 – 10000 cP [52], which is thinner than that of the screen printable inks. A variety of low-cost needles and their inner diameter sizes are illustrated in figure 3.9. For different inks, in order

to achieve required pattern size and resolutions, different needles and printing parameters (pressure, time of each shot, printing gap) should be applied.

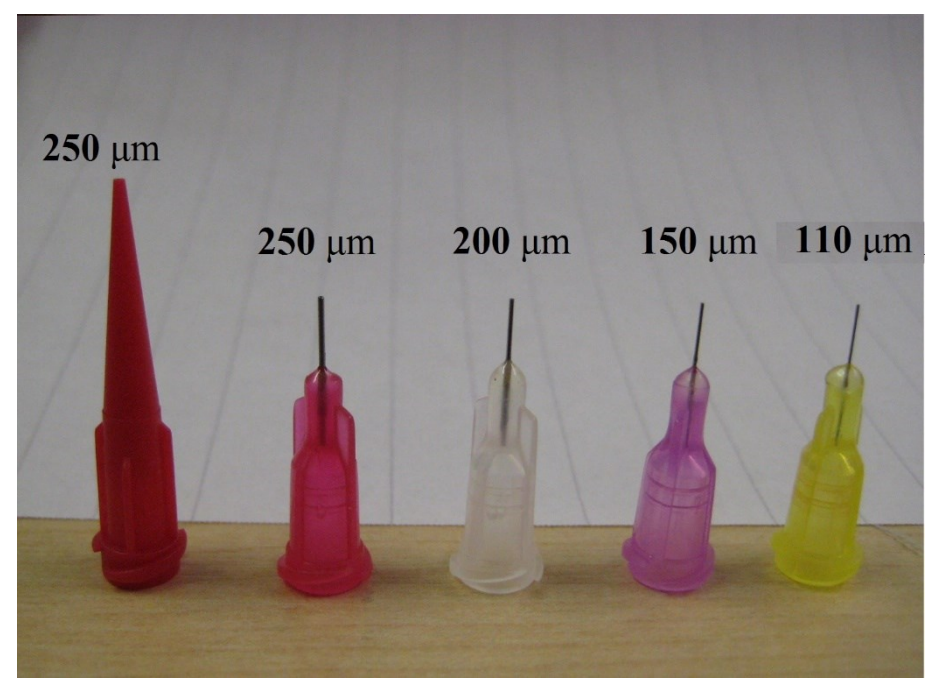


Figure 3.9 Examples of needles and corresponding inner diameters used in dispenser printing. In order to obtain the required pattern, a line for example, single dots should be dispenser printed drop by drop with an adjust step distance. The size of each printed dot is controlled by the pressure, pressing time, ink viscosity, needle shape, needle ends size, gap between the needle head and the substrate and the surface energy of the substrate. Other patterns like rectangular and square can be achieved by numbers of adjacent printed lines. The pattern printing process is illustrated in figure 3.10.

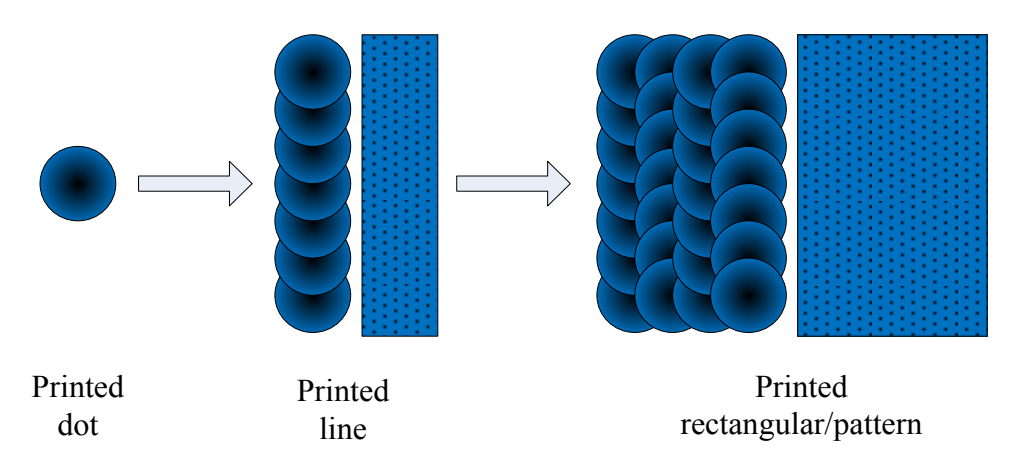


Figure 3.10 Illustration of pattern realization by dispenser printing

Ho and co-workers [53] developed a multilayer zinc micro-battery with an ionic liquid gel electrolyte on Ni substrate using dispenser printing technology. The thickness of the manganese dioxide electrode/gel electrolyte/zinc electrode sandwiched structure

was between 80 and 120 μ m. This demonstrated dispenser printing can be applied as a low cost technology which is capable of fabricating electronic devices with relatively larger thickness (> 50 μ m).

To conclusion, for pattern transferring, two different thick film technologies have been highlighted in this section. Both have lower fabrication cost than micro-machining technologies, which need photolithography and etching to develop the required patterns.

Printing technologies	Screen printing	Dispenser printing		
Paste viscosity	~3000 cP ~25000 cP [44]	~100 cP -~10000 cP [52]		
Pattern transfer	With mesh screen as mask	By bitmap drops or continues line		
Deposition thickness range	~10 μm to ~ 500 μm	~1 µm to ~5 mm		
Pressure source	Squeegee	Air pressure		

Table 3.2 Comparison of technology features between screen printing and dispenser printing Screen printing and dispenser printing have their own advantages and drawbacks. For screen printing, some paste will be wasted during alignment. Conversely, the dispenser printer only prints dots on required places. Moreover, it is harder for screen printing to build up higher thickness compared with dispenser printing because of the pressure generated by the squeegee. A comparison between screen printing and dispenser printing is given in table 3.2. Screen printing is more suitable to produce electronics devices with repeatable patterns while dispenser printing is quicker for evaluating different designs.

3.4 Printed thermoelectric generator devices

Printing thermoelectric materials process requires the material to be in the form of a printable paste. This section reviews the literature for printed TEGs and the materials used.

3.4.1 Printed TEGs in literature

The review of TEGs fabricated by printing is summarized in table 3.3. All the reported values including Seebeck coefficient, resistivity, power factor and figure of merit are obtained at around room temperature.

Thermocouple materials	Binder and vehicle system	Substrate	Fabrication methods	Size of single element (L*W*H) (mm)	Curing condition	Seebeck coefficient $(\mu V \cdot K^{-1})$	Resistivity (Ω·cm)	Power factor (μW·K ⁻² cm ⁻¹)	ZT	Reference	
p-type NiCr	Polyester, cellulose		Screen	404NI/A 4NI/A	N/A	9.37	NT/A	DT/A	N/A	[54, 55]	
n-type Ni-Panipol	and conductive polyaniline	polyester	printing	40*N/A*N/A	N/A	-12.5	N/A	N/A			
p-type ZnSb	Glass frit, α-	Alumina	Screen	5*5*0.05	500 °C	~230	~3.35×10 ⁻²	1.6	N/A	[56-57]	
n-type CoSb ₃	Terpineol	Alullilla	printing	3.3.0.03	300 1	-49	4.75×10 ⁻³	0.5	0.5	[56, 57]	
p-type Sb	ethylene glycol,	-4-11 I	IZ t	Screen	10*0.5*0.002	NI/A	0.7	Order of 10 ⁻²	N/A	NI/A	[50]
n-type Bi _{0.85} Sb _{0.15}		Kapton	printing	10*0.5*0.003	N/A	97	Order of 10 ⁻¹	IN/A	N/A	[58]	
p-type Bi _{0.5} Sb _{1.5} Te ₃	D 1	A1.O	Screen	0*12*0.00	250°C,	123	1.28×10 ⁻¹	N/A	N/A	[59]	
n-type Bi ₂ Sb _{0.3} Te _{2.7}	Polystyrene, toluene	Al_2O_3	printing	8*12*0.08	10 hrs		3.17×10 ⁻²				
p-type Sb ₂ Te ₃	epoxy resin, butyl	Vantan	Dispenser	5*0.64*0.09	250°C, 3	160	1.6×10 ⁻²	1.5	0.19	F(0, (1)	
n-type Bi ₂ Te ₃	glycidyl ether	Kapton	printing	3*0.64*0.09	hrs	-157	2×10 ⁻²	1.4	0.18	[60, 61]	
p-type Bi _{0.5} Sb _{1.5} Te ₃	epoxy resin, butyl glycidyl ether	Kapton	Dispenser printing	5*0.6*0.12	250°C, 12 hrs	278	4.2×10 ⁻²	1.8	0.2	[62]	
p-type Sb _{1.5} Bi _{0.5} Te ₃	3-mercaptopropanoic	Glass,	Ink-jet	N/A	400°C,	177	1.6×10 ⁻²	1.83	N/A	[63]	
n-type Bi ₂ Te _{2.7} Se _{0.3}	acid (MPA), water	Kapton	printing		30 mins	-139	4.8×10 ⁻²	0.77		. ,	
PEDOT:PSS	N/A	N/A Textile	Screen 140	140*10*0.02	120°C,	10	0.74	4×10 ⁻⁴	N/A	[64]	
PANI	1 1/11	10/10/10	printing	110 10 0.02	10 mins		10	136	2×10 ⁻⁶	14/11	[0,1]

Table 3.3 Printed thermocouples and their features from literature

Duby *et al.* fabricated three thermocouples on top of polyester substrate (shown in figure 3.11) using screen printing [55]. 6 thick films were printed and tested in the work: nickel chromium (NiCr), Iron (Fe), Silver (Ag), Ni, Ni-Panipol and NiCr-Ag. For the ink formulation, Panipol M (a conductive poly-aniline) resin, polyester and cellulose formed the binder system in which metal particles were suspended. Other additives were included to improve the electrical properties of the thermocouples. For example, heptanoic acid was introduced into the paste to separate the individual particles from one another and to ensure that the minimum amount of binder is needed to coat each individual particle completely.

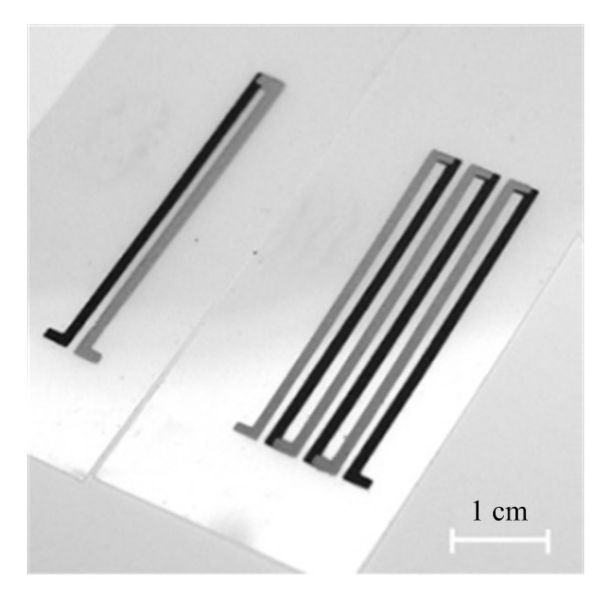


Figure 3.11 Thermocouples printed on polyester substrate, after Duby [55]

The thermoelectrical performance of the printed flexible thermocouples was investigated by measuring the Seebeck coefficient of a single leg. The thermocouple pattern is shown in the above figure. The temperature gradient goes along the thermoelectric legs and three mineral-insulated k-type thermocouples probes were used to monitor the ambient cold-junction and hot-junction temperatures. NiCr and Ni-Panipol were chosen to be the n-type and p-type thermoelectric materials respectively because they demonstrated the highest absolute value of Seebeck coefficients from the samples presented. When $\Delta T = 80$ °C, the voltage generated by a single thermocouple is 1 mV.

Lee *et al.* also demonstrated screen printed μTEGs [56, 57] using ZnSb and CoSb₃ as the p-type and n-type thermoelectric materials respectively and copper as the electrodes. They demonstrated that ZnSb screen printed film annealed in a furnace tube at 580 °C has a maximum power factor of 1.06 mW/mK² compared to a power

factor of 0.258 mW/mK² obtained when annealed in a rapid thermal processing (RTP) chamber at 500 °C. The fabrication process is shown in figure 3.12. Different from other printed planar thermocouple structures mentioned in this section, the ZnSb and CoSb₃ thermocouples were vertically printed to build up the thickness. The size of an individual thermoleg was 5 mm \times 5 mm \times 50 μ m. The output voltage was 13 mV from a temperature difference of 20°C, while the output power is around 10 μ W/cm².

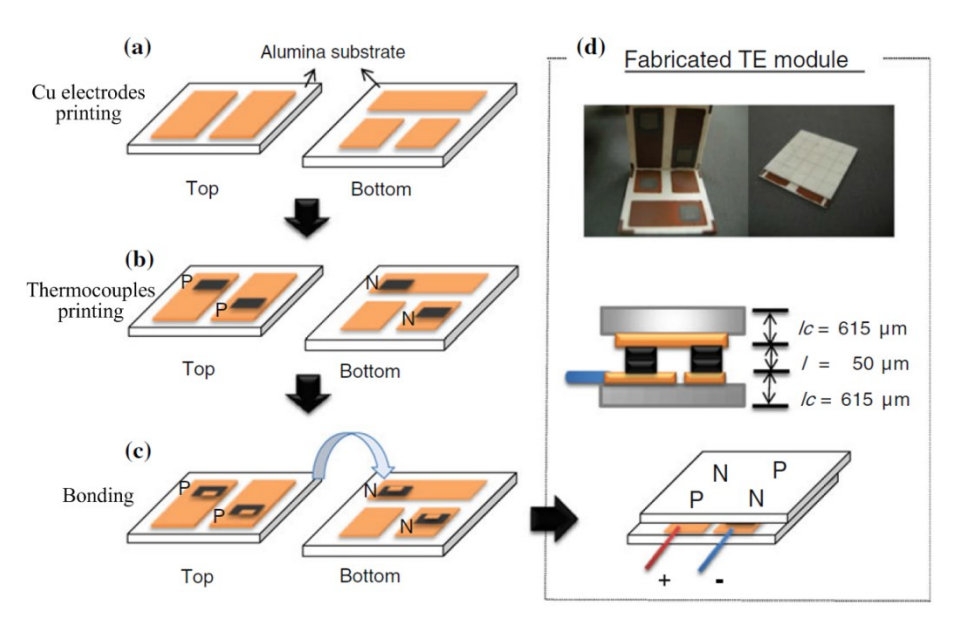


Figure 3.12 Process flow of a thermoelectric module fabricated using screen-printing, after Lee [27] The RTP cured film was found to have a more porous structure than the sample cured in the furnace [56]. The porous structure exhibited a lower carrier concentration which resulted in the decrease of the power factor. The Cu paste is used on the bonding of these thermocouples onto the Cu electrodes. However, the author claimed the high contact resistance reduced the thermoelectric performance of the TEG device [56].

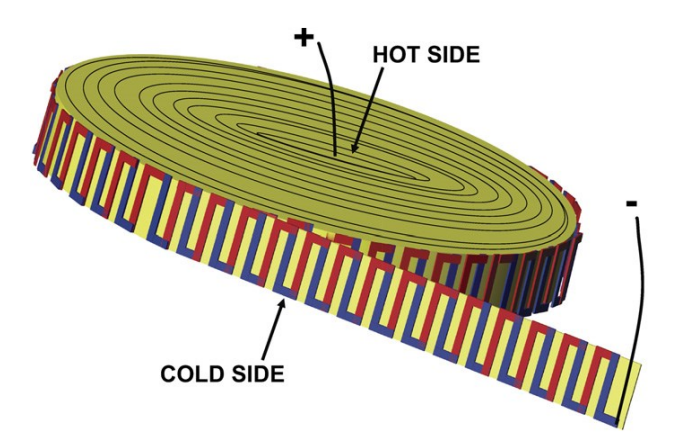


Figure 3.13 Schematic of the coiled-up TEG, after Weber [58]

Because the binders used in the paste for screen printing are typically dielectrics, this decreases the electric conductivity of the printed films, and the figure of merit of

thermocouples will also decrease as a result. Hence, active powders with high Seebeck coefficient are required to offset this disadvantage. The high Seebeck coefficient of Bi-Sb-Te based thermoelectric materials have attracted more interest than other metal based material. Weber et al. [58] demonstrated the possibility of thermocouples can be screen printed on top of polyimide (Kapton) substrate to form a coiled-up TEG. The schematic is shown in figure 3.13. For the paste preparation, Sb (particle size 4µm) and Bi_{0.85}Sb_{0.15}-alloy (particle size 37µm) were used as the thermoelectric materials, ethylene glycol was used as the binder and sodium borohydride was applied to chemically reduce the surface oxidation of Sb and its alloy in order to improve the electrical conductivity of printed track. Bi_{0.85}Sb_{0.15}-alloy was chosen as n-type thermoleg because of a higher thermopower than pure bismuth [65]. The electrical resistivity of the Bi_{0.85}Sb_{0.15} film was around $10^{-1} \Omega$ ·cm, which the author claimed was much higher than the bulk material due to the native surface oxidation and the particles were not melted. For a single screen printed thermocouple, the Seebeck coefficient is about 97 µV/K. This work demonstrated the coil is a potential generator structure for planar thermocouples fabricated by printing.

More recently, Navone *et al.* [59] optimized the screen printing process parameters to improve the thermoelectric performance of the planar device. The expected thickness was 100 μm which is ideal for screen printing technology. The n-type thermoelectric material was Bi₂Se_{0.3}Te_{2.7} while the p-type was Bi_{0.5}Se_{1.5}Te₃. The fabrication process is illustrated below:

- 1. Thermoelectric powder milling. The first step is forming the active part of the thermoelectric pastes. Bi, Te, Se, and Sb powders were mechanically alloyed (MA) in the specific ratio for each thermoleg in a ball mill under purified argon atmosphere using a stainless-steel vessels and balls.
- 2. Thermoelectric paste formation: 22 wt.% toluene was used as the vehicle to provide a suitable viscosity for the paste to ensure printability and structural integrity of the film. 2 wt.% polystyrene was used as the binder that can cross-link between itself and toluene to adhere the printed film on the substrate.
- 3. Printing process: The planar sample was printed on Al₂O₃ rigid substrate using screen printing, then cured at 250°C in an inert gas for 10 h. The size of each thermoelectric material element was 0.8 cm × 1.2 cm × 80 μm (shown in figure 3.14-a). A second sample was printed on polyethylene naphthalate (PEN) flexible

substrate using stencil printing (figure 3.14-b), laser-annealed using a 473 mJ/cm2 excimer laser with various number of pulse [59].

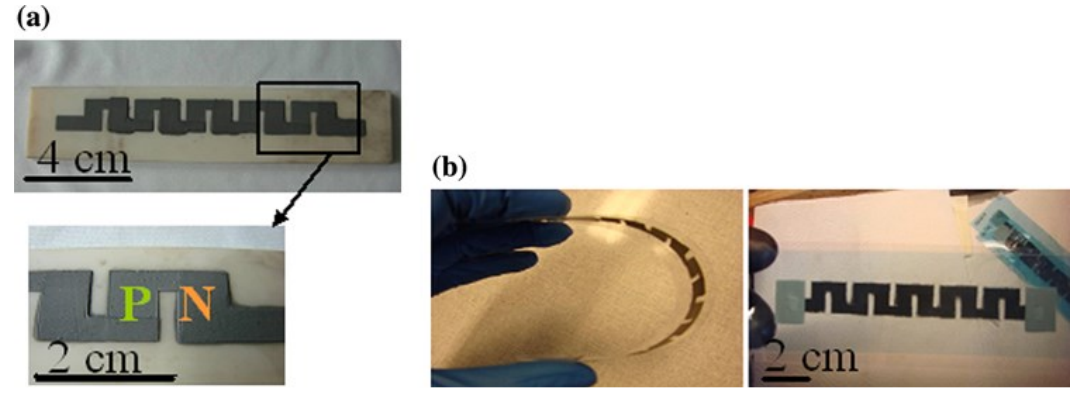
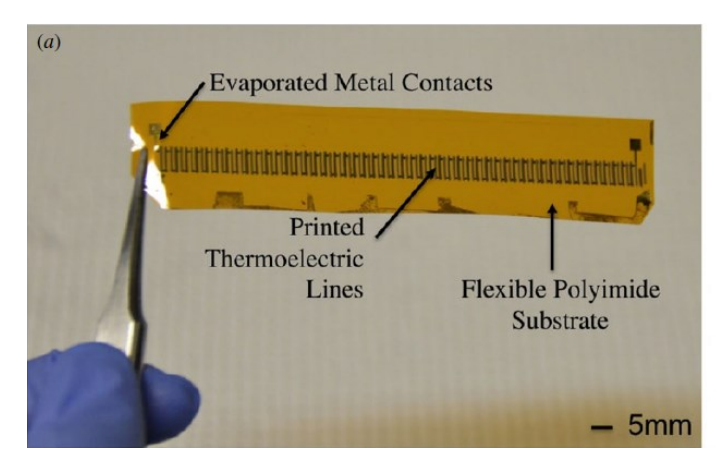


Figure 3.14 Printed thermoelectric devices (a) on alumina substrate, and (b) on polymer substrate, after Navone [59]

For the thermally (250°C) annealed sample with 5 thermocouples on alumina substrate, the generated voltage was 30 mV at a temperature differential of 50°C. The Seebeck coefficient was 123 μ V/K and the resistivity of p-type and n-type screen-printed films were 0.13 Ω ·cm and 3.2×10⁻² Ω ·cm respectively. The laser annealed p-type Bi₂Te₃ sample was printed on PEN. The optimized resistivity and Seebeck coefficient were 0.125 Ω ·cm and 90 μ V/K respectively. The highest power factor reported by Navone was 0.06 μ WK⁻²cm⁻¹ for a single thermoleg [59]. The high resistivity limited the thermoelectric performance.

Chen *et al.* [60] used dispenser printing technology to fabricate a planar thermoelectric device with 50 thermocouples on a polyimide substrate with evaporated metal contacts, shown in figure 3.15-a. This printed planar thermoelectric lines can be rolled to form a high-density array coil (shown in figure 3.15-b) with the temperature gradient along the planar thermocouples. The fabrication process is illustrated in figure 3.16.



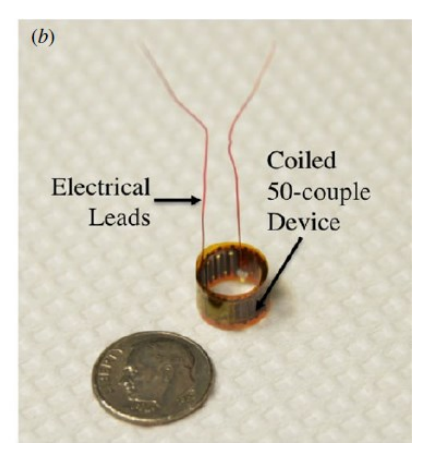


Figure 3.15 Images of (a) dispenser printed 50-couple planar thermoelectric device on a flexible polyimide substrate and (b) coiled prototype with electrical connections, after Chen [60]

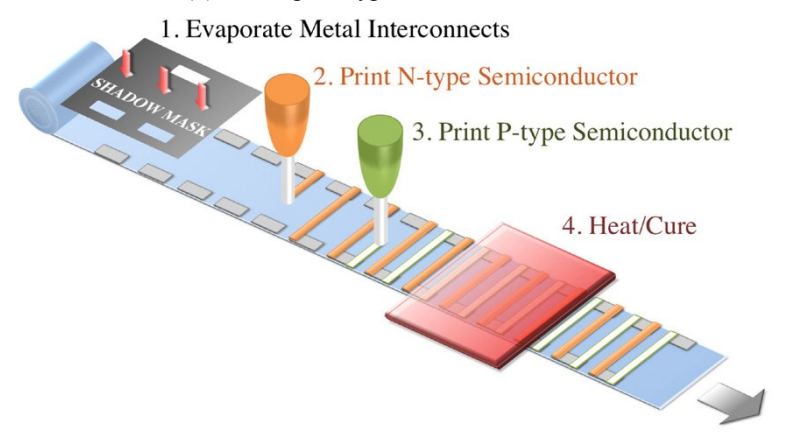
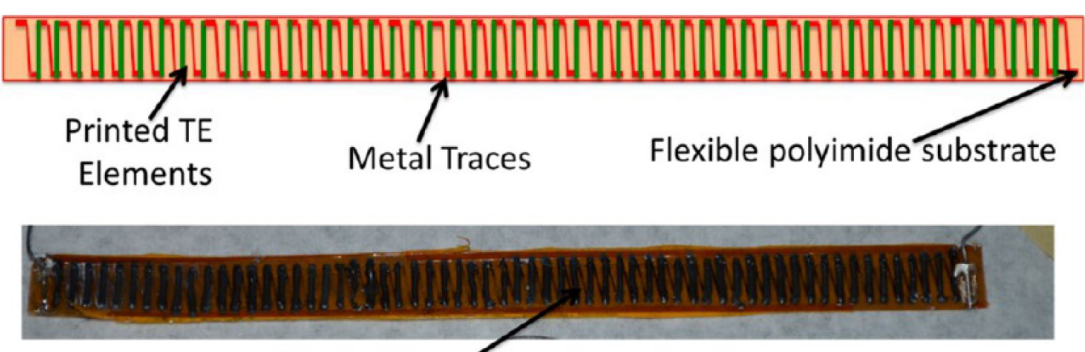


Figure 3.16 Fabrication process for a planer dispenser-printed thermoelectric device, after Chen [60] Firstly, the gold metal interconnects were deposited onto the substrate. Then, the Bi₂Te₃ and Sb₂Te₃ inks were dispenser printed across the top and bottom contacts individually. The average particle size was 10 μ m for both types of materials. Finally, all printed thermocouples were cured at 250°C in an argon atmosphere. The dimension of individual thermolegs was 5 mm \times 640 μ m \times 90 μ m and the space between two adjacent p- and n-type semiconductors was 360 μ m. The thermoelectric properties of these two printed thermocouples are given in table 3.3. When the load resistance was matched, the 50 thermocouples device generated a voltage of 171.6 mV at a current of 61.3 μ A from Δ T=20°C, which gave a power of 10.5 μ W. The thermoelectric properties were optimized under different curing conditions in the same group [61]. The resistivity of Sb₂Te₃ thick film was reduced to 3.2×10⁻³ Ω ·cm while that of Bi₂Te₃ thick film was still high at 5.9×10⁻² Ω ·cm when cured at 350°C for 12 hours.

In order to reduce the resistivity of Bi₂Te₃ thick films, Madan *et al.* [62] developed a TEG with p-type Bi_{0.5}Sb_{1.5}Te₃ only. The structure is shown in figure 3.17. With extra

8 wt.% Te added into the composite, the printed 50 thermocouples generated 130 mV and 20.5 μ W from a temperature gradient of 20°C.



Printed MA Bi_{0.5}Sb_{1.5}Te₃ with 8wt% Te composite lines

Figure 3.17 Illustration and image of dispenser printed p-type $Bi_{0.5}Sb_{1.5}Te_3$ planar TEG, after Madan [62]

Ink-jet printing was also able to be used on fabricating flexible TEGs. Lu *et al.* [63] reported a flexible TEG device with 3 thermocouples on polyimide substrate, which had a similar size and structure with that in figure 3.11. The solution based inks had a viscosity range of 5 - 20 cP, which was around 100 times lower than the viscosity of dispenser printed pastes.

Some polymer based thermoelectric materials can also provide reasonable ZT value compared with the inorganic materials mentioned above. For example, optimized poly(3,4-ethylenedioxythiophene) exhibits a high ZT value of 0.25 at room temperature [66]. Organic based thermoelectric materials have advantages such as mechanical flexibility, low-cost synthesis compared with the inorganic materials, and feasibility for large areas production. Moreover, most organic thermoelectric materials were easily formed into a paste compared with solid state materials, which is another advantage for printing technology.

Seeberg *et al.* [64] presented printed thermocouples using commercial available organic polymers directly on textile, in which the thermoelectric materials were Poly(3,4-ethylenedioxythiophene):poly(4-styrenesulfonate) (PEDOT:PSS) and polyaniline (PANI). The PANI and PEDOT:PSS pastes were all screen printed onto acrylic treated textile substrate (shown in figure 3.18 right), which reduced the wicking of the fabrics. The dimensions of the thermocouples were 1 cm \times 14 cm and according to the SEM figure, the thickness of printed PANI and PEDOT:PSS are 25–50 μ m and 15–20 μ m respectively. One sample thermocouple can generate a voltage of about 1.5 mV at a temperature difference of 40°C. The Seebeck coefficients of individual printed

polymer were estimated by adding another copper strip then measuring the output voltage of Cu/polymer thermocouples in a temperature gradient. For printed PANI sample, the Seebeck coefficient was +15 μ V/K and that of PEDOT:PSS sample was +18 μ V/K. The expected Seebeck coefficient of PEDOT:PSS/PANI thermocouple was +3 μ V/K. However, the observed value was +10 μ V/K, which the author claimed was due to the high noise level in their measurements [64].

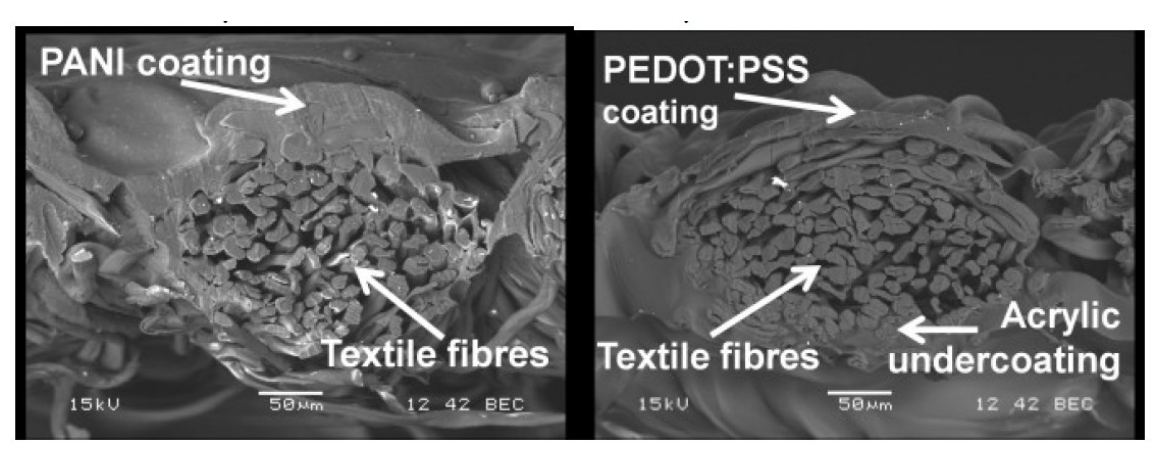


Figure 3.18 Cross-section of cotton textile coated with PANI (left) and PEDOT:PSS (right), after Seeberg [64]

3.4.2 Discussion

Unlike the bulk material fabrication and micro machining technologies, printed TEGs started with functional pastes/inks/slurries loaded with thermoelectric materials with a specific viscosity. The preparation of a printable paste is the first and essential step when printing TEGs.

For solid state thermoelectric materials, including metals and alloys, they must be milled into particles with suitable size. The average size is determined by the printing technology used. Powders with an average size of 10 µm can be applied in dispenser printable paste [60] while inkjet-printed TEGs requires an average particles size below 10 nm [63]. The particles for dispenser and screen printing were normally milled from bulk materials, while the particles for ink-jet printing came from several steps of chemical reactions [63]. This project will focus on screen printing and dispenser printing.

In order to make a printable paste, the thermoelectric materials are typically mixed with suitable vehicle and binders. The principal function of the vehicle is to provide suitable viscosity for the ink, such that it can be screen printed onto the substrate. Binders can be divided into two categories: inorganic binders (e.g. glass frit in

reference [57]) and organic binders (e.g. polyester resin in reference [55]). Generally, inorganic binders are melted under high temperature, which means these pastes can be only deposited on to substrates such as aluminium oxide and silicon wafer. Organic binders can be used for low temperature applications because the polymers cross-link at temperature lower than the melting point of a ceramic binder. The appropriate viscosity can be achieved by adding suitable solvents and most organic binders can be adjusted to enable screen printing.

From the literature in this section, it can be concluded that in printed thermoelectric material thick films, the binders can hold the particles onto the substrate and bind the particles together. Once the particles are physically attached, the Ohmic contact is established. This is the basic operation principle of electrical and thermal conductivity in printed thick film thermoelectric generators [54]. Hence, it can be concluded that thermoelectric device can be fabricated using printing technology.

Low temperature cured printed flexible TEGs had lower Seebeck coefficients and higher electric resistivity than the theoretical bulk materials. This is due to the voids in the present printed thick films and the dielectric binders used in the pastes which increased the electric resistivity [54, 60].

Instant pulse curing can be applied instead of thermal curing because of it is suitable to be used on flexible substrate. A pulse light with specific wavelength can melt and active the fillers in a short time without getting the substrate too hot [67]. This simplifies and shortens the time of the whole printing process, in addition, it improves the performance of the printed thick films somehow.

In contract, pulse curing requires an extremely expensive machine and high energy consumption. From the production cost point of view, thermal curing has its own advantage.

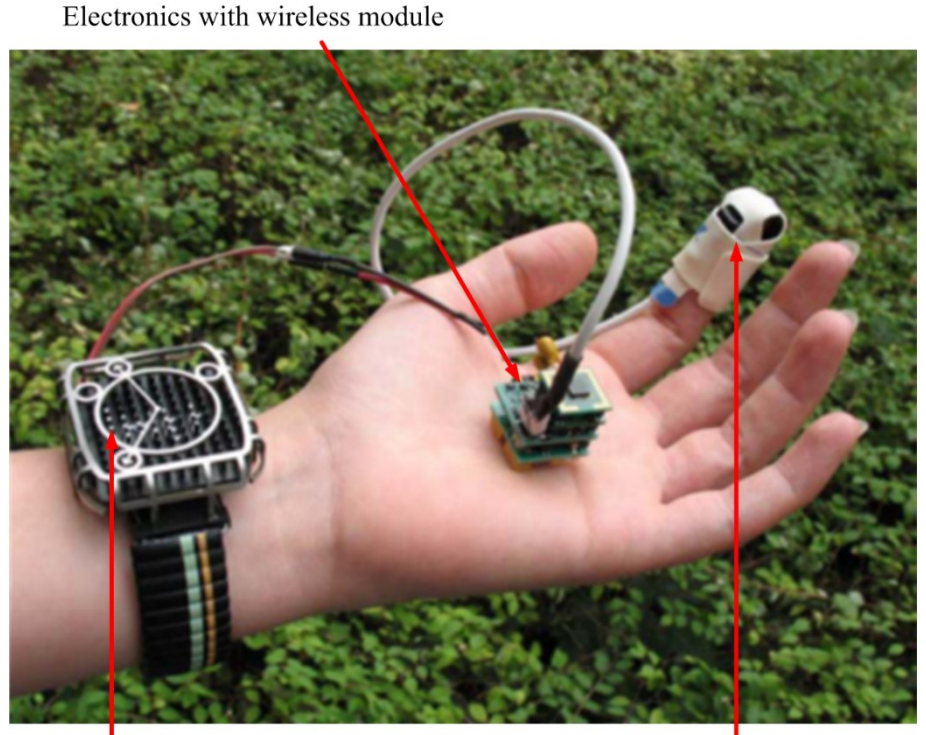
Organic material pastes also have the potential to be applied in fabricating thermoelectric generators based on printing technology. Compared with the powder filled paste, pure polymer pastes have the advantages of ease of processing, lower temperature curing and no need for the expensive powders. However, the thermoelectric performance of organic thermoelectric active materials is not currently as good as the powder filled pastes.

3.5 Applications of thermoelectric generators on the human body

The current wearable low-power wireless sensors have a power consumption range of 0.01 - 10 mW, depending mainly on the data transmission rate [68]. From the discussion in chapter 1, this amount of power can be generated by TEGs using the temperature gradient between the human body and the environment. Hence, wearable low-power electronics, including wireless sensors for health monitoring, are the main target applications for wearable TEGs. Some previous work related to powering wearable sensors with TEGs and wearable TEGs will be introduced in this section.

3.5.1 Human body TEGs in literature

Torfs *et al.* developed a method to power a device to measure oxygen content in arterial blood, known as a pulse oximeter, entirely with a wearable TEG [69]. The three components in this system are illustrated in figure 3.19.



'Watch'-style thermoelectric generator Commercial finger pulse oximeter Figure 3.19 Body heat powered pulse oximeter, after Torfs [69]

In this system, a capacitor was used as a storage element for short-term energy buffering to ensure the full energy autonomy. The required power for the sensor system is 89 μ W, while the capacitor connected with the TEG provided an average power of 100 μ W when the ambient temperature is 22°C or below. A 38 mm \times 34 mm-sized radiator was placed on top of the standard rigid TEG is 38 mm \times 34 mm to improve

the efficiency. It contained 5000 BiTe thermocouples with an individual element size of $0.21 \text{ mm} \times 0.21 \text{ mm} \times 1.27 \text{ mm}$ [70, 71].

Leonov *et al.* integrated a wireless electrocardiography (ECG) system in an office-style shirt (as shown in figure 3.20-a) [5, 72]. In this system, 14 6.5-mm-high TEG modules, with outer metal plates measuring 3 mm × 4 mm acting as radiators, have been integrated into the front side of the shirt (as shown in figure 3.20-b). The TEGs were fabricated by micro machining technologies. These modules occupy less than 1.5% of the total area of the shirt and have a lifetime of about 1.5 – 2 years depending on how often the shirt is worn. In an office environment, 14 TEGs typically provided 0.8-1 mW at about 1V across a matched load. The TEGs were the main power generation elements, while 3 photovoltaic (PV) cells placed on the shoulders were ancillary power generation elements that provided power to initialise for the system when the shirt has not been worn for months.



Figure 3.20 (a): Electrocardiography system integrated in a shirt. (b): (1) TE modules and (2) PV cells after Leonov [72]

In order to make use of more waste heat from the human body and thereby increase the output power and voltage, Kim and co-workers [73] developed a large area TEG on fabric. The TEG was based on p- and n-type Bi₂Te₃ by adjusting different stoichiometric ratios of Te. Large area TEGs on the human body require flexibility for comfortable wearing. The flexibility of this TEG was realized by the voids and fabric threads shown in figure 3.21-a.

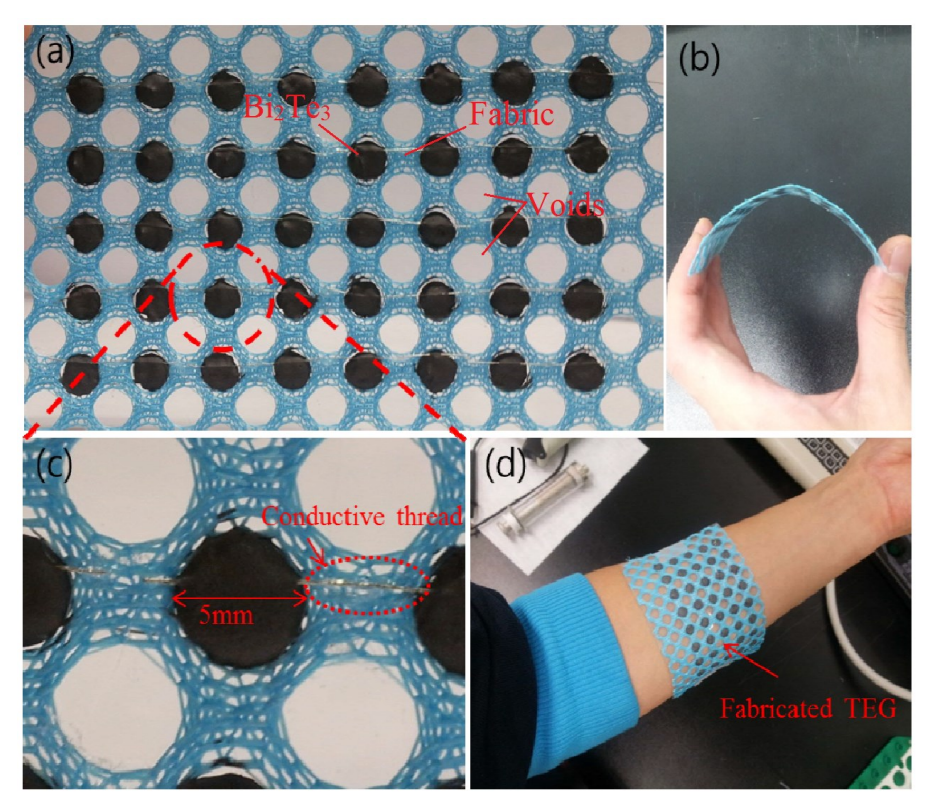


Figure 3.21 (a) Image of 20 dispenser printed single material thermocouples. (b) Demonstration of bending ability. (c) Close view of the electrodes applied. (d) TEG being worn on the human body, after Kim [73].

A Polyethylene terephthalate (PET) film was bonded at the bottom of the fabrics to form the substrate for the Bi_2Te_3 based pastes. The composition was then dispenser printed into the selected voids. Pre-woven silver fibres (figure 3.21-c) were used to form the electrodes to electrically connect the adjacent thermocouples. The curing condition was 100° C for 2 hours to avoid damage the fabric. For a single thermocouple, the Seebeck coefficient was measured as $45 \,\mu\text{V/K}$.

	Torfs	Leonov	Kim		
Integration	'Watch'-style	Hiding under	Use textile as		
methods	watch -style	textile	structure layer		
Fabrication	N/A (Classic commercial	Micro	Dispenser		
methods			printing		
Size of one	38 * 34 * 12	40 * 30 * 6.5	80 * 45 * 0.5		
modular (mm)	38 34 12	40 30 0.3	00 45 0.5		
Hot source	Body heat (32°C)				
Cool source	Room temperature (around 23°C)				
Flexibility	Inflexible	Inflexible	flexible		
Voltage	1.2 – 2 V	71 mV	2.1 mV		
Power output	100 μW	57 – 71 μW	0.015 μW		
Reference	[69]	[72]	[73]		

Table 3.4 Comparison of literatures between different methods of integrating TEGs in textile

Table 3.4 shows a summary and comparison of these three examples mentioned above. With the same temperature difference, the TEG using fabric as a structural layer had a worse thermoelectric performance than the rigid one. The possible reasons could be the poor electrical conductivity of the non-fully-cured thermoelectric material particles and the electrical contact between the woven fibres and BiTe composite from Kim [73].

Leonov *et al.* [74] also compared the thermoelectric performance of different methods of integration of TEGs in textiles for human body heat energy harvesting. Figure 3.22 shows two integration methods identified.

In figure 3.22-(a), if the textile is placed on a hot plate, the only heat radiator material is the outer Al plate. In figure 3.22-(b), the cotton textile is also radiating heat. The output power was improved by 7.7% using structure (b) instead of structure (a) with the same tested TEGs and ambient temperature [74]. This result indicates that cotton textiles can help to increase the temperature difference by covering TEGs in body heat energy harvesting applications because of the larger radiation area.

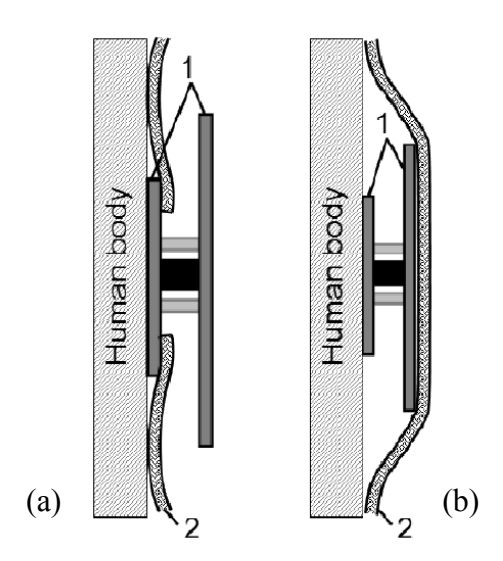


Figure 3.22 Methods of integrating TEGs in cloths. Numbers denote: 1, Al plates. 2, textile, after Leonov [74]

3.5.2 Discussion

The application requirements of TEGs in a piece of clothing are: thin, lightweight, and ideally should sustain repeated laundry and pressing. Therefore, it must be waterproof and either flexible under load or rigid enough to be unbreakable. The accelerations in modern washing machines cause mechanical stresses during the washing of these

devices which necessitate high levels of mechanical strength and shock protection in the device.

The listed examples are wearable applications of TEGs for human body heat energy harvesting. Two different methods of integrating the TEGs with fabrics have been introduced. One method was fabricating thermal materials with metal plates and then integrating these into fabrics [74]. The metal plates increase the mass of the device and will cause discomfort to people who wear it. The other method is pouring thermoelectric materials into openings in the fabric [75]. But the thermoelectric performance is relatively poor. Directly depositing thermoelectric materials on fabrics can potentially overcome this disadvantage.

3.6 Summary and discussion

Most of the TEGs devices reported were fabricated by evaporation and photolithography, which are typically high cost and low productivity processes. Screen printing has cost advantage on large area production when the device quantity is at industrial level, because it does not need complex photolithography technology to develop the pattern.

Moreover, in order to achieve high output voltages and power from the small temperature difference that exists between human body ($\sim 34^{\circ}$ C) and ambient ($\sim 21^{\circ}$ C), thermocouples with high aspect ratio [35] and a thickness of around 100 μ m are required [30, 39]. This can be achieved by screen printing the planar thermocouples structure [55] with few layers of depositions to reach the required thickness more efficiently compared to micro-machining technologies.

The thermoelectric materials currently used in screen printed thermocouples can be classified into 3 categories: metals, polymers and semiconductor alloys. Metal powders offered the printed thick film high electrical conductivity but their low Seebeck coefficient limited their overall figure of merit. Polymer thermal materials had advantage on flexibility and direct printing on textile, but the Seebeck coefficients are low which also results in a low figure of merit. Bi, Sb and Te based semiconductor alloy powders have a high Seebeck coefficient and ZT value in the room temperature range. Once the resistivity and the flexibility of the printed thick films containing these active materials can be improved, they will be ideal for use in a textile-based thermoelectric energy harvester.

The resolution of screen printing technology is not comparable with other technologies such as CVD or PVD. The presented screen printing single thermoelectric leg is on the scale of mm [59], while those fabricated by micro-fabrication deposition can reach the scale of µm [38]. The reasons for this are that the screen printing resolution is defined by the mesh size and also that the alignment between screen and substrate is not as precise as deposition from IC technology. In some applications with strict spatial requirements, such as outer space equipment, TEGs made by screen printing may have a lower thermoelectric efficiency than devices made by evaporation, which have a larger value of output power per area.

In conclusion, the feasibility of fabricating TEGs by printing was studied through the reviewing the literature. Because the printing is a low cost technology when the quantity of devices fabricated is in industrial level and compatible with flexible substrates. With a certain flexibility, it is possible to integrating printed TEGs on textile as next step.

The challenge points concluded from the literature are the printable paste formulation and low down the curing temperature to compatible with textile and other flexible substrate. The maximum working temperature of textile from industry varies from 150°C to 550°C depends on the material. There is also a trade-off between the flexibility and the maximum working temperature. Thus, developing a low temperature TEG is essential to make it compatible with textile.

Although some wearable TEGs have been reported in literature, few are successfully fabricated on a large area of clothing. The aim of this project is to screen print large areas of flexible thermocouples on flexible substrates, ideally textile, which can increase the output power and voltage by increasing the active area without increasing discomfort. In order to realise this, a learning of high temperature cured screen printed TEGs was processed as a start. High temperature curing screen printed thermoelectric materials are not textile compatible as the textile will be destroyed during the process. However, these were examined as a starting point in this project.

Chapter 4. High temperature curing copper and nickel based thermocouples

4.1 Introduction

Based on the literature review in chapter 3, copper (Cu) and nickel (Ni) were chosen as the p-type and n-type thermocouple materials respectively in various TEG designs [36, 38]. However, the micro machining technologies used in these reported works required several photolithography and electrochemical deposition/evaporation steps, which increases the cost for large area production. Screen printing is a low-cost process with a high production rate, which makes it more appropriate for practical fabrication of wearable TEGs.

Copper and nickel are low cost materials and have been used in the work described in this chapter to explore the methodology of formulating various screen printable pastes which will be described in other chapters, as well as evaluation methods for the printed thick films and thermocouples. In addition, a lot of research based on high temperature sintered thick films for various applications has been performed by our group [76, 77]. Therefore, high temperature copper/nickel thick-films thermocouples were chosen as initial prototypes to explore screen printed thermocouples.

The first part in this chapter describes the formulation and characterization of the screen printable high temperature Ni paste. The second part in this chapter is the formulation and characterization of the screen printable high temperature Cu paste. The final part describes the evaluation of printed thermocouples, specifying the output voltage, maximum power and presenting a comparison between the measured results and those from published literature.

4.2 Experimental analysis of screen printed nickel thick films

4.2.1 Experiment procedure

The first step to realise thermoelectric generator using screen printing technology is manufacturing the individual conductive thermoelectric material pastes. In section 3.3.1, the whole fabrication processes of screen printing were introduced briefly, including the pastes making, printing and curing. The process with the mixing machine

(triple roll mill), the printer (DEK printer) and the curing machine (BTU furnace) is illustrated in figure 4.1.

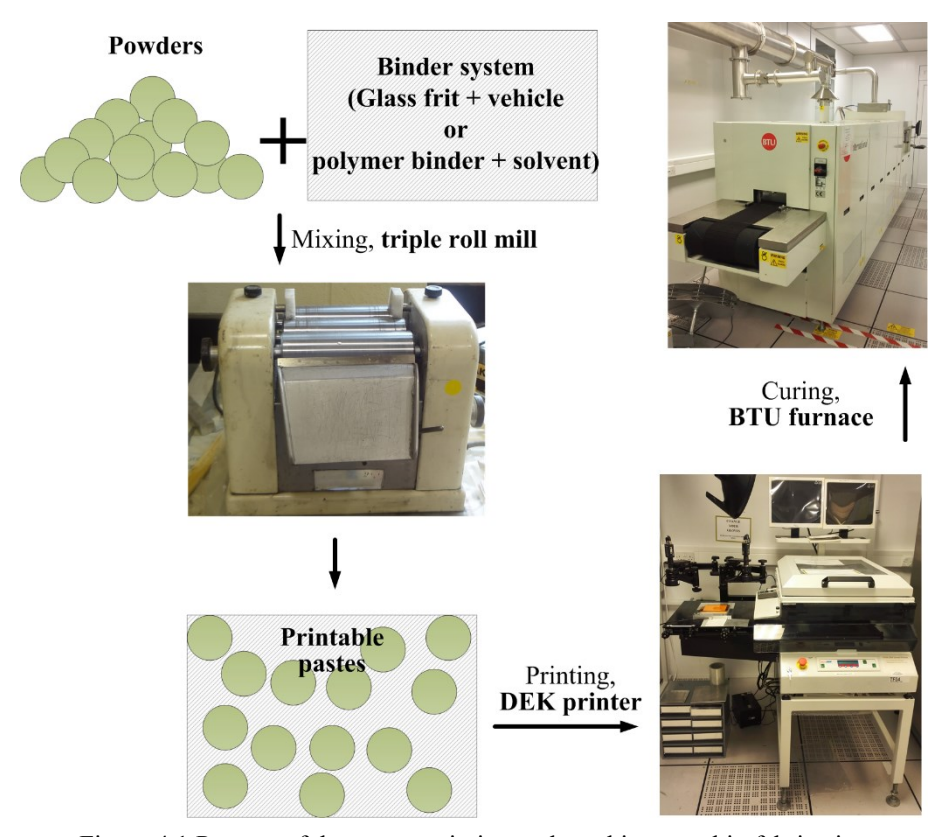


Figure 4.1 Process of the screen printing and machines used in fabrication

The binder system and the powders are all measured by weight. In the first step, the binder system was made and simply mixed with spatula. Then powers with specific ratios were added into the binder system. The mixture were evenly mixed by the triple roll mill. After the pastes made, the patterns were deposited through screen masks. The thickness could be added up by drying the deposited patterns to get tack-free surface. The final stage of the process was the curing using the belt furnace. All the detailed fabrication conditions, including the stoichiometric ratio, deposition times, curing temperature and duration will be given in each section where different patterns are introduced, because the fabrication conditions for different thick films are different.

4.2.2 Nickel thick film paste formation and adhesion improvements

In this experiment, nickel was chosen to be the n-type thermoelectric material of the TEG. Hence, a printable nickel paste is required to form an electrically conductive thick film by screen printing.

High temperature sintering nickel paste systems are composed of nickel particles, a glass binder and a vehicle. The details of these components are listed in the following table.

Component	Details	Percentage by weight
Nickel flakes	Alfa Aesar, -325 mesh, 0.37 micron thick, typically 99.8%	80%
Glass binder	Ferro Corporation, CF07575 VSD	20%
Vehicle	ESL, 400 vehicle	

Table 4.1 Formulation of high temperature nickel ink

The quantity of the vehicle is not included into the mass percentage of the paste because it will be totally removed during drying and firing the printed film at high temperature. For printable nickel paste formulation, 1 gram of nickel powder requires about 1 ml of vehicle to form a paste with the required printable viscosity. The viscosity range of the paste formed ranges from 9000 cP to 15000 cP, as measured by Brookfield High Shear CAP-1000+ cone and plate viscometer.

Two layers of the nickel pattern were screen printed by hand printing. Each layer was composed of 4 depositions. This process was applied on all nickel patterns printed in this chapter. The screen frame has dimensions of 6×8 inches (15.24×20.32 cm) with a mesh opening of 54 μ m and an emulsion thickness of 28 μ m. In this experiment, the drying conditions for each layer of nickel pattern were 125°C in a box oven for 4 min.

Ink formulation			Quality of			
(Nickel : Glass	Firing condition	Sample name	adhesion on			
binder)			substrate*			
,	370°C, 10 min, Nitrogen	Sample01	1			
	370°C, 20 min, Nitrogen	Sample02	1			
	450°C, 10 min, Nitrogen	Sample03	1			
80% : 20%	750°C, 10 min, Nitrogen	Sample04	1			
	850°C, 10 min, Nitrogen	Sample05	1			
	950°C, 10 min, Nitrogen	Sample06	2			
	1000°C, 10 min, Nitrogen	Sample07	3			
85% : 15%	750°C, 10 min, Nitrogen	Sample08	1			
90% : 10%	750°C, 10 min, Nitrogen	Sample09	1			
*Scale: 1-poor; 10-excellent.						

Table 4.2 Formulations and firing conditions of high temperature curing nickel inks

Various different formulations of nickel paste and firing temperatures were trialled, as listed in table 4.2. The purpose of the firing process is to melt the glass binder, which binds the metal powders and adheres them to the substrate and forming a homogenous

film. From the data sheet (seen in Appendix 1), the softening point of the CF7575 binder is 370°C and the melting point is higher than 450°C. All the high temperature processes this chapter were performed in a BTU Fastfire belt furnace with a nitrogen flow supplied to avoid any metal oxidization in air. A tape test was used to test the quality of adhesion to the substrate. This test used a single side low tack transparent adhesive tape (Intertronics) to cover on top of the pattern which is then peeled off to visually inspect the residues on the sticky side.

All the samples listed in table 4.2 had poor adhesion between the nickel paste patterns and alumina substrates. Sample08 and sample09 were very easily removed from the substrate. Samples 01 – 06, with increased glass binder ratio and curing temperatures from 370°C to 950°C were also easily removed from the substrate by tape. This poor adhesion is illustrated in figure 4.2. When the firing temperature is increased to 1000°C, the adhesion is slightly improved (sample07) but was still poor as shown in figure 4.3.

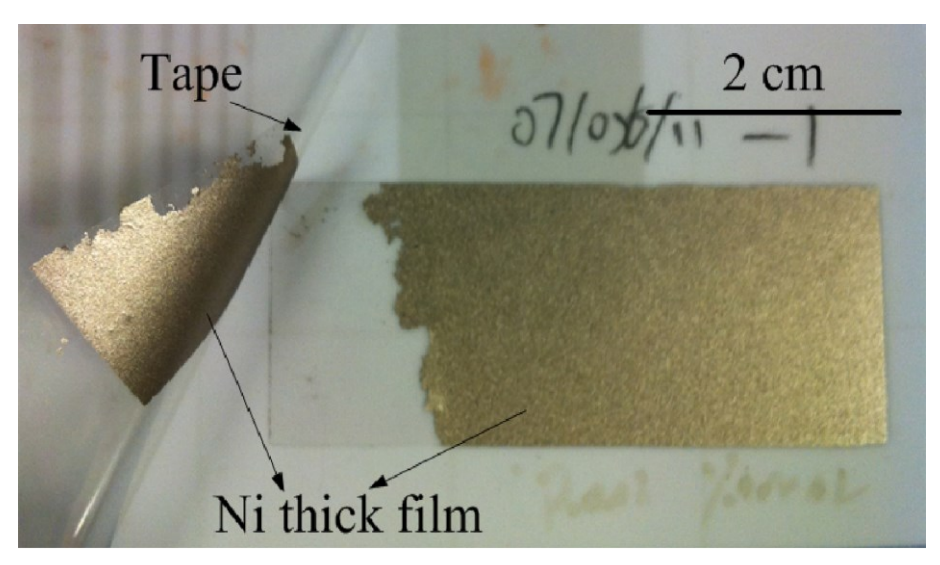


Figure 4.2 Illustration of poor adhesion of nickel thick-films to alumina substrate when fired below from 370 - 950°C

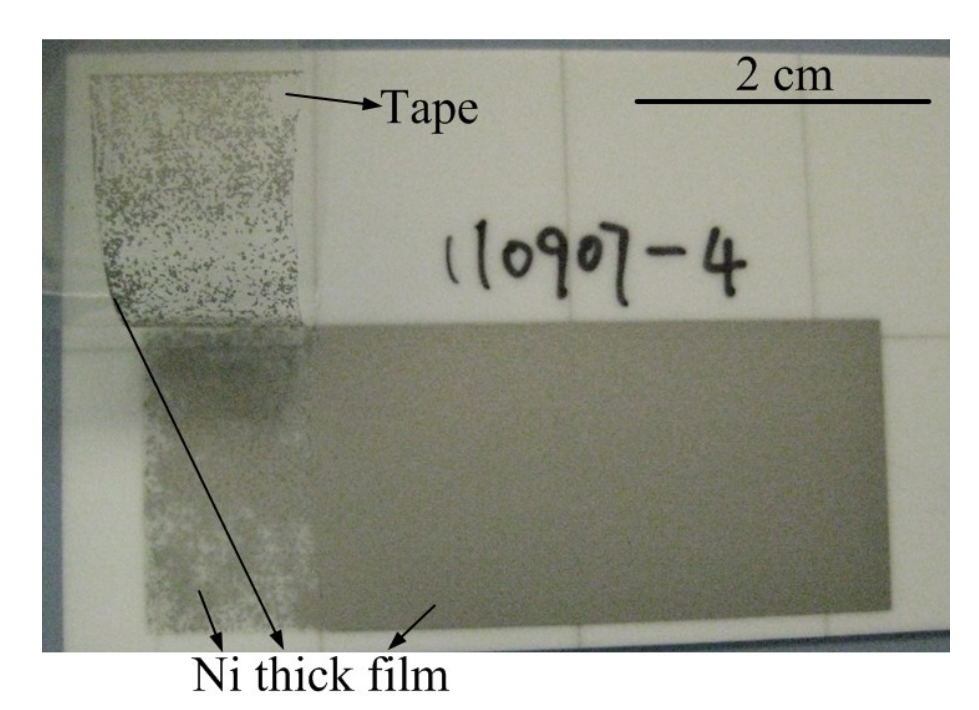


Figure 4.3 Poor adhesion of nickel thick-films (Ni : binder = 80% : 20%) to alumina substrate when fired at 1000° C

The adhesion problems of the Ni layers on alumina substrate is a commonly reported problem in research [78]. To solve this problem, several methods have been investigated.

The first method is increasing the roughness of the substrate by mechanical abrasion and thereby increasing the strength of mechanical interlocking between the two materials. However, the substrate treatment process will greatly increase the cost of the fabrication process. This is contrary to the original goal of this project, which is to use a low-cost process to fabricate a thermoelectric device.

The second one is to increase the percentage by weight of the binder in the paste. By increasing the binder percentage to 30% by weight, the adhesion of the cured sample was improved compared with that of 20% binder in the system. In figure 4.4, the quantity of Ni film stuck to the tape was much less than in figure 4.3. Although this method improved the adhesion, more binder will decrease the electric conductivity of the printed nickel electrode layer.

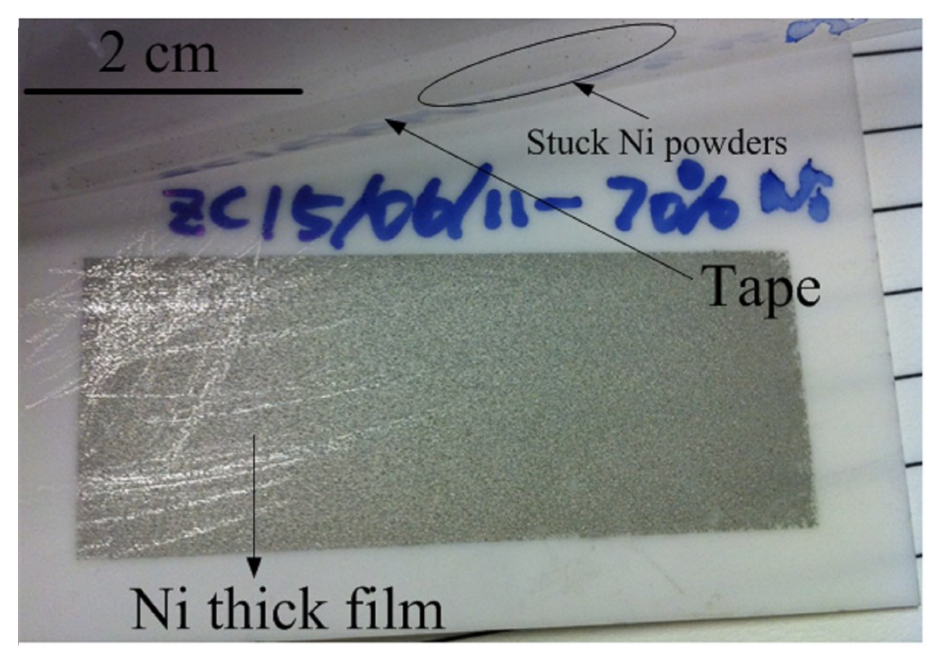


Figure 4.4 Nickel thick film with 30% glass binder fired at 950°C survived after tape test Samples with 20% and 30% glass binder by weight were fired at 950°C for 10 minutes in a Nitrogen atmosphere. Table 4.3 gives a comparison between the sheet resistance nickel thick films with different amounts of glass binder on alumina substrate. The sheet resistance testing is done by a JANDEL multi height probe sheet resistance measurement machine.

	Ni thick film with 20% binder	Ni thick film with 30% binder
Sheet resistance	54.5 mΩ/□	595.57 mΩ/□

Table 4.3 Sheet resistivity of Ni thick films with different binder ratio on alumina substrate

The sheet resistance of Ni thick films with a 30% binder ratio is 10 times higher than that with 20% binder contained. The increased resistance will decrease the figure of merit and the power output of the thermocouples. Consequently, increasing the proportion of glass binder is not a suitable option to solve this problem.

The third method is adding an adhesion layer as an interface between the Ni thick film and alumina substrate. Chromium (Cr), Aluminium (Al) and Titanium (Ti) were evaporated individually on to aluminium nitride substrate before screen printing the nickel electrode layer. A Leybold BAK 600 evaporation machine was used for this process. Ni paste with 80% Ni powder by weight was used in this experiment as deposition material. Experimentation with each interface layer material is described separately below.

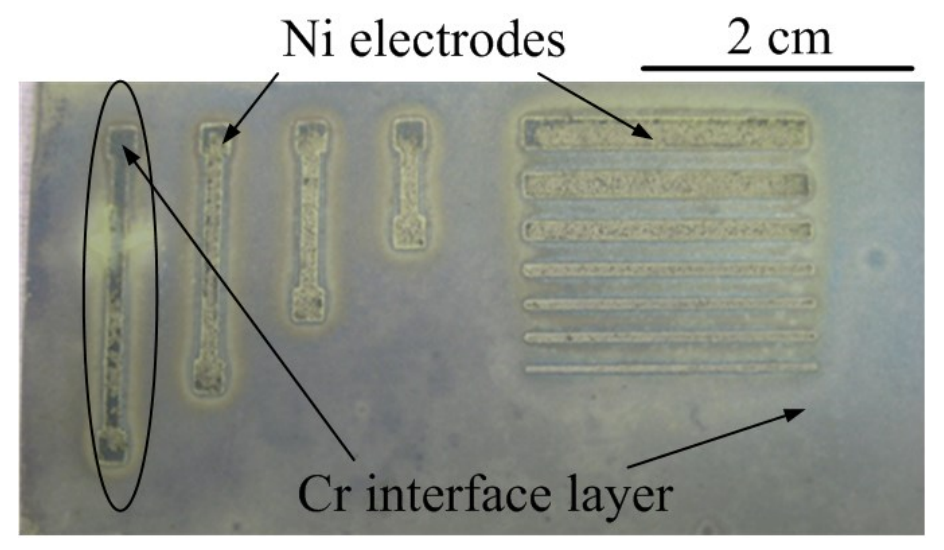


Figure 4.5 Ni electrode layer on evaporated Cr interface layer

A Cr layer with 100 nm thickness was evaporated onto the substrate. Then, a Ni electrode pattern was screen printed on to the Cr interface layer and fired at 950°C in a nitrogen atmosphere for 10 minutes. In figure 4.5 it can be observed that the colour of Ni electrodes was dissimilar, which demonstrated that the distribution of Ni powders in the patterns was non-uniform on the substrate. This is because the nickel powders are removed from the substrate after sintering, leaving some dark areas in the nickel electrode pattern. The nickel powders with poor adhesion might be removed by the nitrogen flow in the belt furnace.

Figure 4.6 shows the adhesion of the Ni thick film on Al interface layer. The thickness of an evaporated Al layer was 300 nm. The firing condition was 950°C for 10 min in a nitrogen atmosphere. After firing, Ni powders were not removed away from the substrate, but most of them still came off during the tape test.

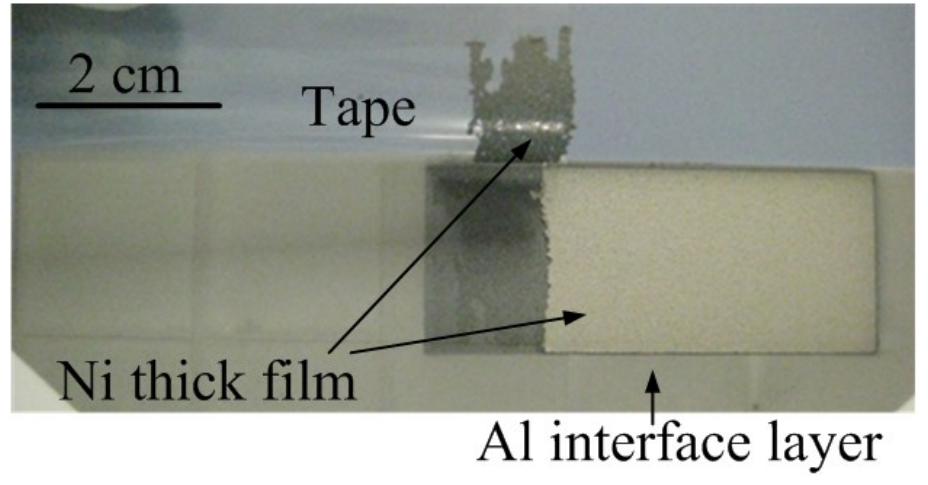


Figure 4.6 Tape test of screen printed Ni layer on evaporated Al film

In figure 4.7-a, a 100 nm thick Ti layer was evaporated as an interface layer. After firing, shown in figure 4.7-b, the Ti interface layer was hard to observe with the naked eye, and the adhesion of Ni thick film remained poor. Ni powders were stuck on the tape after the tape test and the pattern was easily scratched off from the substrate. The firing conditions were: 950°C for 10 min in a nitrogen atmosphere.

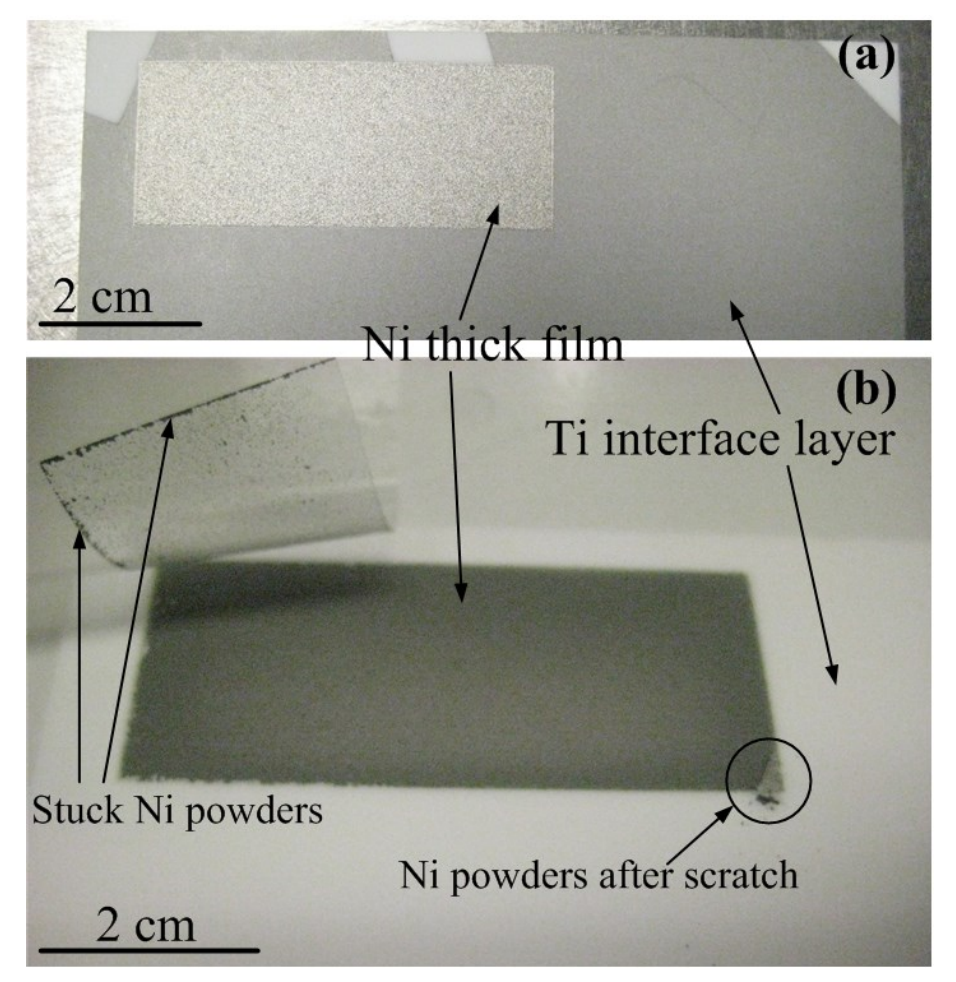
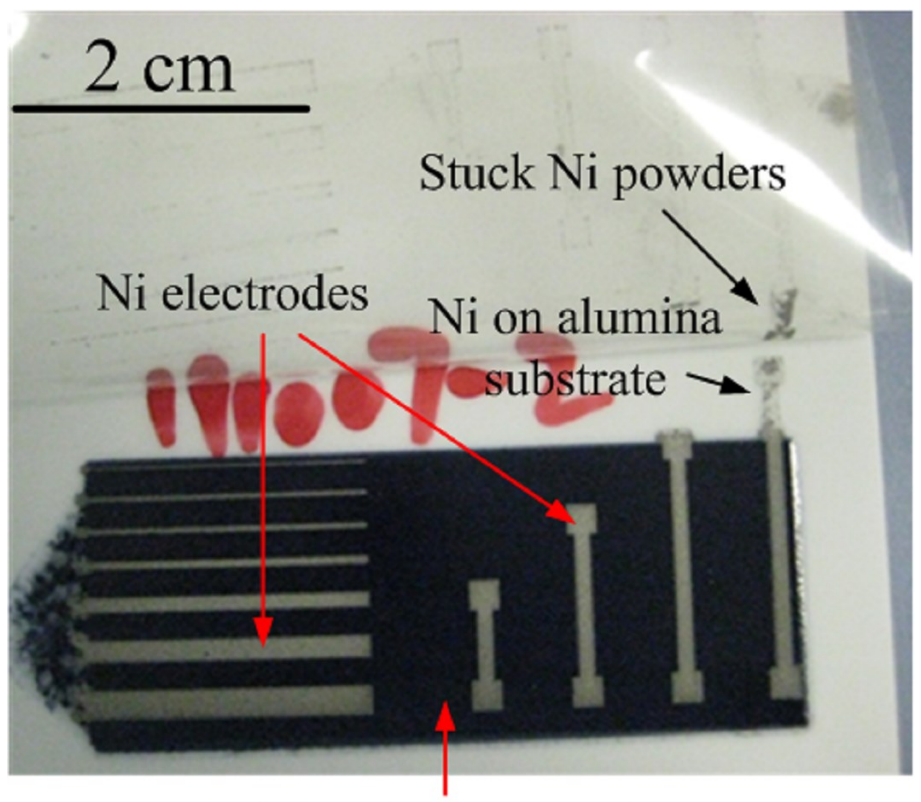


Figure 4.7 Screen printed Ni layer on evaporated Ti interface layer. (a) Sample before firing, (b) Sample after firing

The adhesion issue was eventually solved by adding a dielectric interface layer before printing the nickel layers. ESL 4924 is a dielectric composition that can be screen printed. It should be dried in 125°C for 5 min and then fired at 850°C for 10 minutes according to its datasheet, given in Appendix 2.

One layer of the dielectric interface with 4 deposition was screen printed and then dried. Then the Ni electrode patterns were screen printed onto the dielectric layer and the printed structure was fired at 850°C for 10 minutes. The tape test shows a clear distinction between the cured nickel paste directly on alumina substrate and that on an

ESL 4924 dielectric layer. It can be seen clearly from figure 4.8 that the nickel paste survives the tape test.



Dielectric interface layer

Figure 4.8 Tape test of screen printed Ni electrode patterns on dielectric composition layer Compared with evaporating a metal interface layer, screen printing a dielectric layer can have several advantages. Firstly, the same deposition method, screen printing, is used for both the interface layer and the nickel layer which will reduce the cost of fabrication. Secondly, the high firing temperature of the dielectric paste was compatible with that of the nickel paste, which means the firing processes for these two layers can be performed simultaneously.

4.2.3 Nickel thick film characterisation

In order to test the transport properties and Seebeck coefficient of the printed nickel pattern, samples with electrodes measuring 1.4×1.4 cm were screen printed on alumina substrates with dielectric interface layers. In order to achieve optimized alignment of the printed patterns, a commercial screen printing machine was used in this step. The printing machine used was a DEK 248 screen printer. Patterns were printed using polyester screens from MCI Precision Screens Ltd. The screen frame measures 12×12 inches (30.48×30.48 cm) with mesh openings of $54 \mu m$ and an

emulsion thickness of $28 \mu m$. The samples of Ni thick films on a dielectric interface layer and the dielectric layer alone are both shown in figure 4.9.

Dielectric interface layer

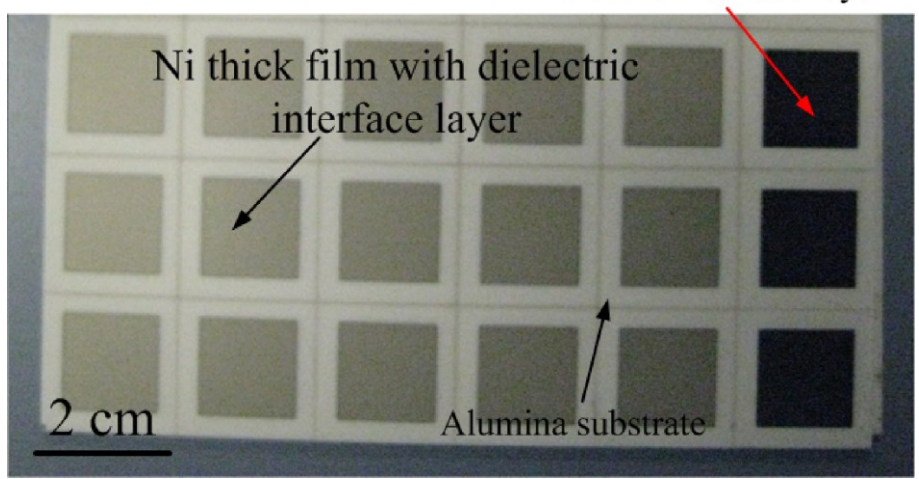
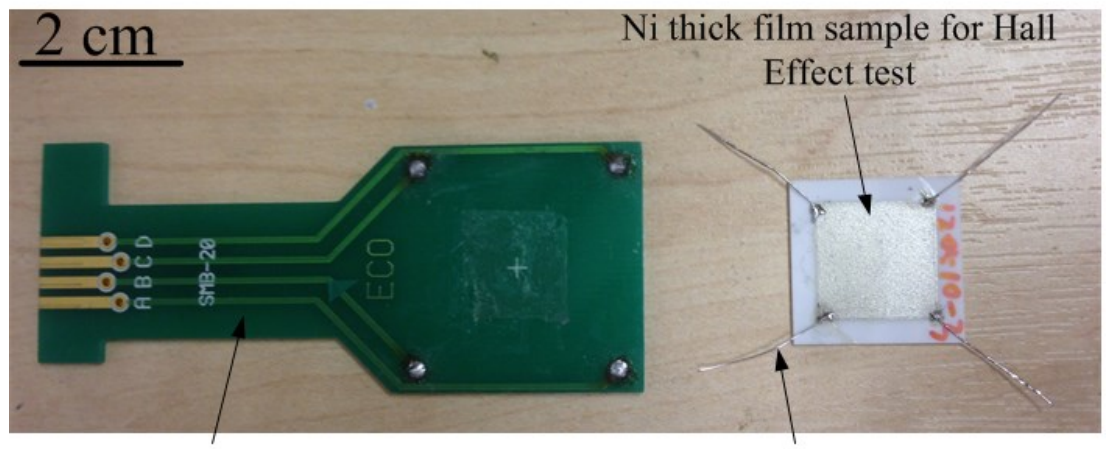


Figure 4.9 Screen printed square samples for Hall effect test

1 layer of nickel thick film with 2 depositions were screen printed on the dielectric interface layer.

The Hall Effect was measured by an Ecopia HMS-3000 Hall Measurement System. The Ni thick-film samples were soldered directly onto a PCB sample holder as shown in the left of figure 4.10. The conductive wires were soldered on to four corners of the Ni thick film pattern, shown in the right of figure 4.10.

The Seebeck coefficients of the thermoelectric thick films were measured using a bespoke test rig developed by another researcher in our group [79, 80]. Copperconstantan thermocouples were positioned directly onto the sample surface at "cold" and "hot" sides. The temperature difference ΔT between two points of the sample and the potential difference ΔV between the same two points were measured. This custom-made Seebeck measurement unit was calibrated against a polycrystalline bismuth foil reference standard. The measurement accuracy was found to be within 5%, and the system was calibrated using copper-constantan thermocouples and a high precision Keithley DMM 2000/E digital multimeter with 0.1% accuracy.



Sample holder

Soldered conductive wire

Figure 4.10 Sample holder for Hall effect test (left) and soldered sample (right)

For the Hall Effect measurement, 3 samples were measured and 10 readings were made for each sample. For the Seebeck coefficient measurement, 3 samples were measured and 3 readings were made for each sample. The results are shown in table 4.4, along with a comparison to values obtained from the literature.

Experimental values					
Physical properties	Minimum value	Maximum value	Average value		
Carrier concentration (cm ⁻³)	-7.1×10^{20}	-1.2×10^{20}	-2.58×10 ²⁰		
Mobility $(cm^2/(V \cdot m))$	1.8	8.5	6.27		
Resistivity (Ω·cm)	4.81×10^{-4}	4.89×10^{-4}	4.86×10 ⁻⁴		
Hall coefficient (cm ³ /C)	-1.5×10^{-3}	-8.8×10^{-3}	-3.05×10 ⁻³		
Seebeck coefficient (µV/K)	-13	-17	-15		
	Literature values				
Carrier concentration (cm ⁻³)	N/A	N/A			
Mobility $(cm^2/(V \cdot m))$	N/A	N/A	N/A		
Resistivity (Ω·cm)	8.1×10 ⁻⁶ [81]	1.1×10 ⁻⁴ [82]			
Hall coefficient (cm ³ /C)	-3.05×10 ⁻³ [83]				
Seebeck coefficient (µV/K)			-19.5 [16]		

Table 4.4 Hall effect and resistivity in nickel screen printed thick-film and their comparison with values reported in literature

The resistivity values of nickel films in literatures are on the order of 10^{-6} to $10^{-4} \,\Omega \cdot \text{cm}$. The average resistivity value of the tested samples is $4.86 \times 10^{-4} \,\Omega \cdot \text{cm}$. The resistivity of the nickel thick film is on the same order as some literature values, which demonstrates that the printed nickel pattern can be applied as conductive electrodes.

The experimental absolute value of the Seebeck coefficient is smaller than the bulk value -19.5 μ V/K [16]. The negative sign of the Hall coefficient indicates that the printed nickel samples were n-type. All the values in table 4.4 are obtained at room temperature.

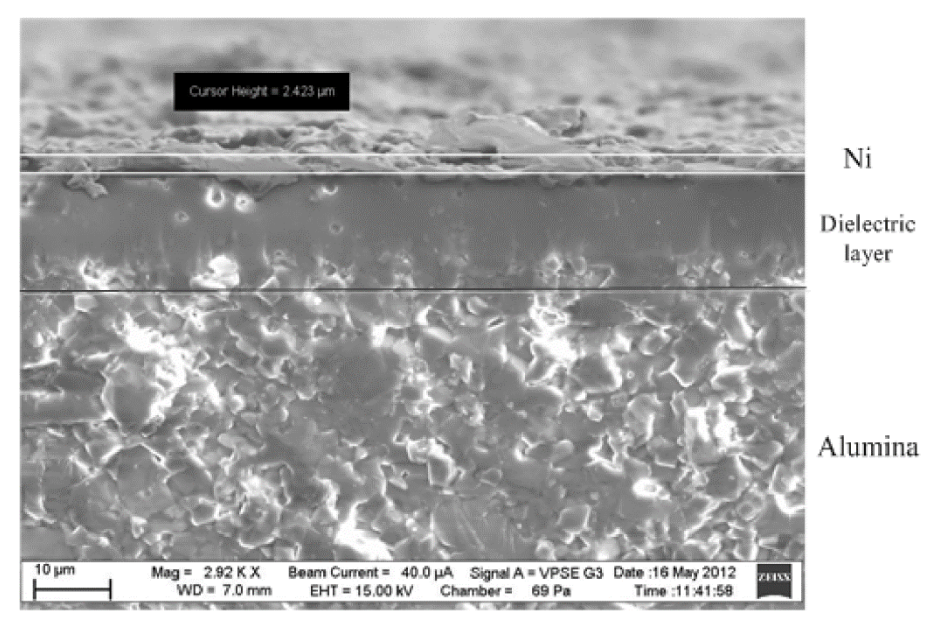


Figure 4.11 SEM cross section view of nickel thick film on dielectric layer

Figure 4.11 shows a cross section view of the screen printed nickel sample on the dielectric layer, which have been cured simultaneously at 850°C.

The morphology of the printed particles in the thick films were observed using a Zeiss EVO Scanning Electron Microscope (SEM). The thickness of the printed nickel layer is below 10 µm. The melting point of nickel is 1455°C in atmosphere pressure (101.325 kPa), which is much higher than the firing temperature. From the uneven surface it is clear that the particles were not melted. Hence, the firing process only melts the glass binder and leaves the nickel in particle form. Moreover, the uneven surface makes the average thickness of the nickel film difficult to measure with the SEM. Alternatively, a profilometer and a micrometer were used to measure the thickness of the active thermoelectric material layer in the device, which will be discussed later.

4.3 Experimental analysis of copper paste

4.3.1 Copper thick-film pattern formation

The relative amounts of the components in a high temperature copper paste are given in table 4.5. Since a copper thick film paste was just studied to evaluated the application of printing technology to TEGs, the ratio of copper to glass binder was taken from the literature [84, 85] without optimisation in this experiment.

Composition in copper ink	Detail type	Percentage by weight
Copper flakes	Alfa Aesar, -325 mesh, 99%	90%
Glass binder	Ferro Corporation, CF07575VSD	10%
Vehicle	ESL, 400 vehicle	N/A

Table 4.5 Formulation of high temperature copper ink

Roughly, for 5 g copper powder, 3 ml vehicle is sufficient to form the paste with the required printable viscosity. The proportion of vehicle to copper powder is therefore about 0.6 ml vehicle per gram solid copper powder. With this ratio, the copper paste can achieve the same viscosity range with the nickel paste described in section 4.2.1 and is screen printable.

Two layers of the copper pattern were printed with each layer consisting of 2 depositions. The printed patterns were dried at 125 °C in a box oven for 3 min. The drying time for the copper film was shorter than that required for nickel paste because the quantity of vehicle was less and the oxidization rate of copper powder is faster than that of the nickel powder [86].

In order to avoid oxidizing the copper during a high temperature process, all firing process were performed in a nitrogen atmosphere. Samples fired at 370°C for 10 min are shown in figure 4.12.

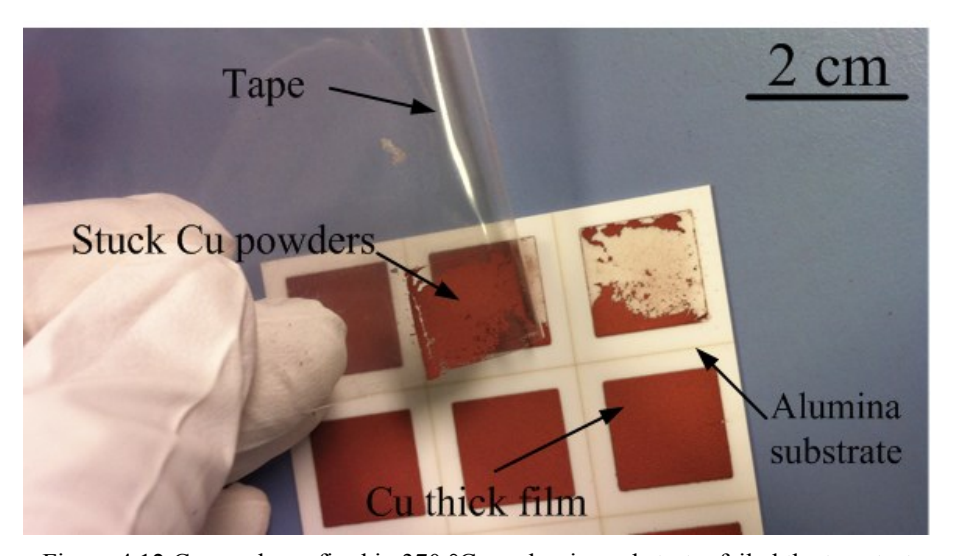


Figure 4.12 Copper layer fired in 370 °C on alumina substrate, failed the tape test

It can be seen that the pattern can be easily removed from the substrate during the tape test. One possible reason is that the glass binder is not melted at this temperature. When the firing temperature was increased to 750°C, the printed copper thick film remained intact through the tape test. Figure 4.13 shows the copper pattern after the tape test.

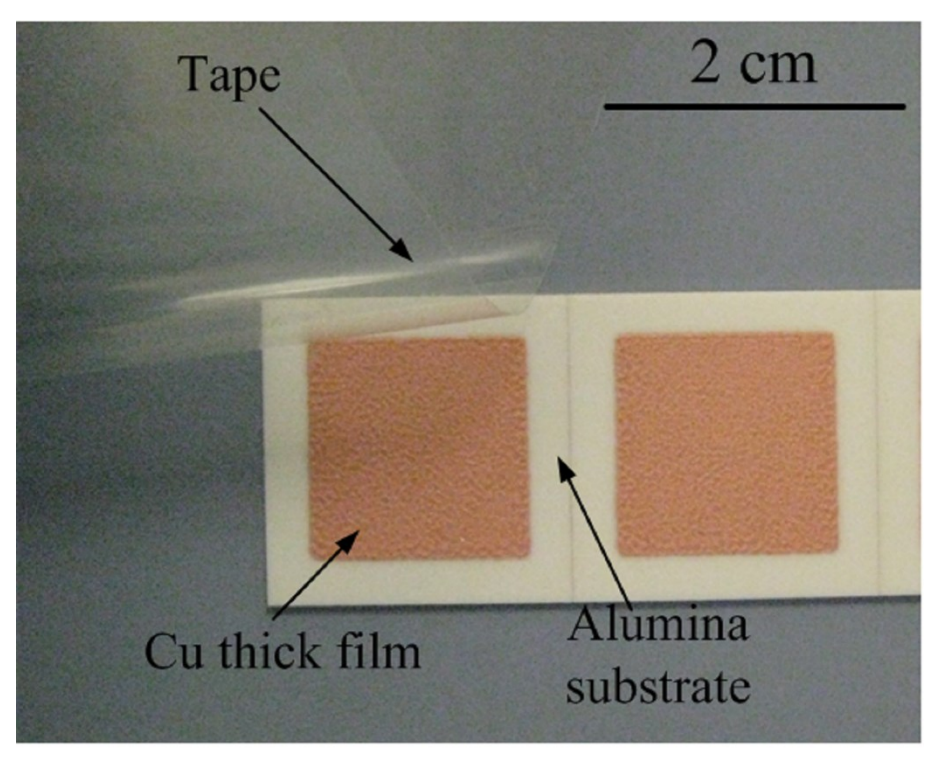


Figure 4.13 Copper layer fired in 750 °C on alumina substrate, intact after the tape test

From the SEM micrograph of the copper pattern after a 750°C firing, figure 4.14, it can be seen that the adjacent copper particles were connected by the melted binder. Some adjacent particles are even attached directly. This provides a path for the free electrons in copper particles to move in the film, which prevents a large increase in the electrical resistivity compared with the bulk value.

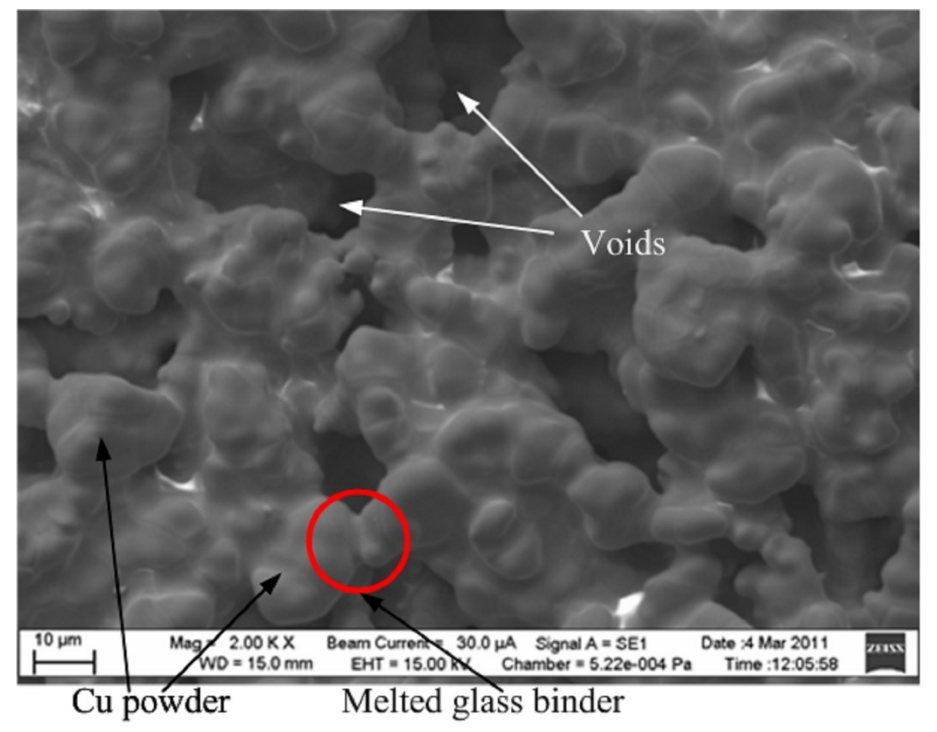


Figure 4.14 SEM image of high temperature firing Cu thick film surface

Because the firing temperature is lower than the melting point of copper (1085°C) [16], the copper is still in particle form and the voids among particles still exist after firing. The voids increase the resistivity of the film compared with bulk material (values given in table 4.7).

4.3.2 Copper thick film characterisation

The thickness measurement of the copper thick-film was taken by several methods, including a Surface Profiler machine (TENCOR P-11 Surface Profiler), a Micrometer (Mitutoyo Digimatic Coolant Proof Micrometer 0-25 mm / 0-1") and a SPIDA (Z-Check 700S, Aprotec Instrumentation Inc.). The cross-section of the copper thick-film was also observed under SEM (shown in figure 4.15), which is assumed to be the accurate value for the thickness. The results are listed in table 4.6.

Measurement methods	Thickness	Variation compared with SEM result
SEM	23.63	N/A
Profiler	19.58	17.2%
Micrometer	22	6.9%
SPIDA	22	6.9%

Table 4.6 Thickness (in µm) measurement of copper thick film by different methods

With the profiler and Micrometer, there is physical contact between the probes and the sample. With the SPIDA, the thickness is measured optically. The micrometer thickness measurement method was the easiest process and the value was close to the SEM value. In the future experiments, it will usually be used to measure the thickness of films on substrates of known thickness. However, the thickness of the nickel thick film on a dielectric layer was measured by the TENCOR P-11 Surface Profiler because the exposed interface area was too small to be measured accurately with a micrometre.

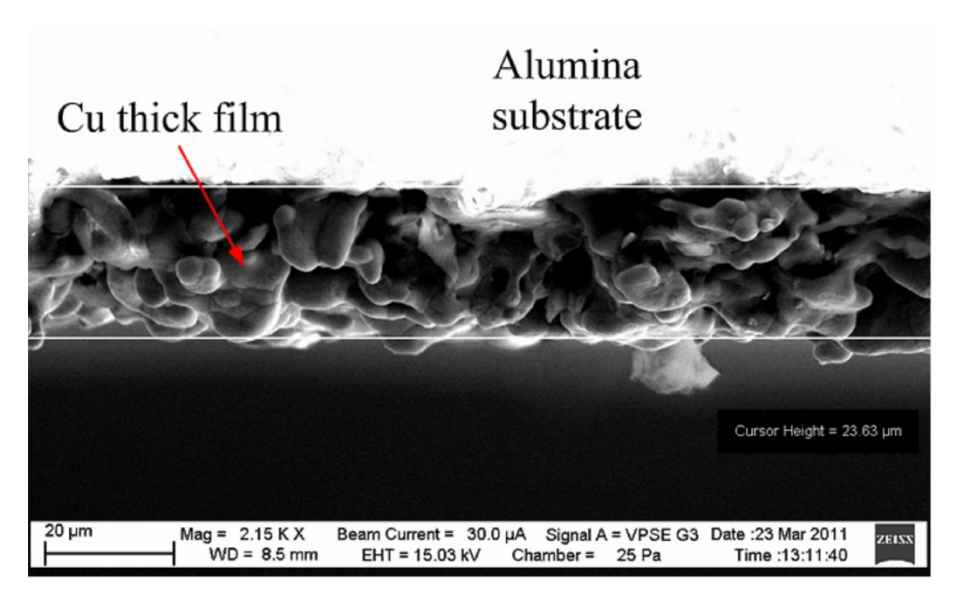


Figure 4.15 SEM cross-section micrograph of high temperature firing copper thick film

For the printed copper thick-film with 22 μ m thickness, the sheet resistance is 9.1 m Ω/\Box . The current between probes is 90 mA. This value is in the same order with the copper thick-film sheet resistance from other researchers. Xu [87] presented a high temperature firing copper thick-film with optimized firing time and temperature also by screen printing technology, which has a lowest sheet resistance value of 5 m Ω/\Box . Also, there are some commercial screen printable copper pastes, such as Heraeus conductor C7257 copper high temperature curing copper paste which has a 2.6 m Ω/\Box maximum resistance. (The datasheet of this material is shown in Appendix 3).

Experimental values					
Physical properties	Minimum value	Maximum value	Average value		
Carrier concentration (cm ⁻³)	-2.42×10^{21}	-1.06×10^{22}	-6.59×10 ²¹		
Mobility $(cm^2/(V \cdot m))$	5.9	84.1	30.5		
Resistivity (Ω·cm)	1.2×10 ⁻⁵	1.6×10 ⁻⁴	6.4×10^{-5}		
Hall coefficient (cm ³ /C)	-3.25×10 ⁻⁴	-2.58×10 ⁻⁴	-5.87×10 ⁻⁴		
Seebeck coefficient (µV/K)			3		
	Literature values				
Carrier concentration (cm ⁻³)	N/A	N/A	-12.1×10 ²² [88]		
Mobility $(cm^2/(V \cdot m))$	N/A	N/A	N/A		
Resistivity (Ω·cm)	1.8×10 ⁻³ [89]	29.7×10 ⁻³ [89]	N/A		
Hall coefficient (cm ³ /C)	-50×10 ⁻⁵ [89]	-5×10 ⁻⁵ [90]	-5.2×10 ⁻⁵ [91]		
Seebeck coefficient (µV/K)			1.83 [16]		

Table 4.7 Hall effect and resistivity of copper screen-printed thick-film and a comparison with values reported in literature

In addition, considering the nickel pattern is on a dielectric layer, the copper thick film was also required to be printed on the same layer to simplify the fabrication process. For the sample prepared to measure the transport properties, I layer of $14 \text{ mm} \times 14 \text{ mm}$

copper thick film composed of 2 depositions was screen printed on top of the cured dielectric interface layer. The transportation properties of a screen printed copper thick film on a dielectric layer are shown in table 4.7. The sample was fired at 750°C for 10 minutes in a nitrogen atmosphere to minimise oxidation.

As with nickel, the carrier concentration and Hall coefficient of copper are also negative, which means in printed copper thick film the electrons are the charge carriers. However, the Seebeck coefficient of copper was positive in the measurement, which demonstrates that copper could act as a p-type thermoelectric material in a working Ni/Cu thermocouple. The resistivity value of an evaporated copper film varies from $29.7 \times 10^{-3} \,\Omega \cdot \text{cm}$ to $1.8 \times 10^{-3} \,\Omega \cdot \text{cm}$ [89], which is higher than that of screen printed high temperature cured copper thick films. The resistivity value of bulk copper is $1.7 \times 10^{-6} \,\Omega \cdot \text{cm}$ [16], which is roughly ten times smaller than the value measured in this experiment. There are several potential reasons. First, glass binders added to the paste and the solvent in the vehicle were likely to be doped additives, which increase the impurity of the copper paste. Second, copper is very easily oxidized in air. Even though the high temperature firing is processed in a nitrogen atmosphere, the vehicle drying process is performed in the oven and could cause some copper particles on the surface of the pattern to be oxidized.

The electrical resistivity of the copper thick film on an alumina substrate was averagely $1.08\times10^{-4}~\Omega\cdot\text{cm}$ which is higher than the resistivity of the copper thick film on a dielectric layer. This indicated that the dielectric layer is helpful to reduce the electrical resistivity.

The SEM cross section micrograph of the copper thick film on a dielectric interface layer is shown in figure 4.16. Compared with the cross section SEM micrograph of a nickel thick film, the grain size of copper particles is larger than that of the nickel particles, which means a copper layer may be thicker than a nickel layer when printing the same number of layers consisting of the same number of depositions.

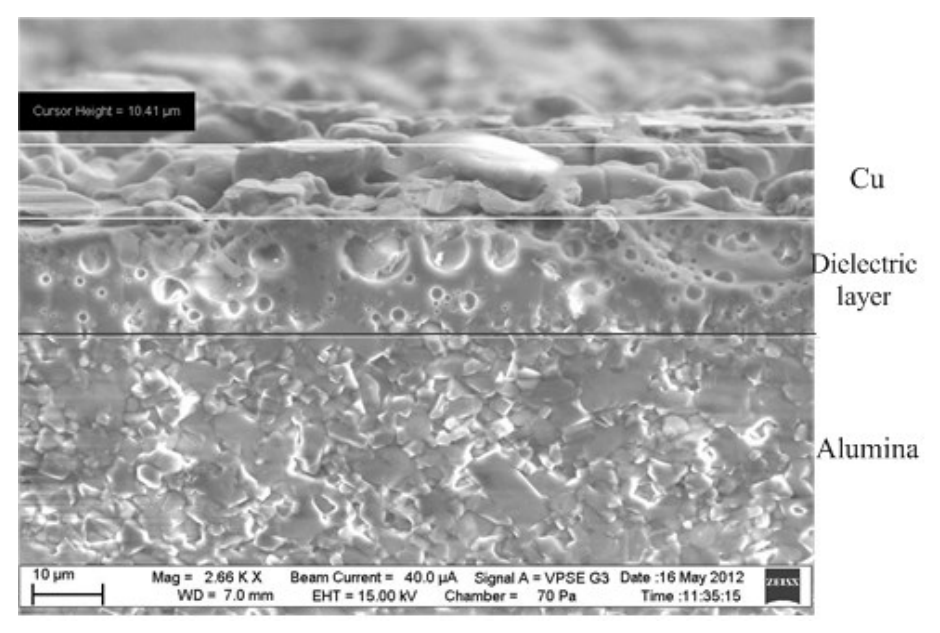


Figure 4.16 SEM cross section micrograph of a copper thick film on a dielectric layer

4.4 Screen printed Ni/Cu thermocouples

Based on the experiments described in section 4.2 and 4.3, the electrical resistivity values and the Seebeck coefficients of screen printed nickel and copper thick films indicated that they demonstrate the possibility to accomplish a TEG device. Here, planar structured thermoelectric legs are screen printed to investigate this possibility.

The first step of the device fabrication was to screen print one dielectric layer with 2 depositions on alumina substrate to dry. Following this, 2 layers of nickel paste were deposited on the dried dielectric layer, with 2 depositions for each layer. After firing at 850°C in nitrogen, another 2 layers of copper paste were deposited on the dielectric layer and fired at 750°C in nitrogen. Finally, a silver polymer top electrode layer was printed and cured to provide electrical connections to the thermocouples. Johnson Matthey S-020 was used as the screen printable silver paste. The silver layer was cured at 125°C for 10 minutes in a box oven as specified in the datasheet. The data sheet is given in Appendix 4. The fabrication process is shown in figure 4.17.

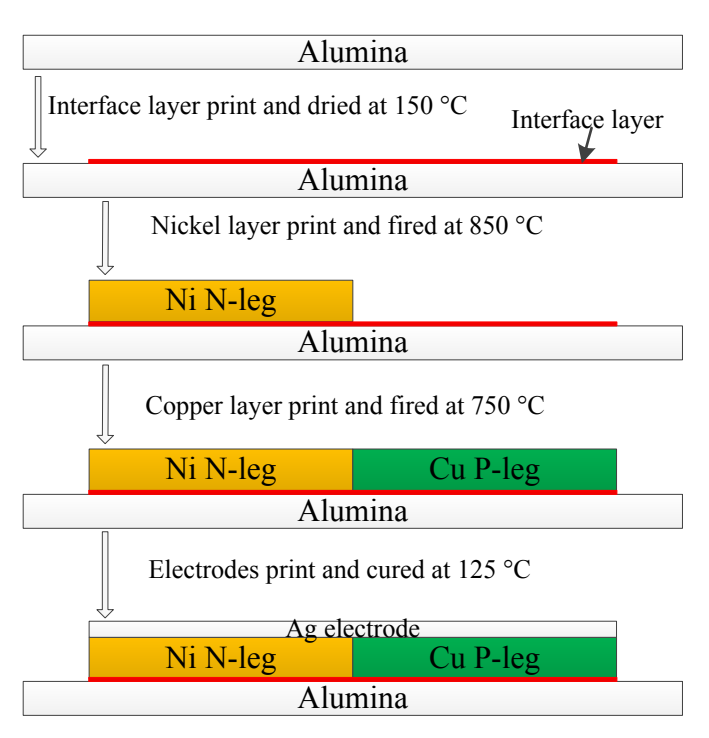


Figure 4.17 Illustration of the high temperature Ni/Cu thermocouple screen printing process

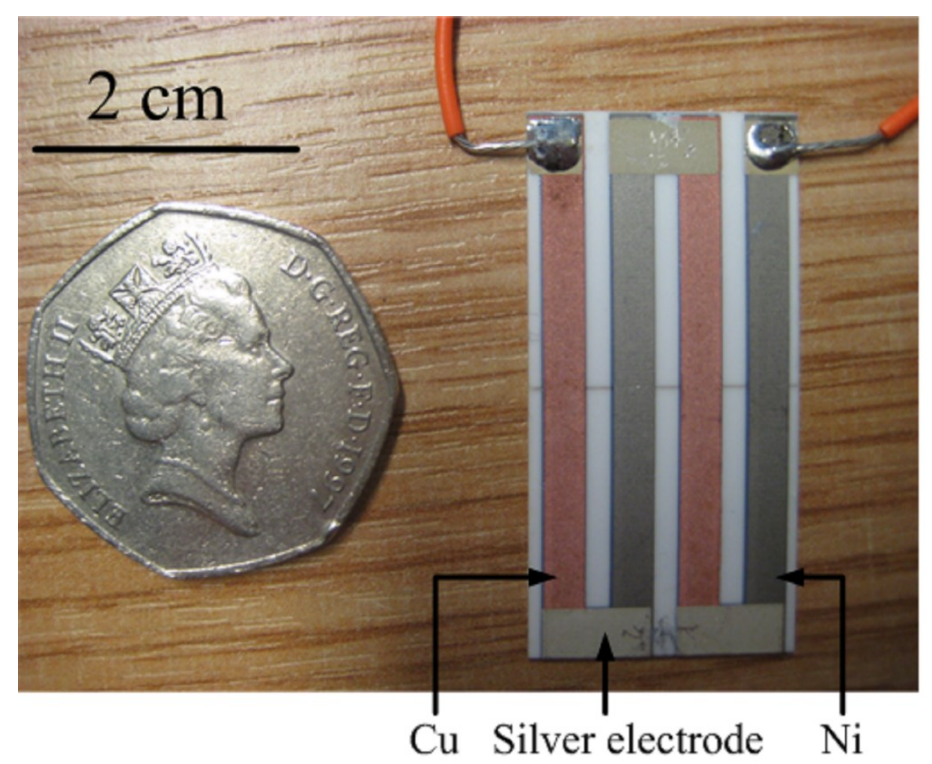


Figure 4.18 Screen printed Ni/Cu thermocouples with Silver electrodes

The completed printed 2 thermocouples is shown in figure 4.18. The conductive wires were soldered on the ends of the thermocouples. The dimension of each thermoleg is 39.8×3 mm. This main objection of this thesis is focus on the printed thermocouples from the material point of view. The dimension is not the important consideration of TEG device. In order to compare the performance with other devices from literature,

the dimension of such TEG is set to be the same with the published paper [54, 55], which is also metal based TEG devices. The dimension used in this literature was 40×3 mm, while in this experiment, the cutting need a tolerance of 0.1 mm at each end. Thus the final length of the thermolegs was 39.8 mm.

The average thickness of copper film is $11.2~\mu m$ and the average thickness of nickel film is $1.5~\mu m$. The distance between two adjacent thermolegs is 2 mm. The thickness difference came from the particles size difference. Comparing the SEM of copper particles (figure 5.4 and figure 4.15) with the SEM of nickel particles (figure 5.5 and figure 4.11), the copper particles are more granular like than flattened flake shape. The particles sizes for both powders are around 10 μm while the thickness of the nickel particle is in the range from 1 to 2 μm because of the flake shape. In this case, with the same paste viscosity, printed layers, the same mesh size and thickness of the screen, and the same printing speed, the printed Cu thick film and Ni thick film will have the different thickness.

The schematic of the Seebeck voltage measurement setup is shown in figure 4.19.

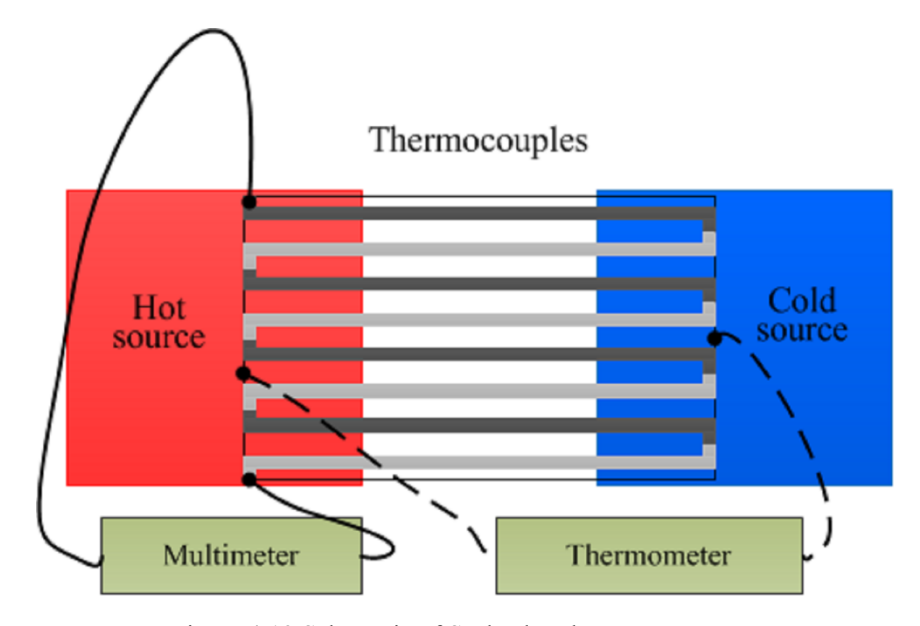


Figure 4.19 Schematic of Seebeck voltage measurement

One end of the planar-structured thermocouples was placed at the hot source and the other was attached to the cold source.

The thermoelectric voltage of the thermocouples was measured using a digital multimeter. The thermocouples were tested using Peltier modules from European Thermodynamics to provide a thermal gradient across the device. The temperature

gradient was measured using a Tenma digital thermometer with dual type K input. The whole setup is shown in figure 4.20.

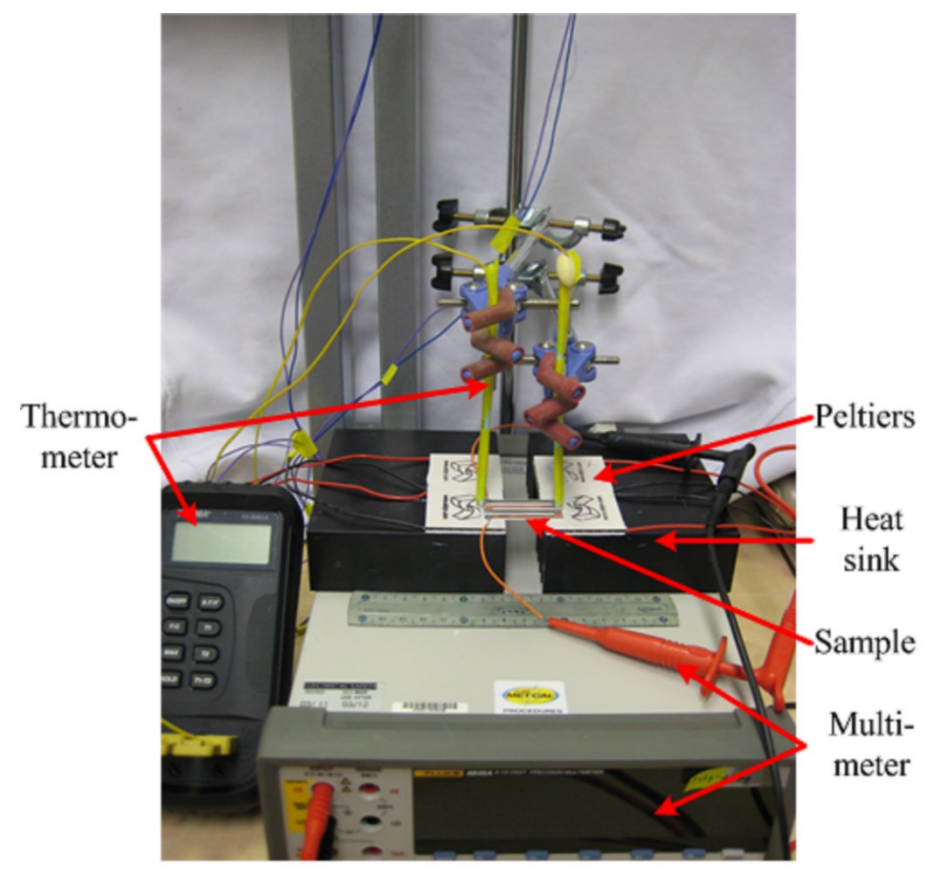


Figure 4.20 Seebeck voltage measurement setup

Heat sinks were used to speed up the heat transfer of the peltiers. Silicone heat compound (grease) was used to increase the thermal conductivity of the thermal interfaces in this setup by filling the air gaps due to uneven surface of the substrate and the peltier heaters. The temperature of two attached surfaces can be considered to be the same with this thermal grease.

When performing the Seebeck voltage and current measurement, a short period was required to establish a temperature gradient, because the temperature changes of the peltier heaters were not instantaneous. Moreover, the generated voltage and current also need a period to stabilize after the temperature gradient established. Therefore, all the values of voltage and current were measured 60 seconds after the input power setting of the peltiers.

Figure 4.21 shows the measured and linear fitted generated voltage of two thermocouples when there is a temperature difference applied across the device.

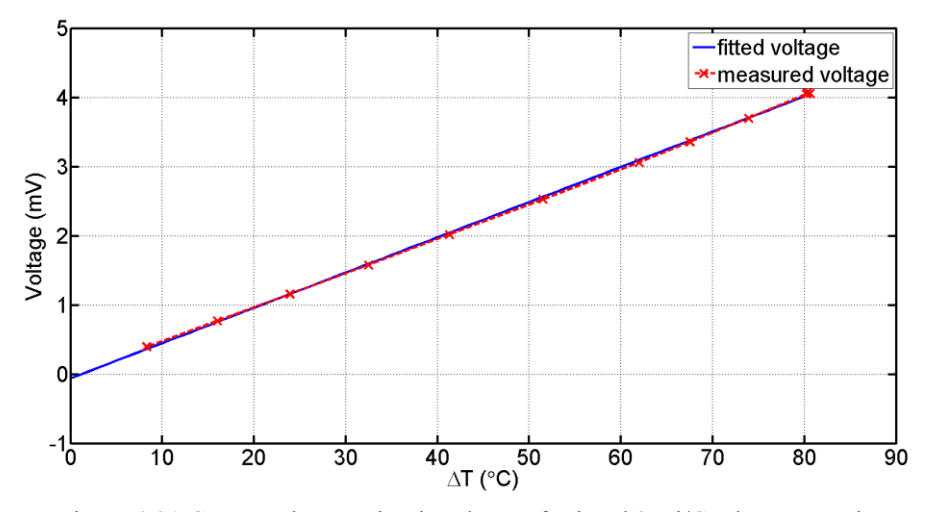


Figure 4.21 Generated open-circuit voltage of printed 2 Ni/Cu thermocouples

The voltage was proportional to the applied temperature difference. The slope of the V- ΔT curve is the Seebeck coefficient of the tested device. From equation 2.3, the Seebeck coefficient for single Ni/Cu thermocouple is 9.8 μ V/K. All calculations were computed with the help of linear fitting in Matlab.

At a temperature difference of 60°C, the generated voltage was 3.0 mV. For a single thermocouple, the generated voltage was about 1.5 mV. This result is higher than the voltage of the screen printed thermocouple published by Duby [54], which was 0.8 mV for single thermocouple when the temperature difference is 60°C.

The power output versus load resistance was measured with 8 thermocouples because of the step limitation of the resistance box. The minimum step of the resistance box was 1 Ω while the resistance of 2 thermocouples was around 4 Ω . The result will be more accurate when the step of variation resistance is much less than the whole resistance of the measured thermocouples. The circuit connection is illustrated in figure 4.22.

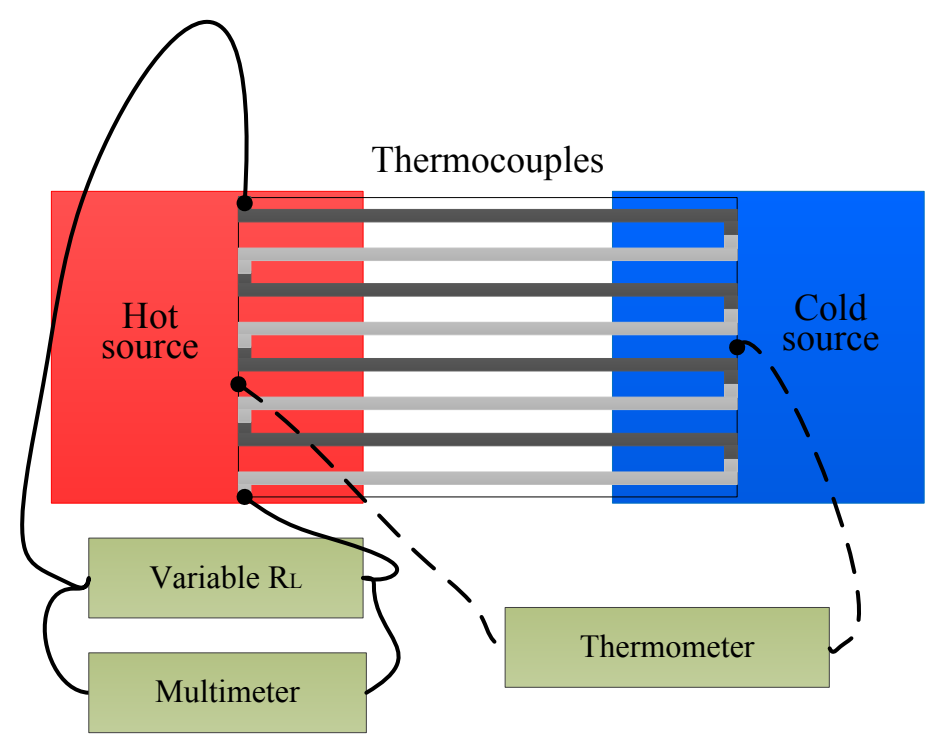


Figure 4.22 Illustration of the power output measurement circuit setup

The power output P is calculated by $P=V^2/R_L$. V is the voltage across the load resistance. R_L is the load resistance. In order to get the accurate maximum power output value, a mathematic fitting was processed.

The data from directing reading are load resistance and voltage. The fitting of voltage is based on $V=R_L\cdot(n\cdot\alpha_{Ni/Cu}\cdot\Delta T)/(R+R_L)=(n\cdot\alpha_{Ni/Cu}\cdot\Delta T)/(1+R/R_L)$, derived from figure 2.8. From this equation, the fitting could be made through few assumptions:

- The number of the thermocouples is fixed for specific TEG device. Here, n=8.
- The Seebeck coefficient of the Ni/Cu thermocouple is unchangeable when the temperature at both ends are fixed. Hence, when ΔT and n are known and unchanged, the denominator part of the above equation, $n \cdot \alpha_{Ni/Cu} \cdot \Delta T$, could be considered as a coefficient a.
- The equivalent resistance of the TEG, R, can be assumed to be unchanged when the ambient temperature has no variation, which can be considered as a coefficient b to instead.
- R_L is variable load resistance read from the resistor panel, each R_L value will result a voltage value.

From the equation above, the load voltage can be expressed by $V=f(R_L)$, here, R_L is the independent variable, V is the dependent variable and f is the function. The Matlab software uses the method of least squares when fitting data. The Matlab code of doing the fitting is shown in Appendix 8.

The load voltage and power output vs. load resistance changing are measured under different temperature gradients, 20°C (figure 4.23) and 40°C (figure 4.24). The voltage across the load resistor increased with the load resistance, while the maximum output power occurred when the load resistance was matched with the TEG's resistance. The fitted curves match the measured raw data with a high degree of accuracy from visual seeing.

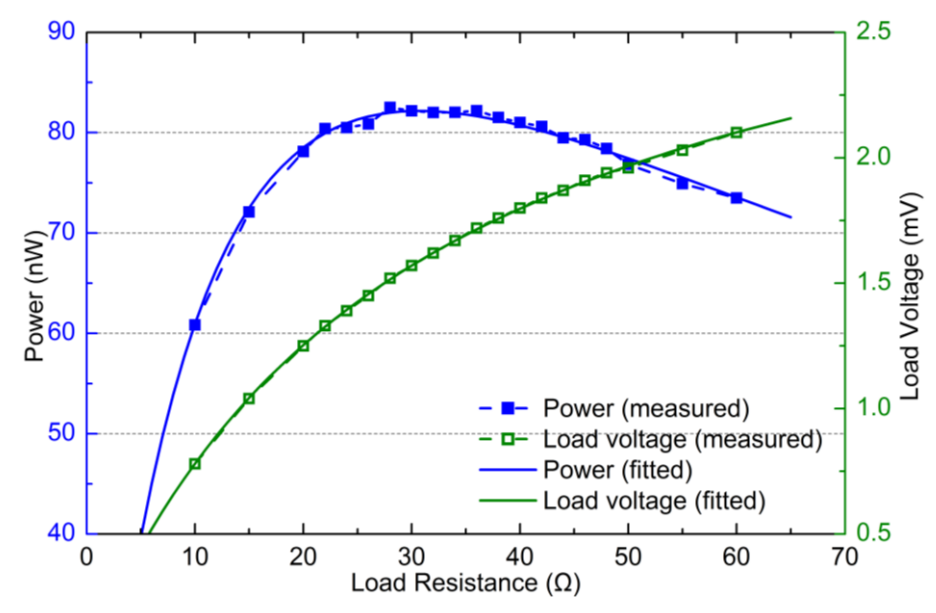


Figure 4.23 power output and voltage of the 8 Cu/Ni thermocouples as a function of load resistance at a 20K temperature difference

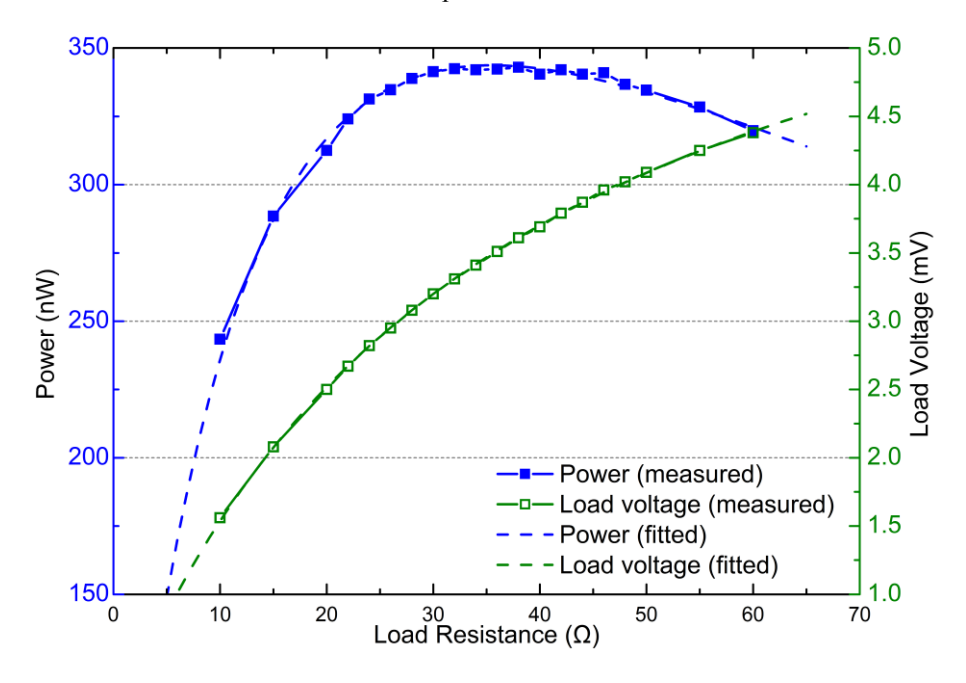


Figure 4.24 power output and voltage of the 8 Cu/Ni thermocouples as a function of load resistance at a 40K temperature difference

The voltage across the load resistor is greater when the temperature gradient is larger. At a temperature difference of 20 °C, the maximum power output was about 82.16 nW when the load resistance was 30.66 Ω for 8 printed thermocouples. At a temperature difference of 40 °C, the maximum power output was about 343.68 nW when the load resistance was 35.48 Ω for the same device. These results, including maximum power output, the resistance of the printed TEG and single thermocouple, and the calculated Seebeck coefficient from the close-loop power output measurement are all summarized in table 4.8.

	ΔT=20°C	ΔT=40°C
Resistance for 8 thermocouples (Ω)	30.66	35.48
resistance for a marmacouples (22)	(30.2 - 31.12)	(34.91 - 36.05)
Pagistance for single thermosouples (O)	3.83	4.44
Resistance for single thermocouples (Ω)	(3.78 - 3.89)	(4.37 - 4.51)
Maximum power output for 8	82.16	343.68
thermocouples (nW)	02.10	343.00
Maximum power output for single	10.27	42.96
thermocouples (nW)	10.27	42.70
Calculated α _{Ni/Cu} from Seebeck voltage	9.	Q
measurement ($\mu V/K$)	9.	o
Calculated $\alpha_{Ni/Cu}$ from close-loop power	19.84	21.83
output measurement $(\mu V/K)$	(19.71 - 19.98)	(21.65 - 22.0)

Table 4.8 Summarize of calculated values from Seebeck voltage and power output measurements with different temperature difference

The resistance of metals will increase when the temperature increases, hence the maximum power output occurs at a higher load resistance at a 40°C temperature gradient than at a 20°C gradient.

4.5 Summary and discussion

Overall, this experiment demonstrated that screen printing technology can be used for the fabrication of TEGs. This is the main purpose of this experimentation with copper and nickel pastes. Hence, no precise optimisation of the paste recipe and firing conditions have been performed. The thickness of the nickel film and copper film could also be optimised by printing different numbers of layers to improve the output voltage and power but this was considered unnecessary.

The absolute value of the Seebeck coefficient of bulk nickel (-19.5 μ V/K) is greater than that of thick-film nickel (-13 – -17 μ V/K). However, the Seebeck coefficient of bulk copper (1.83 μ V/K) is smaller than that of thick-film copper (3 μ V/K). A possible

reason is that the impurities of the nickel and copper paste change the Seebeck coefficient of the whole film. Therefore, it can be assumed that the glass binder has a positive Seebeck coefficient which increases the α value of copper thick film and decrease that of nickel film. According to the Kelvin relationship, the calculated Seebeck coefficient for the screen printed high temperature Ni/Cu device is 16-20 μ V/K, which is very close to the values given in the literature [36].

The Seebeck coefficient calculated from closed-loop power measurement is 19.84 $\mu V/K$ (at ΔT =20°C), compared with 9.8 $\mu V/K$ calculated from open-loop measurements. The former calculation is closer to the values measured from the individual thick films, given in section 4.2.2 and 4.3.2. The close match between the Seebeck coefficient from power measurements of the device and individual thick films demonstrated that the voltage and power measurement method was promising.

	Cu	Ni
change of ρ compared with bulk material	3738%	6226%
change of α compared with bulk material	64%	-23%
Powder percentage	90%	80%

Table 4.9 The resistivity increase of printed thick films compared with their bulk counterpart

In table 4.9, the resistivity change of the thick films compared with the bulk material is much higher than that of the Seebeck coefficient. Hence, it can be conclude that the high resistivity is the bottle neck from achieving a high power output of printed thermocouples. The increase of nickel thick film resistivity compared with bulk material is higher than that of copper because the particle percentage in nickel paste is lower. The change of the Seebeck coefficient of copper thick film is larger than nickel is because the bespoke Seebeck coefficient measurement machine had a Cu based probe and it was difficult for this machine to get an accurate result from a sample consist of the same material with the probe.

The work in this chapter demonstrated that screen printing technology is suitable to be applied to fabricate planar thermocouples. Also, with a dielectric interface layer, nickel thick-films could be successfully deposited on an alumina substrate. The development of high temperature nickel and copper inks showed that these two materials can be used in printed thermocouples. However, in order to move the thermocouples onto a flexible substrate, low temperature nickel and copper pastes must be developed. The related works will be described in next chapter.

Chapter 5. Low temperature curing copper and nickel based thermocouples and evaluation of the interface material of the textile

5.1 Introduction

With the successful development of high temperature screen printing nickel/copper TEG, transferring the Ni/Cu thermocouples onto flexible substrates was investigated in this chapter. This project needs to realise prototype wearable TEGs which require flexibility from a comfort point of view.

The two flexible substrate used in this project are polyimide and polyester-cotton textile. The polyimide substrate, known as Kapton, has a maximum working temperature of 400°C. It is also a good electrical insulator and resists many chemical solvents [92]. Kapton was used in this project as a substrate because of its flexibility, high temperature resistance and smooth surface. Polyester-cotton textile is a common textile used in daily life. Normally, it can resist a temperature of 150°C for a maximum of 45 minutes. The highest working temperature is 180°C for 10 minutes [44].

In order to screen print copper and nickel paste onto a flexible substrate, a low temperature curing process is necessary, because a typical flexible substrate such as polyimide is unable to survive the firing process at 850°C.

Therefore, an alternative binder system (different from the glass binder system in chapter 4) that can be cured in the working temperature range of the flexible substrates needs to be mixed to the copper and nickel paste. The requirements of the binder system include:

- Screen printable: The paste must be compatible with screen printing technology.
 A suitable viscosity and sufficient pot life are crucial for the performance of the paste.
- 2. Thermal curing: UV cured polymer binder systems cannot be fully cured because the UV light does not fully pass through the metal powders in the paste. Therefore, all the polymer binder systems used in the experiments were thermally curable.
- 3. Low temperature curing: The curing temperature of the binder system must be lower than the maximum working temperature of the substrate.

Polymers binders have potential to be applied in screen printing technology because most polymer molecules will cross link at a low curing temperature [93], which helps to bind the particles onto the substrate after curing. In this chapter, in order to realize a low temperature Ni/Cu TEG, attempts are made to deposit Ni and Cu pastes on flexible substrates using screen printing.

The eventual aim of the TEGs should be applied on textile. However, the wavy and uneven surface textile combined with the pilosity of fabric makes it difficult to screen print on precisely. In order to print thermoelectric materials on a textile substrate, and give protection to the electronic material, depositing an interface layer is essential [94]. In this chapter, the usage of silicone as an interface layer on textile is also investigated.

5.2 Low temperature curing copper paste

In this experiment, various binder systems have been tested to achieve a copper thick film with reasonable conductivity. The binders can be classified into three main categories: polyurethane based binder, silicone based binder and epoxy based binder. The general properties of three different types of copper pastes are listed in table 5.1.

Binder system	Polyurethane	Silastic silicone	Sylgard silicone	Ероху	
Percentage of Cu by weight	85%	85%	85%	85%	
Mixing method		Triple r	oll mill		
Printing ability		print	able		
Layers of films		2	2		
Drying condition		85°C, 2mir	ı, box oven		
Curing condition	150°C, 10min, In N ₂	150°C, 10min, In N ₂	150°C, 10min, In N ₂	250°C, 10min, In N ₂	
Substrate	Alumina, Kapton	Kapton	Kapton	Kapton	
Adhesion*	1	5	5	6	
Flexibility (on Kapton)	8	7	7	5	
Sheet Resistance on first day (Ω/\Box)	Out of range	Out of range	5 – 11	2.7 – 4.6	
Sheet Resistance on third day (Ω/\Box)	N/A	N/A	1 k – 100 k	> 300	
*Scale: 10-exellent; 1-very poor. The same condition will be applied in the following tables in this chapter.					

Table 5.1 Fabrication conditions and properties of low temperature Cu thick film deposited by screen printing

The range of the sheet resistance test setup varies from $1\times10^{-3}~\Omega$ ·cm to $5\times10^{8}~\Omega$ ·cm. In this case, out of range indicates the sheet resistance is higher than $5\times10^{8}~\Omega$ ·cm. The

curing temperature of the polyurethane and silicone binders were referred to the datasheet and literature [95], while the curing temperature of the epoxy binder was optimized by experiment which will be introduced in chapter 6.

5.2.1 Polyurethane binder based copper paste

The recipe of the polyurethane binder system was from a project in the EEE group at the University of Southampton. It contains two main parts, polyurethane binder KY-B and emulsifier KY-C. This binder system is water-soluble, hence water can be added as a thinner in the binder system. Thickener (KY-A) can be added to achieve a printable viscosity. The ratios by weight of each composition in this binder system are listed in table 5.2.

Composition	Polyurethane KY-B	Emulsifier KY-C	Water	Thickener KY-A
Ratio	90%	10%	1g filler ~ 1ml water	1% of all mixture

Table 5.2 The ratio of the constituents in the polyurethane binder system

The fabrication conditions of the screen printed Cu paste are also listed in Table 5.1. The quality of adhesion was poor but the flexibility on Kapton was fine. Thinner was not calculated into the ratio of the paste because it will evaporate during the drying process. The paste was printed on both alumina and Kapton substrates. Neither samples showed promising resistance compared to high temperature Cu thick film printed in chapter 4. The electric properties of the samples shows no indication it is suitable for use in a practical application. The quality of adhesion of the printed pattern was poor on both alumina and Kapton substrates (shown in figure 5.1).

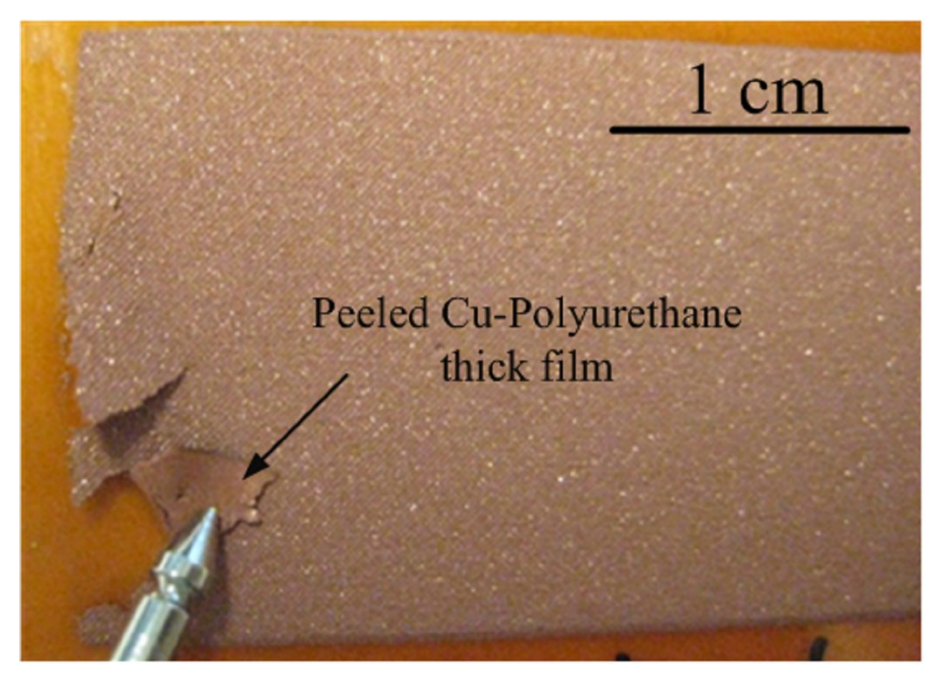


Figure 5.1 Adhesion demonstration of Cu-polyurethane thick film on a Kapton substrate The cross-linking between the polyurethane molecules is also week as the thick film can be easily torn apart. The tests show the polyurethane binder system is not suitable for low temperature copper thick film printing.

5.2.2 Silicone binder based copper paste

Silicone is widely used as a coating and interface material in a number of cases [96-98]. Silicone binder based pastes have advantages similar to silicone thick film, for example, they have good flexibility after curing. Two different types of silicone binder systems were used in this experiment.

Dow Corning Silastic E RTV silicone rubber (datasheet in Appendix 5) is one silicone binder system investigated in this work, the other was Dow Corning Sylgard 184 Silicone Elastomer (datasheet in Appendix 6). The inhibitor used to extend the pot life was Dow Corning SL 9106 Coating. The solvent was ESL 402 thinner.

The viscosity of Silastic silicone (55000 cP) is higher than that of Sylgard silicone (3500 cP), which means the Silastic silicone binder system needs more solvent and thinner to ensure the viscosity of Cu paste with the same filler percentage is in the screen printable range. An added advantage is that the solvent and thinner added in the pastes extended the pot life, which made the paste easier to handle. The optimised parts ratio of the binder system for a printable copper paste is listed in table 5.3. The base and catalyst ratios were from the datasheet while the Inhibitor and Solvent ratios were

optimised by adding these two constituents gradually to reach the screen printable pastes viscosity range.

	Base	Catalyst	Inhibitor	Solvent
Silastic silicone binder	10	1	3 - 3.5	3 - 3.5
Sylgard silicone binder	10	1	3	3

Table 5.3 Optimized ingredients and ratio of Silastic silicone binder system

The fabrication conditions of the copper paste with silicone binders are listed in Table 5.1. Although the silicone-copper pattern printed on Kapton was also very easy to remove (shown in figure 5.2), when peeling off, the printed pattern was not torn apart, demonstrating the cross-linking between silicone molecules is stronger than its polyurethane counterpart.

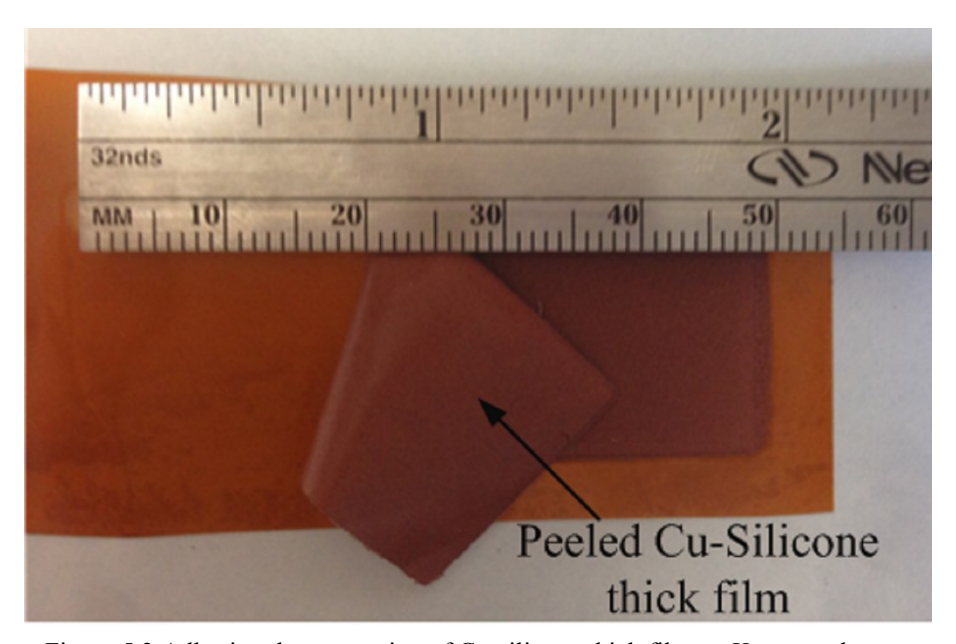


Figure 5.2 Adhesion demonstration of Cu-silicone thick film on Kapton substrate

For Silastic silicone binder based copper pastes, the sheet resistance of printed layer was still too high for use as a thermoelectric material. For Sylgard silicone-copper thick film, although the initial sheet resistance was $5 - 11 \Omega/\Box$, the oxidation of the copper in air made it increase by over 1000 times in three days.

In conclusion, the Sylgard silicone—copper thick film had a lower sheet resistance than the Silastic silicone—copper thick film. The lower viscosity of Sylgard silicone is the possible reason. More thinner was required to achieve a printable viscosity for a silicone binder system with higher viscosity. Thinner is not part of the functional paste and it is only used to tune the viscosity for printing. Work by Yi also demonstrated that more thinner used in the ink will decrease the performance of the printed film [99].

Hence, a binder system with low viscosity is important for thermoelectric material paste formation.

5.2.3 Epoxy binder based copper paste

Epoxy, also known as polyepoxide, normally consists of two parts, resin and hardener. It had been used as a binder for low temperature printable paste in other work [60]. 3M Scotchcast Electrical Resin 280, a low viscosity, flexible, and thermally curable two-part epoxy was chosen to act as the binder system. The viscosity of the epoxy mixture is 4000 cP [100].

The epoxy binder used here is 4,4'-Isopropylidenediphenol-epichlorohydrin polymer based epoxy (3M Resin 280). The molecular formula is C₁₈H₂₁ClO₃. The molecular structure is shown in figure below.

Figure 5.3 Molecular structure of the ingredient in resin 280 epoxy [101]

The solvent used to dilute the paste was ESL 402 thinner. The ratio of copper particles to thinner by weight was between 10:2 and 10:3. The fluidity of the paste meets the requirements for screen printing. The adhesion of epoxy binder copper paste on both Kapton and alumina substrates was good. The flexibility of printed copper pattern on Kapton can be simply tested by rolling it on a pencil with a diameter of 7 mm, shown in figure 5.4. However, when the sample was folded or forced into greater bending, the patterns would peel off from the substrate.

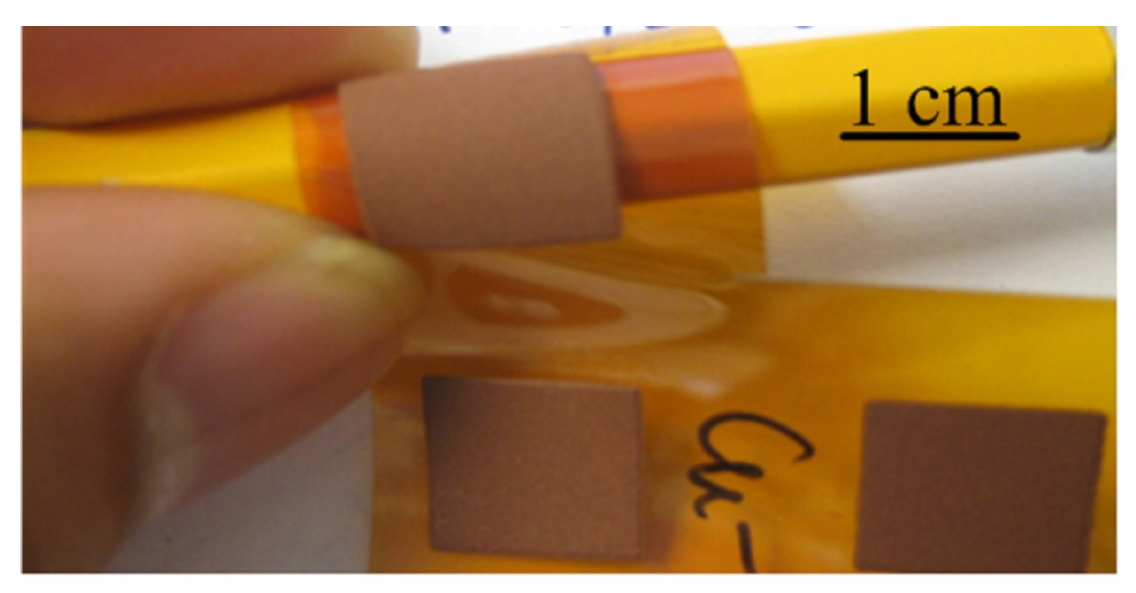


Figure 5.4 Cu-epoxy thick film pattern rolling on a pencil

Compared to other binder systems tested in this chapter, the epoxy binder system was chosen for later experiments due to its advantages in printability, adhesion and flexibility on Kapton. The adhesion problem of the polyurethane binder system and silicone binder systems limits their application. However, Sylgard 184 silicone based binder system still had potential to be applied on textile when using a silicone interface layer.

All the low temperature cured copper samples in this chapter had the problems of increasing resistance with time. Resistance increases quickly during prolonged exposure to open air due to the oxidation of the copper.

All Kapton films were glued onto the alumina substrates in order to ensure the surface was flat and there was no movement during printing. The films were flexed when peeling the patterns off alumina and the resistance increased dramatically. The resistance of a 1 cm \times 1 cm sample before and after peeling off is shown in table 5.4. The resistance was measured by placing multimeter probes across two corners of the square pattern.

R (before peel-off)	$\sim 50~\Omega$
R (after peel-off)	$\sim 400~\Omega$
Percentage changed	700%

Table 5.4 Resistance change of Cu thick film before and after peel-off from alumina substrate The Hall effect measurement was processed with the samples printed on alumina. The average resistivity value of the optimised sample from the Hall Effect Measurement machine was $1.46 \times 10^{-3} \ \Omega \cdot \text{cm}$, which is over 1000 times higher than that of the high

temperature cured samples. The Hall effect measurement results are show in table 5.5. The measurement was done 1 day after the silver epoxy cured in air. The sign of carrier concentration and Hall coefficient indicated that this low temperature cured copper pattern is a p-type material.

Physical properties	Minimum value	Maximum value	Average value
Carrier concentration (cm ⁻³)	6.94×10^{20}	3.48×10^{21}	1.89×10^{21}
Mobility $(cm^2/(V \cdot m))$	1.23	6.14	3.4
Resistivity (Ω·cm)	1.45×10 ⁻³	1.47×10 ⁻³	1.46×10 ⁻³
Hall coefficient (cm ³ /C)	1.79×10 ⁻³	9.0×10 ⁻³	4.98×10 ⁻³

Table 5.5 Transportation properties of Cu paste with epoxy binder

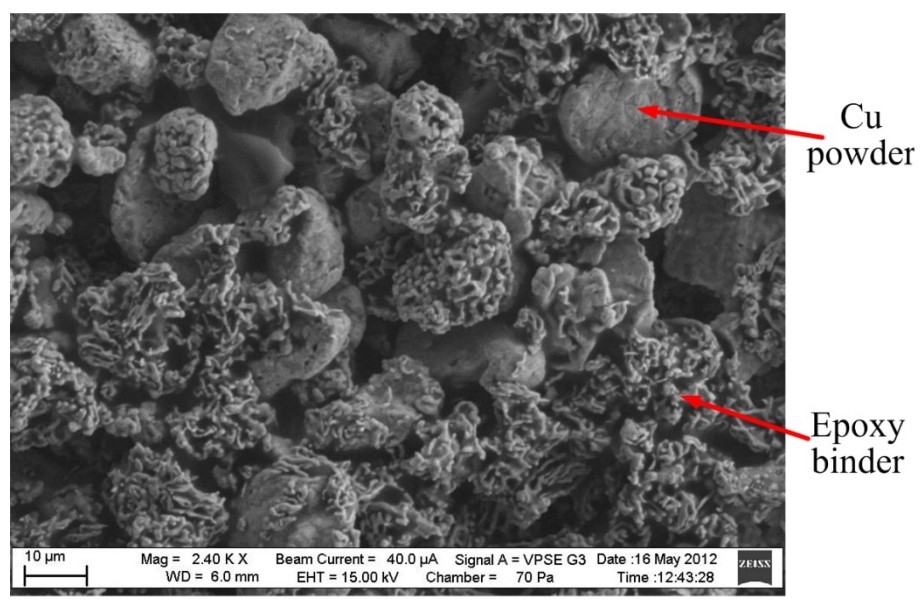


Figure 5.5 SEM image of printed Cu paste with epoxy binder

From the SEM image of the copper pattern in Figure 5.5 it can be seen that the copper particles and epoxy matrix were uniformly mixed after triple roll mill mixing. However, the epoxy shrunk after the curing process, which affected the flexibility of the Cu pattern and made the Cu particles exposed to air, increasing the oxidation rate. Additionally, the higher the curing temperature used in the experiment, the worse the flexibility of the printed sample.

However, Cu-epoxy was still the most promising low temperature copper paste in this experiment compared with other polymer binder systems used.

5.3 Low temperature curing nickel paste

A low temperature nickel paste was also made based on 3M Scotchcast Electrical Resin 280 epoxy binder system. In this experiment, nickel paste needed more thinner to get a screen printable viscosity. The ratio of nickel particles to thinner by weight

was between 10:7 and 10:8, in order to meet the requirement of screen printable viscosity range. The drying and curing conditions were the same as the epoxy-copper paste because the nickel patterns needed to be cured in the same process with copper as thermocouples. The detailed fabrication conditions are listed in table 5.6. The adhesion and flexibility capabilities of nickel patterned onto Kapton were better than the epoxy-copper paste.

The negative carrier concentration and Seebeck coefficient of the nickel pattern shown in table 5.7, indicate that the carriers in the nickel paste were electrons.

Percentage of Ni by weight	78%	
mixing	Triple roll mill	
Screen Printing ability	printable	
Layers of printed films	2	
Drying condition	85°C, 2min, box oven	
Curing condition	250°C, 10min, in N ₂	
Substrate	Kapton	
Adhesion*	7	
Flexibility*	7	
*Scale: 10-exellent; 1-very poor. The same condition will be applied in the following tables in this chapter.		

Table 5.6 Ni paste with 3M Scotchast Resin 280 binder

Similarly with epoxy binder based copper paste, the resistivity of Ni pattern was over 1000 times higher than the bulk value. Also, the absolute value of the Seebeck coefficient for Ni thick film was lower compared with the high temperature cured version. These differences mean that the thermoelectric property of epoxy based nickel paste is worse than the glass binder based nickel paste.

Physical properties	Minimum value	Maximum value	Average value
Carrier concentration (cm ⁻³)	-4.86×10^{20}	-3.99×10^{20}	-4.42×10^{20}
Mobility $(cm^2/(V \cdot m))$	2.41	2.93	2.66
Resistivity (Ω·cm)	5.33×10 ⁻³	5.36×10 ⁻³	5.34×10 ⁻³
Hall coefficient (cm ³ /C)	-1.56×10 ⁻²	-1.29×10 ⁻²	-1.42×10 ⁻²
Seebeck coefficient (µV/K)	N/A	N/A	-10

Table 5.7 Transport properties of Ni paste with epoxy binder

The SEM image of this printed nickel sample is shown in figure 5.6. The flake shape of the nickel particles can be seen clearly. The particle size of both Cu and Ni were around 10 µm from figure 5.5 and figure 5.6. However, compared with the SEM image of the low temperature cured copper sample, the epoxy matrix cannot be seen in figure 5.5. The nickel particles are more flake-like than copper particles. This is the reason

that the copper films are thicker than nickel films despite screen printing the same number of layers and depositions for each layer.

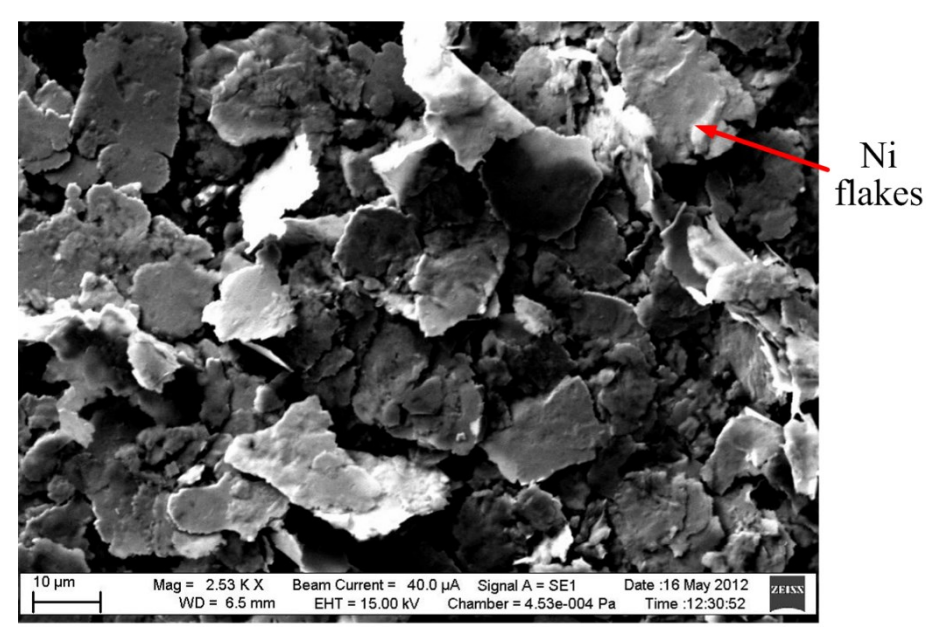


Figure 5.6 SEM image of printed Ni paste with epoxy binder

Moreover, the shape of the particles had an effect on the electrical resistivity of the printed films. The increments in resistances of these different patterns before and after peel-off are listed in table 5.8. The flake shaped particles offered a larger contact area, hence the increment in resistance of the Ni sample was much smaller than that of Cu sample.

R (before peel-off)	$\sim 10 \Omega$
R (after peel-off)	~ 13 Ω
Percentage changed	30%

Table 5.8 Resistance changes of printed nickel sample before and after peel-off

5.4 Low temperature curing nickel/copper based thermocouples

Two layers of both copper and nickel thermolegs were printed, with 2 depositions for each layer. The detailed fabrication process is shown in figure 5.7.

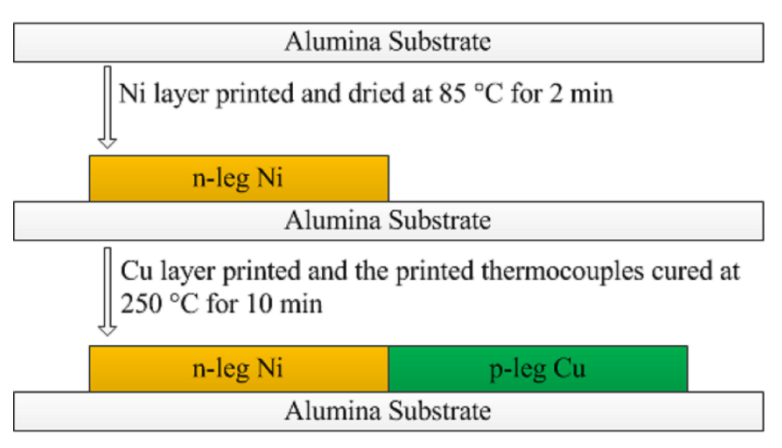


Figure 5.7 Fabrication process of low temperature Ni/Cu thermocouples

The thickness of the Cu was 91 μ m and that of the Ni was 18.7 μ m. The planar dimension of the printed thermocouple was the same as the high temperature cured version. An image of the screen printed Ni/Cu thermocouples is shown in figure 5.8.

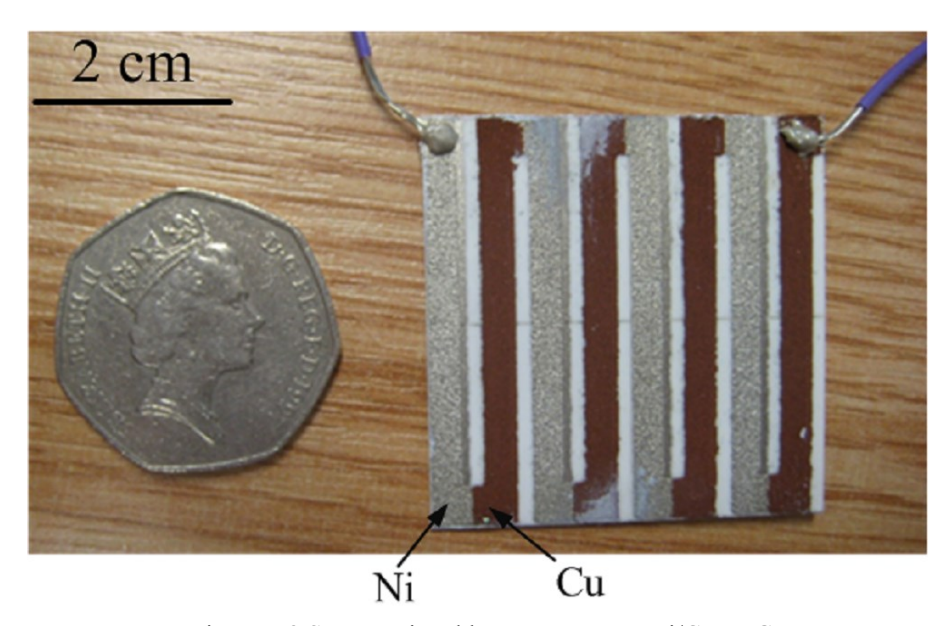


Figure 5.8 Screen printed low temperature Ni/Cu TEG

As the problem of resistance changing dramatically when peeling the Kapton from the alumina substrate was not solved, the low temperature Ni/Cu thermocouples were only printed on an alumina substrate to test. The voltage and current generated by these four thermocouples at different temperature gradients is shown in figure 5.9.

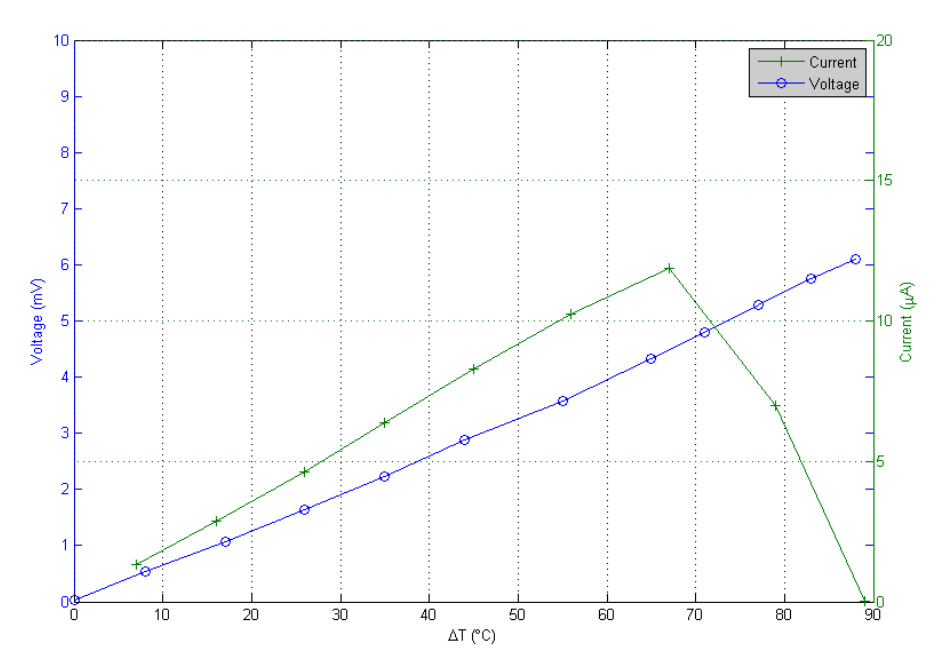


Figure 5.9 Generated thermoelectric voltage and current of 4 epoxy-Ni/Cu thermocouples on an alumina substrate

It can be seen that the current decreased dramatically when the temperature gradient increased above 70°C. When the temperature approached 90°C, the generated current of these four thermocouples was close to 0 A. The variation of electric resistance before and after the open circuit voltage test is shown in table 5.9. The resistance was measured using a Fluke multimeter. In this experiment, when heating one end of the thermocouples above 70°C, the resistance increased over 1000 times.

	R of 4 low temperature Ni/Cu thermocouples
Before open circuit voltage test	~ 100 Ω
After open circuit voltage test	$> 100 \text{ k}\Omega$

Table 5.9 Resistance change of the thermocouples before and after Seebeck voltage test It was obvious that the oxidation of thick films will speed up when heated, which increased the total resistance of the device and in turn decrease the current.

When measuring the power output measurement, the voltage over the load resistor was out of range because of the low circuit current. All the results indicate that the rapid resistance increase of these thermocouples is not practical for TEGs application.

5.5 Failure analysis of low temperature Ni/Cu thermocouples

The average values of the transport properties of the copper and nickel pattern were compared between the samples cured at 850°C and those cured at 250°C. The ratios of the transport properties of the samples cured at different temperatures are concluded in table 5.10.

	Cu sample	Ni sample
Carrier concentration (cm ⁻³)	3.5:1	0.58:1
Mobility (cm $^2/(V \cdot m)$)	9:1	2.36:1
Resistivity (Ω·cm)	1:22.73	1:11.11
Hall coefficient (cm ³ /C)	1:8.33	1:4.76

Table 5.10 Ratio of high temperature cured samples' transport properties to low temperature cured ones (samples cured at 850°C/samples cured at 250°C)

From the above table, lower curing temperature leads to a lower mobility and a large resistivity increasing. Actually, the increment in resistance was the main issue for the low temperature cured Ni/Cu based thermocouple, especially for copper thick films. There are two reasons for this problem. Firstly, the non-flake form of the copper particles decreased the contact area of adjacent particles. Secondly, the easy oxidation of copper [86] made the operation life of low temperature Ni/Cu based thermocouples very short.

It is possible to solve this problem by Intense Pulsed Light (IPL) sintering technology. The IPL can sinter the copper ink without damaging the flexible substrates in an extremely short time (2 ms) [67]. Because the wavelength of the generated pulsed light is only compatible with the excitation energy of the copper atoms. It avoids making the substrate too hot to be damaged. Intrinsiq Materials [102] has developed screen printable copper paste on flexible substrate using IPL sintering.

5.6 Approaches to textile surface treatment for depositing electronics

In order to move the printed thermocouples onto normal polyester-cotton textiles, not only does the curing temperature need to be decreased to fit the operational temperature of polyester-cotton textile (maximum around 150°C) [94], but also the surface of the textile needs to be suitably treated for depositing thermoelectric materials.

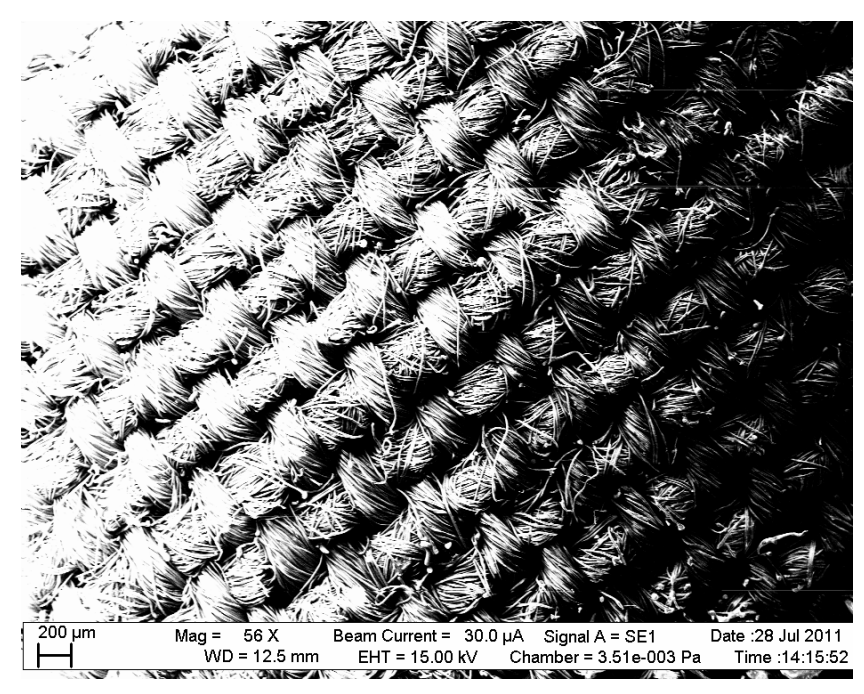


Figure 5.10 SEM image of polyester-cotton textile surface

The uneven surface polyester-cotton of textile is shown in figure 5.10. Silicone and polyurethane are two types of polymer applied as interface layer to cover the uneven surface of the textile. In table 5.11, a comparison of silicone rubber and polyurethane shows that the tensile elongation of silicone is three times larger, which means it is more flexible on a wearable textile. Silicone is also softer (smaller durometer hardness value) and has higher heat resistivity than polyurethane. In addition, it has a longer pot life which is important for the screen printing industry. Silicone rubber is a potential interface layer material because of its advantageous mechanical properties, UV resistivity and waterproof ability [96-98].

	Polyurethane	Silicone
Tensile Strength (Test condition: Yield, 22.8°C)	11.0 to 6700 psi	33.0 to 1030 psi
Tensile Elongation (Test condition: Yield, 22.8°C)	2.0 to 150%	50 to 410%
Durometer Hardness (22.8°C)	38 to 90	20 to 81
Thermal Conductivity (W/m°C)	0.0375 to 0.332	0.0144 to 1.59
Max. Continuous Use Temperature	120 to 130 °C	203.3 to 261.1 °C
Resistivity (Ω·cm at 22.8°C)	5.2E+6 to 1.5E+15	0.0040 to 2.5E+16
Pot Life (22.8°C)	0.033 to 30 min	0.22 to 13000 min
Thermoset Mix Viscosity (22.8°C)	35.0 to 15000 cP	35.0 to 77500 cP
Contact angle (at 21°C)	80°	112°
Surface energy (mN/m at 21°C)	32	11

Table 5.11 Properties comparison of common polyurethane and Silicone [103-105]

However, silicone has adhesion problems for other materials printed on top of its surface because the surface energy is very low for a cured silicone interface layer [105]. The research into improving the quality of adhesion on the silicone interface layer can be considered as a sub-topic of this thesis.

5.7 Quality of adhesion of silicone interface layer improvement

The silicone rubbers are typically made by crosslinking functionalized polysilanes and polysiloxanes, the backbone units of which are -Si-Si-Si- and -Si-O-Si- bonds respectively. When the silicone layer was just printed onto textile, the pattern is wet and these bonds are open. After thermal or infrared (IR) light curing, the bonds are closed because they become cross-linked with each other. Hence the surface energy of silicone interface layer changes from high to low during the curing process [106, 107]. In this solution, the aim is to investigate whether a conductive silver paste can be screen printed onto the silicone interface layer when the surface energy of it is still high, i.e., before it has been fully cured.

The silicone for screen printing was purchased from Dow Corning. The basic silicone paste includes a silicone base and catalyst. However, it was found that this basic silicone paste is too thick to be screen printed and has a short pot life (roughly 2 hours depending on the temperature and humidity of the processing environment). Here, thinner is added into the paste in order to reduce the viscosity and extend the pot life to 4 hours. The detail is shown in table 5.12.

Composition	Product	Ratio	Viscosity
Silicone base	Dow Corning LCF-9601 Textile	100	
	Printing Base		22255 B
Catalyst	Dow Corning 9600 Series Textile	3.0	33375 cP
Catalyst	Printing Ink Catalyst	3.0	
Thinner	ESL T402 thinner	4.5-6.0	

Table 5.12 Silicone paste for interface layer used in the experiment with ratio and viscosity. The viscosity of silicone paste higher than the screen printable range. Hence, in this experiment stencil printing was chosen to deposit the silicone interface layer.

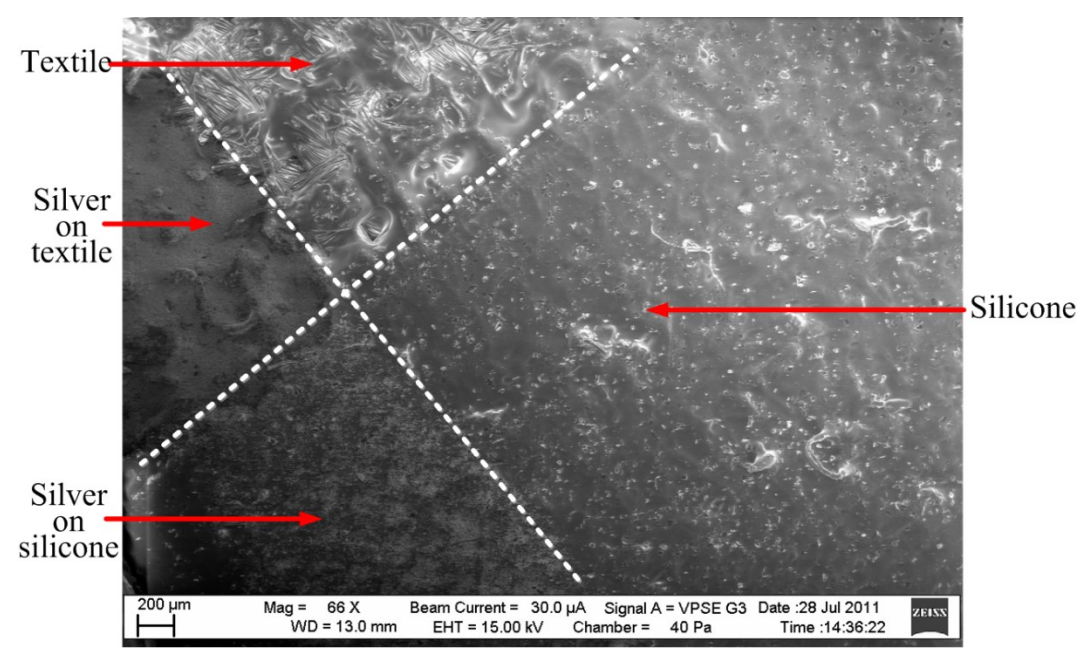


Figure 5.11 SEM of silver on silicone interface layer and fabric

In figure 5.11, the area coated with silicone interface layer was much smoother than the textile surface. Moreover, the silver paste directly printed on fabrics had a coarse surface and the pattern edge was rough. The smoothness of silver on silicone interface layer was improved, which proved that silicone interface layer can provide a relatively flat surface to print other materials on textile. However, the silver printed on silicone interface layer was easy to scratch off. The adhesion of silver was very poor on the silicone surface.

The typical procedure of all the processes in this experiments are:

- 1. Manufacture a silicone paste.
- 2. Stencil print a silicone interface layer on textile substrate.
- 3. Dry the silicone interface layer and built up the thickness if necessary.
- Screen print a conductive silver electrode layer after drying the last silicone interface layer.
- 5. Cure the interface layer and silver electrode layer as a whole.

Different printing methods and variety curing methods were tried to achieve an optimized quality of adhesion of silver pattern on silicone. The adhesion quality was tested by using a spatula to scratch the silver pattern. The investigation methods and results are shown in table 5.13.

Silicone interface layer	Drying condition	quality of adhesion of	
production method	(method, time)	silver electrode layer*	
	Oven**	1	
	Hot plate, 100°C, 30s	1	
	Hot plate, 100°C, 60s	4	
	IR, 24s	1	
	IR, 21s	1	
Hand stancil mainting	IR, 18s	1	
Hand stencil printing	IR, 17s	2	
	IR, 16s	2	
	IR, 15s	2	
	IR, 14s	5	
	IR, 13s	4	
	IR, 10s	4	
	IR, 14s	2	
	IR, 12s	3	
	IR, 10s	3	
	IR, 8s	3	
Machine stencil printing	IR, 6s	4	
	IR, 5s	5	
	IR, 4s	5	
	IR, 3s	5	
	IR, 2s	5	
*Scale: 10-exellent; 1-very poor.			
**Shown are the best results from different curing times.			

Table 5.13 Results of the adhesion test for samples fabricated using different processes and curing methods

In this experiment, hand stencil printing and machine stencil printing were both applied to print the silicone interface layer. The thickness of the stencil for hand printing was 300 µm while that for the machine printing was 100 µm. In order to build up the pattern thickness, the former-printed silicone layers must be dried to get a tackfree surface before another layer is added on. All silver electrode patterns were printed one layer with two deposition. In this experiment, a short time was needed to setup the silver printing screen. For hand printing, it takes 30 seconds to setup the screen. For machine printing, it takes 15 seconds to setup the machine before printing silver. Thus, a short period of cross-linking in silicone could not be avoided in this experiment. At the end of printing process, all samples in the experiment need to be cured in the oven at 125°C for 15 min.

Because the stencil for manual printing was thick enough for printing a silver layer on top of it, there is no need to increase the thickness of the silicone interface layer. Hence,

drying operation before adding another silicone interface layer is not needed in this step. The oven dried samples have very poor quality of adhesion for another silver layer printed on top. From figure 5.12, it can be seen that some parts of the silicone (part 1) come off from the textile substrate, which is because the half cured silicone interface layer is still wet enough to stick on the screen. After printing silver, these parts stuck on the back of the silver screen and spoilt the silicone pattern and blocked the screen meshes, preventing later depositions. For part 2, most areas were dry enough to only stick to the silver paste. But after the final curing, the silver electrodes easily come off from the silicone interface layer.

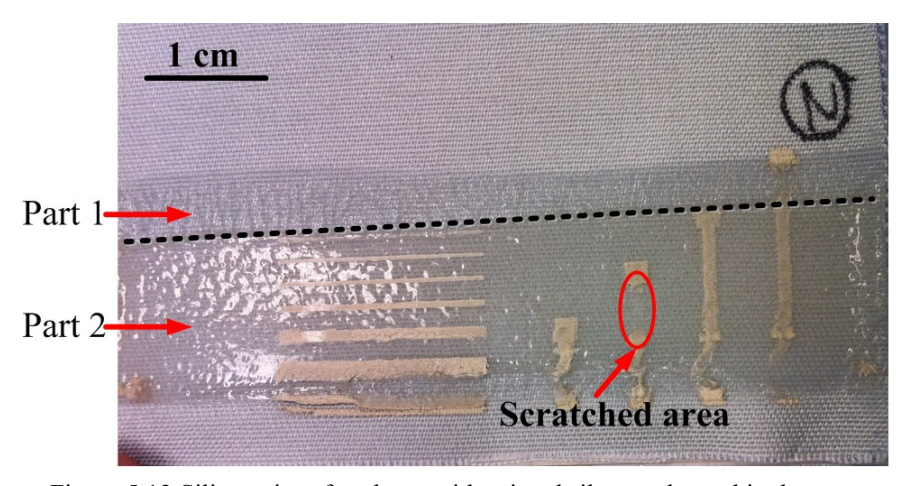


Figure 5.12 Silicone interface layer with printed silver and cured in the oven

For hot plate drying method, the heat flux is from bottom to top of the silicone interface layer. The bottom of silicone layer will be dried first, leaving a not fully cross-linked top surface. The best result with this method is shown in figure 5.13. The quality of adhesion was slightly increased than oven cured samples but can still be scratched off by spatula. The ambient temperature was difficult to control and the thickness of hand printing varied, making the experiments hard to repeat.

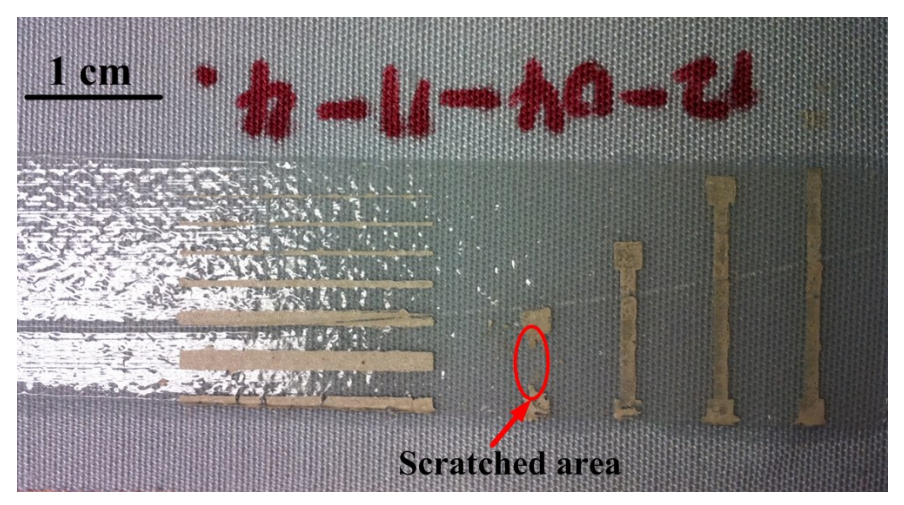


Figure 5.13 Example of hand printed stencil steel sample cured on hot plate

Infrared light drying is advantageous because the drying time is short and can be controlled preciously. But the non-uniformly drying problem of the thick silicone layer still cannot be fixed. In figure 5.14, it can be seen that even the silver electrode pattern cannot be printed completely and some patterns are missing, because the silicone stuck on the back of the screen and blocked the meshes.

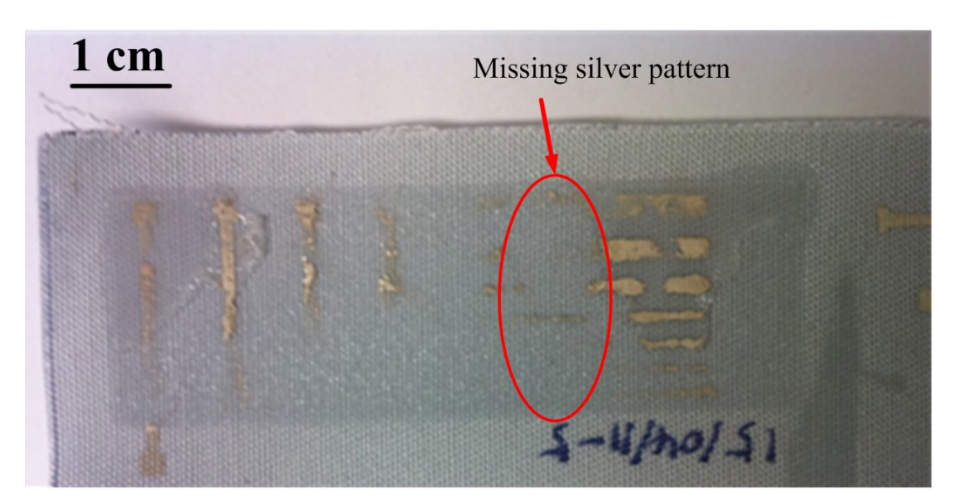


Figure 5.14 Example of IR dried hand stencil printed samples

The silicone interface layer is not dried uniformly for the above 3 samples. The possible reason is that the silicone interface layer is uneven and too thick. Then it is hard to get uniform drying conditions over the large area of silicone pattern.

In order to get a uniform drying condition, proper machine stencil printing was applied to make the silicone interface layer even and reduce the thickness, because a steady force can be applied using a squeegee. However, in figure 5.15, the silicone pattern with one layer deposition is too thin to tell whether the printed silver electrodes are mechanically bound or chemically bound to the silicone layer. Hence, the thickness needs to be built up by drying under the silicone layer for 15 seconds using an IR flash

dryer before another layer is added. In this experiment, all samples were deposited with 7 layers of silicone. The drying conditions listed in table 5.13 are only for the last silicone layer, which is the surface of silicone interface layer. The best quality adhesion obtained by this method is when the drying time is 2-4 seconds. In the experiment, there was still some silicone paste sticking on the silver screen which decreases the amount of silver paste going through the screen mesh.



Figure 5.15 Example of machine stencil steel printed sample, IR dried, 1 layer printed

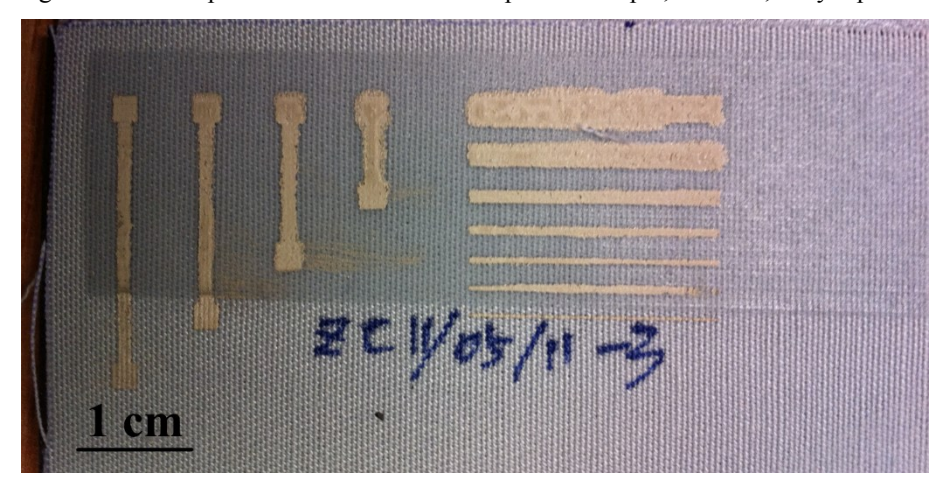


Figure 5.16 Example of IR dried machine stencil printing sample with thickness building up Moreover, the silver pattern on top of the silicone interface layer is not uniform due to the blockage of the mesh screen. Figure 5.17 shows that some areas of the silicone interface layer are not covered by silver paste. Hence, the adhesion problem of the silicone interface layer cannot be solved by decreasing the drying time only. In the future, this solution can be tried by using other deposition method, such as dispenser printing, to avoid silicone paste sticking onto the screen.

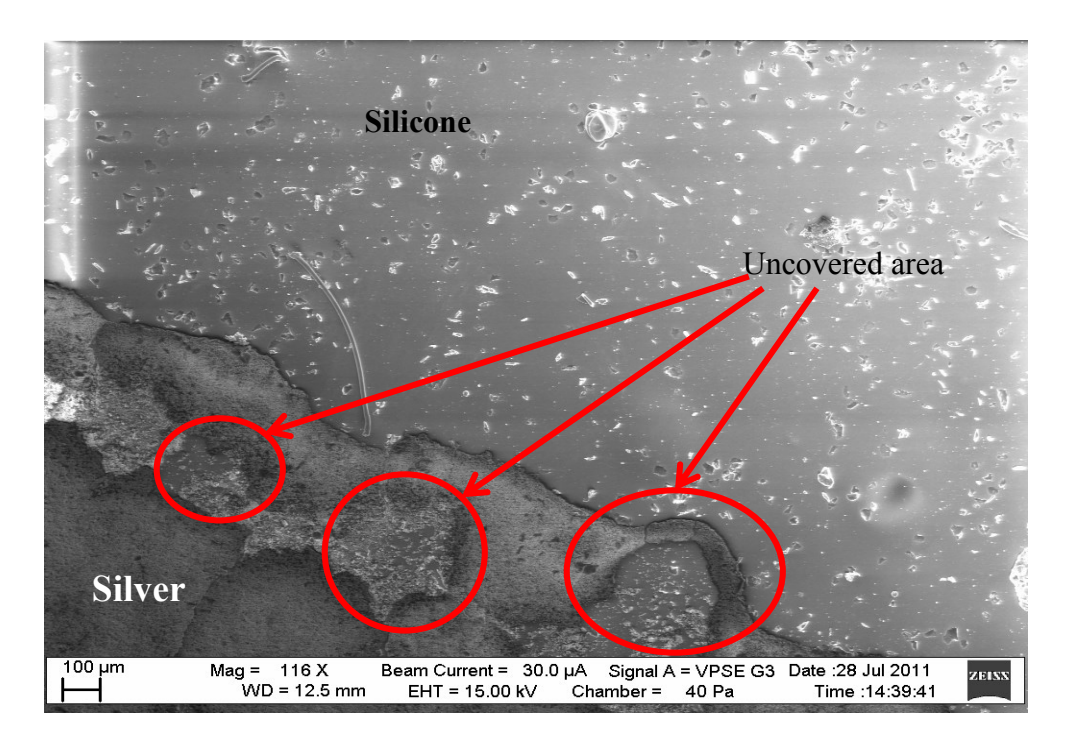


Figure 5.17 Silver electrode layer on non-fully cured silicone interface layer

5.8 Summary and discussion

For the experiment of low temperature Ni/Cu thermocouples, the results demonstrated that the high resistivity of copper and nickel thick films prevented the application on wearable TEGs. Other materials, such as bismuth and antimony, can be tried to improve the thermoelectric performance. This will be discussed in the next chapter.

For the experiment about the adhesion quality of silicone interface layer investigation, it could be seen that a non-fully cured silicone interface layer provides better quality adhesion than a fully cured one, but the silver electrode layer deposition was still hard to realise by screen printing technology. Because once the silicone surface is not fully cured to adhere silver paste, the non-track-free surface has a tendency to stick to the screen of following printings and then the mixture of silver paste and silicone paste will block the meshes.

Direct write printing technologies may solve this problem by avoiding direct contact with the silicone interface layer, which will be considered as a future work for improving the application of TEGs onto textile.

Chapter 6. Screen printing bismuth and antimony based thermocouples

6.1 Introduction

Bulk bismuth (Bi) and antimony (Sb) based thermocouples have a higher Seebeck coefficient than Ni/Cu based thermocouples. The typical Seebeck coefficient of bulk Bi and Sb are -70 μ V/K and 40 μ V/K respectively [19]. Ideally, a thermocouple with Bi as the n-type material and Sb as the p-type material will have a Seebeck coefficient of 110 μ V/K, which means the Bi/Sb thermocouples will have better thermoelectric performance than the Ni/Cu thermocouples. The material cost of Bi and Sb powders is less than their alloy counterparts (bismuth tellurium (BiTe) and antimony tellurium (SbTe) mentioned in chapter 2 [108]). Moreover, there is no screen printable Bi and Sb ink reported in literature. A screen printed Bi/Sb TEG has potential for energy harvesting applications.

6.2 Experimental analysis of screen printed Bi thick films

Bi powders used in this work were sourced from Alfa Aesar with size of 325 meshes and purity of 99.5%. 3M Scotchcast Electrical Resin 280 epoxy was used as the binder system of the Bi paste. For this two parts epoxy binder, the mix ratio of part A to part B is 2:3 by weight. The thinner used was ESL 402 thinner. The approximate ratio of epoxy binder mixture to thinner is 5:2 by weight.

From chapter 4, the experiment has demonstrated that high particle ratios in the paste system will decrease the resistivity of the conductive thick films. Theoretically, the thermoelectric properties of the thick films strongly depend on the amount the active material loaded in the paste. Thus, the particle ratio can be adjusted to be as high as possible to achieve better thermoelectric properties, while ensuring the viscosity of the paste is within the printable range. In this experiment, the powder ratio of the Bi paste was adjusted to 93–94%. Any paste with a powder ratio high than 94% was observed to have a poor screen printing quality.

The samples were hand printed in 1 cm \times 1 cm squares. Each pattern was printed using two layers and with four depositions for each layer. The detailed fabrication conditions of screen printable Bi paste are listed in table 6.1. The samples are printed onto alumina

substrates to verify the performance of the paste. The adhesion of the printed Bi patterns on alumina substrate was good for all samples.

Percentage of Bi by weight	93-94%
Mixing	Triple roll mill
Mesh opening	149 μm
Mesh thickness	130 μm
Layers of printed films	2
Drying condition	100°C, 3min, box oven
Curing condition	250°C, 10min, in N ₂
Substrate	Alumina
Adhesion ¹	9

Table 6.1 Screen printing conditions of Bi paste with epoxy binder

Three different curing temperature, 200°C, 250°C, 270°C and 300°C, were investigated in this experiment. Four samples were cured at each temperature for 10 minutes respectively. The resistivity values of samples cured at different temperature were summarized in table 6.2. The resistivity of Bi thick film cured at 250°C was around 2 orders lower than 200°C cured samples, and the samples cured at 300°C was not conductive.

Curing temperature	200°C	250°C	270°C	300°C	Bulk value
Resistivity (Ω·cm)	1.09-4.11×10 ⁰	7.26-7.27×10 ⁻	N/A	N/A	1.07×10 ⁻⁴

Table 6.2 Resistivity of Bi thick film samples cured at different temperatures compared with bulk value

The outlooks of samples cured at 200°C, 250°C, 270°C and 300°C are shown in figure 6.1. The melting point of Bi is 271°C [16]. Samples cured at 200°C and 250°C were still in films form. When sample cured at 270°C the Bi thick film was easily to be scratched off from the substrate (figure 6.1-(e)), which made the thick film unconducive after polishing. When cured at 300°C, Bi thick film was no longer attached to the substrate. In figure 6.1–(f), the Bi thick film was melted into metallic balls that can be easily wiped off from substrate, which explained why there was no conductivity for this sample. Moreover, the samples annealed at 250°C results less defects than those cured at 200°C, which reduces the resistivity [61]. Hence, the chosen curing condition for Bi paste was 250°C for 10 minutes in nitrogen atmosphere.

¹ Scale: 10-exellent; 1-very poor. The same condition will be applied in the following tables in this chapter.

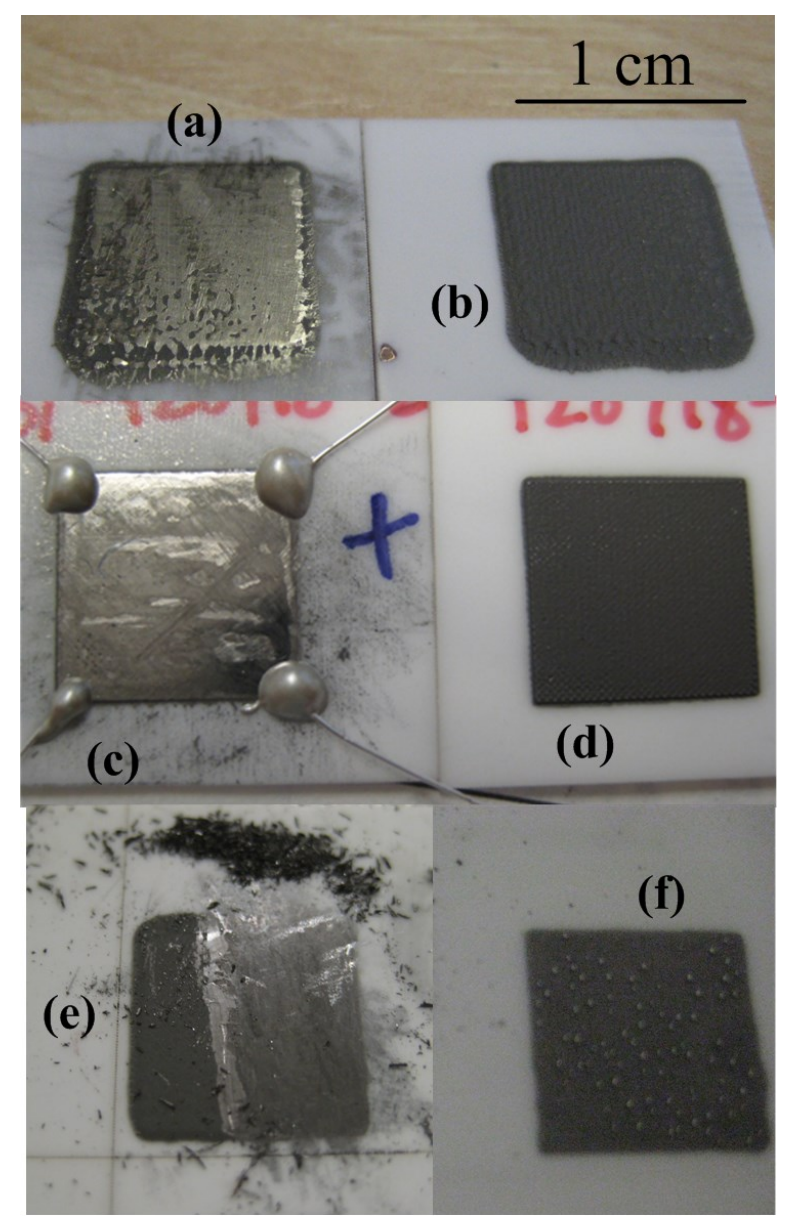


Figure 6.1 Bi thick film samples (a) 200°C cured, polished, (b) 200°C cured, unpolished, (c) 250°C cured, polished, (d) 250°C cured, unpolished, (e) 270°C cured sample after polish, (f) 300°C cured.

The cured Bi thick film samples were not conductive when tested using a multimeter. A possible reason is that the heavy bismuth powders sunk down to the bottom of the pattern during the printing process, leaving a non-conductive epoxy matrix on top of the paste. By polishing the sample, the top epoxy polymers are removed from the Bi pattern surface, leaving a metallic lustre (seen in figure 6.1–(a), (c)). After polishing the sample became conductive, measured using a FLUKE multimeter.

Table 6.3 gives the weight ratio of carbon (C), Oxygen (O) and Bi on polished and original Bi thick film surface. The weight ratio percentage test was completed using a INCA Energy-dispersive X-ray spectroscopy (EDX) test system.

Element	Weight % on unpolished surface	Weight % on polished surface
С	38.02	23.24
0	5.77	7.42
Bi	53.57	66.67

Table 6.3 Elements ratio on Bi thick film surface before and after polish

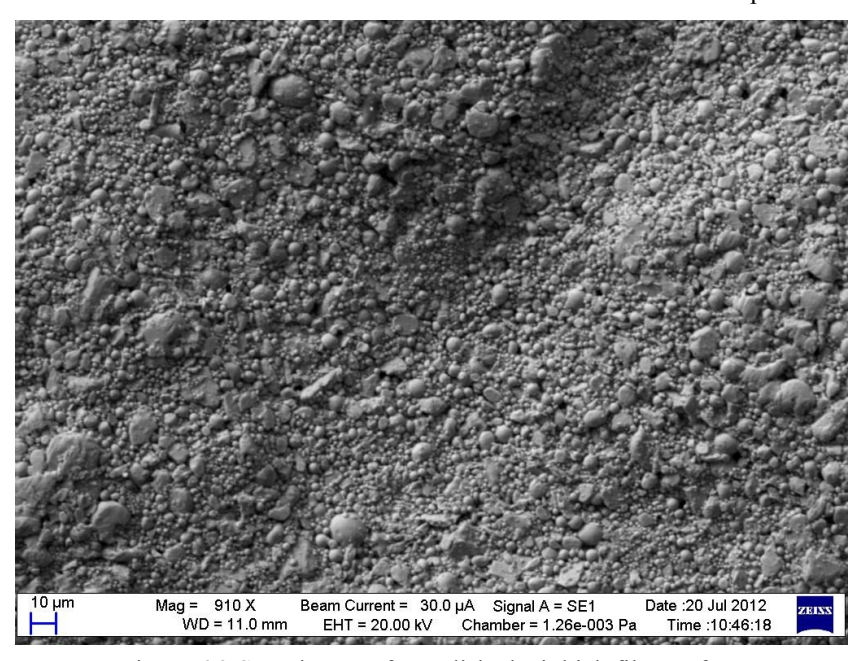


Figure 6.2 SEM image of unpolished Bi thick film surface

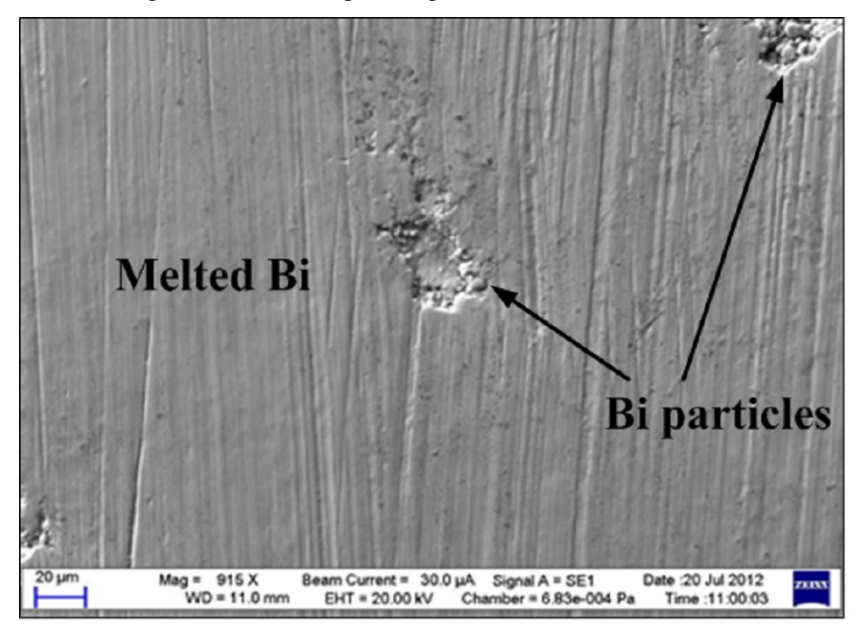


Figure 6.3 SEM image of polished Bi thick film surface

From figure 6.2 it can be seen that the unpolished surface was rough and the individual particles can be clearly observed. In the image of the polished Bi surface (figure 6.3), it can be seen that Bi powders were melted and turned into a continuous metal like material in one piece. In only a few areas the particle shapes of the Bi powders can be recognised. The samples were cured at 250°C, which is below the melting point of Bi,

however the particles were melted. This can be explained by the melting-point depression phenomenon, which means the melting temperature of particles will reduce with the reduction of the solid particle size dimension [109, 110]. The curing temperature of Bi thick films should not exceed 271°C to prevent it melting into small metallic balls because of the melting-point depression.

The Hall effect measurements were carried out on polished samples, corners of which were glued to conductive wires with silver epoxy (ITW Chemtronics CW2400-A).

As shown in table 6.4, the carrier concentration of Bi thick film is much lower than copper and nickel. This is because the Bi is a semi-metal, hence the resistivity was much higher than screen-printed high-temperature copper and nickel samples. Also, a higher curing temperature increased the carrier mobility in the Bi thick film, which made the resistivity decrease.

Values of screen printed Bi thick film 200°C cured				
	Minimum	Maximum	Average	
Carrier concentration (cm ⁻³)	-4.63×10 ¹⁷	-7.71×10 ¹⁶	-3.22×10 ¹⁷	
Mobility (cm ² /(V·m))	7.67×10^{0}	1.98×10 ¹	1.21×10^{1}	
Resistivity (Ω·cm)	1.09×10^{0}	4.09×10^{0}	2.43×10^{0}	
Hall coefficient (cm ³ /C)	-1.35×10 ¹	-8.01×10 ¹	-2.85×10 ¹	
Values of screen printed Bi thick film 250°C cured			ured	
Carrier concentration (cm ⁻³)	-4.30×10 ¹⁷	-3.19×10 ¹⁷	-3.07×10 ¹⁷	
Mobility (cm ² /(V·m))	3.02×10^2	4.62×10^{2}	3.80×10^{2}	
Resistivity (Ω·cm)	4.81×10 ⁻²	4.88×10 ⁻²	4.53×10 ⁻²	
Hall coefficient (cm ³ /C)	-1.96×10 ¹	-1.45×10 ¹	-1.70×10 ¹	
Bulk va	Bulk values in room temperature			
Carrier concentration (cm ⁻³)	N/A	N/A	-2.2×10 ¹⁸ [19]	
Mobility (cm ² /(V·m))	N/A	N/A	N/A	
Resistivity (Ω·cm)	N/A	N/A	1.07×10 ⁻⁴ [16]	
Hall coefficient (cm ³ /C)	N/A	N/A	N/A	

Table 6.4 Transport properties of Bi thick films

The Seebeck coefficient of Bi thick film was measured using a bespoke machine and the results are listed in the table below. The Seebeck coefficient for the Bi thick film was 16% smaller than the bulk value.

Range of Seebeck coefficient (µV/K)	- 60 ∼ - 57
Average Seebeck coefficient value ($\mu V/K$)	-58.7
Reduction compared with bulk value	16%

Table 6.5 Experiment Seebeck coefficients of Bi thick film sample

6.3 Experimental analysis of screen printed Sb thick films

The binder system of the Sb paste in this experiment was the same as that used in screen printable Bi paste, including the thinner. Because the density of Sb powders (6.697 g/cm⁻³) is lower than that of Bi powders (9.78 g/cm⁻³) [16], the maximum ratio of Sb powders in a screen printable Sb paste with the same binder system in this experiment was 90%. The approximate ratio of epoxy binder mixture to thinner is 5:3 by weight.

The surface of the Sb thick film was conductive without polishing after curing at the same conditions as the Bi paste. Figure 6.4 shows the surfaces of unpolished (left) and polished (right) Sb thick film surface.

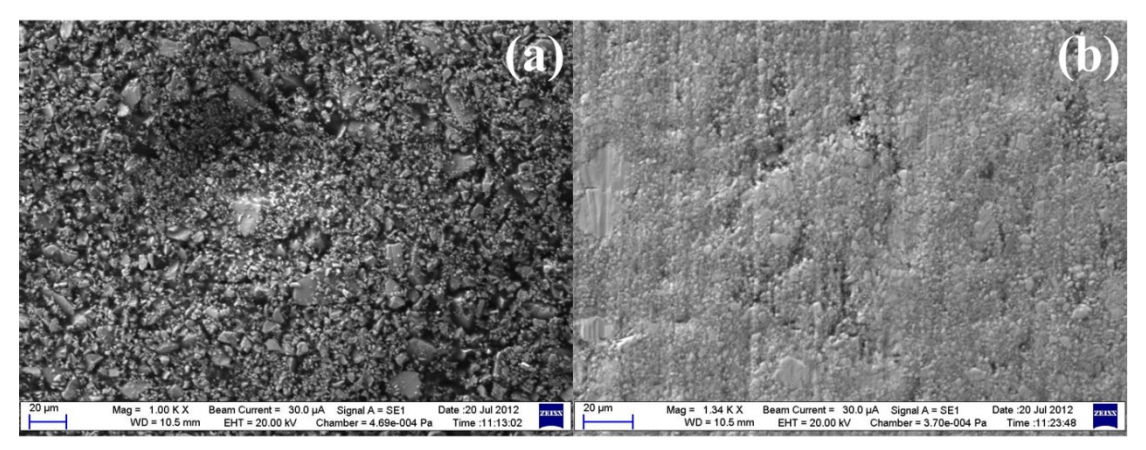


Figure 6.4 Surface SEM images of Sb thick films. (a): unpolished; (b): polished

For the unpolished Sb film surface, the boundaries of Sb particles were shaper than that of the polished Bi film surface. After polishing, most Sb grains can still be recognized clearly. The boundaries between the Sb grains revealed that the curing temperature can still be increased to get a better electric conductivity for the Sb thick film.

To optimise the curing temperature of the Sb thick film, the printed samples were cured at four different temperatures: 250°C, 270°C, 350°C and 450°C. All these chosen curing temperatures were below the melting point of Sb, which is 630.6°C [16], avoiding the printed films melting into balls. The curing temperature of 270°C was initially chosen to investigate whether both Sb and Bi samples could anneal together. The detailed fabrication conditions are listed in table 6.6.

Percentage of Sb by weight	90%				
mixing		Triple roll mill			
Mesh opening		149	μm		
Mesh thickness		130	μm		
Screen Printing ability		printable			
Layers of printed films	2				
Drying condition	100°C, 3min, box oven				
Curing condition	250°C, 10min, in N ₂	270°C, 10min, in N ₂	350°C, 10min, in N ₂	450°C, 10min, in N ₂	
Substrate	Alumina				
Adhesion	10	10 9 5 2			

Table 6.6 Screen printing conditions of Sb paste with epoxy binder

Physical properties	Minimum value	Maximum value	Average value	
Sample 1: 250°C cured				
Carrier concentration (cm ⁻³)	5.95×10 ¹⁸	6.94×10^{19}	3.35×10^{19}	
Mobility (cm ² /(V·m))	3.11	36.4	16	
Resistivity (Ω·cm)	2.89×10 ⁻²	2.90×10 ⁻²	2.89×10 ⁻²	
Hall coefficient (cm ³ /C)	8.99×10 ⁻²	1.05×10^{0}	4.62×10 ⁻¹	
Seebeck coefficient (µV/K)	15	23	18.5	
	Sample 2: 270°C			
Carrier concentration (cm ⁻³)	1.17×10^{20}	1.80×10^{20}	1.38×10^{20}	
Mobility $(cm^2/(V \cdot m))$	28	43.4	37.7	
Resistivity (Ω·cm)	1.24×10 ⁻³	1.24×10 ⁻³	1.24×10 ⁻³	
Hall coefficient (cm ³ /C)	3.46×10 ⁻²	5.36×10 ⁻²	4.67×10 ⁻²	
Seebeck coefficient (µV/K)	25.1	28.7	27.6	
	Sample 3: 350°C			
Carrier concentration (cm ⁻³)	1.24×10^{20}	1.48×10^{20}	1.34×10^{20}	
Mobility $(cm^2/(V \cdot m))$	58.5	73.6	65.3	
Resistivity (Ω·cm)	7.14×10 ⁻⁴	7.22×10 ⁻⁴	7.18×10 ⁻⁴	
Hall coefficient (cm ³ /C)	4.22×10 ⁻²	5.30×10 ⁻²	4.69×10 ⁻²	
Seebeck coefficient (µV/K)	23	25	24	
Sample 4: 450°C cured				
Carrier concentration (cm ⁻³)	8.99×10 ¹⁹	1.20×10^{20}	1.06×10^{20}	
Mobility $(cm^2/(V \cdot m))$	42.4	61.9	53	
Resistivity (Ω·cm)	1.12×10 ⁻³	1.12×10 ⁻³	1.12×10 ⁻³	
Hall coefficient (cm ³ /C)	5.19×10 ⁻²	6.94×10 ⁻²	5.93×10 ⁻²	
Seebeck coefficient (µV/K)	26.6	27.1	26.8	
Bulk values in room temperature				
Carrier concentration (cm ⁻³)	N/A	N/A	$4.2 \times 10^{19} [19]$	
Mobility $(cm^2/(V \cdot m))$	N/A	N/A	N/A	
Resistivity (Ω·cm)	N/A	N/A	3.9×10 ⁻⁵ [16]	
Hall coefficient (cm ³ /C)	N/A	N/A	N/A	
Seebeck coefficient (µV/K)	N/A	N/A	40	

Table 6.7 Transport properties of Sb screen printed samples

The resistivities of the Sb thick film samples cured at different temperatures are shown in table 6.7. Generally, a higher curing temperature lead to a lower resistivity of the Sb pattern. The resistivity of sample 2 was over 2000% lower than that of sample 1 and the Seebeck coefficient of sample 2 was 50% higher than sample 1. For sample 3 and 4, compared with sample 2, the maximum electrical resistivity decrease was 50% and the Seebeck coefficient had no improvement.

Based on the research in chapter 4, 350°C was the best choice to get maximum Z value because sample 3 had the lowest resistivity. However, for printed thick films, the adhesion onto substrate is another factor to be considered for practical applications. In figure 6.5, Sb thick films can be easily scraped off by using a spatula after curing at 350°C and 450°C, while only small amount of powder on the top surface came off for samples 1 and 2. The surface scraping was done on all substrates in the same conditions using a flat stainless steel spatula. The reason some samples showed low adhesion was the curing temperature was too high and caused the epoxy binder to decompose.

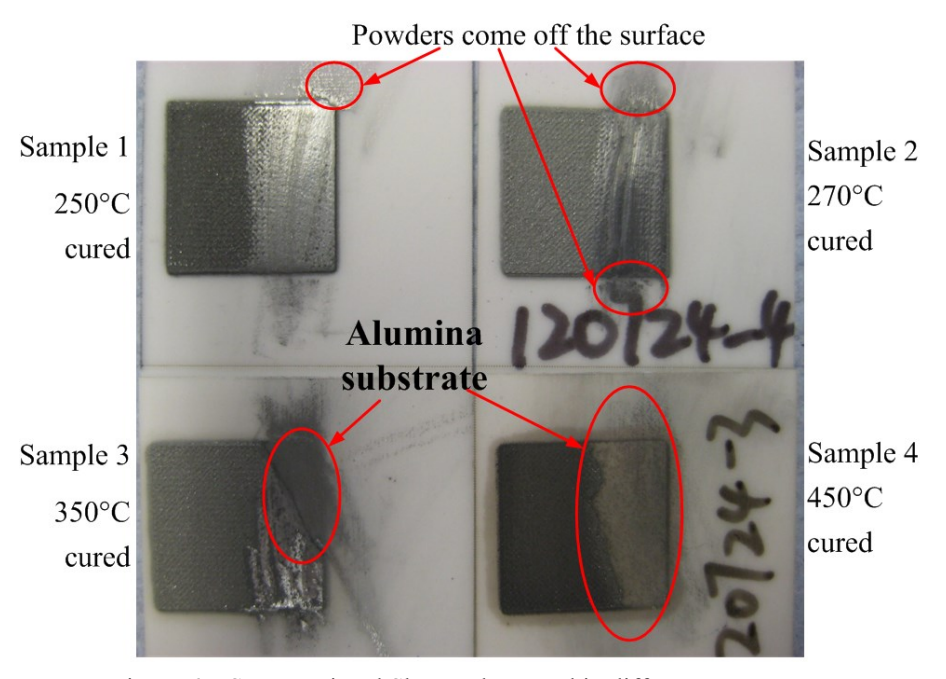


Figure 6.5 Screen printed Sb samples cured in different temperature

Although more powders came off from sample 2 than sample 1, the quantity that remained on both was acceptable. Hence, the curing condition for Sb paste was chosen to be 270° C 10 minutes in N₂.

6.4 Bismuth and Antimony based thermocouples

For printed Bi thick films on Kapton substrates, it was found to be very easy to crack the printed layer after curing when bending after curing. In figure 6.6-(a), the unpolished Bi thick film cracked after peeling the Kapton substrate off the alumina holder. Here, the average thickness of the screen printed samples is $78.2 \, \mu m$ ($58.2 - 116 \, \mu m$). When bending it around a ball pen with a diameter of 13 mm, more cracks appeared on both polished and unpolished samples (figure 6.6-(b)). The cracking is caused by the material properties of bismuth - which is a brittle material and easy to crack when the printed pattern is melted [111].

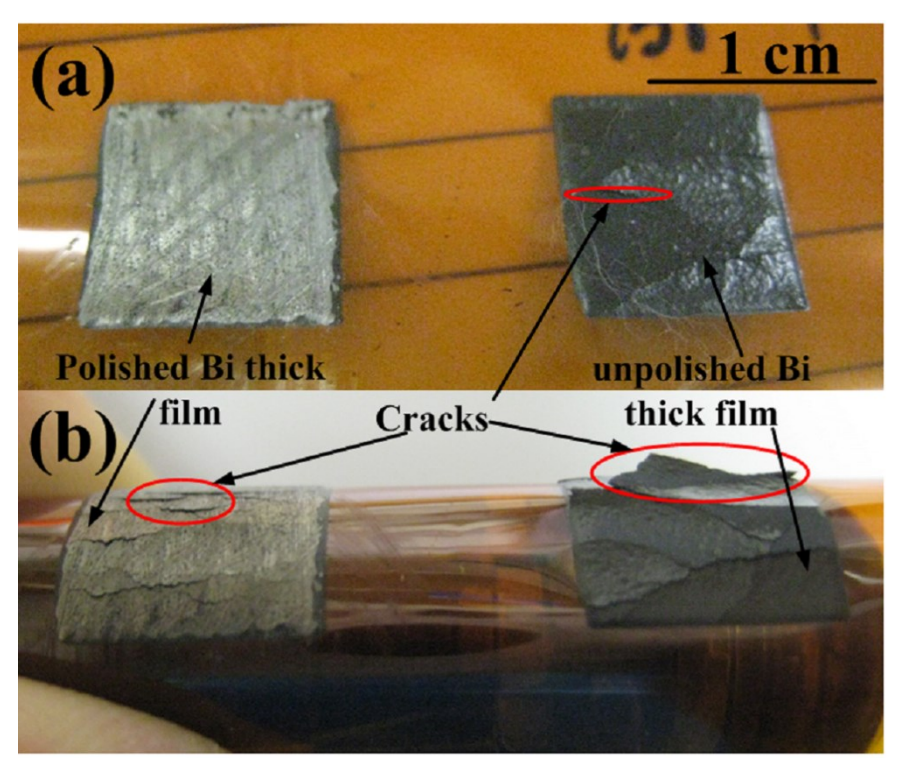


Figure 6.6 Cracking of Bi thick films when (a) peeling off Kapton from alumina holder, (b) rolling on a ball pen with diameter of 13 mm

Hence, the Bi/Sb thermocouples were printed onto an alumina substrate. The fabrication process is shown in figure 6.7. The silver paste used in this experiment is the same as the silver used in previous chapters.

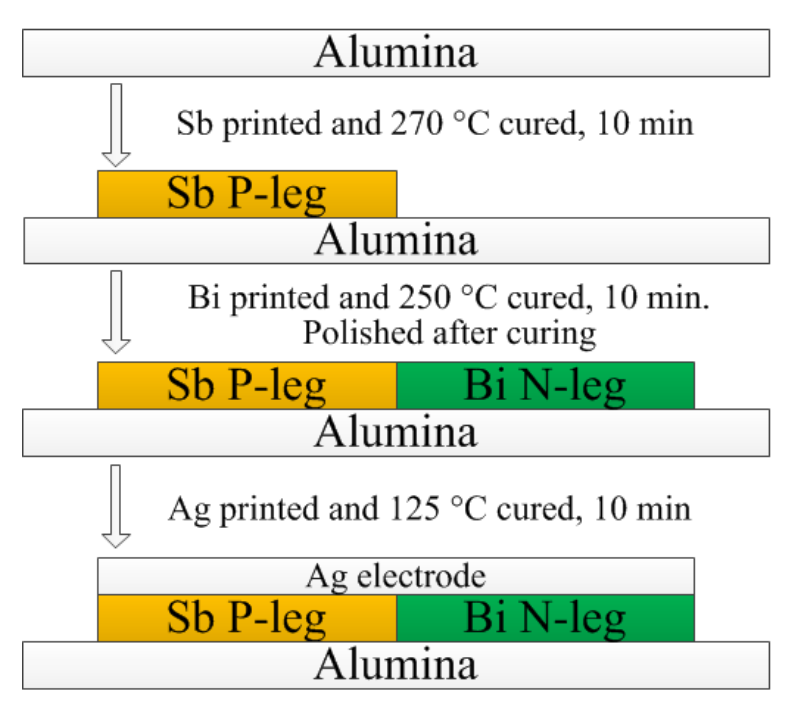


Figure 6.7 Fabrication process of screen printed Bi/Sb thermocouples

The patterns size of printed Bi/Sb thermolegs was the same as Cu/Ni thermocouples. The thickness varied because of the different paste viscosities. The average thickness of Bi thermolegs after polishing was $105.2 \mu m$, while that of Sb thermolegs was $78.9 \mu m$. The printed sample is shown in figure 6.8.

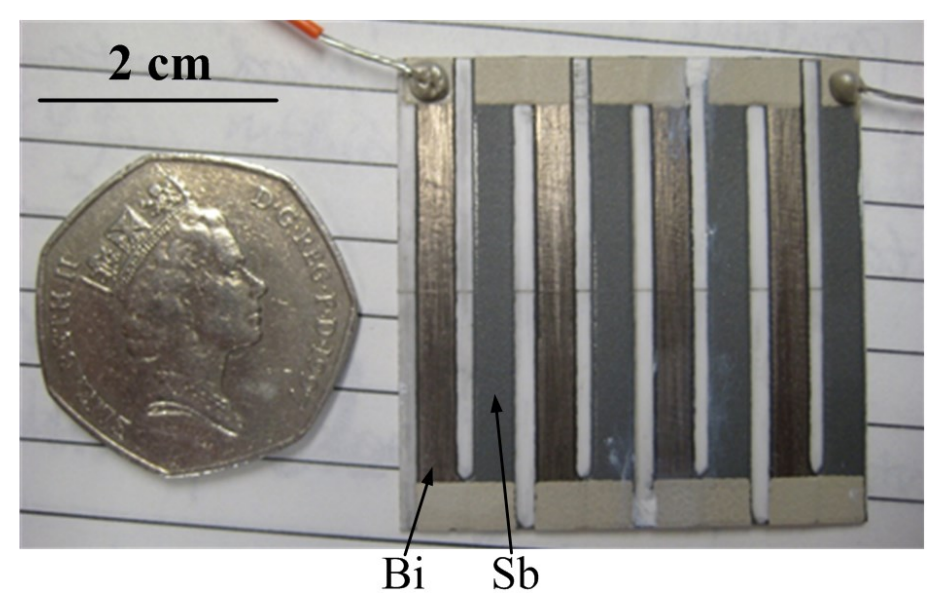


Figure 6.8 Screen printed 4 Bi-Sb thermocouples

The voltage and current generated by these four thermocouples in a variety of temperature gradients is shown in figure 6.9. The relationship between the open circuit voltage and temperature gradient can be considered as linear, a similar conclusion can be made for I and ΔT .

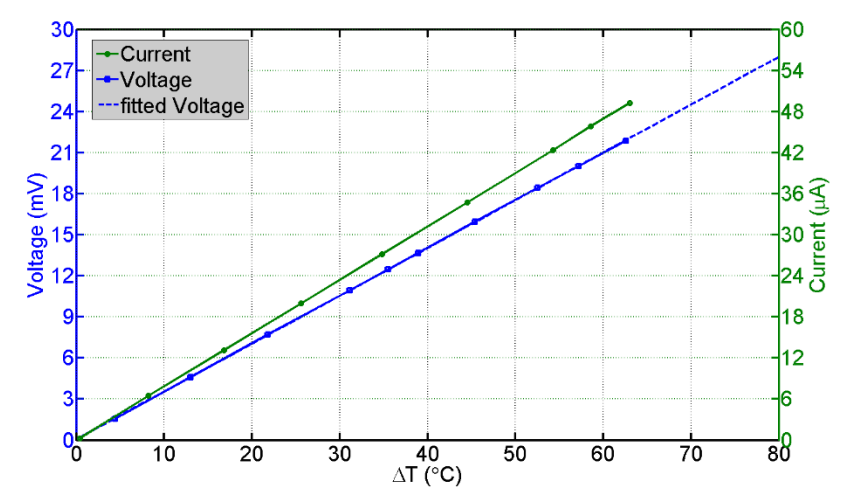


Figure 6.9 Generated open circuit voltage and current of 4 printed Bi-Sb thermocouples

At a temperature gradient of 60° C, 4 Bi-Sb thermocouples can generate a voltage of 21 mV and a current of 45 μ A, approximately 5 mV and 11 μ A for a single thermocouple. The generated open circuit voltage (V) for individual Bi-Sb thermocouples is higher than the Cu-Ni ones, which are about 1.5 mV. However, the generated current I for single Cu-Ni thermocouples in chapter 5 is about 14 μ A, which is higher than the Bi-Sb sample. The high resistivity of both Bi and Sb thick films limited high current from being generated by the device.

The temperature gradients set to measure the power output of these 4 thermocouples were 20°C (figure 6.10) and 40°C (figure 6.11) respectively. Based on the same voltage fitting regulation described in chapter 4, the power vs. load resistor figures clearly show the maximum power output in the chosen range of load resistance.

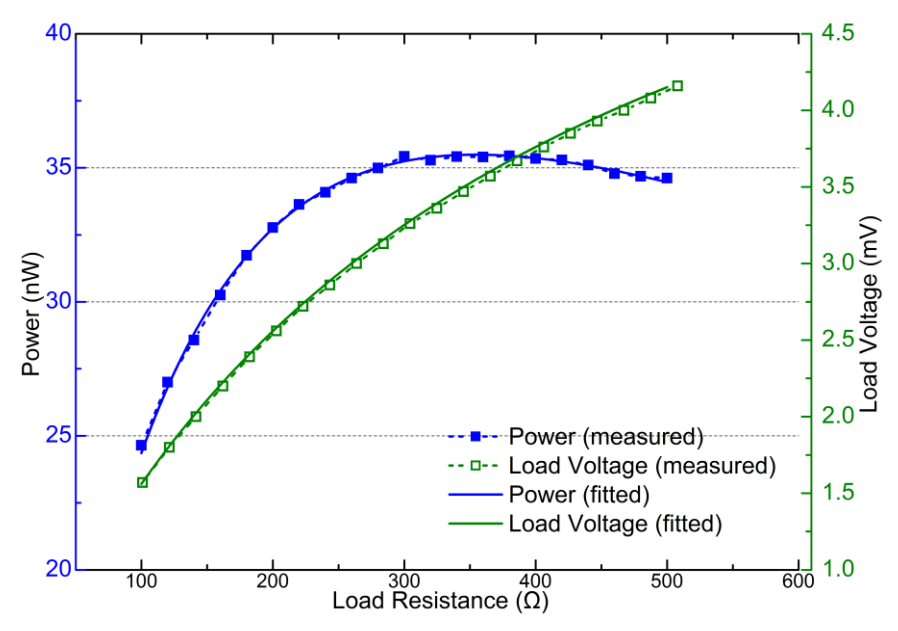


Figure 6.10 Power output and voltage over the load resistor of the 4 Bi-Sb thermocouples as a function of load resistance at a 20K temperature difference

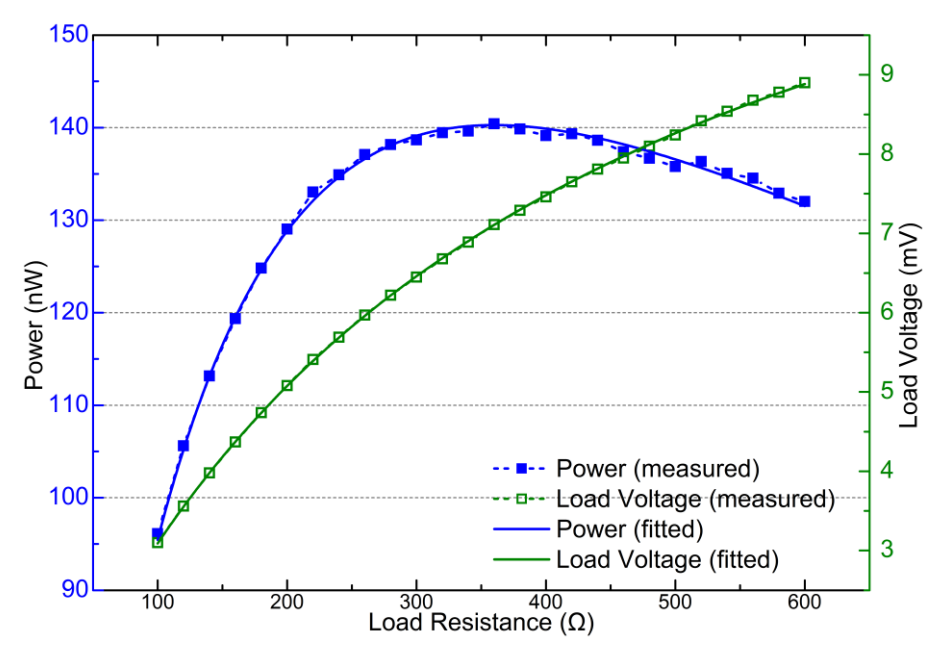


Figure 6.11 Power output and voltage over the load resistor of the 4 Bi-Sb thermocouples as a function of load resistance at a 40K temperature difference

The resistance, the maximum power output and the calculated Seebeck coefficient of Bi/Sb thermocouples are concluded in table 6.8. It can be seen that in higher ΔT , the resistance of the TEG is higher than that in the lower ΔT . This is because the resistivity of metals will increase with an increasing surrounding temperature.

	ΔT=20°C	ΔT=40°C
Resistance for 4 thermocouples (Ω)	354.6	360.1
Resistance for 4 thermocoupies (22)	(351.6 - 357.6)	(356.8 - 363.4)
Resistance for single thermocouple (Ω)	88.65	90.00
Resistance for single thermocoupie (\$2)	(87.9 - 89.4)	(89.2 - 90.85)
Maximum power output for 8	35.49	140.28
thermocouples (nW)	33.47	140.26
Maximum power output for single	8.87	35.07
thermocouples (nW)	0.07	33.07
Calculated α _{Bi/Sb} from Seebeck voltage	87	28
measurement ($\mu V/K$)	07.	20
Calculated $\alpha_{Bi/Sb}$ from close-loop power	88.69	88.88
output measurement ($\mu V/K$)	(88.3 - 89.05)	(88.44 - 89.25)

Table 6.8 Summarize of calculated values from Seebeck voltage and power output measurements with different temperature difference of 4 Bi/Sb thermocouples

The $\alpha_{Bi/Sb}$ value calculated from the sum of individual materials is 86.3 μ V/K from section 6.2 and 6.3. Compared with the values calculated from the Seebeck voltage measurement and the power output measurement of the device, it has an error range of 1.1% and 3.0%. The small error range demonstrated that the Seebeck voltage and power output setup is promising for the measurements.

6.5 Safety handling and processing in experiment

Bismuth and antimony are naturally oral, inhalation and dermal harmful for human body [112], especially in powder form, due to the high risk of inhalation. Thus, a shot guidance for handling and processing is necessary in this section.

For handling, in order to avoid contact with skin and eyes and avoid formation of dust and aerosols, appropriate exhaust ventilation facilities mush be provided at where the dust is potentially formed. Specifically, before BiTe is mixed into paste form, all the processed mush be done in the fume cabinet and dust mask must be wear all the time. After the powders were made into pastes the polymers would hold the particles prevent them turning into dust. The pastes could then be processed out of the fume cabinet. General clean room clothes must be wear all the time, including the heir cover and gloves. Double gloves is helpful when processing these materials. Once the outer gloves are dirty, they can get changed fast to avoid contamination.

For storage, the powders must be stored in tightly closed containers and putted in a dry and well-ventilated place, where should be cool.

For disposal, all wasted wipes and containers with toxic materials attached should go into sealed bags with name and quantity on it. When the toxic waste bin is full, contact a licensed professional waste disposal service to dispose of this material.

These handling and processing rules can be also applied to bismuth telluride and antimony telluride powders in next chapter.

6.6 Summary and discussion

In this chapter, screen printable Bi and Sb pastes with polymer binder were synthesised. The Seebeck coefficient and transport properties of printed films were also measured. The cross-section SEM images of Bi and Sb thick films after curing at optimised conditions are shown in figure 6.12. In the Bi thick film, more particles were melted into small balls compared with the Sb counterpart. The balling phenomenon happens with the decrease of free energy, but the formation process and mechanism are complicated and not currently understood [113]. In addition, the epoxy matrix among Sb particles can be observed more clearly from the Sb SEM image than the Bi thick film, because the ratio of polymer binder in Sb paste is higher than that in the Bi paste.

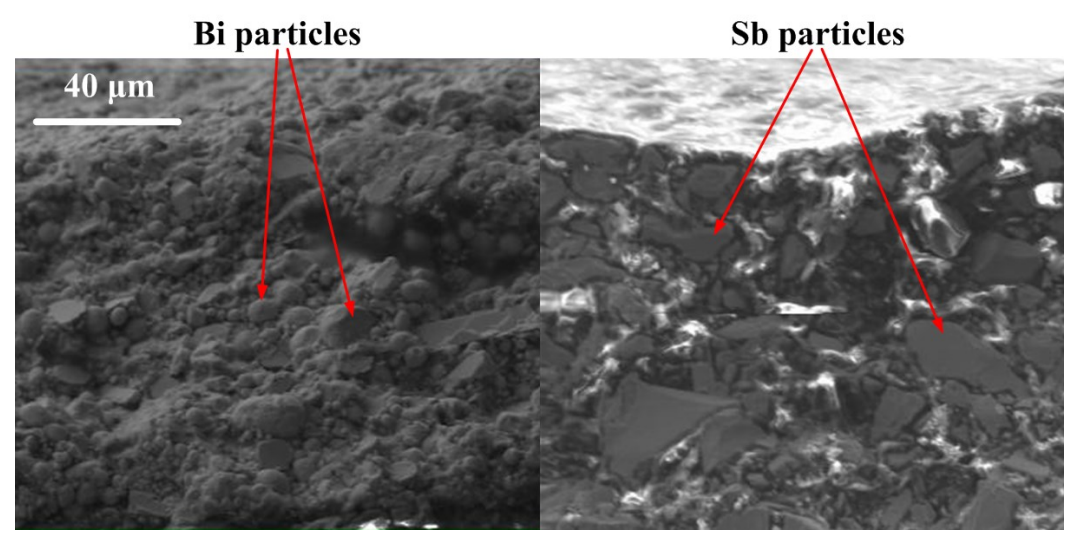


Figure 6.12 Cross section image of Bi and Sb thick films

The resistivity and Seebeck coefficient changes when compared with bulk values are shown in table 6.9. It can be seen that the resistivity of Bi thick film increased much more than the Sb thick film when compared to the bulk values. Two reasons could explain this larger change. First, the balling phenomenon increased the voids between Bi particles, which decreased the Ohmic contact area of adjacent particles then increased the resistivity. Secondly, Bi has a strongly oxidizing nature in comparison with Sb [114, 115]. Hence, the same fabrication process will lead to a larger variation in resistivity of Bi compared with Sb.

	Bi	Sb
Particles percentage in paste	93-94%	90%
Resistivity changes	42200%	3080%
Seebeck coefficient changes	16%	31%

Table 6.9 The changing ratios in percentage between experiment values and bulk values of Bi and Sb From the above table, the variation of the Bi Seebeck coefficient was smaller than that of the Sb value. The paste with a higher powder percentage had a smaller deviation of Seebeck coefficient.

The maximum output power appeared when the load resistance matched the TEGs resistance. In chapter 4, at a temperature difference of 40°C, a single Cu-Ni thermocouple can generate an output power of 42.96 nW over a resistance of 4.44 Ω . For a single Bi-Sb thermocouple above in this chapter, the generated power is 35.07 nW over a resistance of 90 Ω . From a voltage point of view, at a temperature difference of 40°C, 3.5 mV was generated by a single Bi/Sb thermocouple while 0.99 mV was generated by single high temperature cured Ni/Cu thermocouple. According to P=V²/R,

a larger increasing in R than V^2 would decrease the power output of the device, even the generated voltage increased.

In conclusion, this experiment demonstrated that screen printable pastes with an epoxy binder are promising in the application of printed low temperature TEGs on alumina substrate. Moreover, the polymer binder potentially allows the printed thick films to bend when printed on a flexible substrate. Hence, it is worth attempting to use BiTe & SbTe based pastes to achieve flexible TEGs for energy harvesting applications because they have been proven to have highest figure of merit value at room temperature range from chapter 2.

Chapter 7. Screen-printed flexible BiTe/SbTe based thermoelectric generator

7.1 Introduction

The fabrication and testing of Bismuth Telluride (BiTe) – Antimony Telluride (SbTe) based flexible TEGs using screen printing technology are described in this chapter. From previous studies, the chosen epoxy binder system has been proven to be suitable for use in low temperature TEGs, which demonstrated the feasibility for pastes with this binder to be used on flexible substrates, e.g., Kapton. In this study, screen printable BiTe and SbTe pastes were developed and the transport properties of the thick films were measured.

7.2 Development of the screen printable BiTe and SbTe paste

The screen printable thermoelectric pastes reported here contains thermoelectric materials Bi₂Te₃ and Sb₂Te₃ alloy powders and an epoxy binder system. A solvent was also added to the paste to decrease the viscosity to a screen printable level. The binder system and solvent for the pastes in this chapter are the same as those in the last chapter.

N-type BiTe alloy normally exists as a composition of Bi₂Te₃, the ratio of Te affects the thermoelectric performance of the device. When the atomic ratio of Te is 64%, the BiTe alloy will have the highest Z value with negative Seebeck coefficient [116]. From figure 8.1 it can be seen that when the Te content is below 62%, BiTe alloy is p-type. When the Te ratio is higher than 62%, there is also a figure of merit variation with Te content. The actual formulation of this n-type semiconductor material is Bi_{1.8}Te_{3.2}.

For p-type Sb_2Te_3 , the alloy only shows p-type thermoelectric properties. The $Bi_{1.8}Te_{3.2}$ and Sb_2Te_3 powders are from Testbourne Ltd, with the size of 325 mesh (average 44 μ m) and a purity of 99.99%.

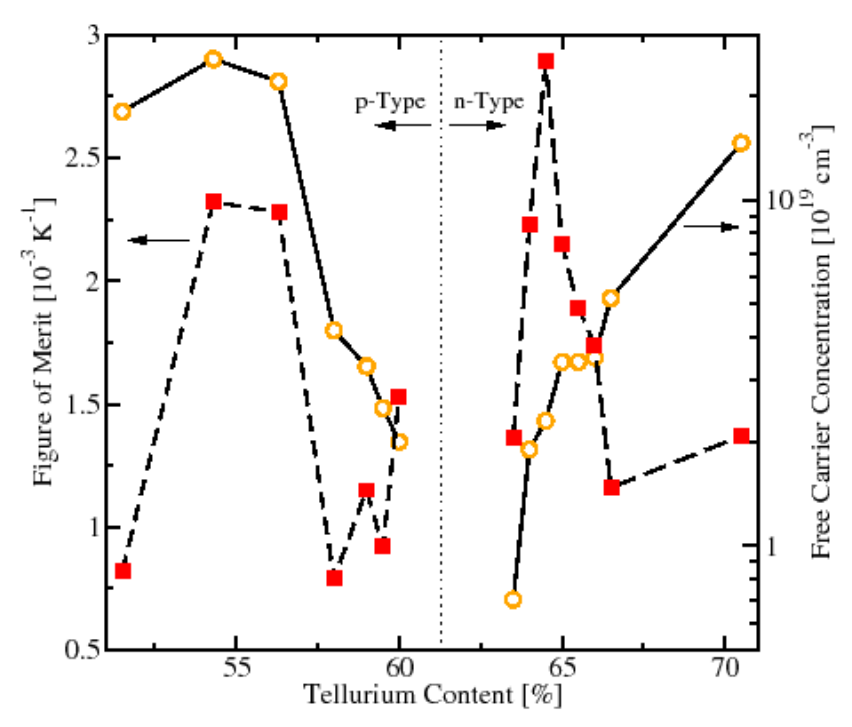


Figure 7.1 Free carrier concentration as well as figure of merit with respect to material composition for Bi_2Te_3 [116]

The ratio of the compositions in the pastes were based on the trade-off between the printability and the highest thermoelectric properties, which was described in chapter 6. The densities of BiTe and SbTe are 7.62 g/cm³ and 6.5 g/cm³ respectively [16]. Hence, the ratio by weight of BiTe in the paste was higher than that of SbTe in order to achieve a screen printable viscosity range.

Particles fillers in pastes	Bi _{1.8} Te _{3.2}	SbTe
Density of particles (g/cm ³)	7.62	6.5
Melting point of particles (°C)	585	580
Percentage of Bi by weight	93%	90%
Mixing	Triple roll mill	
Mesh opening	149 μm	
Mesh thickness	130 μm	
Layers of printed films	2	
Drying condition	80 °C, 3min, box oven	
Curing condition	250 °C, 3 hours, in N ₂	
Substrate	Kapton	
Adhesion*	9 - 10	
*Scale: 10-exellent; 1-very poor. The same scale will be applied in the following tables in this chapter.		

Table 7.1 Conclusion of fabricating conditions of BiTe and SbTe pastes

From the literature, the powder based BiTe and SbTe thermoelectric materials were thermally cured at temperature from 250 °C to 350 °C for minimum 3 hours [59-62, 117, 118]. Hence, based on the literatures, 4 different curing temperatures (250°C,

270°C, 300°C, 350°C) were tried to find the optimized curing condition. 4 samples were cured under each curing condition.

In the experiment, when the curing temperature was higher than 300 °C for 3 hours, cracks could be visually observed and the deposited powder and binder compositions were easily scratched from both polyimide and alumina substrates. Patterns cured at 350 °C even peeled off when bending. In figure 7.2-(b), the quality of adhesion of samples cured at different temperatures was illustrated. When BiTe samples were cured at 270 °C, the patterns could be scratched off from the substrate under the same conditions as in chapter 5 (figure 7.2-(c) and (d)). Hence, the thermoelectric materials in this experiment were cured at 250 °C for 3 hours.

In this section, 1 cm \times 1 cm square samples were printed and tested. The thickness of the samples varied from 70 μ m to 130 μ m. The test equipment was the same as those applied in last chapter.

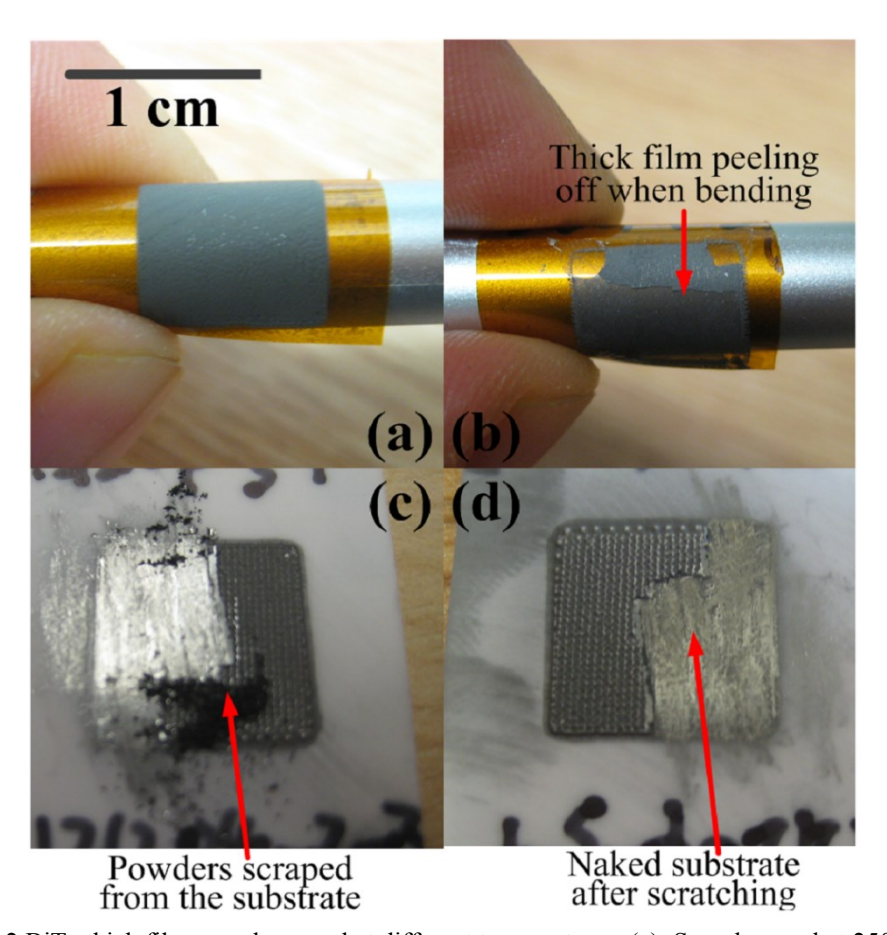


Figure 7.2 BiTe thick film samples cured at different temperatures. (a): Sample cured at 250 °C. (b): Sample cured at 350 °C. (c): Most powders were scratched from the alumina substrate for the sample cured at 270 °C. (d): Alumina substrate with a thin melted BiTe layer exposed after scratching for sample cured at 270 °C.

Figure 7.3 shows the surface and cross-section images of BiTe and SbTe thick films, which demonstrates that both pastes were mixed uniformly. However, the voids observed from both the surface and the cross-section of both printed films decreases the density of the material, which increases the resistivity. Moreover, comparing both the surface and cross-section images, there are more voids in BiTe thick film than in SbTe thick film.

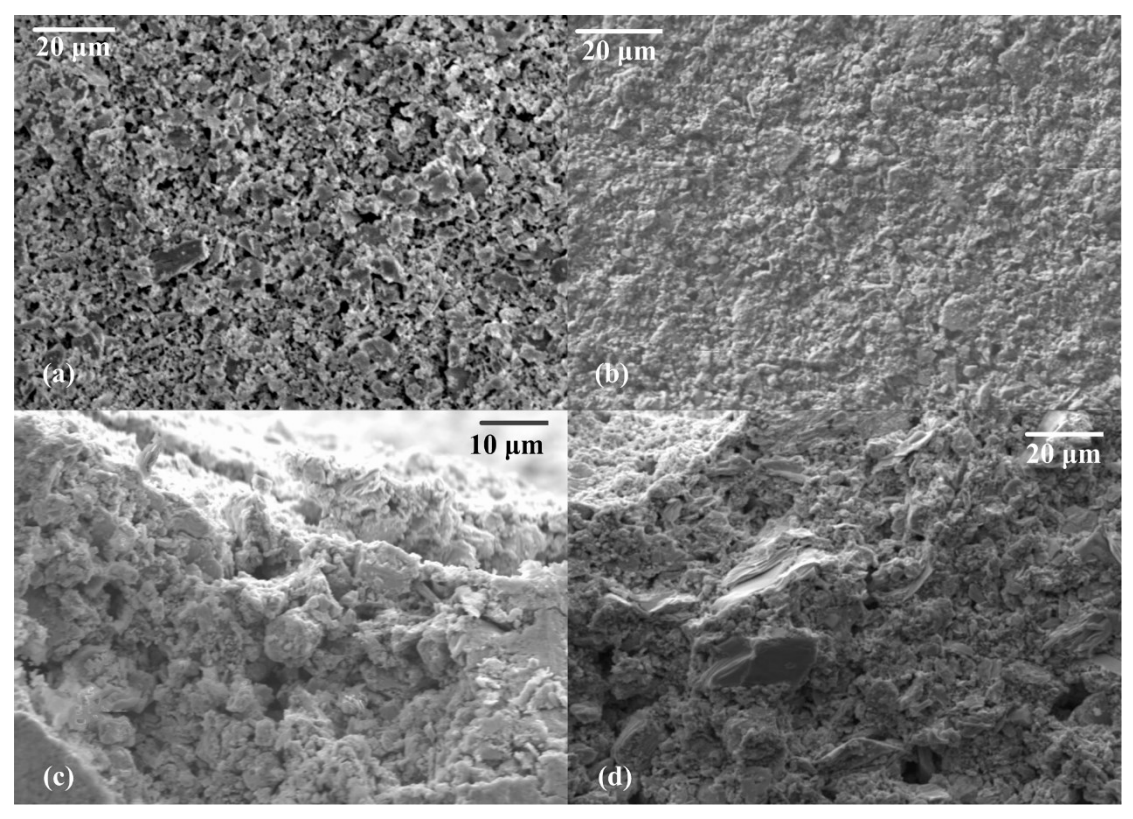


Figure 7.3 SEM images of printed thick films. (a): surface of the BiTe thick film. (b): surface of the SbTe thick film. (c): Cross-section of BiTe thick film. (d): Cross-section of SbTe thick film.

This structural feature can be used to partly explain the increasing resistivity of the thick film materials compared with their bulk values. From table 7.2, the resistivity of BiTe thick films is 215 times higher than its bulk value, while the resistivity of SbTe thick film is 63 times higher than its bulk value.

Values of screen printed Bi _{1.8} Te _{3.2} thick film			
	Minimum	Maximum	Average
Carrier concentration (cm ⁻³)	-1.69×10^{20}	-4.22×10 ¹⁶	-8.89×10^{18}
Mobility $(cm^2/(V \cdot m))$	2.14×10 ⁻²	5.93×10^2	1.69×10^{1}
Resistivity (Ω·cm)	2.35×10 ⁻¹	3.50×10^{0}	5.62×10 ⁻¹
Hall coefficient (cm ³ /C)	-1.48×10^2	-3.69×10 ⁻²	-6.82×10^{0}
Bulk values of Bi ₂ Te ₃ in room temperature			
Carrier concentration (cm ⁻³)	-3.38×10^{19}	-1.02×10^{18}	N/A
Mobility $(cm^2/(V \cdot m))$	2.7×10^3	1.8×10^4	N/A
Resistivity (Ω·cm)	1.4×10^{-3}	3.8×10^{-3}	2.6×10^{-3}
Hall coefficient (cm ³ /C)	N/A	N/A	N/A
Values of screen printed Sb ₂ Te ₃ thick film			
Carrier concentration (cm ⁻³)	9.02×10^{17}	1.17×10^{20}	2.13×10^{19}
Mobility $(cm^2/(V \cdot m))$	2.12×10^{0}	2.59×10^{2}	2.42×10^{1}
Resistivity (Ω·cm)	1.38×10 ⁻²	4.71×10 ⁻²	2.73×10 ⁻²
Hall coefficient (cm ³ /C)	5.36×10 ⁻²	6.92×10^{0}	5.79×10 ⁻¹
Bulk values of Sb ₂ Te ₃ in room temperature			
Carrier concentration (cm ⁻³)	N/A	N/A	1.5×10^{20}
Mobility (cm ² /(V·m))	N/A	N/A	2.7×10^2
Resistivity (Ω·cm)	2.5×10 ⁻⁴	6×10 ⁻⁴	4.3×10 ⁻⁴
Hall coefficient (cm ³ /C)	N/A	N/A	N/A

Table 7.2 Transport properties summary of screen printed BiTe and SbTe thick film with the comparison of their bulk counterpart [23]

Another explanation for the increase in resistivity is the oxidation of the printed thick film. The oxidising nature of the Bi-Sb-Te based alloy powders in open air [119] and the oxidation of BiTe alloy based thick film when annealing [120] both indicated that the resistivity of the printed BiTe and SbTe thick films might be affected by the oxidation problem. In this experiment, the resistivity of both thick-films varied with time (shown in figure 7.4). In 50 days, the $Bi_{1.8}Te_{3.2}$ thick film shows an increase ρ of 47% compared with the original value. For Sb_2Te_3 thick films, the variation is only 7.8% over 50 days. Here, two samples of each material were chosen and five measurements were taken for each sample.

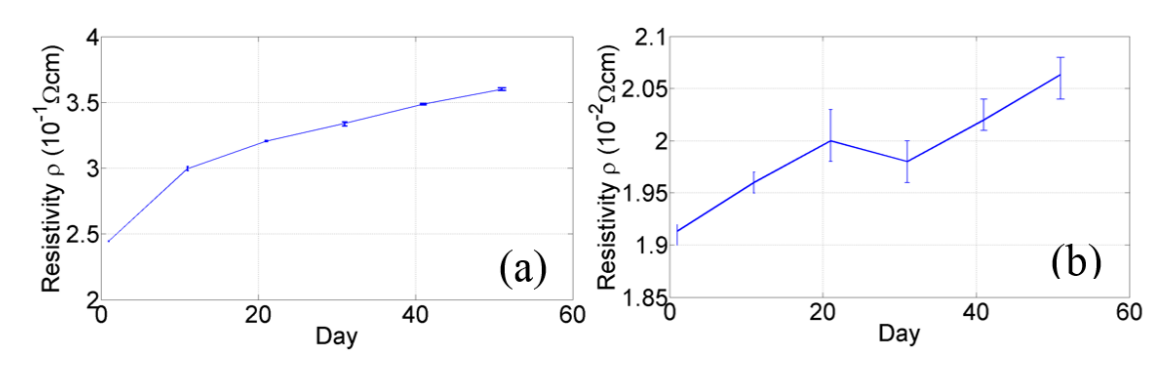


Figure 7.4 Resistivity of selected printed thick-films varying with time. (a):Bi_{1.8}Te_{3.2}; (b):Sb₂Te₃

From table 7.2 and table 7.3, the negative/positive signs of the carrier concentration, Hall coefficient and the Seebeck coefficient indicated that BiTe thick film is an n-type semiconductor and SbTe thick film is a p-type semiconductor.

α (μV/Κ)	Bi _{1.8} Te _{3.2}	Sb ₂ Te ₃
Day 1	-129.2 (-134 – -119)	105.7 (101 – 110)
Day 100	-130.2 (-132129)	103.75 (101 – 107)
Bulk value [6]	-227	110

Table 7.3 Seebeck coefficient of screen printed Bi₂Te₃ and Sb₂Te₃ thick-films

Moreover, from table 7.3, the variation of the average α value is within 2% for a period of 100 days, which can be considered as a stable parameter over time. There was also a reduction of the Seebeck coefficient on the screen-printed materials compared with the bulk ones.

7.3 BiTe/SbTe based thermocouples

In this experiment, the resistance of the cured thermoelectric thick films increases after curing with the top silver electrode layer attached. The increase in the BiTe thick film sheet resistance due to this re-curing process is shown in the following table. The curing time under each temperature was 10 minutes.

Re-curing temperature	150°C	125°C	100°C	75°C
The sheet resistance increasing percentage	4.7%	3.3%	9.1%	8.2%

Table 7.4 The BiTe thick film sheer resistance increasing due to the re-curing effect

To achieve lower resistivity, the thermoelectric material patterns were designed to print directly attached to adjacent thermolegs. The SEM image shows that there is no gap between the junction of BiTe and SbTe (figure 7.5-a), which ensures the establishment of Ohmic contact between adjacent thermolegs. Thus, no top silver electrode layer was printed on the TEG.

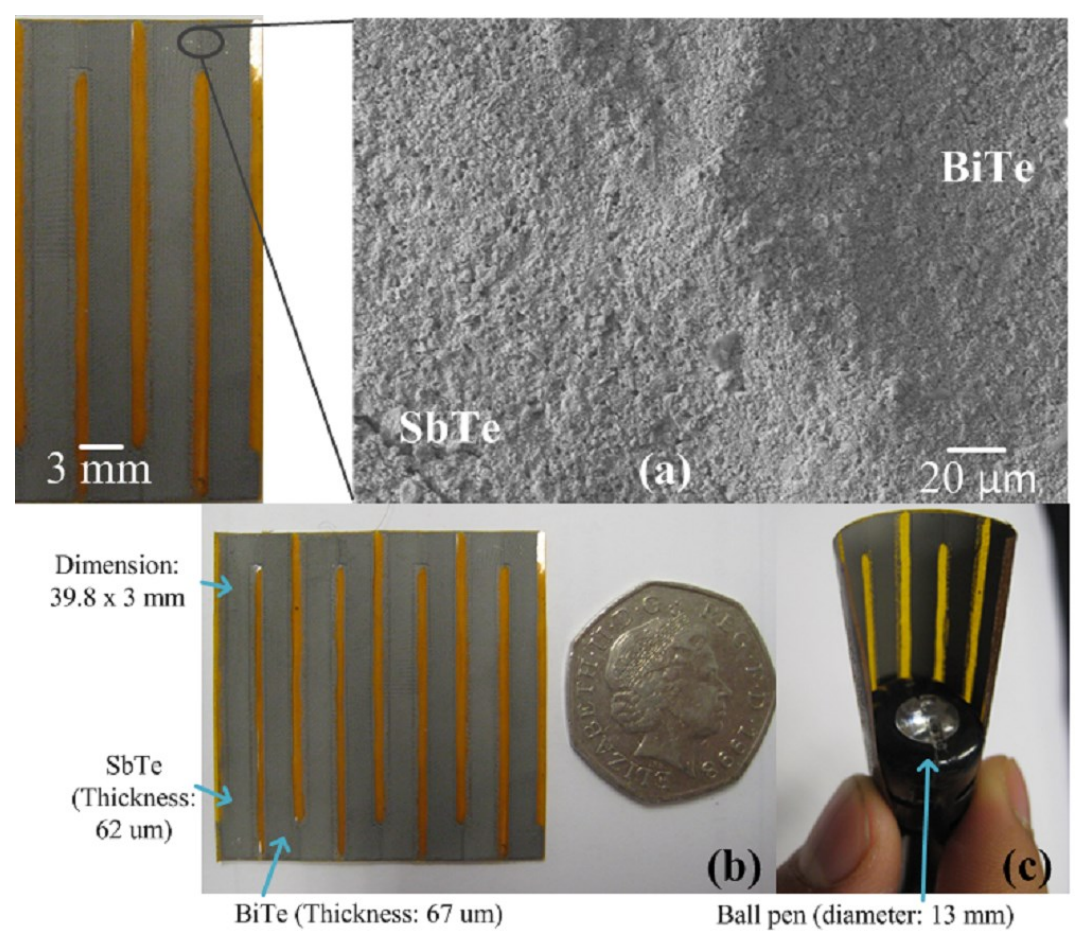


Figure 7.5 Printed BiTe/SbTe thermocouples. (a): SEM of the BiTe/SbTe junction (b): sample size comparing with a 50 pence coin; (c): sample rolling on a 13 mm diameter ball pen

The fabrication process of the screen-printed BiTe/SbTe TEG prototype is shown in figure 7.6. It only involves deposition of two thermal material layers and a curing process. The thickness of the active thermoelectric layers can be built up by drying each layer at 80 °C to evaporate the solvent and then repeating the printing step. After the deposition of both materials, they were cured at 250 °C for 3 hours. The prototype with 4 thermocouples and its flexibility were shown in figure 7.5-(b) and (c) respectively.

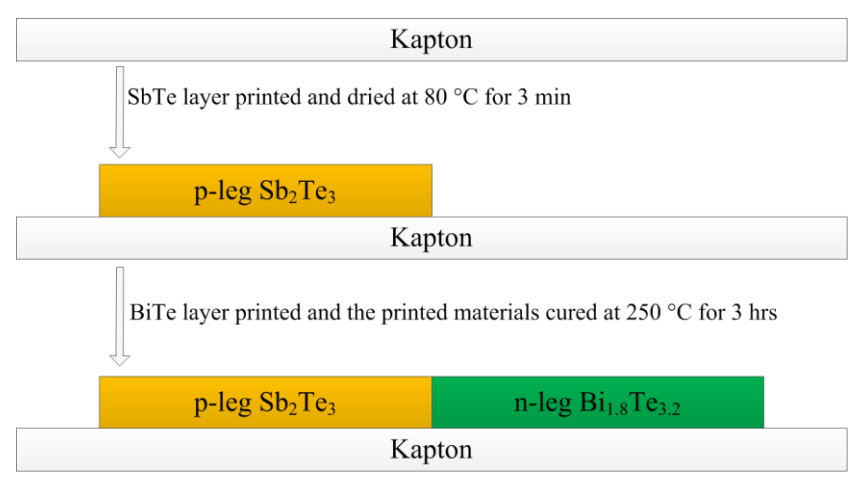


Figure 7.6 Fabrication process of screen printed BiTe/SbTe thermocouple The tests here are the same as those in previous chapters.

7.4 Device characterization results

Figure 7.7 shows the Seebeck voltage of 4 screen-printed BiTe/SbTe thermocouples at different temperature differences. A single Bi_{1.8}Te_{3.2}/Sb₂Te₃ thermocouple can generate 16.6 mV at a temperature difference of 60° C, which is better than the 5 mV of a single Bi/Sb thermocouple previously achieved by our group at the same temperature difference [6]. In addition, the variation of the Seebeck voltage when Δ T=60°C was within 5% from figure 7.7.

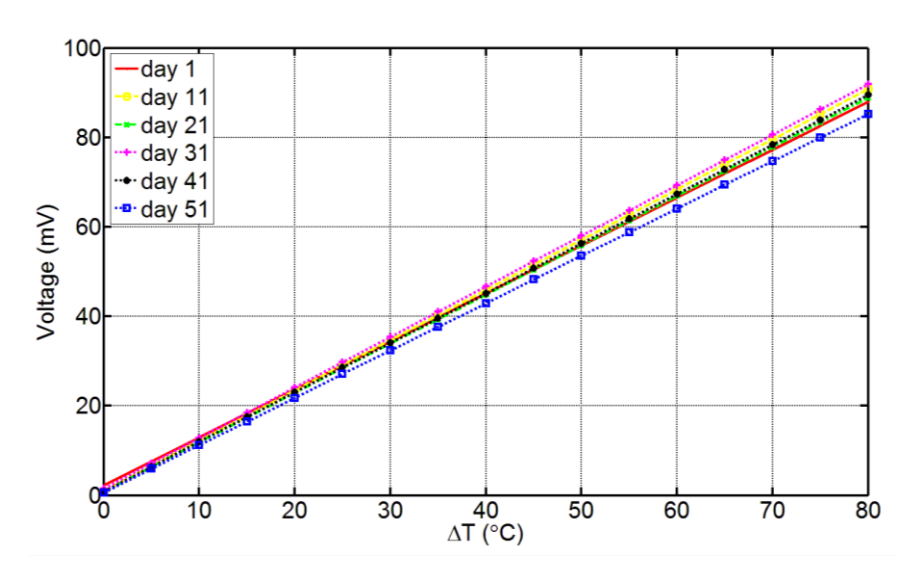


Figure 7.7 Generated Seebeck voltage of 4 printed thermocouples, varying with time From the definition of Seebeck Effect (α =V/ Δ T), for a single thermocouple of this sample, the Seebeck coefficient was calculated in the range of 262–282 μ V/K (figure 7.8).

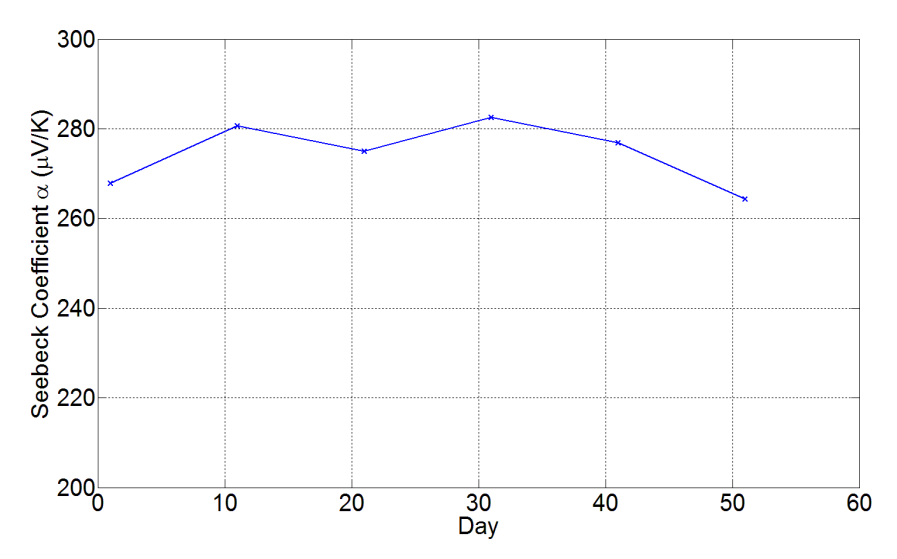


Figure 7.8 Calculated Seebeck coefficient for single thermocouple varying with time from Seebeck voltage measurement

The power output versus load resistance at a temperature difference of 20 °C is shown in figure 7.9. The square-marked dashed line represents the measured output power, while the solid line is the fitted value. The fitting rule is the same as that used in previous chapters. The matching of the measured curve and the fitted curve proves that the thermoelectric battery model suggested in figure 2.9 is promising in output power measurement.

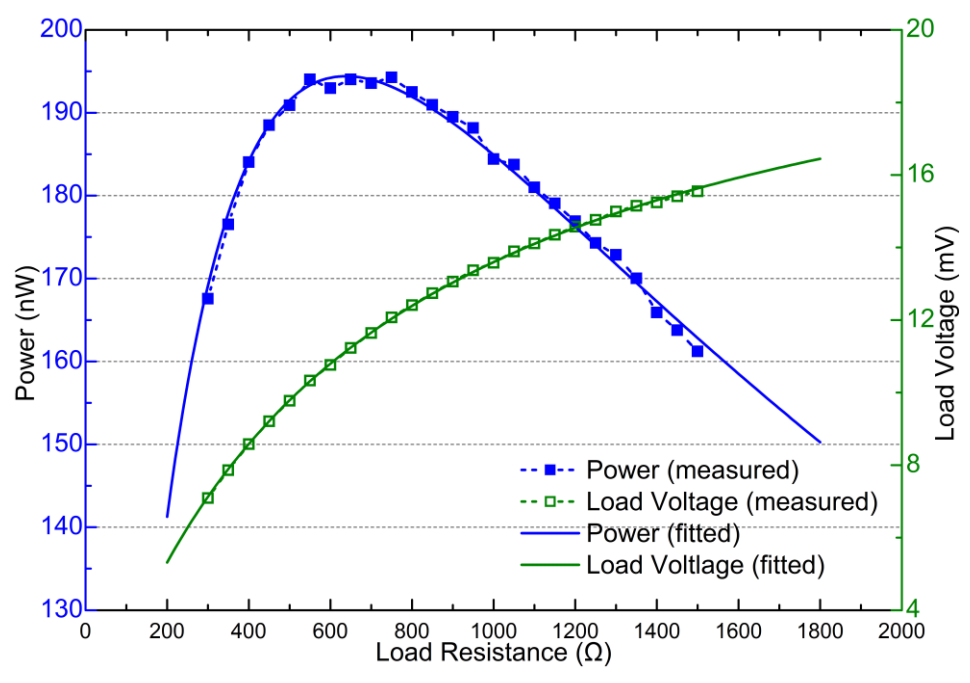


Figure 7.9 The voltage across the load resistor and the power output vs. load resistance of 4 BiTe/SbTe thermocouples with their fitted values

The voltage across the load increased with the increasing load resistance and the maximum output power occurred when the load resistance matched the TEGs resistance.

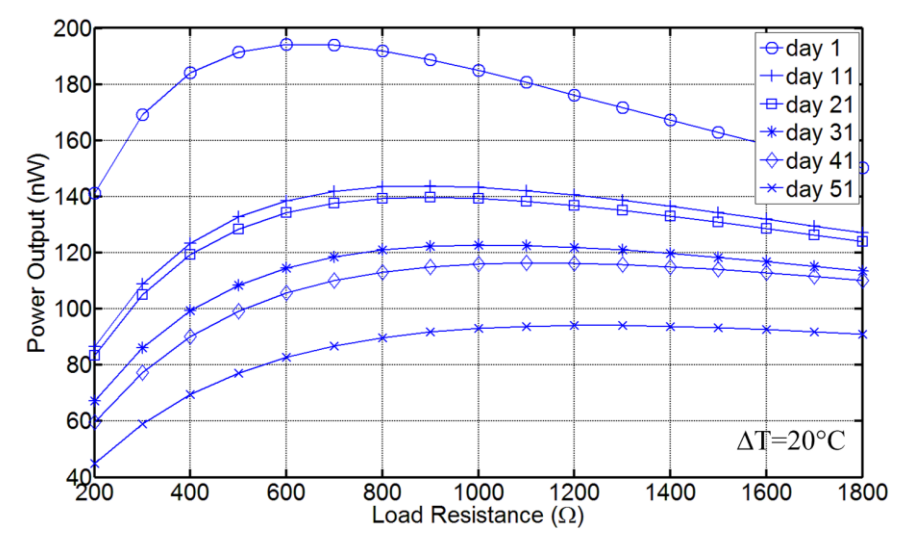


Figure 7.10 Power output of four printed BiTe/SbTe thermocouples varying with load resistance over 50 days

However, from figure 7.10, it can be observed that the maximum power output kept decreasing with time due to oxidation of the thermoelectric thick films in air. For a single thermocouple, the original maximum power was 48.6 nW. This value decreased to 23.5 nW after 50 days, while the resistance of a single thermocouple increased from 160 Ω to 310 Ω during the same period. According to figure 7.10, the power output would decrease to about 50% of its original value within 50 days.

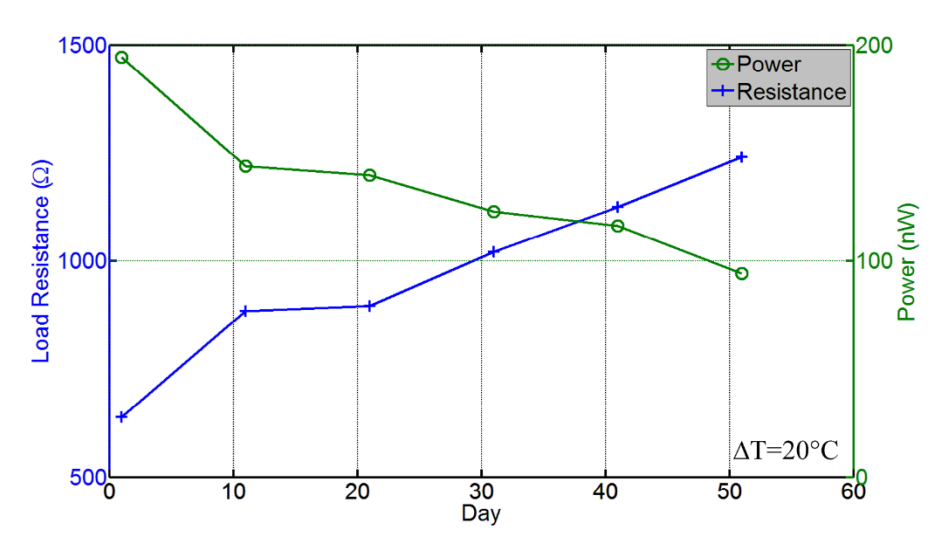


Figure 7.11 Maximum power output and self-resistance of 4 printed BiTe/SbTe thermocouples varying with time

The reason for the low power mainly comes from the high resistivity of the BiTe thick-film. The porous structure of the thick films created a larger contact area between air and thermoelectric particles, which speed up the oxidation of the particles.

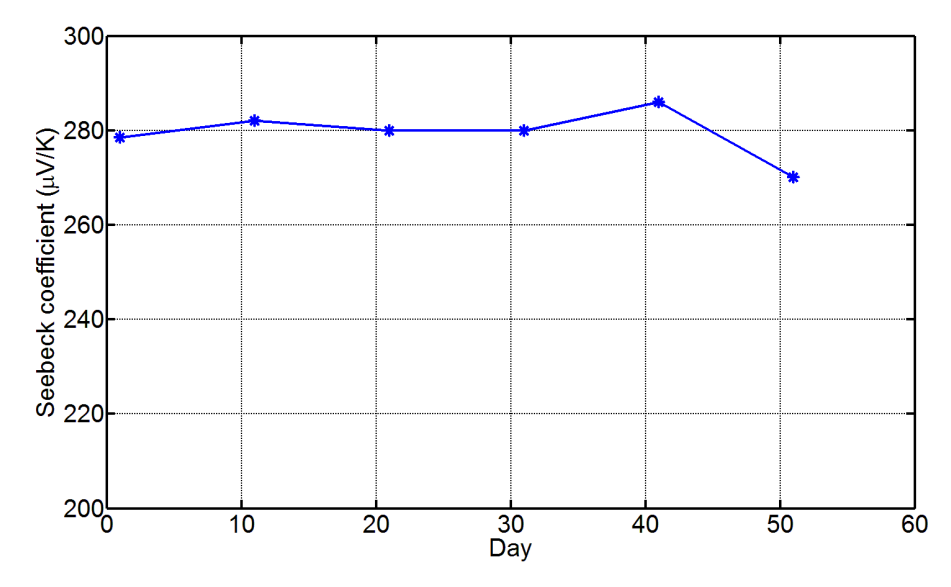


Figure 7.12 Calculated Seebeck coefficient for a single thermocouple varying with time from power output measurement

For a single thermocouple of this sample, from the power output measurement, the Seebeck coefficient was calculated in the range of 270–286 μ V/K, which corresponds to the values from Seebeck voltage measurement.

7.5 Summary and discussion

This work demonstrates that the low cost screen printing technology can be used to fabricate BiTe/SbTe based TEGs for room temperature energy harvesting applications. Although the power output is low for a single thermocouple, the flexibility allows the screen printed TEGs to be connected in series and rolled in to a coil. Then, higher power outputs can be achieved by deploying more thermocouples in this way. Future work includes the measurement of thermal conductivity, which will enable the calculation of ZT.

In table 7.5, it is clear that the resistivity of BiTe thick film has the biggest change compared with that of SbTe thick film. Moreover, compared with the literature, the resistivity of the SbTe thick film was in the same order while the resistivity of BiTe thick film was one order higher [60].

	BiTe	SbTe
The change of ρ compared with bulk value	11600%	5300%
The change of α compared with bulk value	43%	5%

Table 7.5 Deviations between experiment values and bulk values of BiTe and SbTe (thick film value/bulk value)

Based on the Seebeck coefficient and electrical resistivity measurement, it can be concluded that the there is a larger decrease in α and ρ for BiTe than SbTe. Thus, it is worth to analysis the elements composition in the BiTe thick films, the main restriction of limiting the thermoelectric performance. From the EDX spectrum (figure 7.13), in the BiTe thick film, the carbon (C) and oxygen (O) was introduced into the film from the binder and solvent.

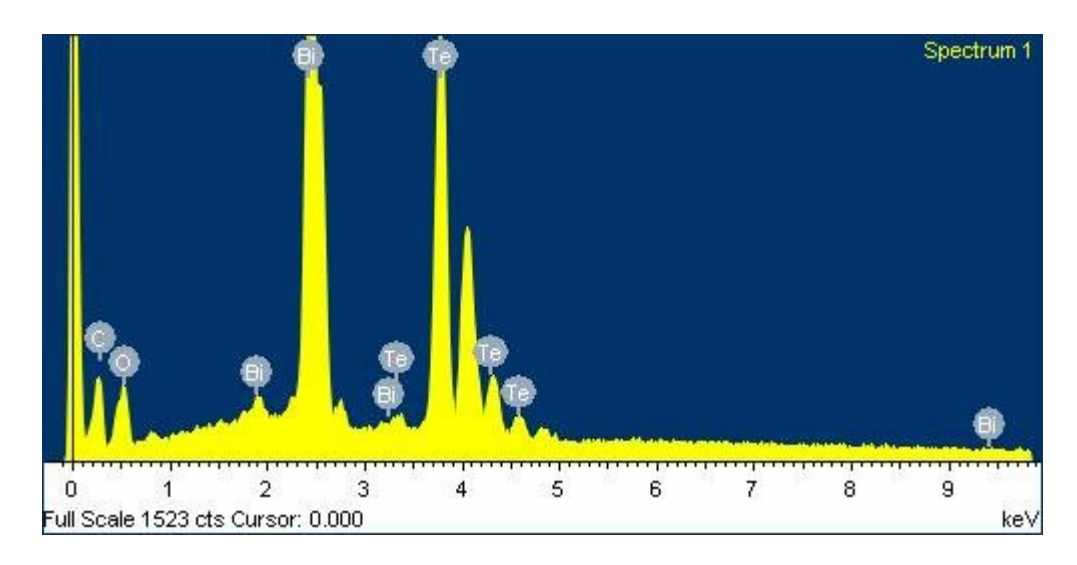


Figure 7.13 EDX composition analysis of BiTe thick film

In addition, from the structure shown in figure 5.3, the -OH and -Cl functional group is easy to form hydrogen bond with the ambient water molecular H_2O , which is a potential reason of the oxidization of the printed thick films. This will be investigated by applying a binder system without -OH functional group.

In summary, the high and fast increase in electrical resistivity of Bi_{1.8}Te_{3.2} thick film is an issue for reaching a higher power output for the screen-printed TEG. Oxidisation of bismuth tellurium powders is the likely cause. Future work will explore the optimisation of design and material processing to decrease the resistivity. From a material processing point of view, the quantity and dimension of voids in the thick films could be reduced by filling with smaller-sized thermoelectric particles or module densifying technology, e.g., isostatic pressing. From a structure point of view, a

vertical-structured thermocouple has the potential to achieve a higher power output than the planer-structure ones [39]. Thus, a dispenser printed TEG with 3D structure will be introduced in the following chapter.

Chapter 8. Dispenser printed BiTe/SbTe based TEGs with 3-Dimentional (3D) structure

8.1 Introduction

In the last chapter, flexible planar-structured thermocouples have demonstrated that screen-printing technology is promising to fabricate BiTe/SbTe TEGs. However, from a design point of view, vertically fabricated TEGs, which have a lower ratio of cross-sectional areas of insulation to active material in the plane perpendicular to the heat flow, were claimed to have a higher thermoelectric efficiency than the planar-structured TEGs [39].

Utilising screen-printing, it is difficult to realise a 3D-structured thermocouples. The earlier printed patterns will create a large gap between the screen mesh and substrate, stopping the screen reaching the lower areas of the substrate. While in dispenser printing, the separation distance between the needle and substrate can be adjusted by moving the needle vertically (seen in figure 8.1). Hence, in principle, dispenser printing the thermoelectric material pastes layer by layer can build up the thickness of the vertical thermocouples.

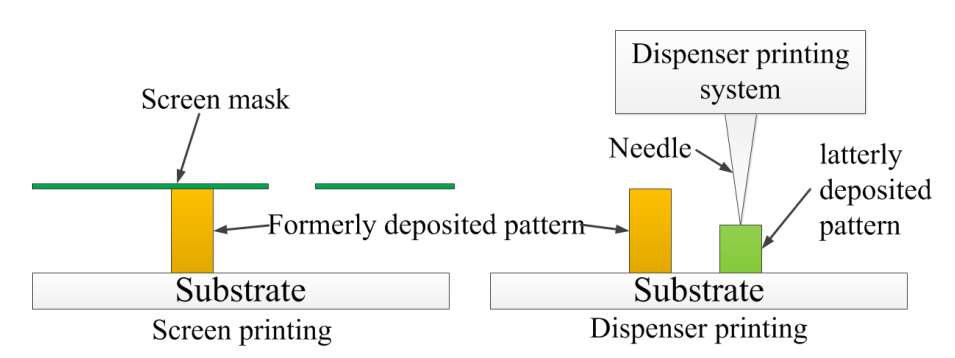


Figure 8.1 Comparison of TEGs fabricated by screen printing and dispenser printing
In this chapter, the TEGs with 3D BiTe and SbTe cubes fabricated by dispenser

printing are introduced. The voltage and power measurements are also presented and analysed.

8.2 Fully dispenser printed 3D-structured TEGs

8.2.1 Experiment set-up

The setup for dispenser printing includes a 3 axis stage, a stage controller, a dispenser and an air pump. All of the equipment is shown in figure 8.2. National Instrument LabVIEW is the software used to control the entire system.

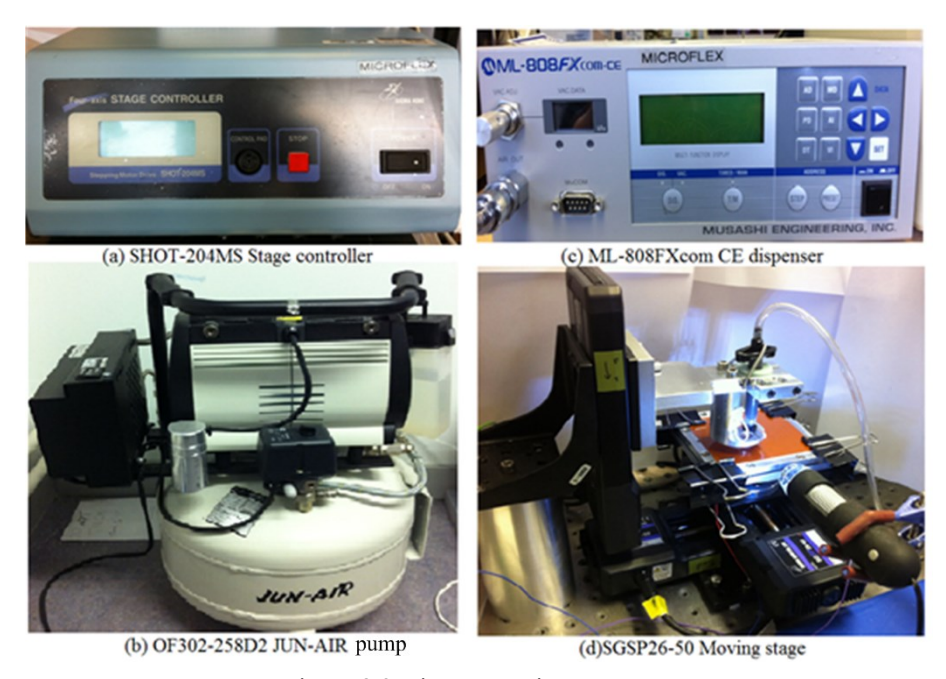


Figure 8.2 Dispenser printer systems

In this experiment, the ML-808FXcom-CE dispenser printer is a pneumatic type dispenser printer. Generally, this dispenser machine could print pastes with a wild range of viscosity by varying the nozzle size, air pressure and dispensing time. The empirical requirements of the paste properties and dispensing conditions can be concluded as follow.

- The liquid is not compressible: if the liquid or paste is compressible, it will absorb the pressure from the compressed air. Thus, the paste is not possible to be pressed out from the syringe.
- Liquid evaporation rate: this is determined by the vapour pressure of the solvent used in the pastes. Ideal solvent should have a vapour pressure lower than 0.001kPa, which will provide a slow dry nozzle/air interface.
- Nozzle size: depend on the resolution aiming to achieve. The minimum line width can be achieved is between the outer diameter and the inner diameter of the nozzle.
- Particle size: the ideal particle size should be between 1/100 and 1/10 of the inner diameter of the dispensing nozzle.

- Suspensions: particles should not settle or agglomerate rapidly. A suitable stabiliser (dispersant) could be added into the paste if the particle suspension is poor.
- Droplet size: depends on the needle's dimension, ink rheology, applied pressure, vacuum pressure and dispensing time.
- Pattern morphology: depends on the droplet size, the dispensing gap, the stage moving steps and speed.
- Nozzle size (inner diameter): 0.1 µm to 2 mm.
- Dispensing time: 0.01 second to 999.9 seconds [121].
- Pneumatic pressure: 20 kPa to 800 kPa [121].

8.2.2 Fabrication of TEGs

For a working TEG the thermocouples should be connected electrically in serial, which requires both the top and the bottom of the thermoelectric material cubes to be connected to electrodes. This 3D structure is illustrated in figure 8.3.

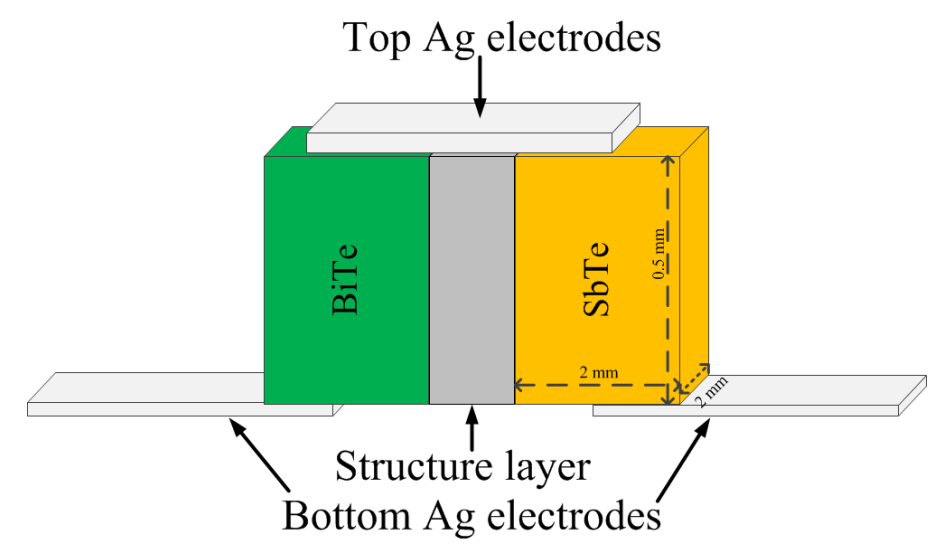


Figure 8.3 Illustration of a 3D-structured dispenser printed BiTe/SbTe thermocouple

The bottom electrodes can be printed onto the substrate, while a structure layer need to be printed in order to support the top electrodes layer. The ultraviolet (UV) curable epoxy OG675 from EPO-TEC was applied as the structure layer material. This UV curable single component epoxy has a pot life over 3 hours and fast curing time of 2 seconds, which makes it suitable for dispenser printing. Also, a non-thermal cured structure layer minimises the oxidation of the thermoelectric materials. The data sheet can be seen in Appendix 7. The thermoelectric materials pastes and Ag paste are the same as that used in the experiments in previous chapters. The dispensing nozzle for all the pastes has an inner diameter of 250µm and a needle length of 6.35 mm (1/4 inch).

Firstly, the Ag paste was dispenser printed onto the Kapton substrate and cured. Then, the SbTe and BiTe pastes were dispenser printed onto the Ag electrodes in the required patterns. The stage was heated up to 60° C using a Peltier plate. The printed patterns were dried using the heated stage in order to build up the thickness of the cubes. The dimensions of the individual cube were $2 \times 2 \times 0.5$ mm. The distance between adjacent cubes was 1.2 mm. The thickness of the bottom silver electrodes is 10 μ m. The stage controller has a resolution of 1 μ m, which meets the requirement of these dimensions. The fabrication processes were illustrated in figure 8.4.

Because the patterns of the thermoelectric modules are transferred from the bitmap for the current dispenser printing technology, the size of each thermoleg side equals to $n\times0.25$ mm (n is the number of the dots in the bitmap pattern). Each layer has a thickness of 20 μ m. The deposition speed is slow due to this dot by dot printing. It required over 10 hours to print 8 thermocouples (4 × 4 matrix thermolegs), which will be discussed in detail in section 8.4. The dimension of 2 × 2 × 0.5 mm is the maximum size of single thermoleg in practical.

Moreover, based on the resistance calculation equation R=pA/l (A is the thermoleg area, 1 is the thermoleg length), the larger area of thermoleg could result a lower resistance, which will provide a higher power output. Hence, such dimension was chosen in this experiment.

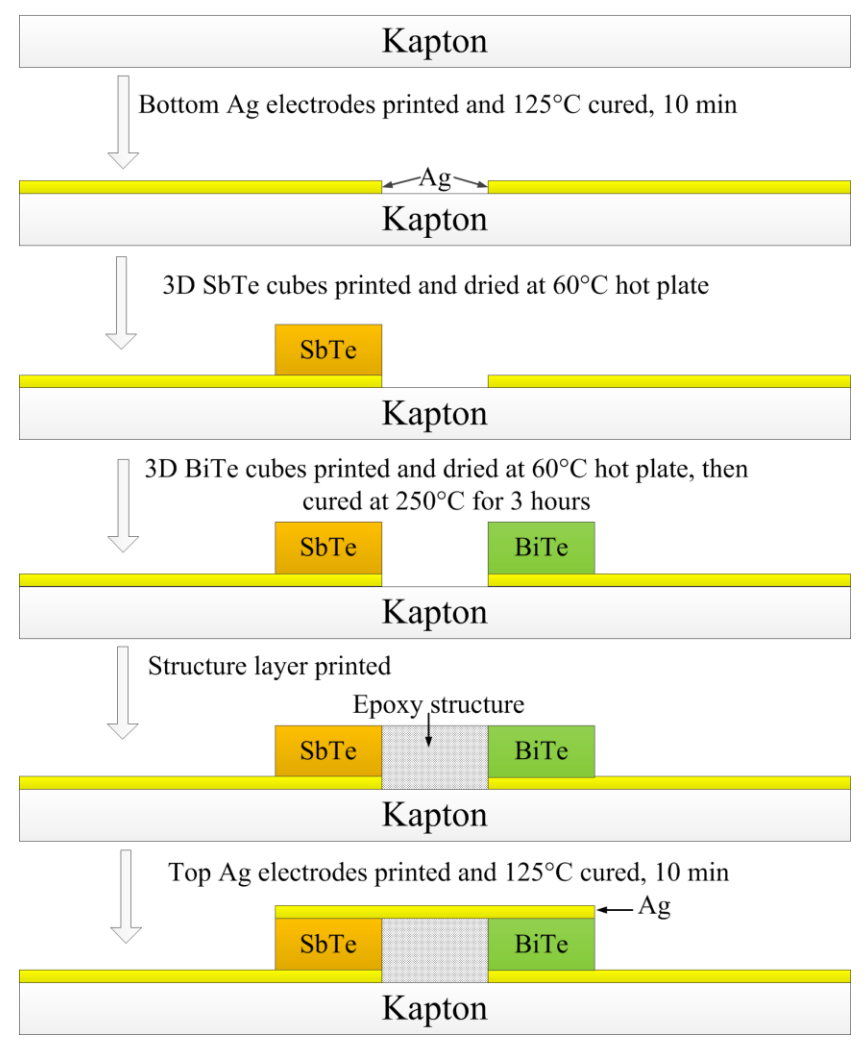


Figure 8.4 Fabrication process of the fully dispenser printed TEGs

The images of a dispenser printed TEG sample in different processes are shown in figure 8.5. BiTe was printed after SbTe because it has a faster oxidation rate, as found in previous studies. The dimensions of the printed cubes were controlled by the stage controller.

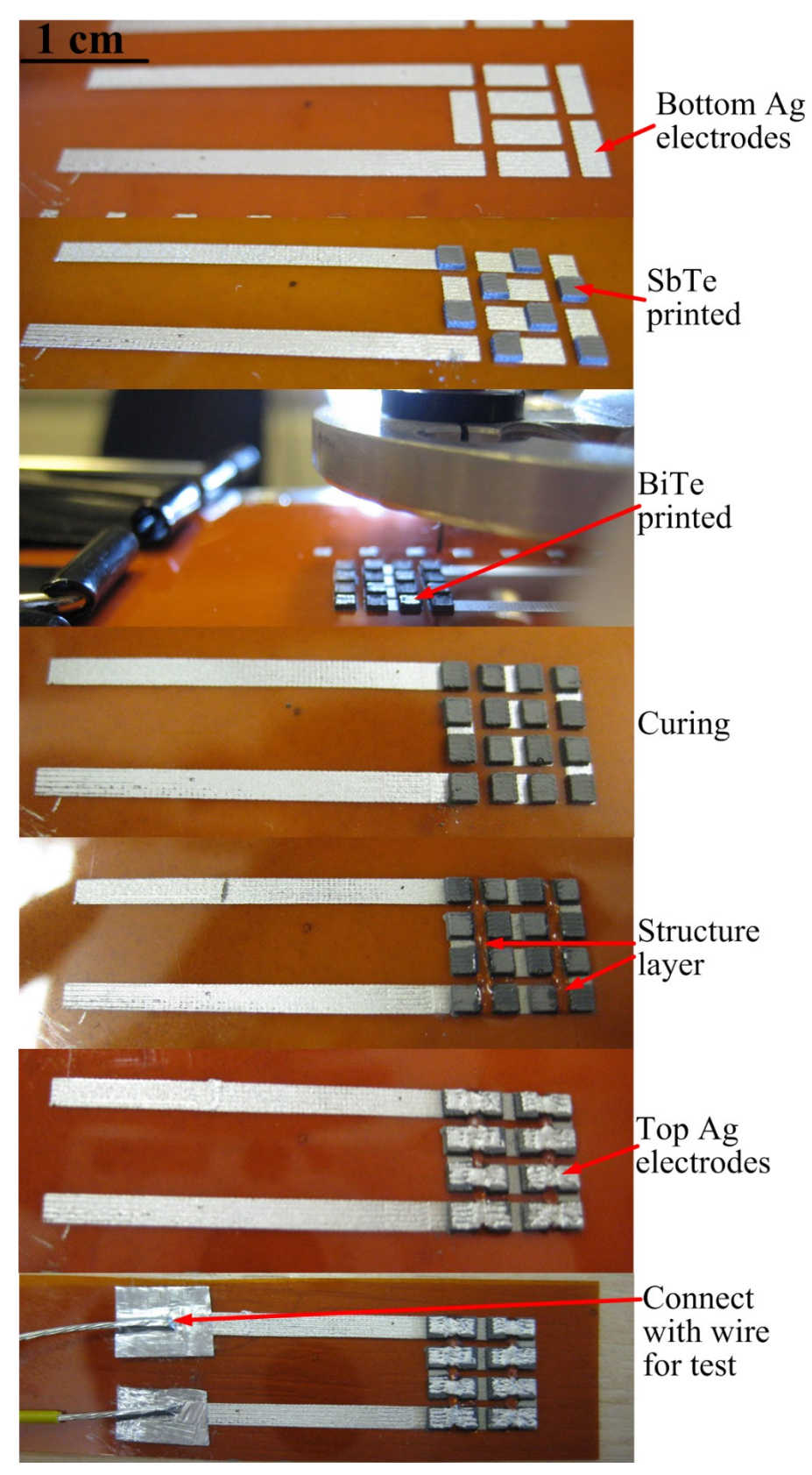


Figure 8.5 Images of a fully dispenser printed TEGs with 8 thermocouples in different fabrication processes

In this experiment, 3 samples with the same thermoelectric material cubic size but different number of thermocouples were dispenser printed. The matrix of the cubes

were 1×2 , 2×2 and 4×4 for sample (a), sample (b) and sample (c) respectively. The flexibility of the samples is shown in figure 8.6.

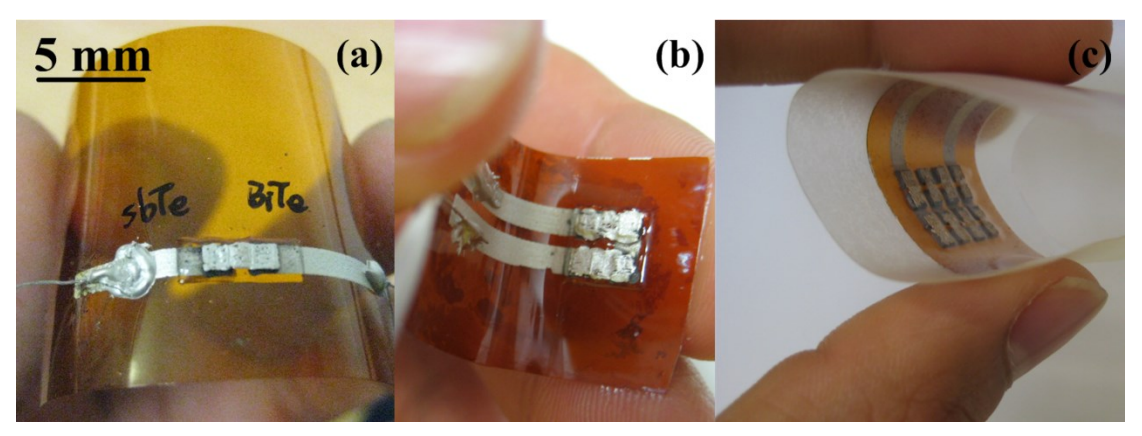


Figure 8.6 Flexibility demonstration of 3 fully dispenser printed TEGs. Sample (a): 1 thermocouple with 1×2 cubes. Sample (b): 2 thermocouples with 2×2 cubes. Sample (c): 8 thermocouples with 4×4 cubes

8.2.3 Measurement and results

The setup for measuring the Seebeck voltage and power output for vertically fabricated TEGs was different from the planer samples. For dispenser printed 3D TEGs, the heat flux was perpendicular to the substrate. Thus, the temperatures on each side of the vertical sample can only be measured from the hot and cold source it is attached to. In figure 8.7, Al blocks were used as heat conductors to allow the temperature to be measured, while also supplying a temperature gradient.

However, for body-work devices, the heat conductivity is not as good as the heat sink used in this setup, which is one limitation of this test setup. The heat conductivity of human body is 0.543 W/mK in average while that of aluminium heat sink is 237 W/mK. For practical application, the actual temperature gradient is difficult to be maintained as stable as in such setup. In addition, the vertically fabricated device is on polyimide substrate, which has a low heat conductivity (0.005 W/mK). This will limit the accuracy of the Seebeck voltage and power test.

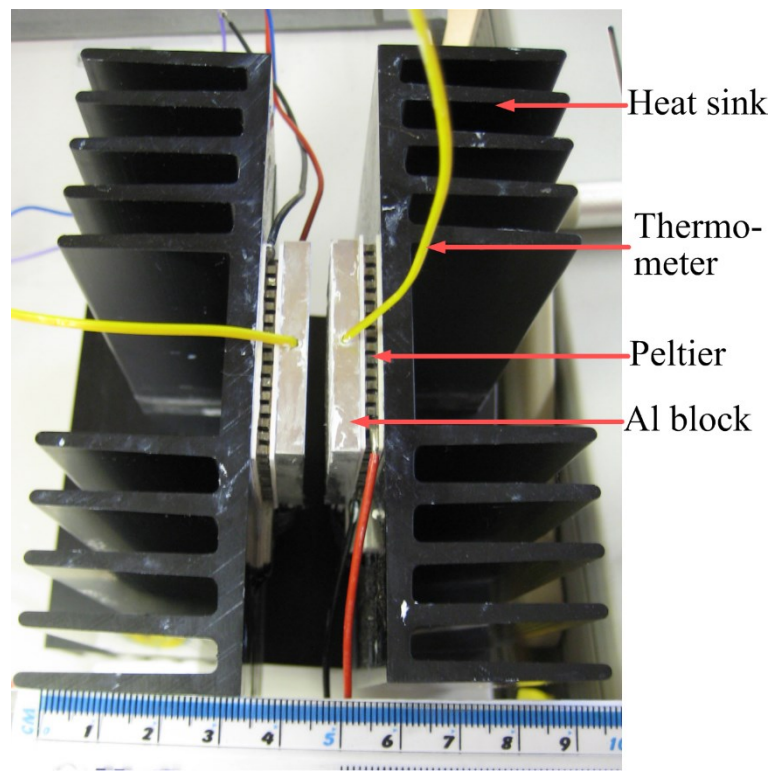


Figure 8.7 The Seebeck voltage and power output measurement setup

As shown in the figure above, TEGs with 3D structures were placed between two Al blocks. The thermal conductivity of the Al is 205 W/(m·K), which is 5 times higher than 41 W/(m·K) of the ceramic plates used on the Peltier [16, 122]. The high thermal conductivity guaranteed the uniform temperature distribution over the surface of the TEGs. Figure 8.8 shows the temperature distribution over these 2 Al blocks, which was measured by the Testo 875 thermal Imaging Camera.

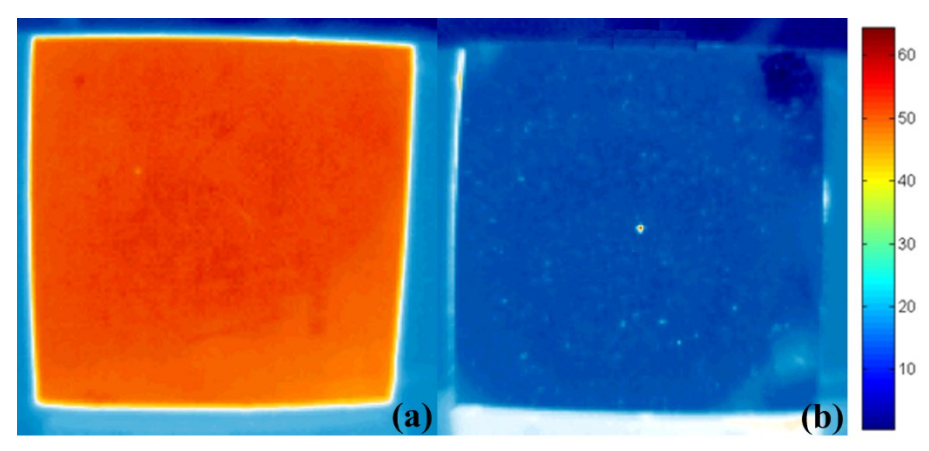


Figure 8.8 The temperature distribution over the Al blocks. (a) hot side. (b) cold side

The probes of the thermometer were put in the middle of the Al blocks by drilling a hole into the centre, and sealed with thermal grease. The measured Seebeck voltages of these three samples are shown in figure 8.9.

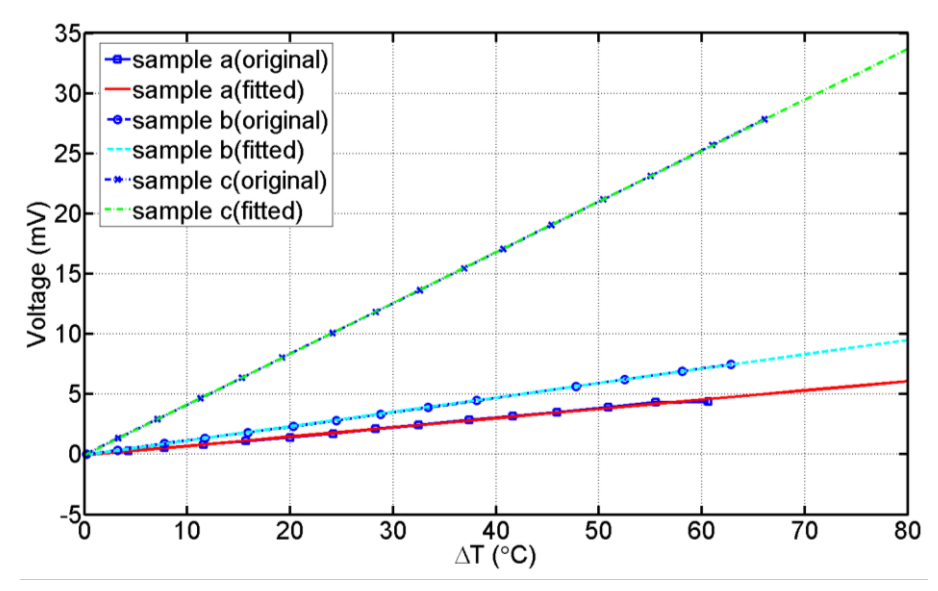


Figure 8.9 Generated Seebeck voltages of dispenser printed TEGs increase with the temperature gradient

From the above figure, it can be seen that the output voltage increased linearly with an increase in the temperature gradient. At a temperature gradient of 60°C, a single thermocouple can generate a voltage of 4.5 mV, 3.6 mV and 3.2 mV calculated from sample a, sample b and sample c respectively, which are all lower than the 16.6 mV generated by a single planer BiTe/SbTe thermocouple.

In addition, the voltage measurement over the load resistor also shows a lower power output compared to the planar thermocouple (in figure 8.10). The maximum power per single thermocouple among sample a, b and c is 1.5 nW at a temperature difference of 20 °C, which is much lower than the 48.6 nW for the planar thermocouple.

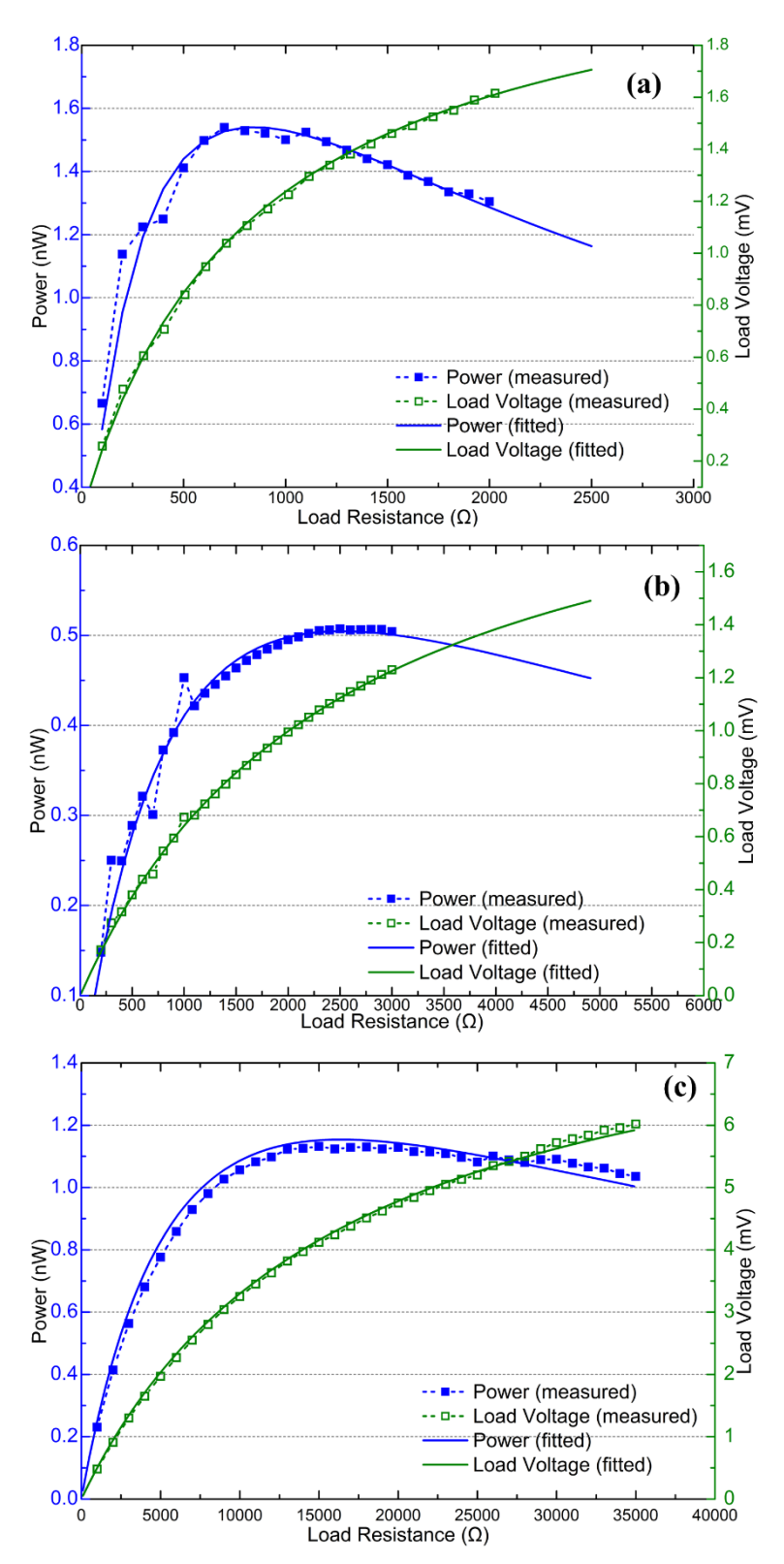


Figure 8.10 The original and fitted voltage and power output on the load resistor, $\Delta T=20$ °C. (a): sample a. (b): sample b. (c) sample c.

	Sample	Sample	Sample
	a	b	С
α calculated from Seebeck voltage	76.9	59.8	52.9
measurement($\mu V/K$)			
α calculated from power output measurement	114.0	56.4	57.0
$(\mu V/K)$			
$R(\Omega)$	844	1260	2276
Maximum power at ΔT=20°C	1.54 nW	0.25 nW	0.14 nW

Table 8.1 The Seebeck coefficient α and resistance R for single BiTe/SbTe thermocouple

The calculated α value from both the Seebeck voltage and power measurement along with the resistance of the single thermocouple for these three samples are shown in table 8.1. The resistance of a single dispenser printed thermocouple is much higher than the screen-printed planar one (160 Ω).

The aging effect for the dispenser printed 3D-structured TEGs was investigated using sample b. Similarly with the screen printed samples in chapter 7, the slope of the Seebeck voltage vs. temperature gradient (figure 8.11-a), which equals to the Seebeck coefficient, had a change in the range of $\pm 3\%$ in 7 days.

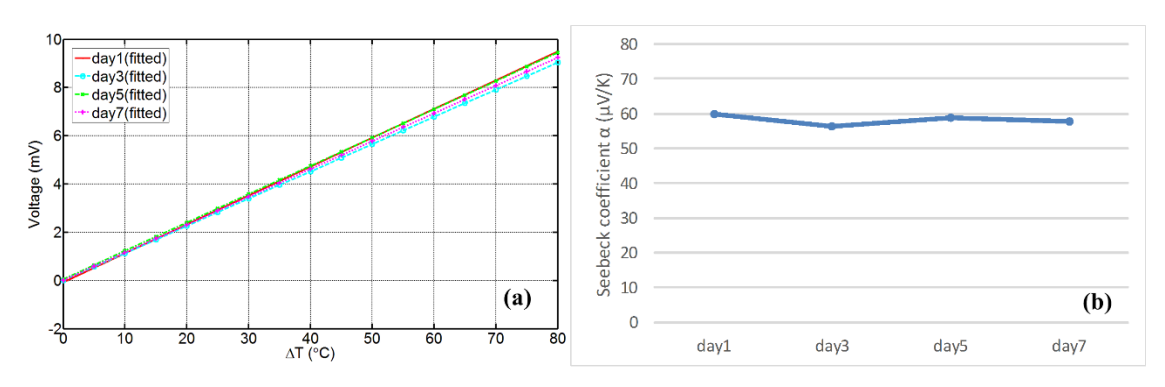


Figure 8.11 (a): The generated Seebeck voltage of sample b in 7 days. (b): calculated Seebeck coefficient of single thermocouple in 7 days

However, the maximum power output decreased from 0.5 nW to 0.25 nW (figure 8.12-a) due to the increasing resistance. The change in resistance after 7 days is 143%. After linearly fitting (figure 8.12-b), the change of resistance in 50 days is 1168%, higher than the 94% of the screen-printed planer sample.

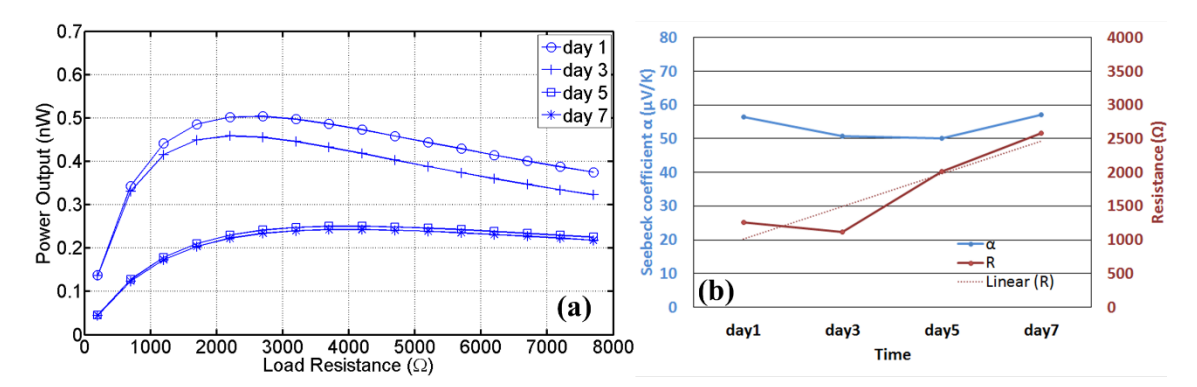


Figure 8.12 (a): The power output of sample b with the changing of load resistance in 7 days. (b): calculated Seebeck coefficients and resistance of single thermocouple in 7 days

8.3 Top electrodes-binding dispenser printed TEGs

Top electrodes-binding dispenser printed TEGs were also investigated because there is no structure layer needed to support the top electrodes. This non-fully dispenser printed 3D-structured TEG has no structure layer to support the top electrodes. Instead, the top electrodes were bonded onto the thermoelectric cubes using conductive Ag epoxy. The detailed fabrication process is illustrated in figure 8.13.

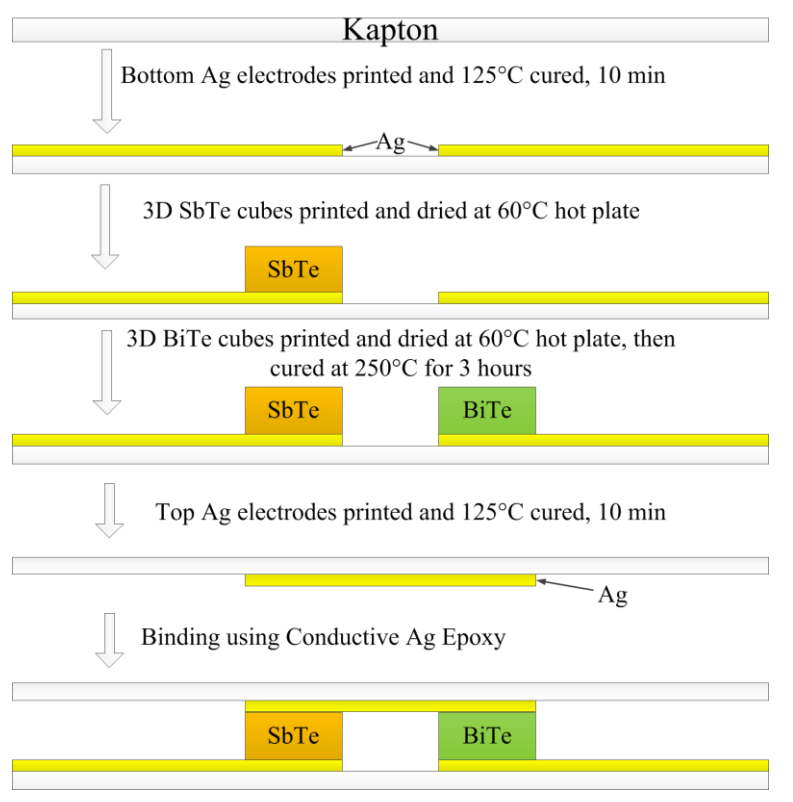


Figure 8.13 Fabrication process of the dispenser printed TEGs

For the binding process, conductive silver epoxy was smeared onto the cured cubes using a nozzle. Then the separately printed top silver electrodes pattern was bonded onto the cubes under a pressure, which is shown in figure 8.14. Here, the conductive silver epoxy was the same with that used in binding the conductive wire.

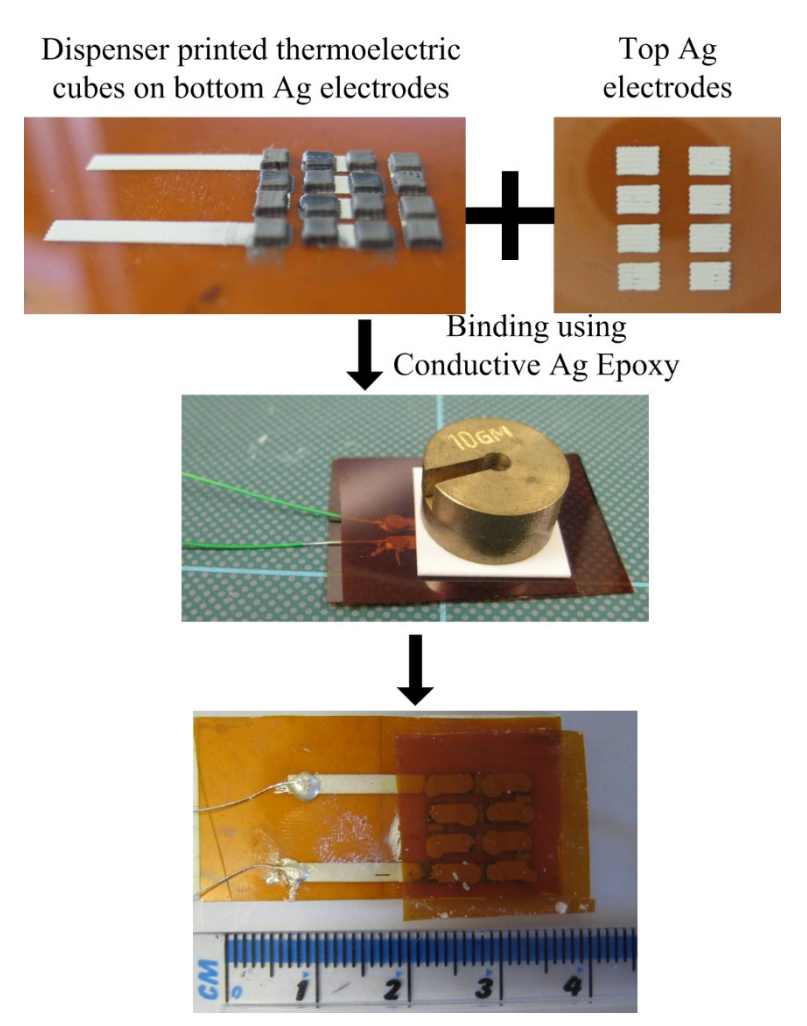


Figure 8.14 Images of a fully dispenser printed TEGs with 8 thermocouples in different fabrication processes

In this experiment, two types of samples were fabricated. Sample 1 had a 2×2 cube matrix (2 thermocouples), while sample 2 had a 4×4 cube matrix (8 thermocouples). The Seebeck voltages along with the temperature gradient are shown in figure 8.15.

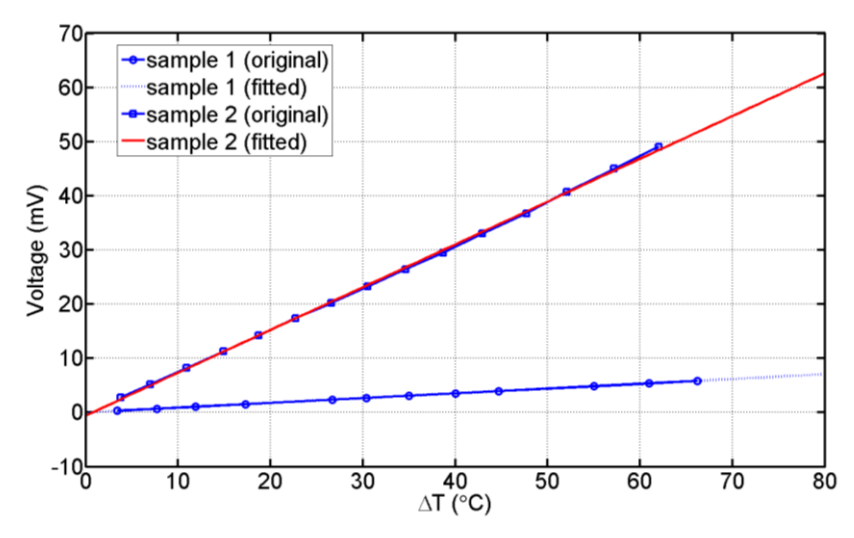


Figure 8.15 The generated Seebeck voltage of top electrodes-binding dispenser printed TEGs

At a temperature gradient of 60°C, a single thermocouple can generate a voltage of 2.65 mV and 5.9 mV calculated from sample 1 and sample 2 respectively.

The curves of power output versus load resistor for sample 1 and sample 2 are shown in figure 8.16 and 8.17 respectively. The maximum measured power for a single thermocouple was only 0.18 nW, lower than that of the dispenser printed TEGs with a structure layer.

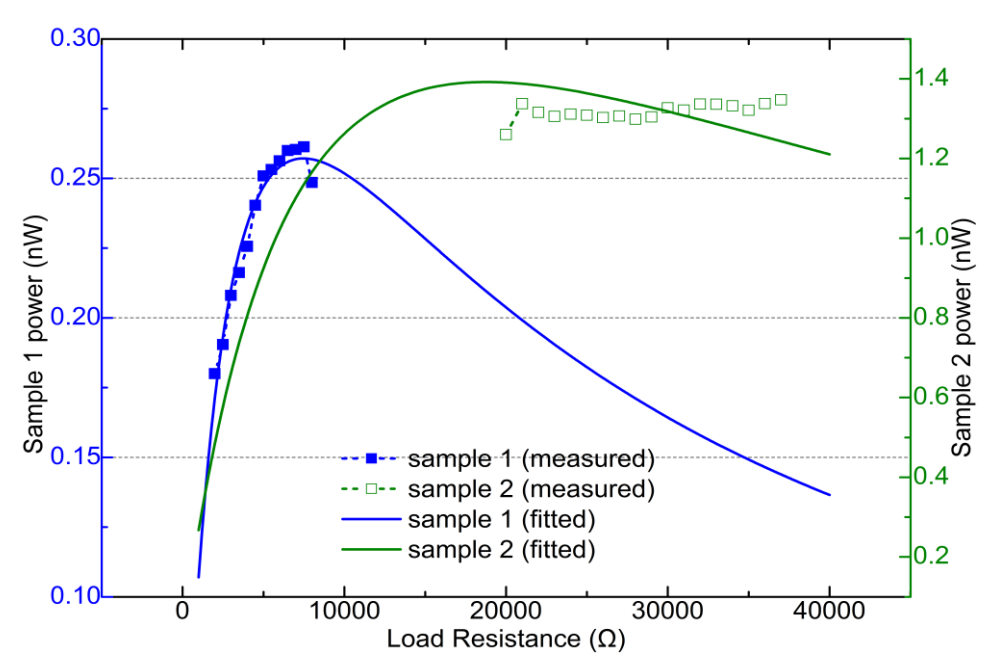


Figure 8.16 The power output of top electrodes-binding dispenser printed TEGs, $\Delta T=20^{\circ}C$

8.4 Discussion and future work

In this chapter, using dispenser printing technology to vertically fabricate TEGs was investigated. The dispenser printer was demonstrated an ability to build up 3D-structured thermocouples. However, the time spent on printing the cubes increased with the number of the cubes. From figure 8.17, with the desired resolution, printing the two cubes in sample (a) took nearly 100 minutes while printing the 16 cubes in sample (c) took over 700 minutes.

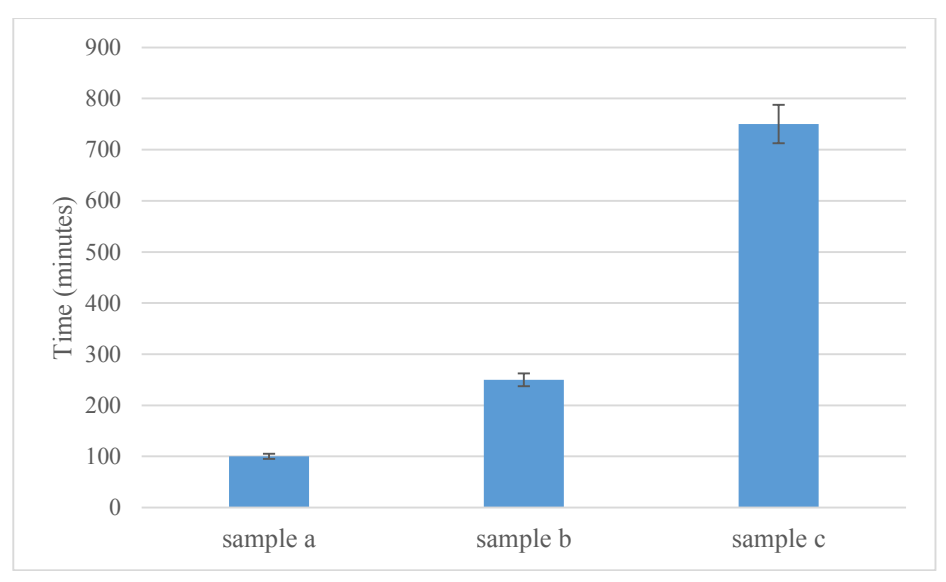


Figure 8.17 Time to print the thermoelectric materials cubes for different samples

The printing time can be decreased by applying a dispenser printer with multiple nozzles to build up the thickness of the repeated pattern. Figure 8.18 illustrates a design for an inkjet printing head with 5 nozzles to print copper arrays [123], which demonstrated the idea of decreasing the fabrication time for printing repeated patterns.

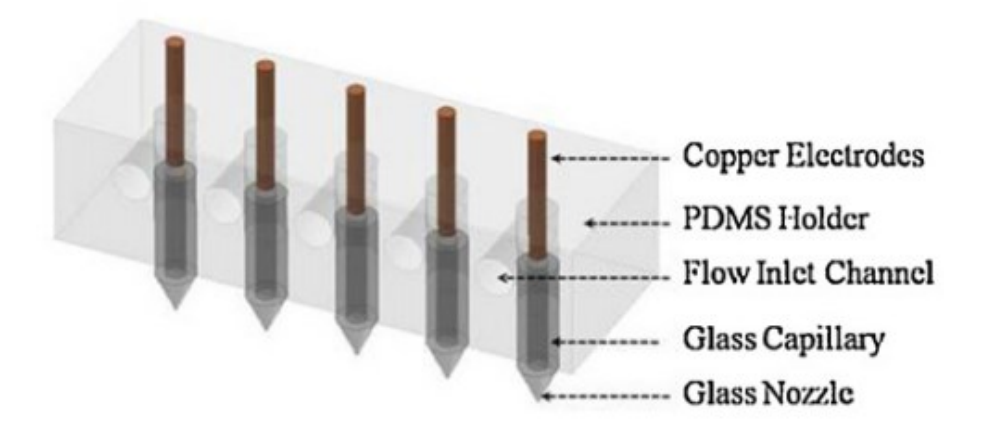


Figure 8.18 An illustration of inkjet printing head with 5 nozzles, after Khan [123]

A possible reason behind the dispenser printed samples having a higher resistance than screen-printed samples, comes from the contact resistance of the junction between silver electrodes and the thermoelectric materials. For 8 printed thermocouples with bottom silver electrodes shown in figure 8.19, the whole resistance was 480 k Ω . The same BiTe and SbTe pastes were applied in this experiment.



Figure 8.19 Printed BiTe/SbTe thermocouples on silver electrodes

The resistance measured using a multimeter is shown in table 8.2. The resistance of the junctions contributed 85% of the entire resistance. The resistance was measured using a Wayner Kerr 4300 LCR Meter. The applied AC voltage had a frequency of 1 kHz.

	Number	range	average
BiTe legs	8	$1.4 \text{ k}\Omega \sim 2.0 \text{ k}\Omega$	$1.6~\mathrm{k}\Omega$
SbTe legs	8	$8 \sim 26 \ \Omega$	16.3 Ω
Junctions	15	$411 \Omega \sim 9.6 \text{ k}\Omega$	$4.9~\mathrm{k}\Omega$

Table 8.2 Resistance of different functional parts in the above 8 planar thermocouples

In addition, from figure 8.19, the overlap areas of the silver patterns and the thermoelectric materials patterns show a different colour from the other parts. A potential reason is that there was a chemical reaction between the silver electrode patterns and the uncured thermoelectric materials during the curing process.

Elements	BiTe	SbTe	BiTe over	SbTe over
Elements	film	film	Ag	Ag
C	9.28	11.05	9.25	11.87
O	5.50	2.97	4.39	3.19
Bi	36.49	0	25.67	0
Sb	0	23.65	0	23.35
Te	47.28	49.68	39.22	60.10
Ag	0	0	12.35	0.17
C+O in all detected elements	14.97%	15.88%	15.01%	15.26%

Table 8.3 Element ratio (weight %) from EDX measurement

EDX measurements were taken to identify the elements in the BiTe and SbTe thick films and their overlapped area with silver. The thickness of the X-ray source can penetrate is set to be $20 \mu m$, which is lower than the thickness of the BiTe and SbTe

thermolegs ($70 \,\mu\text{m} - 90 \,\mu\text{m}$). From table 8.3, there are 12.35% of and 0.17% of silver in the overlapped area with BiTe and SbTe, respectively. This demonstrated that silver particles migrated into BiTe and SbTe thick films. But the reason of the silver migration is much less in SbTe thick film rather than BiTe thick film is still unclear, which need further investigation. In addition, the weight ratio was initially mixed to be 7% - 10 %, which increased to around 15% after curing. The increase of C and O in thick film could partly explain the resistivity increasing in the thick films.

In conclusion, dispenser printing is able to fabricate TEGs with 3D structures. However, the mechanism behind the high contact resistance needs to be further investigated. Evaporating and sputtering could be alternative solutions to deposit the bottom conductive electrodes.

Chapter 9. Conclusion and future work

In this thesis, the object is developing materials and processes that enable the fabrication of thermocouples on flexible substrate using printing technology for body heat energy harvesting application. Therefore, a flexible TEG device was essential to be achieved to match the nature uneven surface of human skin and meet the comfortable requirement of users. This object has been realising step by step from the previous chapters in this thesis.

Ni/Cu based high temperature planer thermocouples have been printed on alumina substrate to investigate the possibility of printing technologies on fabricating TEGs devices. The poor adhesion of Ni thick film on ceramic substrate was successfully improved by printing a dielectric interface layer.

In order to achieve TEG on flexibly substrate like Kapton, a suitable polymer binder should be applied instead of the glass binder for high temperature application. In this thesis, Bi and Sb screen printable pastes with epoxy binder systems were developed and Bi/Sb based low temperature thermocouples were fully screen printed and tested. An polishing process was found to make the printed Bi thermolegs conductive.

With the developed polymer binder, low temperature screen printable BiTe and SbTe pastes were formed. A flexible TEG device was fully screen printed. The transport property tests for individual thick films suggested that the high electrical resistivity and the aging effect of the resistivity limited the thermoelectric performance of the TEG device, especially for BiTe material.

Novel dispenser printed BiTe/SbTe TEGs with 3D-structured thermocouples were also presented in this thesis. However, the contact resistance between the electrodes and the thermoelectric materials remained as an issue to be solved in future work.

The Seebeck coefficient and electrical resistivity of the pastes developed in this work are conclude in table 9.1. The resistivity increases with the increase of the carrier concentration. From chapter 2, the highest power factor appeared at the carrier concentration range of $10^{18} - 10^{20}$ cm⁻³, which correspond to the range of semiconductor materials. However, due to the high resistivity of the printed films, the power factor of BiTe and SbTe had no advantageous over their counterparts currently.

	Carrier concentration (cm ⁻³)	Resistivity $(\Omega \cdot cm)$	Seebeck coefficient (µV/K)	Power factor (µWcm ⁻¹ K ⁻²)		
		n-type material				
Ni	-2.58×10^{20}	4.86×10 ⁻⁴	-15	0.5		
Bi	-3.07×10^{17}	4.53×10 ⁻²	-58.7	0.08		
BiTe	-8.89×10^{18}	2.45×10 ⁻¹	-129.2	0.07		
	p-type material					
Cu	-6.59×10^{21}	6.40×10 ⁻⁵	3	0.1		
Sb	1.38×10^{20}	1.24×10 ⁻³	27.6	0.6		
SbTe	2.13×10 ¹⁹	1.92×10 ⁻²	105.7	0.6		

Table 9.1 The Seebeck Coefficients, resistivity and carrier concentration of the developed pastes

In order to integrate the printed thermocouples with the textile, an interface layer is required to provide a smooth surface for printing. In this thesis, a study on improving the adhesion quality of the silicone interface layer was made as well.

From the research in this thesis, in the future, works about reducing the resistivity of the printed thick films will be done, which is pivotal to improve the power output.

Cold Isostatic Pressing (CIP) is going to be applied on the low temperature BiTe and SbTe thick films to decrease the number of voids and densify the film. From the SEM images of the printed thick films, it can be observed that there are voids and holes between adjacent particles. Due to the flexibility requirement, the voids cannot be eliminated by melting the particles. Generally, the CIP process will apply a high pressure from all directions of the sample to densify it. The working principle is shown in figure 9.1.

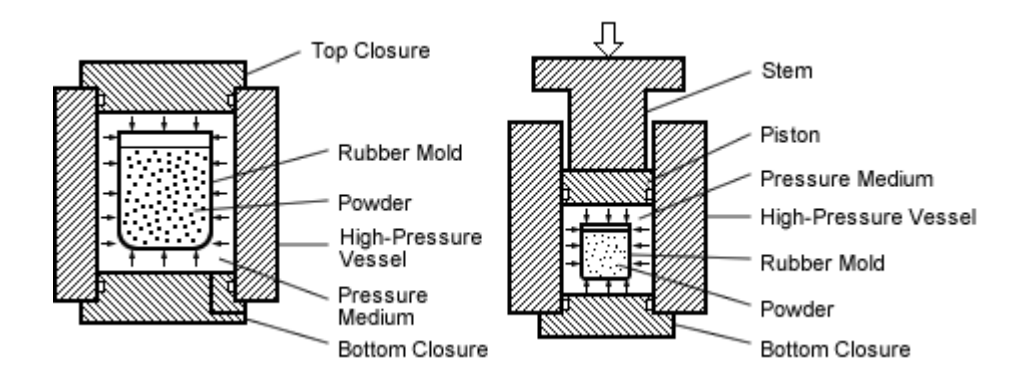


Figure 9.1 Illustration of wet cold isostatic pressing, after Kobelko [124]

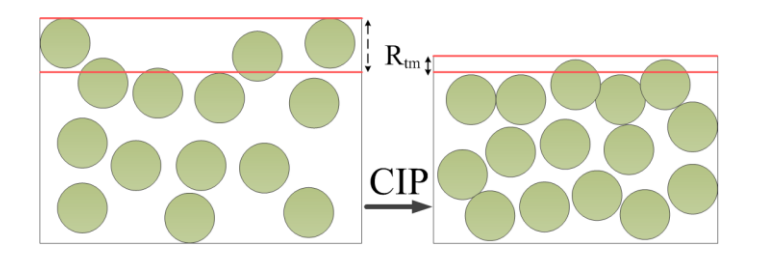


Figure 9.2 Illustration of particles densification in CIP process

The average distance between the highest peak and lowest valley in each sampling length is defined as a parameter (R_{tm}) and used as the measure of the surface roughness. After pressing, the R_{tm} value will decrease, while the size and number of the voids will also decrease theoretically.

Another approach to densify the thick film is replacing the binder system with one that has a lower viscosity. More powers can be loaded into the pastes with the same viscosity because of a lower thinner binder, which also densify the thick films from the pastes point of view.

Addictive of conductive polymer is another potential solution for applying TEGs onto textile [64]. With conductive polymers (normally PEDOT:PSS), the printed films will reach a reasonable resistivity by curing the films around 150°C. According to Kato and Jiang [125, 126], a PEDOT:PSS coated BiTe film could provide a resistivity of around 1-3 ×10-2 Ω ·cm and a Seebeck coefficient of around 20-30 μ V/K. However, PODOT:PSS was naturally separate from the BiTe particles when in paste form. Investing and optimizing the fabrication process of PEDOT + BiTe/SbTe pastes are valuable for realising TEGs on textile.

Reference

- [1] D. Rowe, "Thermoelectrics, an environmentally-friendly source of electrical power," *Renewable Energy*, vol. 16, pp. 1251-1256, 1999.
- [2] M. E. Kiziroglou, S. W. Wright, T. T. Toh, P. D. Mitcheson, T. Becker, and E. M. Yeatman, "Design and Fabrication of Heat Storage Thermoelectric Harvesting Devices," *Industrial Electronics, IEEE Transactions*, vol. 61, pp. 302-309, 2014.
- [3] V. V. Gusev, A. A. Pustovalov, N. N. Rybkin, L. I. Anatychuk, B. N. Demchuk, and I. Y. Ludchak, "Milliwatt-Power Radioisotope Thermoelectric Generator (RTG) Based on Plutonium-238," *Journal of Electronic Materials*, vol. 40, pp. 807-811, 2011.
- [4] S. B. Riffat and X. Ma, "Thermoelectrics: a review of present and potential applications," *Applied Thermal Engineering*, vol. 23, pp. 913-935, 2003.
- [5] V. Leonov and R. J. M. Vullers, "Wearable electronics self-powered by using human body heat: The state of the art and the perspective," *Journal of Renewable and Sustainable Energy*, vol. 1, p. 062701, 2009.
- [6] R. Sarpeshkar, *Ultra low power bioelectronics* vol. 1: Cambridge University Press Cambridge, UK, 2010.
- [7] S. Park and S. Jayaraman, "Smart textile-based wearable biomedical systems: a transition plan for research to reality.," *IEEE transactions on information technology in biomedicine : a publication of the IEEE Engineering in Medicine and Biology Society*, vol. 14, pp. 86-92, 2010.
- [8] H. J. Goldsmid, *Applications of Thermoelectricity*. London: Methuen, Wiley, 1960.
- [9] S. O. Kasap, *Principles of electronic materials and devices*: McGraw-Hill, 2006.
- [10] T. Geballe and G. Hull, "Seebeck Effect in Germanium," *Physical Review*, vol. 94, pp. 1134-1140, 1954.
- [11] C. Herring, "Theory of the Thermoelectric Power of Semiconductors," *Physical Review*, vol. 96, pp. 1163-1187, 12/01/1954.
- [12] S. Kasap, "Thermoelectric effects in metals: thermocouples," *Department of Electrical Engineering University of Saskatchewan Canada*, pp. 1-11, 2001.
- [13] S. Beeby and N. White, *Energy Harvesting for Autonomous Systems*: Artech House, 2010.
- [14] G. Min, D. M. Rowe, and K. Kontostavlakis, "Thermoelectric figure-of-merit under large temperature differences," *Journal of Physics D: Applied Physics*, vol. 37, pp. 1301-1304, 2004.
- [15] D. M. Rowe and C. M. Bhandari, *Modern thermoelectrics*: Holt Rinehart and Winston, 1983.
- [16] W. M. Haynes and D. R. Lide, CRC Handbook of Chemistry and Physics: A Ready-Reference Book of Chemical and Physical Data: Taylor & Francis Group, 2010.
- [17] C. L. Chien and C. R. Westgate, *The Hall effect and its applications*: Plenum Press, 1980.
- [18] J. E. Parrott and A. D. Stuckes, *Thermal conductivity of solids*: Pion, 1975.
- [19] G. S. Nolas, J. Sharp, and H. J. Goldsmid, *Thermoelectrics: Basic Principles and New Materials Developments*: Springer, 2001.
- [20] V. Shubha and T. Ramesh, "Continuous and rapid measurement of Seebeck coefficient using operational amplifier circuitry," *Journal of Physics E: Scientific Instruments*, vol. 9, p. 435, 1976.

- [21] A. Shakouri, "Recent Developments in Semiconductor Thermoelectric Physics and Materials," *Annual Review of Materials Research*, vol. 41, pp. 399-431, 2011
- [22] I. B. Cadoff and E. Miller, Thermoelectric materials and devices: Lectures presented during the course on thermoelectric materials and devices sponsored by the Dept. of Metallurgical Engineering in cooperation with the Office of Special Services to Business and Industry, New York University, New York, N. Y., June 1959 and 1960: Reinhold Pub. Corp., 1960.
- [23] O. Madelung, Semiconductors: Data Handbook: Springer, 2004.
- [24] H. J. Goldsmid, Introduction to Thermoelectricity: Springer, 2009.
- [25] G. J. Snyder and E. S. Toberer, "Complex thermoelectric materials.," *Nature materials*, vol. 7, pp. 105-14, 2008.
- [26] G. J. Snyder, "Small Thermoelectric Generators," *The Electrochemical Society Interface*, pp. 54-55, 2008.
- [27] M. Lossec, B. Multon, H. Ben Ahmed, and C. Goupil, "Thermoelectric generator placed on the human body: system modeling and energy conversion improvements," *The European Physical Journal Applied Physics*, vol. 52, p. 11103, 2010.
- [28] Rowe, Morgen, and Kiely, "Miniature Low-Power/High-Voltage Thermoelectric Generator," *Electronics Letters*, vol. 25, pp. 166-168, 1989.
- [29] M. Strasser, "Miniaturized thermoelectric generators based on poly-Si and poly-SiGe surface micromachining," *Sensors and Actuators A: Physical*, vol. 97-98, pp. 535-542, 2002.
- [30] M. Strasser, "Micromachined CMOS thermoelectric generators as on-chip power supply," *Sensors and Actuators A: Physical*, vol. 114, pp. 362-370, 2004.
- [31] S. M. Yang, M. Cong, and T. Lee, "Application of quantum well-like thermocouple to thermoelectric energy harvester by BiCMOS process," *Sensors and Actuators A: Physical*, vol. 166, pp. 117-124, 2011.
- [32] E. Topal, O. Zorlu, H. Kulah, and A. Muhtaroglu, "A Cr-Ni thermoelectric MEMS energy harvester for low profile applications," in *Energy Aware Computing (ICEAC)*, 2011 International Conference on, 2011, pp. 1-6.
- [33] H. Bottner, J. Nurnus, a. Gavrikov, G. Kuhner, M. Jagle, C. Kunzel, *et al.*, "New Thermoelectric Components Using Microsystem Technologies," *Journal of Microelectromechanical Systems*, vol. 13, pp. 414-420, 2004.
- [34] M. Kishi, H. Nemoto, T. Hamao, M. Yamamoto, S. Sudou, M. Mandai, *et al.*, "Micro thermoelectric modules and their application to wristwatches as an energy source," in *Thermoelectrics*, 1999. Eighteenth International Conference on, 1999, pp. 301-307.
- [35] N. Kouma, T. Nishino, and O. Tsuboi, "A high-output-voltage microthermoelectric generator having high-aspect-ratio structure," *Journal of Micromechanics and Microengineering*, vol. 23, p. 114005, 2013.
- [36] K. Itoigawa, H. Ueno, M. Shiozaki, T. Toriyama, and S. Sugiyama, "Fabrication of flexible thermopile generator," *Journal of Micromechanics and Microengineering*, vol. 15, pp. S233-S238, 2005.
- [37] I. Stark and M. Stordeur, "New micro thermoelectric devices based on bismuth telluride-type thin solid films," in *Eighteenth International Conference on Thermoelectrics. Proceedings, ICT'99 (Cat. No.99TH8407)*, 1999, pp. 465-472.

- [38] W. Glatz and C. Hierold, "Flexible micro thermoelectric generator," in *Micro Electro Mechanical Systems*, 2007. MEMS. IEEE 20th International Conference on, 2007, pp. 89-92.
- [39] W. Glatz, E. Schwyter, L. Durrer, C. Hierold, and S. Member, "Bi2Te3 -Based Flexible Micro Thermoelectric Generator With Optimized Design," *Microelectromechanical Systems*, vol. 18, pp. 763-772, 2009.
- [40] L. Francioso, C. De Pascali, I. Farella, C. Martucci, P. Cretì, P. Siciliano, *et al.*, "Flexible thermoelectric generator for ambient assisted living wearable biometric sensors," *Journal of Power Sources*, vol. 196, pp. 3239-3243, 2011.
- [41] P. J. Holmes and R. G. Loasby, *Handbook of thick film technology*: Electrochemical Publications, 1976.
- [42] N. White and J. Turner, "Thick-film sensors: past, present and future," *Measurement Science and Technology*, vol. 8, pp. 1-20, 1997.
- [43] H.-W. Lin, C.-P. Chang, W.-H. Hwu, and M.-D. Ger, "The rheological behaviors of screen-printing pastes," *Journal of Materials Processing Technology*, vol. 197, pp. 284-291, 2008.
- [44] Y. Wei, R. Torah, K. Yang, S. Beeby, and J. Tudor, "Screen printing of a capacitive cantilever-based motion sensor on fabric using a novel sacrificial layer process for smart fabric applications," *Measurement Science and Technology*, vol. 24, p. 075104, 2013.
- [45] P. J. Holmes and R. G. Loasby, *Handbook of thick film technology*: Electrochemical Publications, 1976.
- [46] K. Gilleo, *Polymer Thick Film: Today's Emerging Technology for a Clean Environment Tomorrow*. New York: Thomson publishing, 1996.
- [47] F. Garnier, R. Hajlaoui, A. Yassar, and P. Srivastava, "All-polymer field-effect transistor realized by printing techniques," *Science*, vol. 265, p. 1684, 1994.
- [48] G. Neudeck and A. Malhotra, "An amorphous silicon thin film transistor: Theory and experiment," *Solid-State Electronics*, vol. 19, pp. 721-729, 1976.
- [49] S. Franssila, *Introduction to Microfabrication*: John Wiley and Sons, 2010.
- [50] A. Piqué and D. B. Chrisey, *Direct-Write Technologies for Rapid Prototyping Applications*: Academic Press, 2002.
- [51] P. Wright, D. Dornfeld, and A. Chen, "Dispenser printing for prototyping microscale devices," *Trans. of NAMRI/ SME*, vol. 38, pp. 555-561, 2010.
- [52] A. Chen, "Thermal Energy Harvesting with Thermoelectrics for Self-powered Sensors: With Applications to Implantable Medical Devices, Body Sensor Networks and Aging in Place," ed, 2011.
- [53] C. C. Ho, J. W. Evans, and P. K. Wright, "Direct write dispenser printing of a zinc microbattery with an ionic liquid gel electrolyte," *Journal of Micromechanics and Microengineering*, vol. 20, p. 104009, 2010.
- [54] S. Duby, B. Ramsey, D. Harrison, and G. Hay, "Printed thermocouple devices," in *Sensors*, 2004. Proceedings of IEEE, ed: IEEE, 2004, pp. 1098-1101.
- [55] S. Duby and B. Ramsey, "Printed thick-film thermocouple sensors," *Electronics Letters*, vol. 41, pp. 6-7, 2005.
- [56] H. B. Lee, J. H. We, H. J. Yang, K. Kim, K. C. Choi, and B. J. Cho, "Thermoelectric properties of screen-printed ZnSb film," *Thin Solid Films*, vol. 519, pp. 5441-5443, 2011.
- [57] H.-B. Lee, H. J. Yang, J. H. We, K. Kim, K. C. Choi, and B. J. Cho, "Thin-Film Thermoelectric Module for Power Generator Applications Using a Screen-Printing Method," *Journal of Electronic Materials*, vol. 40, pp. 615-619, 2011.

- [58] J. Weber, K. Potjekamloth, F. Haase, P. Detemple, F. Volklein, and T. Doll, "Coin-size coiled-up polymer foil thermoelectric power generator for wearable electronics," *Sensors and Actuators A: Physical*, vol. 132, pp. 325-330, 2006.
- [59] C. Navone, M. Soulier, M. Plissonnier, and a. L. Seiler, "Development of (Bi,Sb)2(Te,Se)3-Based Thermoelectric Modules by a Screen-Printing Process," *Journal of Electronic Materials*, vol. 39, pp. 1755-1759, 2010.
- [60] a. Chen, D. Madan, P. K. Wright, and J. W. Evans, "Dispenser-printed planar thick-film thermoelectric energy generators," *Journal of Micromechanics and Microengineering*, vol. 21, p. 104006, 2011.
- [61] D. Madan, A. Chen, P. K. Wright, and J. W. Evans, "Dispenser printed composite thermoelectric thick films for thermoelectric generator applications," *Journal of Applied Physics*, vol. 109, p. 034904, 2011.
- [62] D. Madan, Z. Wang, and A. Chen, "High-Performance Dispenser Printed MA p-Type Bi0. 5Sb1. 5Te3 Flexible Thermoelectric Generators for Powering Wireless Sensor Networks," *ACS applied materials & interfaces*, vol. 5, pp. 11872-11876, 2013.
- [63] Z. Lu, M. Layani, X. Zhao, L. P. Tan, T. Sun, S. Fan, *et al.*, "Fabrication of Flexible Thermoelectric Thin Film Devices by Inkjet Printing," *Small*, vol. 10, pp. 3551-3554, September 10 2014.
- [64] T. M. Seeberg, A. Royset, S. Jahren, and F. Strisland, "Printed organic conductive polymers thermocouples in textile and smart clothing applications.," *Conference proceedings : ... Annual International Conference of the IEEE Engineering in Medicine and Biology Society. IEEE Engineering in Medicine and Biology Society. Conference*, vol. 2011, pp. 3278-81, 2011.
- [65] T. Ohta, T. Kajikawa, and Y. Kumashiro, "Characteristics of (Bi, Sb)2 (Te, Se)3-based thick-film thermoelectric elements for power generation," *Electrical Engineering in Japan*, vol. 110, pp. 14-23, 1990.
- [66] O. Bubnova, Z. U. Khan, A. Malti, S. Braun, M. Fahlman, M. Berggren, *et al.*, "Optimization of the thermoelectric figure of merit in the conducting polymer poly(3,4-ethylenedioxythiophene)." *Nature materials*, vol. 10, pp. 429-33, 2011.
- [67] H.-S. Kim, S. R. Dhage, D.-E. Shim, and H. T. Hahn, "Intense pulsed light sintering of copper nanoink for printed electronics," *Applied Physics A*, vol. 97, pp. 791-798, 2009.
- [68] V. Leonov, "Simulation of maximum power in the wearable thermoelectric generator with a small thermopile," *Microsystem Technologies*, vol. 17, pp. 495-504, 2011.
- [69] T. Torfs, V. Leonov, and R. Vullers, "Pulse oximeter fully powered by human body heat," *Sensors & Transducers Journal*, vol. 80, pp. 1230-1238, 2007.
- [70] V. Leonov, P. Fiorini, and S. Sedky, "Thermoelectric MEMS generators as a power supply for a body area network," *The 13th International Conference on Solid-State Sensors, Actuators and Microsystems*, pp. 291-294, 2005.
- [71] V. Leonov, T. Torfs, P. Fiorini, and C. Van Hoof, "Thermoelectric Converters of Human Warmth for Self-Powered Wireless Sensor Nodes," *IEEE Sensors Journal*, vol. 7, pp. 650-657, 2007.
- [72] V. Leonov, T. Torfs, C. Van Hoof, and R. J. M. Vullers, "Smart wireless sensors integrated in clothing: an electrocardiography system in a shirt powered using human body heat," *Sensors Transducers J.*, vol. 107, pp. 165-176, 2009.

- [73] M. K. Kim, M. S. Kim, S. E. Jo, H. L. Kim, S. M. Lee, and Y. J. Kim, "Wearable thermoelectric generator for human clothing applications," in 2013 Transducers & Eurosensors XXVII: The 17th International Conference on Solid-State Sensors, Actuators and Microsystems (TRANSDUCERS & EUROSENSORS XXVII), ed: IEEE, 2013, pp. 1376-1379.
- [74] V. Leonov, R. J. M. Vullers, and C. V. Hoof, "Thermoelectric generator hidden in a shirt with a fabric radiator," in *9th European Comference on Thermoelectrics* vol. 556, ed, 2012, pp. 556-559.
- [75] S. Jo, M. Kim, M. Kim, H. Kim, and Y. Kim, "HUMAN BODY HEAT ENERGY HARVESTING USING FLEXIBLE THERMOELECTRIC GENERATOR FOR AUTONOMOUS MICROSYSTEMS," in 16th International Conference on Miniaturized Systems for Chemistry and Life Sciences, ed. Okinawa, Japan, 2012, pp. 839-841.
- [76] S. P. Beeby, R. N. Torah, N. Grabham, M. J. Tudor, and N. M. White, "Thick-Film Piezoelectric Materials for High Temperature Applications," *Ferroelectrics*, vol. 313, pp. 63-69, 2004/01/01 2004.
- [77] H. Sun, D. Zhu, N. M. White, and S. P. Beeby, "A miniature airflow energy harvester from piezoelectric materials," *Journal of Physics: Conference Series*, vol. 476, p. 012057, 2013.
- [78] J. Severin and R. Hokke, "The adhesion of electroless Ni (P) on alumina ceramic using a vacuum-deposited Ti-Pd activator layer," *J. Electrochem. Soc.*, vol. 140, 1993.
- [79] J. Kuleshova, E. Koukharenko, X. Li, N. Frety, I. S. Nandhakumar, J. Tudor, *et al.*, "Optimization of the electrodeposition process of high-performance bismuth antimony telluride compounds for thermoelectric applications," *Langmuir*, vol. 26, pp. 16980-16985, 2010.
- [80] E. Koukharenko, "Elaboration et caractérisation microstructurale et électrique de tellurures de bismuth et d'antimoine élabores par utratremple," PhD, Université de Montpellier II (France), 2000.
- [81] T. Maruyama, "Nickel thin films prepared by chemical vapour deposition from nickel acetylacetonate," *Journal of materials science*, vol. 28, pp. 5345-5348, 1993.
- [82] D. H. Im, S. H. Hyun, S. Y. Park, B. Y. Lee, and Y. H. Kim, "Preparation of high dispersed nickel pastes for thick film electrodes," *Journal of Materials Science*, vol. 41, pp. 6425-6430, 2006.
- [83] S. a. Boye, P. Lazor, and R. Ahuja, "Magnetoresistance and Hall-effect measurements of Ni thin films," *Journal of Applied Physics*, vol. 97, p. 083902, 2005.
- [84] J. D. Grier, "Copper thick film conductor," ed: Google Patents, 1978.
- [85] T. Ogawa, M. Ootani, T. Asai, M. Hasegawa, and O. Ito, "Effect of inorganic binders on the properties of thick film copper conductor," *IEEE Transactions on Components, Packaging, and Manufacturing Technology: Part A*, vol. 17, pp. 625-630, 1994.
- [86] W. E. Campbell and U. B. Thomas, "The Oxidation of Metals," *Transactions of The Electrochemical Society*, vol. 91, pp. 623-640, April 1, 1947 1947.
- [87] X. Xu, H. Zhuang, W. Li, and G. Jiang, "Bonding behavior of copper thick films containing lead-free glass frit on aluminum nitride substrates," *Ceramics International*, vol. 30, pp. 661-665, 2004.
- [88] C. E. Armentrout, "The Hall effect in copper: An undergraduate experiment," *American Journal of Physics*, vol. 58, p. 758, 1990.

- [89] J. Steinberg, "Hall Effect and Specific Resistance of Evaporated Films of Silver, Copper and Iron," *Physical Review*, vol. 21, pp. 22-29, 1923.
- [90] T. Berlincourt, "Hall Effect, Magnetoresistance, and Size Effects in Copper," *Physical Review*, vol. 112, pp. 381-387, 1958.
- [91] a. H. Hitchcock and J. Stringer, "The temperature dependence of the Hall effect in α-phase copper-base alloys at high temperatures," *Journal of Physics D: Applied Physics*, vol. 4, pp. 810-817, 1971.
- [92] M. Ghosh, *Polyimides: Fundamentals and Applications*: Taylor & Francis, 1996.
- [93] P. J. Flory, *Principles of Polymer Chemistry*: Cornell University Press, 1953.
- [94] K. Yang, R. Torah, Y. Wei, S. Beeby, and J. Tudor, "Waterproof and durable screen printed silver conductive tracks on textiles," *Textile Research Journal*, vol. 83, pp. 2023-2031, 2013.
- [95] K. Yang, C. Freeman, R. Torah, S. Beeby, and J. Tudor, "Screen printed fabric electrode array for wearable functional electrical stimulation," *Sensors and Actuators A: Physical*, vol. 213, pp. 108-115, 2014.
- [96] G. Momen and M. Farzaneh, "Survey of Micro/Nano filler use to improve silicone rubber for outdoor insulators," *Rev. Adv. Mater. Sci*, vol. 27, pp. 1-13, 2011.
- [97] S. Pavlidou, S. Mai, T. Zorbas, and C. Papaspyrides, "Mechanical properties of glass fabric/polyester composites: Effect of silicone coatings on the fabrics," *Journal of applied polymer science*, vol. 91, pp. 1300-1308, 2004.
- [98] R. Hackam, "Outdoor HV composite polymeric insulators," *IEEE Transactions on Dielectrics and Electrical Insulation*, vol. 6, pp. 557-585, 1999.
- [99] Y. Li, R. Torah, S. Beeby, and J. Tudor, "Inkjet printed flexible antenna on textile for wearable applications," in *Textile Institute World Conference*, ed. Selangor, Malaysia, 2012.
- [100] 3M, "3M Scotchcast Electrical Resin 280 data sheet."
- [101] cas.chemnet.com. *Araldite* 502. Available: http://www.chemnet.com/cas/supplier.cgi?terms=25068-38-6&l=en&exact=dict&f=plist&mark=&submit.x=19&submit.y=12&submit=search
- [102] Intrinsiqmaterials. Copper Screen Paste. Available: http://intrinsiqmaterials.com/our-products/
- [103] PROSPECTOOR. *Polyurethane (PUR) Typical Properties Generic PUR, Unspecified.* Available: http://plastics.ides.com/generics/45/c/t/polyurethane-pur-properties-processing
- [104] PROSPECTOR, "Title," unpublished.
- [105] C. Wetzel, J. Schönfelder, W. Schwarz, and R. H. W. Funk, "Surface modification of polyurethane and silicone for therapeutic medical technics by means of electron beam," *Surface and Coatings Technology*, vol. 205, pp. 1618-1623, 2010.
- [106] J. Dai, "Surface modification of clays and clay–rubber composite," *Applied Clay Science*, vol. 15, pp. 51-65, 1999.
- [107] J. Roth, V. Albrecht, M. Nitschke, C. Bellmann, F. Simon, S. Zschoche, *et al.*, "Surface functionalization of silicone rubber for permanent adhesion improvement.," *Langmuir : the ACS journal of surfaces and colloids*, vol. 24, pp. 12603-11, 2008.

- [108] P. Vaqueiro and A. V. Powell, "Recent developments in nanostructured materials for high-performance thermoelectrics," *Journal of Materials Chemistry*, vol. 20, p. 9577, 2010.
- [109] a. N. Goldstein, C. M. Echer, and a. P. Alivisatos, "Melting in semiconductor nanocrystals.," *Science (New York, N.Y.)*, vol. 256, pp. 1425-7, 1992.
- [110] P. Couchman and W. Jesser, "Thermodynamic theory of size dependence of melting temperature in metals," *Nature*, vol. 269, p. 481, 1977.
- [111] V. I. Sarrak, "BRITTLE FRACTURE OF METALS," *Soviet Physics Uspekhi*, vol. 2, pp. 150-164, 1959.
- [112] Sigma-Aldrich. (2006). *Bismuth Telluride material safty data sheet*. Available: http://www.sigmaaldrich.com/MSDS/MSDS/DisplayMSDSPage.do?country eB&language=en&productNumber=401099&brand=ALDRICH&PageToG http://www.sigmaaldrich.com/MSDS/MSDS/DisplayMSDSPage.do?country=GB&language=en&productNumber=401099&brand=ALDRICH&PageToG http://www.sigmaaldrich.com/MSDS/MSDS/DisplayMSDSPage.do?country=GB&language=en&productNumber=401099&brand=ALDRICH&PageToG http://www.sigmaaldrich.com%2Fcatalog%2Fproduct%2Faldrich%2F401099%3Flang%3Den
- [113] R. Li, J. Liu, Y. Shi, L. Wang, and W. Jiang, "Balling behavior of stainless steel and nickel powder during selective laser melting process," *The International Journal of Advanced Manufacturing Technology*, vol. 59, pp. 1025-1035, 2011.
- [114] N. C. Norman, Chemistry of Arsenic, Antimony and Bismuth: Springer, 1997.
- [115] J. Fang, K. L. Stokes, J. A. Wiemann, W. L. Zhou, J. Dai, F. Chen, *et al.*, "Microemulsion-processed bismuth nanoparticles," *Materials Science and Engineering: B*, vol. 83, pp. 254-257, 2001.
- [116] J. P. Fleurial, L. Gailliard, R. Triboulet, H. Scherrer, and S. Scherrer, "Thermal properties of high quality single crystals of bismuth telluride—Part I: Experimental characterization," *Journal of Physics and Chemistry of Solids*, vol. 49, pp. 1237-1247, 1988.
- [117] C. Navone, M. Soulier, J. Testard, J. Simon, and T. Caroff, "Optimization and Fabrication of a Thick Printed Thermoelectric Device," *Journal of Electronic Materials*, vol. 40, pp. 789-793, 2011.
- [118] G. Delaizir, J. Monnier, M. Soulier, R. Grodzki, B. Villeroy, J. Testard, *et al.*, "A new generation of high performance large-scale and flexible thermogenerators based on (Bi,Sb)2 (Te,Se)3 nano-powders using the Spark Plasma Sintering technique," *Sensors and Actuators A: Physical*, vol. 174, pp. 115-122, 2012.
- [119] B. Poudel, Q. Hao, Y. Ma, Y. Lan, A. Minnich, B. Yu, *et al.*, "High-thermoelectric performance of nanostructured bismuth antimony telluride bulk alloys.," *Science (New York, N.Y.)*, vol. 320, pp. 634-8, 2008.
- [120] S. Li, H. M. a. Soliman, J. Zhou, M. S. Toprak, M. Muhammed, D. Platzek, *et al.*, "Effects of Annealing and Doping on Nanostructured Bismuth Telluride Thick Films," *Chemistry of Materials*, vol. 20, pp. 4403-4410, 2008.
- [121] Musashi. *ML-808FXcom-CE Specifications*. Available: http://www.musashi-engineering.co.jp/english/products/168/3-1-1-3-1.html
- [122] G. Gromov. *Thermoelectric Cooling Modules*. Available: http://rmtltd.ru/docs/technology/publications/Thermoelectric_Cooling_Modules.pdf
- [123] A. Khan, K. Rahman, D. S. Kim, and K. H. Choi, "Direct printing of copper conductive micro-tracks by multi-nozzle electrohydrodynamic inkjet printing process," *Journal of Materials Processing Technology*, vol. 212, pp. 700-706, 2012.

- [124] kobelco. *What is Cold Isostatic Pressing (CIP)?* Available: http://www.kobelco.co.jp/english/machinery/products/ip/technology/cip.html
- [125] Q. Jiang, C. Liu, H. Song, H. Shi, Y. Yao, J. Xu, *et al.*, "Improved thermoelectric performance of PEDOT:PSS films prepared by polar-solvent vapor annealing method," *Journal of Materials Science: Materials in Electronics*, vol. 24, pp. 4240-4246, 2013.
- [126] K. Kato, H. Hagino, and K. Miyazaki, "Fabrication of Bismuth Telluride Thermoelectric Films Containing Conductive Polymers Using a Printing Method," *Journal of Electronic Materials*, vol. 42, pp. 1313-1318, 2013.



Electronic & Technical Glasses

Product Data Tables

Product	Composition Family	Glass Type	Peak Fire Temp (°C)	Time @ Peak Temp (mins)	CTE @ 260 ℃	CTE @ Set Pt	Softening Point	Tg	DEN	Typical Powder Form
IP 550	Pb-Si-B-Al	V	585	10	65.0	74.4	551	453	4.44	RWG
CF 7586	Pb-Zn-B-Si	D	600	30	66.5	76.5	513	413	5.04	TF
EG 2012	Pb-B-Zn, Composite	V	425	15	74.0	76.9	*350	323	5.40	VEG
EG 1187	Pb-Si-Al-B	V	575	10	71.0	81.0	550	460	5.44	VWG
EG 2012	Pb-B-Zn, Composite	V	425	15	74.0	81.0	*350	305	5.44	VEG
EG 2016	Pb-B-Zn, Composite	V	430	15	73.0	81.0	*350	310	7.00	VEG
CF 7583	Pb-Zn-B	D	450	15	80.5	82.0	*372	269	6.08	VEG
EG 2018	Pb-B-Zn, Composite	V	430	10	78.0	83.0	*350	310	6.85	VEG
EG 1145	Pb-Si-Al-B	V	575	10	69.0	83.5	540	460	4.82	VWG
EG 2992	Bi-Zn-B	D	535	15	77.0	83.5	456	420	5.92	SRRG, VWG
EG 2964	Bi-Zn-B	V	560	15	63.5	84.5	520	480	4.85	VEG, VWG
EG 2922	Bi-Zn-Si	V	550	15	77.0	85.5	505	465	5.80	VWG
EG 4000	Pb-B-Zn, Composite	V	420	15	81.5	86.0	*350	295	5.90	VEG
EG 4015	Pb-B-Al-Si	V	580	10	75.0	86.0	515	435	5.20	VWG
CF 7575	Pb-Zn-B, Composite	D	450	60	83.0	91.1	370	285	6.20	VSD, TF
CF 7575	Pb-Zn-B, Composite	D	450	60	83.0	91.1	370	285	6.20	VSD, TF
EG 2020	Pb-B-Zn, Composite	V	390	10	84.0	93.8	*350	309	5.83	VEG
IP 530	Pb-Si-B-Al	V	540	10	80.0	94.0	498	417	5.21	RWG
CF 1417	Pb-B-Al	V	487	15	87.0	95.0	427	365	5.60	VSD
CF 7572	Pb-Zn-B	D	450	60	97.0	95.0	370	310	6.35	VSD, TF
EG 2749	B-Zn-Si-P-Ba	V	560	15	73.5	95.5	505	480	2.90	VWG

Notes:

Vitreous

Ď Crystallizing

Softening Point for base glass Fired Thermal Expansion

www.ferro.com

DISCLAIMER: Reasonable care has been taken in the preparation of this information, but FERRO EXTENDS NO WARRANTIES, MAKES NO REPRESENTATIONS AND ASSUMES NO RESPONSIBILITY AS TO ACCURACY OR SUITABILITY OF THIS INFORMATION OF THIS PRODUCT FOR ANY PURCHASER'S OR USER'S USE OR FOR ANY CONSEQUENCE OF ITS USE. FERRO DISCLAIMS ANY WARRANTY OF MERCHANTABILITY OR WARRANTY OF FITNESS FOR ANY PARTICULAR USE. All statements, technical information and recommendations contained herein are based on Seller's or Manufacturer's test and the test of others, and are believed to be accurate, but no guarantee of accuracy is made. Judgment as to the suitability of information herein or the user's purposes are necessarily the user's responsibility. Users shall determine the suitability of the products for their own intended application.

Users assume all risk of use or handling whether or not in accordance with any statements or recommendation of the seller or manufacturer, Liability, if any, is and shall be limited to the replacement of such quantity of material proved not to conform to specifications as set out in product specification. Statements concerning the possible use of these products are not intended as recommendation to use these products in infringement of any patent. No guarantee is made that any use of the products does not infringe third-party intellectual property or patent rights anywhere in the world.

Page 2 of 3 Rev 09/07



416 EAST CHURCH ROAD KING OF PRUSSIA, PA 19406-2625 USA T: 610.272.8000 F: 610.272.6759

www.electroscience.com

INSULATING COMPOSITION

4924

HOS Heaters on Steel® . COS Circuits on Steel® . TFOS Thick Film on Steel®

Cadmium, Lead, Nickel and Barium-Free*

ESL 4924 is a dielectric composition designed to insulate unabraded, unoxidized, ferritic steels. The 4924 is non-porous and its TCE closely matches that of BS970/1449 Type 430-S17 or AISI Type 430 stainless steel. Three separately fired layers of 4924, having a total minimum thickness of 80 micrometers, provide excellent breakdown voltage between top conductive prints and the stainless steel base. It is essential that the stainless steel is only handled using protective gloves and that all printing is carried out in clean room conditions. With ESL 9695 or 9501-CH terminations and 29XXX Series resistors used as heating elements 4924 is recommended as an 850°C firing overglaze. These materials are also useful in other TFOS (Thick Film on Steel)® applications.

PASTE DATA

RHEOLOGY: Thixotropic, screen printable paste

VISCOSITY:

(Brookfield RVT, ABZ Spindle, 10 rpm, 25.5° C $\pm 0.5^{\circ}$ C) 120 \pm 20 Pa-s COLOR: Dark blue SHELF LIFE: (25 °C) 6 months

PROCESSING

SCREEN MESH/EMULSION: 165 S/S, $0.0 \mu m$

LEVELING TIME: 5-10 minutes

DRYING AT 125 °C:

(Depending upon substrate volume) > 15 minutes FIRING TEMPERATURE: 850 °C to 930 °C

OPTIMUM: 850 °C

TIME AT PEAK: 10 minutes

4924 0412-C

Heraeus

Conductors

C7257

Nitrogen Fireable Copper Conductor

Description:

C7257 copper conductor is a practical alternative to precious metal materials in many applications. The advanced powder technology in C7257 results in improved fired film properties.

Key Benefits :

- Exceptionally high conductivity
- Migration resistant
- Low cost
- Leach resistant

Typical Properties:

Resistivity:

≤ 2.6 milliohms per square at 13 microns fired film thickness

Adhesion:

80x80 mil pad 62Sn/36Pb/2Ag @ 230°C RMA flux Initial ≥ 5.0 lbs

Aged ≥ 3.0 lbs (48 hours @ 150°C)

Solderability:

63Sn/37Pb @ 230°C 5 sec dip, RMA flux >95%

Solder Leaching : 10 sec Dips % Line Lost 63Sn/37Pb @ 230°C ≤ 5% <u><</u> 10% RMA Flux

Coverage: 100 cm²/g

Viscosity:

135-165 Kcps, Brookfield HBT, SC4-14@ 10 rpm, 25°C.

Solids:

90.0 ±1%

Recommended Processing Guidelines:

Printing:

280 stainless steel mesh screen 0.5 mil emulsion

Dry at 125°C for 15 minutes.

Firing Profile:

Fire in Nitrogen 900°C peak Dwell time of 9-11 minutes. Typical rise time of 20-23 minutes (measured from 100°C entry point) Total cycle time of 50-65 minutes

Line Resolution:

8 mils (200 microns)

Thickness:

Dried: 28 microns Fired: 11-15 microns

Heraeus RV-507 (Texanol®)

Warranty:

Material guaranteed to meet specifications for 6 months from date of shipment.

Storage:

Store in a dry location at 5°C-25°C. DO NOT REFRIGERATE. Allow paste to come to room temperature prior to opening. Spatulate well before using.

YY1010 8

W. C. Heraeus

Johnson Matthey Silver & Coating Technologies

S-020

Silver polymer thick film conductor ink

PRODUCT DATASHEET

Description

S-020 is a thermoplastic, screen-printable, highly conductive silver ink based on advanced silver flake technology. It is suitable for use in membrane switches and flexible circuits, and is designed for use with graphite inks C-810 and C-820 and UV dielectric inks K-910 and K-920. It has a long screen life and is compatible with all commonly used PET and flexible plastic substrates.

Features

- Excellent adhesion to polyester film
- Excellent line definition
- Excellent screen life
- Good shelf life

TYPICAL PHYSICAL PROPERTIES

Solids Content 73.3 wt%

Sheet Resistance $< 15 \text{ m}\Omega/\text{sq} @ 25 \mu\text{m}$

Viscosity 24,500 cP (Brookfield RVT, Spindle 6 at 20 rpm, 25°C)

Curing Conditions 15 minutes at 120°C in box oven

Shelf Life 12 months at 20°C

The information contained herein is based on data believed to be reliable, but Johnson Matthey makes no warranties expressed or implied as to its accuracy and assumes no liability arising out of its use by others. This publication is not to be taken as granting any licence to operate under patents, nor is it to be construed as implying that such operation will be free of infringement.



Johnson Matthey, Orchard Road, Royston, Herts, SG8 5HE, United Kingdom Tel: +44 (0)1763 253393 E-mail: silver@matthey.com



Product Information Silicone

Rubber Silastic® E RTV Silicone Rubber

FEATURES

- Easy release
- · High elongation
- · Minimum shrinkage
- Long working time
- Heat-accelerable cure
- High strength
- Tear resistance
- · Acceptable for food contact

COMPOSITION

 Two-part silicone rubber supplied as pourable liquid; cures to a flexible rubber

High-strength, tear-resistant silicone rubber creates flexible molds to reproduce intricate detail

APPLICATIONS

After mixing with its curing agent, Silastic® E RTV Silicone Rubber becomes a pourable liquid capable of forming durable, flexible molds for producing parts with unusual configurations, severe undercuts and close tolerances.

TYPICAL PROPERTIES

Specification Writers: These values are not intended for use in preparing specifications. Please contact your local Dow Corning sales office or your Global Dow Corning Connection before writing specifications on this product.

Method	Test	Unit	Result
As Supplied			
CTM ¹ 0176	Appearance		
	base		White
	curing agent		Clear
	Mixing Ratio,		
	base to curing agent, by weight		10:1
As Catalyzed –	10:1 Ratio, by weight		
CTM 0176	Appearance		White
CTM 0050	Viscosity2 at 25°C (77°F)	mPa-s (poise)	55,000(550)
CTM 0055	Pot Life ³	hours	2
CTM 0092A	Cure Time ⁴		
	at 25°C (77°F)	hours	24
As Cured - Ph	ysical Properties ⁵		
CTM 0099	Durometer Hardness, Shore A	points	35
CTM 0137A	Tensile Strength	MPa (psi)	5.5 (800)
CTM 0137A	Elongation, Die C	percent	350
CTM 0159A	Tear Strength, Die B	kN/m (ppi)	19 (110)
CTM 0022	Specific Gravity at 25°C (77°F)	417	1.14
CTM 0157	Linear Shrink		
	24 hours	percent	Nil
	7 days	percent	0.1

CTMs (Corporate Testing Methods) correspond to ASTM standard tests in most instances. Copies of CTM procedures are available upon request.

Protochfeld Viscometer Model HAF, spindle #6 at 5 Tpm.

Time required to double initial catalyzed viscosity.

**Based on sample thickness of 125 mils, cured 24 hours at 25°C (77°F).

DESCRIPTION

Silastic® E RTV Silicone Rubber is a two-part silicone rubber designed for use as a flexible moldmaking material. This high-strength, tear-resistant silicone rubber cures at room temperature with an addition-reaction

An easy-to-mix ratio of 10:1 base to curing agent ensures accurate measuring or blending by hand or machine. The material cures in unlimited thickness, regardless of part configuration or degree of confinement.

Product Information Electronics



Sylgard® 184 Silicone Elastomer

FEATURES & BENEFITS

- Flowable
- · Room temperature and heat cure
- · Good dielectric properties
- Rapid, versatile cure processing controlled by temperature
- High transparency allows easy inspection of components

COMPOSITION

- Two-part
- 10 to 1 mix ratio
- Polydimethylsiloxane elastomer

Transparent encapsulant with good flame resistance

APPLICATIONS

Sylgard® 184 Silicone Elastomer is suitable for:

- LED Lighting encapsulation
- Power supplies
- Connectors
- Sensors
- Industrial controls
- Transformers
- Amplifiers
- · High voltage resistor packs
 - Relays
- · Adhesive/encapsulant for solar cells
- · Adhesive handling beam lead integrated circuits during processing

TYPICAL PROPERTIES

Specification Writers: These values are not intended for use in preparing specifications. Please contact your local Dow Corning sales office or your Global Dow Corning Connection before writing specifications on this product.

Property	Unit	Result
One or Two Part		Two
Color		Colorless
Viscosity (Base)	cP	5100
	Pa-sec	5.1
Viscosity (Mixed)	cP	3500
	Pa-sec	3.5
Thermal Conductivity	btu/hr ft °F	0.15
	W/m °K	0.27
Specific Gravity (Cured)		1.03
Working Time at 25°C (Pot Life - hours)	hours	1.5
Cure Time at 25°C	hours	48
Heat Cure Time at 100°C	minutes	35
Heat Cure Time at 125°C	minutes	20
Heat Cure Time at 150°C	minutes	10
Durometer Shore		43
Dielectric Strength	volts/mil	500
	kV/mm	19



Preliminary Product Information Sheet

(Note: These are typical properties to be used as a guide only, not a specification. Data below is not guaranteed.

Different batches, conditions and applications yield differing results.)

MATERIAL ID: EPO-TEK® OG675 (formerly 75-145)

Date: Sep 2013

Rev:

Material Description: A UV fast curing, optically clear adhesive offering compliance and high strength.

Number of Components: Single Mix Ratio by Weight: N/A

Recommended Cure: 100mW/cm² @ 240-365 for > 2 seconds, depending on thickness - under an F-type Mercury lamp

Specific Gravity: 1.11

Pot Life: N/A

Shelf Life: One year at room temperature

NOTE: Container(s) should be kept closed when not in use. Filled systems should be stirred thoroughly before mixing and prior to use.

MATERIAL CHARACTERISTICS:

PHYSCIAL PROPERTIES:	
Color (before cure):	Clear/Colorless
Consistency	Pourable liquid
Viscosity (23°C):@ 100 rpm	3,426 cPs
Thixotropic Index:	N/A
Glass Transition Temp:	0.24 °C
Coefficient of Thermal Expan	nsion (CTE):
Below Tg:	41 x 10 ⁻⁶ in/in°C
Above Tg:	201 x 10 ⁻⁶ in/in°C
Shore A Hardness:	70
Degradation Temp:	365 ℃
Weight Loss:	
@ 200°C	0.33 %
@ 250°C	1.11 %
@ 300°C	2.53 %
Operating Temp:	
Continuous:	- 55°C to 200°C
Intermittent:	- 55°C to 300°C

ELECTRICAL AND THERMAL PROPERTIES:			
Thermal Conductivity:	N/A		
OPTICAL PROPERTIES @ 23°C:			
Spectral Transmission:	≥ 98% @ 400-1660 nm		
Index of Refraction:	1.479 @ 589 nm		

The data above is INITIAL only - it may be changed at anytime, for any reason without notice to anyone. It is provided only as a guide for evaluation/consideration.

EPOXY TECHNOLOGY, INC. 14 FORTUNE DRIVE, BILLERICA, MA 01821 (978) 667-3805, FAX (978) 663-9782 WEB SITE: www.epotek.com

^{*}These material characteristics are typical properties that are based on a limited number of samples/batches. All properties are based on the cure indicated above. Some properties may vary as manufactured quantities are scaled up to commercialized production levels.

```
f=fittype('a/(b*x^{(-1)+1)'},'coefficients',('a','b'));\\ Vfunc=fit(RL,V,f);\\ R=5:100;\\ v=(Vfunc(R))';\\ \% \ fit \ Power\\ p=1000*(v.^2)./r;
```